

UC San Diego

UC San Diego Electronic Theses and Dissertations

Title

Stabilization, dynamics, and control of chiral magnetic textures in thin-film multilayers

Permalink

<https://escholarship.org/uc/item/5cr1q1rm>

Author

Brock, Jeffrey Adams

Publication Date

2022

Peer reviewed|Thesis/dissertation

UNIVERSITY OF CALIFORNIA SAN DIEGO

Stabilization, dynamics, and control of chiral magnetic textures in thin-film multilayers

A dissertation submitted in partial satisfaction of the
requirements for the degree
Doctor of Philosophy

in
Materials Science and Engineering
by

Jeffrey A. Brock

Committee in charge:

Professor Eric E. Fullerton, Chair
Professor David Fenning
Professor Alex Fraño
Professor Vitaliy Lomakin
Professor Oleg Shpyrko

2022

Copyright
Jeffrey A. Brock, 2022
All rights reserved.

The dissertation of Jeffrey A. Brock is approved, and it is acceptable in quality and form for publication on microfilm and electronically.

University of California San Diego

2022

TABLE OF CONTENTS

Dissertation Approval Page	iii
Table of Contents	iv
List of Figures	vii
Acknowledgements	xvii
Vita.....	xix
Abstract of the Dissertation	xxiii
Chapter 1: Introduction.....	1
1.1 Motivation and Historical Background.....	1
1.2 Quantization of Angular Momentum	2
1.3 Magnetic Dipole Moment from Orbital Momentum.....	5
1.4 Dipole Moment from Spin Angular Momentum.....	7
1.5 Coupling of the Spin and Orbital Angular Momenta.....	10
1.6 Magnetic Ordering in Materials	12
1.7 Langevin Treatment of Ferromagnetic Ordering	15
1.8 Heisenberg Treatment of Ferromagnetic Order	20
1.9 Band Theory of Ferromagnetism	24
1.10 Domains in Ferromagnetic Materials: Demagnetizing Fields and Energy	26
1.11 Magnetic Anisotropy.....	29
1.12 Domain Walls.....	33
1.13 The Interfacial Dzyaloshinskii-Moriya Interaction.....	35
1.14 Skyrmion Stabilization: Material Considerations	41
1.15 Detecting iDMI and Exploitation of Magnetic Chirality	45
1.16 References	53
Chapter 2: Experimental Techniques.....	57
2.1 Sputter Deposition.....	57
2.2 X-ray Reflectivity Measurements	59
2.3 UV Photolithography	63
2.3 Vibrating Sample Magnetometry.....	66
2.4 Magneto-optic Kerr Effect Imaging.....	69

2.5	Magnetic Transmission X-ray Microscopy	72
2.6	Micromagnetic and Multiphysics Modeling	74
2.7	References	77
Chapter 3: Current-induced Skyrmion Generation in Pt/Co/Os/Pt Thin Films		78
3.1	Introduction	78
3.2	Experimental Techniques	79
3.3	Skyrmion Velocity and Population Dynamics	80
3.4	Imaging of Skyrmion Formation Processes	86
3.5	Conclusion.....	93
3.6	References	94
Chapter 4: Creating Skyrmion Phases Using Joule Heating.....		97
4.1	Introduction	97
4.2	Experimental Methods	98
4.3	Experimental Results and Discussion	102
4.4	Conclusion.....	119
4.5	References	120
Chapter 5: Domain Morphology Phase Transitions in the Limit of Low Exchange Stiffness ...		123
5.1	Introduction	123
5.2	Experimental Techniques.....	125
5.3	Experimental Results.....	126
5.4	Discussion and Modeling.....	139
5.5	Spatiotemporal Dynamics of the Domain Fluctuations	146
5.6	Conclusion.....	156
5.7	References	157
Chapter 6: Dynamic Symmetry Breaking in Chiral Magnetic Systems		162
6.1	Introduction	162
6.2	Experimental Techniques.....	162
6.3	Experimental Results.....	164
6.4	Analytical Modeling.....	174
6.5	Conclusion.....	183
6.6	References	184

Chapter 7: Half-skyrmions and Spin-orbit Torque	187
7.1 Introduction	187
7.2 Experimental Techniques	189
7.3 Experimental Results.....	190
7.4 Analytical Modeling and Discussion	195
7.6 References	204
Chapter 8: Conclusion.....	207
8.1 Dissertation Summary	207
8.2 Future Outlook	209

LIST OF FIGURES

Figure 1.1: The possible m values of an electron in a p orbital relative to an applied magnetic field H	5
Figure 1.2: A schematic depiction of the Stern-Gerlach experiment.	8
Figure 1.3: The possible orientations of the spin angular momentum with respect to an applied magnetic field H for spin magnetic quantum numbers m_{spin} of $\pm 1/2$	9
Figure 1.4: The orientation of magnetic dipole moments in paramagnets, antiferromagnets, ferromagnets, and ferrimagnets. This schematic depiction assumes zero applied magnetic field.....	15
Figure 1.5: Plots of both the Langevin function and the Weiss molecular field as a function of $\alpha = mH/k_B T$	19
Figure 1.6: Net magnetization (relative to the value at $T = 0$) predicted for Fe, Co, and Ni as a function of temperature (normalized to the Curie temperature). Curve (a) was calculated using the Langevin treatment, while curves (b) and (c) were calculated using the Brillouin treatment with $J = 1$ and 0.5 , respectively.	20
Figure 1.7: Possible spin configurations for a He atom where each electron is confined to its own s -orbital.	21
Figure 1.8: (a) Density of electronic states D as a function of energy E under the assumption of the rigid band model for the $4s$ and $3d$ electronic bands. Schematic depictions of the spacing between energy levels and the energy range of the $4s$ (b) and $3d$ (c) electronic bands.	26
Figure 1.9: Schematic depiction of the demagnetizing field H_d generated when an ellipsoid-shaped sample is magnetized along its long axis.....	27
Figure 1.10: Demonstration of the magnetization (red arrows) and demagnetizing fields (yellow arrows) associated with the uniformly polarized and domain states in the thin-film geometry.	29

Figure 1.11: (a) Schematic depictions of the [100], [110], and [111] family of crystallographic directions in bcc Fe. (b) Schematic depictions of the degree of electron orbital overlap when a ferromagnetic sample is magnetized along different directions. (c) Experimentally determined magnetization along different crystal axes in bcc Fe.	31
Figure 1.12: Schematic depiction of Bloch and Néel-type DWs in a ferromagnetic thin film. The + signs indicate where the magnetic charges are localized.....	34
Figure 1.13: SPLEEM image of a system exhibiting achiral Bloch-type magnetic domain walls.	35
Figure 1.14: The non-centrosymmetric B ₂₀ -type crystal structure of the weak ferromagnet MnSi.	37
Figure 1.15: The action of the interfacial Dzyaloshinskii-Moriya interaction at an interface between Ir and Fe.	37
Figure 1.16: Schematic depiction of how the tendency of the iDMI to favor certain transitions between electronic orbitals in turn sets a handedness to how the magnetic moment transitions when moving in space between regions of a ferromagnet with different magnetic polarizations relative to the z-axis..	39
Figure 1.17: SPLEEM image of a system exhibiting chiral Néel-type domain walls.	39
Figure 1.18: Cross-sectional profile of the magnetic orientation when traveling from an “up” to “down” to “up” domain in a system with chiral Néel-type domain walls.	40
Figure 1.19: Mapping of the two-dimensional profile of a Néel-type skyrmion (bottom) to completely cover the three-dimensional unit sphere exactly one time (top).	42
Figure 1.20: The predicted sign and magnitude of iDMI energy density originating at different heavy metal/ferromagnet interfaces.	42
Figure 1.21: An example of how structural inversion asymmetry and material choice can be used to impart a net iDMI to a ferromagnetic layer. Note the parallel alignment of the <i>D</i> vectors indicated at the Ir/Fe and Co/Pt interfaces.	43

Figure 1.22: Asymmetric domain expansion in a system exhibiting iDMI and PMA exposed to a static in-plane magnetic field (H_x) and a pulsed out of plane magnetic field (H_z).	47
Figure 1.23: Demonstration of how a charge current J_C can lead to the development of a transverse spin current J_S in thin layers of heavy metals with large spin-orbit coupling.	49
Figure 1.24: Schematic depiction of a ferromagnetic film with perpendicular magnetic anisotropy and right-handed Néel-type domain walls grown on top of a heavy metal layer with large spin-orbit coupling.	50
Figure 1.25: Overview of the vertical DW racetrack memory architecture and how data/ domain states can be read using a magnetoresistive sensor and written to the racetrack using the Oersted field created by a stripline.	51
Figure 1.26: (a) Schematic illustration of reservoir computing, whereby the input signals act on a disordered, randomly linked ensemble of dynamical elements to give rise to a non-linear output. (a) illustration of how the memory architecture demonstrated in (a) can be realized from an ensemble of magnetic skyrmions.	53
Figure 2.1: Schematic depiction of the sputtering process.....	58
Figure 2.2: Schematic diagram of the geometry and principle of an X-ray reflectivity (XRR) measurement of film thickness.	61
Figure 2.3: X-ray reflectivity (XRR) profile of a CoO thin film, collected using Cu $K\alpha$ radiation.	63
Figure 2.4: Schematic depiction of several important steps of the photomask lithography process when a negative-tone photoresist is used. The yellow layers indicate a generic metal layer deposited using sputter deposition.	65
Figure 2.5: Schematic depiction of the vibrating sample magnetometry (VSM) measurement technique, as discussed in Chapter 2.3.....	68
Figure 2.6: Schematic illustration of the magneto-optic Kerr effect.....	70

Figure 2.7: Polar MOKE image of a Pt/Co/Ni-based multilayer sample. Dark (light) coloring indicates regions where the perpendicular magnetization component is oriented “up” (“down”) relative to the film plane. This image was obtained using a 50x objective lens. 71

Figure 2.8: Schematic illustration of the beam path of the XM-1 microscope, located at the Advanced Light Source, Lawrence Berkeley National Laboratory..... 74

Figure 2.9: Schematic illustration of the damping and precessional terms of the Landau-Lifshitz-Gilbert (LLG) equation that describe the dynamics of the magnetization M about the effective magnetic field H_{eff} 76

Figure 3.1: MOKE images of the same region of a Pt/Co/Os/Pt sample collected immediately before and 10 seconds after electrical current densities of 0.03 MA/cm² and 0.17 MA/cm² were applied 81

Figure 3.2: (a) Average velocity of skyrmions moving under the influence of several current densities, as a function of time. (b) The number of skyrmions present within the 180 μm x 100 μm field of view as a function of time.. 82

Figure 3.3: (a) Number of skyrmions present in the field of view immediately before the electrical current was removed. (b) Number of skyrmions present in the field of view 10 seconds after the electrical current was removed. (c) For an applied field of $H_z = +0.7$ Oe, a comparison of the findings of (a) and (b)..... 84

Figure 3.4: (a)-(e) Time-lapse MOKE images of the process by which a stripe domain (red outline) elongates, kings, and generates a skyrmion. (f)-(j) Sequential MOKE images of the depinning of a stripe domain (pink outline), mediated by a passing skyrmion. 87

Figure 3.5: (a)-(c) The number of skyrmions present within a 180 μm x 33 μm field of view as a function of time for a variety of regions along the y axis of the wire (d) the z component of the Oersted field generated by a 0.23 MA/cm² electrical current.. 90

Figure 4.1: Experimental techniques used to estimate the temperature changes due to Joule heating for a Ta (2)/Pt (5)/[Co (0.7)/ Ni (0.5)/Pt (0.7)]₂₀/Ta (5) device patterned in to a 3 mm-long, 10 μm -wide wire on a SiN membrane 101

Figure 4.2: Simulations of the temperature change due to Joule heating in a [Co/Ni/Pt]-type sample	102
Figure 4.3: MTXM images illustrating the effect of a 60 μ s-long current pulse of density 1.7×10^{10} A/m ² on the domain morphology of a [Co (0.7 nm)/ Ni (0.5 nm)/ Pt (0.7 nm)] ₂₀ wire for $\mu_0 H_z = 0$ (a,d), +50 mT (b,e), and +250 mT (c,f).....	104
Figure 4.4: MTXM images of the magnetic domain morphology as the out-of-plane magnetic field was swept from zero towards positive saturation then back to zero in a [Co (0.7 nm)/ Ni (0.5 nm)/ Pt (0.7 nm)] ₂₀ sample.	105
Figure 4.5: MTXM images of the skyrmion phase in the [Co (0.7 nm)/ Ni (0.5 nm)/ Pt (0.7 nm)] ₂₀ sample as the out-of-plane field strength was varied.....	106
Figure 4.6: $\tau - \mu_0 H_z$ phase maps for the (a) [Co (0.7 nm)/ Ni (0.5 nm)/ Pt (0.7 nm)] ₂₀ and (b) [Co (0.7 nm)/ Tb (0.4 nm)/ Ni (0.5 nm)/ Pt (0.7 nm)] ₂₀ samples indicating the change in domain morphology observed after pulses of $j = 1.7 \times 10^{10}$ A/m ² (a) and 2.4×10^9 A/m ² (b) were applied.....	107
Figure 4.7: (a) Out-of-plane and (b) in-plane vibrating sample magnetometry data for the [Co (0.7)/Spacer (0.4)/Ni (0.5)/Pt (0.7)] ₂₀ (thicknesses in nm) samples, collected at room temperature. (c) Saturation magnetization M_s and effective perpendicular anisotropy energy density K_{eff} of the samples determined from (a) and (b).....	109
Figure 4.8: (a) the saturation magnetization M_s as a function of temperature and (b) in-plane hysteresis loops at selected temperatures of an unpatterned [Co (0.7)/ Tb (0.4)/ Ni (0.5)/ Pt (0.7)] ₂₀ (thicknesses in nm) sample, determined using vibrating sample magnetometry.	110
Figure 4.9: MTXM images of the magnetic domain morphology of a [Co (0.7)/ Tb (0.4)/ Ni (0.5)/ Pt (0.7)] ₂₀ (thicknesses in nm) sample as an out of plane magnetic field was swept from zero towards positive saturation, then back to zero field.	111
Figure 4.10: MTXM images depicting the domain morphology (a) before and (b) after a 200 μ s-long pulse of current density 2.4×10^9 A/m ² was applied in a perpendicular magnetic field of +40 mT. The blue arrow indicates the electron flow direction j_e , and the scale bar represents 500 nm.	112

- Figure 4.11: MTXM images collected before and after a 50 μs -long current pulse with current density $1.7 \times 10^{10} \text{ A/m}^2$ was applied to a $[\text{Co/Ni/Pt}]_{20}$ -type sample capped with Pt (a,c) or Ta (b,d) in an applied magnetic field of +50 mT. The scale bar indicates 400 nm. 113
- Figure 4.12: (a) depiction of the composite pulse employed to delineate between Joule heating and spin-orbit torques. (b-i) MTXM images of a $[\text{Co (0.4)/ Tb (0.4)/ Co (0.4)/ Ni (0.5)/ Pt (0.7)}]_{20}$ sample (thicknesses in nm) illustrating the effects of delivering the same Joule heating a by changing the relative delay of the spike pulse 114
- Figure 4.13: (a) Schematic depictions of the variation in pulse duration and current density used to supply an equivalent amount of Joule heating using different duration pulses. (b-g) MTXM images of a $[\text{Co (0.4)/ Tb (0.4)/ Co (0.4)/ Ni (0.5)/ Pt (0.7)}]_{20}$ sample (thicknesses in nm) illustrating the effect of delivering the the pulses in (a) 115
- Figure 4.14: The energy profile of isolated bubble domains at several perpendicular field strengths in proximity to the lowest $\mu_0 H_z$ necessary for skyrmion nucleation in the (a) $[\text{Co/Ni/Pt}]_{20}$ and (b) $[\text{Co/Tb/Ni/Pt}]_{20}$ samples..... 117
- Figure 4.15: (a) The experimentally estimated temperature change due to Joule heating $\Delta T_{\text{est, st} \rightarrow \text{sk}}$ and (b) perpendicular magnetic field ($\mu_0 H_{z, \text{st} \rightarrow \text{sk}}$) necessary to initiate a complete stripe-to-skyrmion transformation in the $[\text{Co/Ni/Pt}]$ -based samples discussed in this chapter..... 118
- Figure 5.1: Polar MOKE images of domain growth of a $+M_z$ domain in a $[\text{Pt/Co (0.35 nm)}]_2$ sample after several out-of-plane magnetic field pulses were applied in in-plane fields $\mu_0 H_x$ of (a) 0 mT and (b) +50 mT. (c) the expansion velocity of “up” to “down” and “down” to “up” domains as a function of $\mu_0 H_x$ 128
- Figure 5.2: (a) Saturation magnetization as a function of temperature for $[\text{Pt/Co}]_2$ samples with varying Co thicknesses. (b) Polar MOKE hysteresis loops for $[\text{Pt/Co}]_2$ samples with $0.23 \text{ nm} \leq t_{\text{Co}} \leq 0.26 \text{ nm}$, collected at $T = 296 \text{ K}$. (c-f) Room temperature ($T = 296 \text{ K}$) remanent states of the $[\text{Pt/Co}]_2$ samples with different t_{Co} 130
- Figure 5.3: For the $[\text{Pt/Co (0.24 nm)}]_2$ sample: (a) Out-of-plane and (b) in-plane magnetometry data collected in the temperature range of $294 \text{ K} \leq T \leq 302 \text{ K}$. (c-f) Polar MOKE images collected as the perpendicular magnetic field strength $\mu_0 H_z$ was quasi-statically stepped from $\mu_0 H_z = 0$ toward negative saturation at $T = 296 \text{ K}$ 132

Figure 5.4: Polar MOKE images of the [Pt/Co (0.26 nm)] ₂ sample, collected as the perpendicular magnetic field strength $\mu_0 H_z$ was quasi-statically stepped from $\mu_0 H_z = 0$ towards negative saturation. When imaging, the sample temperature was approximately 315 K.....	133
Figure 5.5: (a-d) Polar MOKE images (collected at $T = 296$ K) depicting the motion of several skyrmions in the [Pt/Co (0.24 nm)] ₂ sample before and after a current density of $j_e = 7.6 \times 10^9$ A/m ² was passed through the sample (e) Velocity of skyrmions along the x -axis (v_x) in the [Pt/Co (0.24 nm)] ₂ sample as a function of j_e	135
Figure 5.6: (a) Remanent domain morphology of the [Pt/Co/Ni/Re] ₂ sample, where the Co layers were grown such that t_{Co} decreases by ~ 0.06 % when moving from left to right across the field of view. Remanent state and densest $\mu_0 H_z$ -induced skyrmion phases observed in the (b,c) [Pt/Co/Ni/Re] ₂ and (d,e) [Pt/Co/Ni] ₂ samples.....	137
Figure 5.7: For the [Pt/Co/NiCu] ₁ sample: (a) out-of-plane and (b) in-plane magnetometry data collected at various temperatures. (c) Saturation magnetization M_s over the temperature range $250 \text{ K} \leq T \leq 360 \text{ K}$ Polar MOKE images collected in perpendicular magnetic fields of 0 and -0.04 mT ((d) and (e), respectively).	139
Figure 5.8: Micromagnetic and analytic modeling results for the [Pt/Co/NiCu] ₁ sample.	141
Figure 5.9: $\Delta\varepsilon$ and σ as a function of A_{ex} and K_u for different values of D in the [Pt/Co/NiCu] ₁ sample	143
Figure 5.10: Images of the remanent domain morphology in at [Pt/ Co (0.24 nm)] ₂ sample collected at temperatures of (a) 293.6 K, (b) 294.2 K, (c) 294.8 K, and (d) 295.7 K. (e) The measured domain periodicity as a function of temperature for the same [Pt/ Co (0.24 nm)] ₂ sample.	147
Figure 5.11: For a [Pt/ Co (0.24 nm)] ₂ sample, (a) the pixel fraction changed as a function of time at various temperatures, and (b) the average pixel fraction change per frame as a function of temperature.....	148
Figure 5.12: “Heatmaps” for a [Pt/ Co (0.24 nm)] ₂ sample, indicating the switching activity of each pixel over the course of 60 s of observation in zero applied magnetic field.	150

- Figure 5.13: (a) Anomalous Hall resistance R_{Hall} as a function of perpendicular magnetic field for a [Pt/ Co (0.24 nm)]₂ sample, patterned in to a 50 μm -wide wire using UV metal liftoff photolithography. (b) dc susceptibility χ as a function of temperature for the same sample..... 151
- Figure 5.14: ac susceptibility measurements of a [Pt/ Co(0.24 nm)]₂ sample, collected at several different frequencies. The amplitude of the sinusoidal ac field used during the measurements was ~ 0.3 mT. To measure the Hall resistance (and obtain the susceptibility using Equation 5.2), a sensing current of 10 μA was used..... 154
- Figure 6.1: Room temperature magnetic hysteresis loops of the [Co(0.7 nm)/ Ni(0.5 nm)/ Pt(0.7 nm)]_N samples collected in the (a) out-of-plane and (b) in-plane geometries using vibrating sample magnetometry..... 164
- Figure 6.2: Polar MOKE images of magnetic domain growth in the [Co/Ni/Pt]₂ (a-d) and [Co/Ni/Pt]₃ (e-l) samples in response out-of-plane (a-h) and into-plane (i-l) magnetic field pulses. (m) The favored growth direction of dendritic stripe domains in the [Co/Ni/Pt]₃ sample for different permutations in domain orientation. 165
- Figure 6.3: Expansion velocity as a function of in-plane magnetic field $\mu_0 H_x$ of \uparrow to \downarrow and \downarrow to \uparrow domain walls in the [Co/Ni/Pt]₂ sample. Data was collected using 5 ms-long perpendicular field pulses of 15 mT. Blue arrows indicate the commonly attributed measure of the effective magnetic field generated by the iDMI $\mu_0 H_{\text{DMI}}$ 167
- Figure 6.4: The long-wavelength stiffness $\tilde{\sigma}$ (solid lines) and 1D linear DW energy density σ (dashed lines) of a domain wall as a function of in-plane applied magnetic field $\mu_0 H_x$ for \uparrow to \downarrow and \downarrow to \uparrow domain walls in the [Co/Ni/Pt]₂ sample. The $\tilde{\sigma}$ and σ have been normalized to the resting energy of a Bloch domain wall σ_0 168
- Figure 6.5: Lorentz TEM images of the [Co/Ni/Pt]₅ sample, collected in zero applied magnetic fields when the sample was tilted (a) 30° and (b) 0° relative to the imaging beam. A domain state was formed before imaging through the application of a perpendicular magnetic field..... 169
- Figure 6.6: MOKE images depicting the growth of dendritic stripe domains in the [Co/Ni/Pt]_{0.7} sample for different permutations of domain orientation and in-plane field $\mu_0 H_x$ magnitudes and directions..... 170

- Figure 6.7: Brillouin light scattering (BLS) spectroscopy of the [Co/Ni/Pt]₅ sample, collected in the Damon-Eshbach geometry using a 532 nm-wavelength laser beam at an incidence angle of $\pi/4$. The sample magnetization was saturated in the film plane during the BLS measurement..... 171
- Figure 6.8: The growth direction θ_{growth} of “up” ($+M_z$) and “down” ($-M_z$) dendritic domains as a function of $\mu_0 H_x$, determined both experimentally (symbols) and analytically with steady-state dynamics and dispersive stiffness (lines)..... 172
- Figure 6.9: Polar MOKE images of the [Co/Ni/Pt]₃ sample as 5 ms-long, +15 mT perpendicular magnetic field pulses were applied in static in-plane fields of (a) -40 mT, (b) +120 mT, (c) -40 mT, and (d) +200 mT. The initial dendrite state was obtained by applying several perpendicular field pulses in a static in-plane field of -40 mT. 173
- Figure 6.10: Verification of the creep scaling law in the [Co/Ni/Pt]₃ sample, obtained from measurements of the expansion velocity v (in $\mu\text{m/s}$) for different perpendicular fields $\mu_0 H_z$ and in-plane fields $\mu_0 H_x$ 175
- Figure 6.11: Predicted DW magnetization profiles in the [Co/Ni/Pt]₃ sample under the assumption of static equilibrium (gold arrows) and steady-state dynamic reorientation (blue arrows) under applied in-plane fields of (a) $\mu_0 H_x = +5$ mT, (b) +40 mT, (c) +120 mT, and (d) +200 mT..... 177
- Figure 6.12: Dispersive stiffness $\tilde{\sigma}/\tilde{\sigma}_{\text{max}}$ (blue lines) and predicted relative expansion velocity v/v_{max} (red lines) as a function of azimuthal position θ for $+M_z$ dendritic stripe domains in the [Co/Ni/Pt]₃ sample in applied in-plane fields $\mu_0 H_x$ of (a) +5 mT, (b) +40 mT, (c) +120 mT, and (d) +200 mT. 181
- Figure 6.13: Relative velocity v/v_{max} as a function of azimuthal position θ for $+M_z$ dendritic stripe domains in the [Co/Ni/Pt]₃ sample in an applied in-plane field of +37 mT, calculated using the long-wavelength ($L \rightarrow \infty$) dispersive stiffness treatment... 182
- Figure 6.14: Plots showing the φ -dependence of the (a) calculated domain wall energy σ and (b) normalized restoring torque σ_φ at azimuthal positions of $\theta = 80^\circ$ (black) and $\theta = 150^\circ$ (red) for the [Co(0.7 nm)/Ni(0.5 nm)/Pt(0.7 nm)]₃ sample. 183

Figure 7.1: Room temperature hysteresis loops for the Pt/Co sample collected in the (a) out-of-plane and (b) in-plane geometry using vibrating sample magnetometry (VSM). 191

Figure 7.2: Ratio in the velocity of expansion of a $\downarrow\uparrow$ domain wall over that of a $\uparrow\downarrow$ domain wall in a [Co/Pt]₂ sample as a function of in-plane magnetic field $\mu_0 H_x$ 191

Figure 7.3: Polar MOKE images of the Co/Ni/Pt sample after several 10 ms-long current pulses of current density 3.5×10^{11} A/m² were applied in zero magnetic field. 193

Figure 7.4: Polar MOKE images of the Co/Pt sample after several 10 ms-long current pulses of current density 5.2×10^{11} A/m² were applied in zero magnetic field. The lower-right inset of (c) depicts the directional conventions used throughout this work. 194

Figure 7.5: For the Co/Ni/Pt sample, the growth direction θ_{growth} and expansion velocity v as a function of applied current density J 195

Figure 7.6: (a) The conventions used throughout this chapter to define the azimuthal angle on a half-skyrmion β and the DW core magnetization orientation ϕ . (b,c) Schematic depiction of the DW magnetization profile and SOT force interrelationship in a half-skyrmion. 198

Figure 7.7: (a) DW core magnetization orientation ϕ and (b) normalized Slonczewski effective perpendicular field H_{SL} as a function of azimuthal position β (c) Experimentally (solid markers) and analytically determined favored growth direction of half-skyrmions in the Co/Ni/Pt sample. 202

ACKNOWLEDGEMENTS

First and foremost, I would like to thank Prof. Eric Fullerton for his support and guidance over the past few years. I am enormously appreciative of his valuable suggestions, explanations, critiques, and the considerable degree of latitude he granted me in how I chose to spend my time in the lab. Additionally, his sense of humor and stories always managed to put any issues I was encountering into perspective and turn frustrations into learning experiences. While I am somewhat melancholy about leaving his group, I will always be thankful for the opportunities he has afforded me, and I know that he will continue serving as a role model to me throughout my future career.

Secondly, I would like to thank Profs. Lomakin, Shpyrko, Fraño, and Fenning for agreeing to serve on my doctoral committee. Their guidance regarding mathematical and experimental treatments outside of our group's usual toolbox has been particularly helpful in understanding some of the material presented in this dissertation.

Next, I would like to thank all Fullerton group members – both past and present. While one hears horror stories about the ultra-competitive nature of some research groups, I think that our group does an abnormally good job working together to divide the responsibilities associated with keeping an experimental lab running and sharing equipment so that everyone gets to perform their research in a timely manner. I can only hope that I continue working in groups that share this synergy. I would specifically like to thank Rob Tolley and Pierre Vallobra for the invaluable camaraderie and lessons they provided when I first arrived at UC San Diego. I also thank Sergio Montoya for allowing me to be a part of his work and introducing me to the world of synchrotron experiments. I also acknowledge the undergraduate and visiting students that have worked with

me over the past few years (Ruben Saatjian, Daan Swinkels, and Jacqueline Montes). It is my sincere hope that you had fun working in the lab, and that you gained some knowledge and skills along the way. I am also thankful to Marina Robenko and Octavio Ochoa for all they do to keep CMRR up and running while dealing with absent-minded researchers.

I would also like to acknowledge all the co-authors associated with the research presented in this dissertation. Thanks for the unique insights and research techniques you added to our work, and for allowing me to include these studies in my dissertation. I would also like to thank Prof. Mahmud Khan, my research advisor during my years at Miami University, for the guidance he provided and patience he exhibited as I took my first steps as a researcher.

Finally, I would like to thank my parents and Allison for their constant support during my graduate studies. It goes without saying that there were times where I skirted family and personal commitments during my graduate studies. I take this opportunity to thank you for your patience in dealing with my long hours, the times I forgot to respond to your messages, and the times that my work took me away for long periods of time. The research contained in this dissertation wouldn't have been possible without your behind-the-scenes understanding and compassion.

Chapter 3, in part, contains a reprint of research published as “Current-induced generation of skyrmions in Pt/Co/Os/Pt thin films” by J.A. Brock, P. Vallobra, R.D. Tolley, S.A. Montoya, S. Mangin, and E.E. Fullerton in *Physical Review B* 102, 024443 (2020). The dissertation author was the primary investigator and author of the manuscript.

Chapter 4, in part, contains a reprint of research published as “Energy-efficient generation of skyrmion phases in Co/Ni/Pt-based multilayers using Joule heating” by J.A. Brock, S.A. Montoya, M.-Y. Im, and E.E. Fullerton in *Physical Review Materials* 4, 104409 (2020). The dissertation author was the primary investigator author of the manuscript.

Chapter 5, in part, contains a reprint of research published as “Skyrmion stabilization at the domain morphology transition in ferromagnet/heavy metal heterostructures with low exchange stiffness” by J.A. Brock and E.E. Fullerton in *Advanced Materials Interfaces* (2021). The dissertation author was the primary investigator and author of the manuscript.

Chapter 6, in part, contains a reprint of research published as “Dynamic symmetry breaking in chiral magnetic systems” by J.A. Brock, M.D. Kitcher, P. Vallobra, R. Medapalli, M.P. Li, M. De Graef, G.A. Riley, H.T. Nembach, S. Mangin, V. Sokalski, and E.E. Fullerton in *Advanced Materials* 33, 2101524 (2021). The dissertation author was a co-primary investigator and author of the manuscript.

Chapter 7 is based on a manuscript being prepared for submission to a journal as “Interplay of the half-skyrmion topology and spin-orbit torque on the growth directionality of magnetic stripe domains” by J.A. Brock and E.E. Fullerton. The dissertation author was the primary investigator and author of the manuscript.

VITA

- 2022 Doctor of Philosophy in Materials Science and Engineering,
University of California San Diego
- 2017 Master of Science in Physics, Miami University
- 2015 Bachelor of Science in Physics, Miami University

PUBLICATIONS

- G.Q. Yan, S. Li, H. Lu, M. Huang, Y. Xiao, L. Wernert, J.A. Brock, E.E. Fullerton, H. Chen, C.R. Du, and H.L. Wang, “Nanoscale quantum sensing and imaging of spin-orbit torque-driven spin dynamics in noncollinear antiferromagnet Mn_3Sn ”, Submitted (2021).
- D. Turenne, A. Yaroslavtsev, X. Wang, V. Unikandanuni, I. Vaskivskyi, M. Schneider, E. Jal, R. Carley, G. Mercurio, R. Gort, N. Agarwal, B. Van Kuiken, L. Mercadier, J. Schlappa, L. Le Guyader, N. Gersimova, M. Teichmann, D. Potorochin, D. Mukkattukavil, J.A. Brock, N. Zhou Hagstrom, A.H. Reid, X. Shen, X.J. Wang, P. Maldonado, Y. Kvashnin, K. Carva, J. Wang, Y.K. Takahashi, E.E. Fullerton, S. Eisebitt, P.M. Oppeneer, S. Molodtsov, A. Scherz, S. Bonetti, E. Iacocca, and H.A. Durr, “Non-equilibrium self-assembly of spin wave solitons in FePt nanoparticles”, Submitted (2021).
- N.Z. Hagstrom, R. Jangid, Meera, D. Turenne, J.A. Brock, E. Lamb, B. Stoychev, J. Schlappa, N. Gerasimova, B. Van Kuiken, R. Gort, L. Mercadier, L. Le Guyader, A. Samartsev, A. Scherz, G. Mercurio, H. Durr, A.H. Reid, H. Nembach, J.M. Shaw, E. Jal, E.E. Fullerton, M.W. Keller, R. Kukreja, S. Bonetti, T.J. Silva, and E. Iacocca, “Ultrafast dynamical symmetry breaking in nanoscale magnetic domains”, Submitted (2021).
- J.A. Brock and E.E. Fullerton, “Skyrmion stabilization at the domain morphology transition in ferromagnet/heavy metal heterostructures with low exchange stiffness”, *Advanced Materials Interfaces*, Accepted (2021).
- J.A. Brock, M.D. Kitcher, P. Vallobra, R. Medapalli, M.P. Li, M. De Graef, G.A. Riley, H.T. Nembach, S. Mangin, V. Sokalski, and E.E. Fullerton, “Dynamic symmetry breaking in chiral magnetic systems”, *Advanced Materials* 33, 2101524 (2021).
- I. Vaskivskyi, R.S. Malik, L. Salemi, D. Turenne, R. Knut, J.A. Brock, R. Stefanuik, J. Soderstrom, K. Carva, E.E. Fullerton, P.M. Oppeneer, O. Karis, and H.A. Durr, “Element-specific magnetization dynamics in Co-Pt alloys induced by strong optical excitation”, *Journal of Physical Chemistry C* 125, 11714 (2021).

- T. Kim, R.E. Kumar, J.A. Brock, E.E. Fullerton, and D.P. Fenning, “How strain alters CO₂ electroreduction on model Cu(001) surfaces”, *ACS Catalysis* 11, 6662 (2021).
- J.A. Brock, S.A. Montoya, M.-Y. Im, and E.E. Fullerton, “Energy-efficient generation of skyrmion phases in Co/Ni/Pt-based multilayers using Joule heating”, *Physical Review Materials* 4, 104409 (2020).
- J.A. Brock, P. Vallobra, R.D. Tolley, S.A. Montoya, S. Mangin, and E.E. Fullerton, “Current-induced generation of skyrmions in Pt/Co/Os/Pt thin films”, *Physical Review B* 102, 024443 (2020).
- Z. Ali, D. Basaula, W. Zhou, J.A. Brock, M. Khan, and K.F. Eid, “Controlling the charge transport mode in permalloy films using oblique angle deposition”, *Journal of Magnetism and Magnetic Materials* 484, 430 (2019).
- Reigle, K. Mason, J. Slattery, S. Lee, T. Jamison, A. Eggert, V. Vincely, D. Wong, Y. Guo, J.A. Brock, and M. Khan, “Superconducting properties of In doped ZrNi₂Ga_{1-x}In_x”, *Solid State Communications* 291, 28 (2019).
- W. Zhou, J.A. Brock, M. Khan, and K.F. Eid, “Oblique angle deposition-induced anisotropy in Co₂FeAl films”, *Journal of Magnetism and Magnetic Materials* 456, 353 (2018).
- D.R. Basaula, J.A. Brock, and M. Khan, “The effect of TM doping on the superconducting properties of ZrNi_{2-x}TM_xGa (TM = Cu, Co) Heusler compounds”, *AIP Advances* 8, 055704 (2018).
- J.A. Brock and M. Khan, “Magnetocaloric effects and electrical resistivity of Ni₂Mn_{0.55}Co_xCr_{0.45-x}Ga – A Heusler alloy system exhibiting a partially-decoupled first-order phase transition”, *AIP Advances* 8, 056429 (2018).
- P. Carroll, A. Williams, M. Caudle, L. Darkins, A. Eaton, B. Fitzgerald, B. Knauf, M. Rurka, E. Shlonsky, P. Wilson, J.A. Brock, and M. Khan, “Enhanced magnetic refrigeration capacities in minutely Co doped Mn_{1-x}Co_xGe₃ compounds”, *Intermetallics* 89, 10 (2017).
- M.U. Khan, J.A. Brock, A. Provino, C. Belfortini, and P. Manfrinetti, “Observation of unusual ferromagnetic cluster glass behavior in CrAlGe”, *Physical Review Materials* 1, 034402 (2017).
- J.A. Brock and M. Khan, “Unusual nature of the martensite and ferromagnetic transitions in Ni₂Mn_{0.4-x}Fe_xCr_{0.6}Ga Heusler alloys”, *AIP Advances* 7, 056432 (2017).
- J.A. Brock, N. Bell-Pactat, H. Cai, T. Dennison, T. Fox, B. Free, R. Mahyub, A. Nar, M. Saaranen, T. Schaeffer, and M. Khan, “The effect of Fe doping on the magnetic and magnetocaloric properties of Mn_{5-x}Fe_xGe₃ compounds”, *Advances in Materials Science and Engineering* 2017, 9854184 (2017).

- J.A. Brock and M. Khan, “Large refrigeration capacities near room temperature in $\text{Ni}_2\text{Mn}_{1-x}\text{Cr}_x\text{In}$ ”, *Journal of Magnetism and Magnetic Materials* 425, 1 (2017).
- M. Khan, J.A. Brock, and I. Sugerma, “Anomalous transport properties of $\text{Ni}_2\text{Mn}_{1-x}\text{Cr}_x\text{Ga}$ Heusler alloys at the martensite-austenite phase transition”, *Physical Review B* 93, 054419 (2016).

CONFERENCE PRESENTATIONS

- “Domain morphology phase transitions and skyrmion stabilization in thin ferromagnet/heavy metal heterostructures with low exchange stiffness”, 2021 Front Range Advanced Magnetism Symposium (poster), September 18-19, 2021, Ft. Collins, CO
- “Dynamic symmetry breaking in chiral magnetic systems” (oral), 2020 Magnetism and Magnetic Materials Conference, November 2-6, 2020, Virtual.
- “Chiral magnetism and skyrmion nucleation in Co/Ni/Pt-based heterostructures” (oral, invited), 2019 Nebraska Nanomagnetism Symposium, December 11-12, 2019, Lincoln, NE.
- “Skyrmion nucleation in Co/Ni/Pt-based heterostructures” (oral), 2019 Magnetism and Magnetic Materials/Intermag Joint Conference, November 4-8, 2019, Las Vegas, NV.
- “Chiral magnetism and skyrmion nucleation in Co/Ni/Pt-based heterostructures” (oral, invited), 2019 Advanced Light Source Users’ Meeting, October 1-3, 2019, Berkeley, CA.
- “Chiral magnetism and skyrmion nucleation in Co/Ni/Pt-based heterostructures” (oral), 2019 International Conference on Vacuum Ultraviolet and X-ray Physics, July 1-5, 2019, San Francisco, CA.
- “A comparison of Dzyaloshinskii-Moriya interaction measurement techniques” (poster), 2019 Magnetism and Magnetic Materials/Intermag Joint Conference, January 14-18, 2019, Washington, DC.
- “Directional growth in Co/Ni/Pt multilayers” (poster), 2018 International Colloquium on Magnetic Films and Surfaces, July 22-27, 2018, Santa Cruz, CA.
- “Directional growth in Co/Ni/Pt multilayers” (oral), 2018 American Physical Society March Meeting, March 5-9, 2018, Los Angeles, CA.
- “Magnetocaloric effects and electrical resistivity of $\text{Ni}_2\text{Mn}_{0.55}\text{Co}_x\text{Cr}_{0.45-x}\text{Ga}$ – A Heusler alloy system exhibiting a partially-decoupled first-order phase transition” (oral), 2017 Magnetism and Magnetic Materials Conference, November 6-10, 2017, Pittsburgh, PA.

- “Magnetic entropy changes with zero hysteresis loss near the first-order phase transition in $\text{Ni}_2\text{Mn}_{0.55}\text{Co}_x\text{Cr}_{0.45-x}\text{Ga}$ ” (oral), 2016 American Physical Society March Meeting, March 13-17, 2017, New Orleans, LA.
- “Unusual nature of the martensite and ferromagnetic transitions in $\text{Ni}_2\text{Mn}_{0.4-x}\text{Fe}_x\text{Cr}_{0.6}\text{Ga}$ Heusler alloys” (oral), 2016 Magnetism and Magnetic Materials Conference, October 31-November 4, 2016, New Orleans, LA.
- “Anomalous transport properties of $\text{Ni}_2\text{Mn}_{1-x}\text{Cr}_x\text{Ga}$ Heusler alloys at the martensite-austenite phase transition” (poster), 2016 American Physical Society March Meeting, March 14-18, 2016, Baltimore, MD.
- “Observation of ferromagnetic and reentrant spin glass behavior in CrAlGe ” (poster), 2016 Magnetism and Magnetic Materials/Intermag Joint Conference, January 11-16, 2016, San Diego, CA.

ABSTRACT OF THE DISSERTATION

Stabilization, dynamics, and control of chiral magnetic textures in thin-film multilayers

by

Jeffrey A. Brock

Doctor of Philosophy in Materials Science and Engineering

University of California San Diego, 2022

Professor Eric E. Fullerton, Chair

In this dissertation, we investigate the stabilization and dynamics of chiral domain walls and skyrmions in several ferromagnet/heavy metal thin-film multilayers. In each material system, the ferromagnet/heavy metal interfaces were engineered to give rise to an interfacial Dzyaloshinskii-Moriya interaction (iDMI) – a spin-orbit coupling mediated effect known to promote the formation of chiral magnetic textures. Throughout several comprehensive studies (presented herein as separate chapters), we explore the stabilization and dynamics of skyrmions in three distinct types of material systems: Thin-films close to experiencing a spin-reorientation transition, ultrathin films with low ferromagnetic exchange and high perpendicular magnetic anisotropy, and thick multilayers with large perpendicular magnetic anisotropy. Through experimental and theoretical studies, we explore the processes by which skyrmions can be created

and moved in response to both quasi-static and transient electrical currents, magnetic fields, and temperature changes. In all cases, the systematic variation of material properties and experimental conditions to better understand and control the mechanisms by which skyrmions are stabilized is a key underlying theme.

In another thrust, we have studied the field-driven dynamics of chiral domain walls and have characterized a new effect in which magnetic stripe domains with chiral domain walls unidirectionally expand in response to applied magnetic fields, with growth symmetries that cannot be understood from the static energy frameworks typically employed to understand the impact of the interfacial Dzyaloshinskii-Moriya interaction in thin-film systems. Using analytical models, we have found that the in-plane torques generated by perpendicular magnetic fields stabilize steady-state domain wall magnetization profiles that are highly asymmetric in elastic energy, resulting in abnormal growth behaviors that are in line with the experimental findings. Building on this understanding of the field-driven dynamics of stripe domains, we expand this understanding to the growth directionalities observed when stripe domain motion is induced by spin-orbit torque.

Chapter 1: Introduction

1.1 Motivation and Historical Background

In order to understand the current state of the art in magnetism, it is important to understand the historical development of the field. Although humankind has been exploiting magnetism for the better part of the past millennium, an understanding of the processes that give rise to magnetic behavior is a very recent development. Even though ancient explorers were utilizing the mysterious properties of “lodestone” as early as 600 B.C. and there was a general suspicion that the earth itself may have magnetic properties, the first rigorous, academic explorations of magnetism did not occur until the early part of the 19th Century. Through the pioneering work of Hans Christian Oersted, the links between electric currents and magnetic properties were first solidified. Much of the ensuing work in this field by Ampere, Biot, Savart, and Faraday further expounded on this idea that moving electrons are a source of magnetic fields. This phenomenological understanding of the interplay between electricity and magnetism eventually led to Maxwell’s well-known codification of the nature of electric and magnetic fields in the language of vector calculus.

While these initial forays greatly expanded our understanding of how magnetic fields could be created, an explanation as to the atomic origins of magnetism (*i.e.*, why lodestone was appropriate to use in a compass, but copper is not) was still lacking. Additionally, there was no framework to understand and predict the different types of magnetic behavior that a material could exhibit (*e.g.*, ferromagnetism, antiferromagnetism, diamagnetism, paramagnetism, or ferrimagnetism). Over the subsequent subsections of this dissertation, we will demonstrate that our

current understanding and exploitation of these magnetic properties are heavily underpinned by quantum mechanical principles not understood until the early part of the 20th Century.

Building on this background information on the origins of magnetic behavior, we will introduce the concept of chirality in magnetism. In recent years, chiral magnetic textures have attracted significant research attention due to their potential use in next-generation energy-efficient, high-density memory storage and computing architectures. While the field of chiral magnetism is no longer nascent – evidenced by the wide body of literature on the subject – understanding the materials systems capable of hosting these features, as well as detecting and exploiting their chirality remains an ongoing area of interest. In this chapter, an understanding of chiral magnetic features will be developed through examination of four central ideas: a.) the interfacial Dzyaloshinskii-Moriya interaction (iDMI), b.) how the iDMI acts within magnetic domain walls to create chiral magnetic states, c.) engineering materials systems with iDMI capable of hosting chiral magnetic features, and d.) techniques for detecting and exploiting the chirality of magnetic features.

1.2 Quantization of Angular Momentum

To begin our understanding of how magnetic behavior originates at the atomic scale, we will consider the simple model system of an isolated hydrogen atom. To solve for the allowed electronic states in this system (*e.g.*, energy, position), the time-independent Schrodinger equation can be used, given as:

$$H\Psi = E\Psi$$

Equation 1.1

In Equation 1.1, E represents the energy of the atomic state, Ψ is the wavefunction describing the probability of finding the electron at a particular position, and H is the Hamiltonian operator of the system. In the case of the hydrogen atom, H consists of two terms: A kinetic energy term accounting for the motion of a single electron orbiting around the nucleus, and a potential energy term that describes the Coulombic interaction between the orbiting electron and the proton in the nucleus. Equation 1.1 in a form specific to the situation described above is given by:

$$\frac{-\hbar}{2m_e} \nabla^2 \Psi - \frac{e^2}{4\pi\epsilon_0} \Psi = E\Psi$$

Equation 1.2

In Equation 1.2, \hbar is the reduced Planck's constant, m_e is the mass of an electron, ∇^2 is the Laplace operator, ϵ_0 is the vacuum permittivity. For a bound system such as the electron and proton in the hydrogen atom, the allowed solutions to Ψ take the form:

$$\Psi_{n,l,m}(r, \theta, \varphi) = R_{n,l}(r)Y_{l,m}(\theta, \varphi)$$

Equation 1.3

where n is the principal quantum number, l is the orbital angular momentum quantum number, and m is the magnetic quantum number. r , θ , and φ are the radial position, azimuthal angle, and elevation angle of the electron, respectively. Equation 1.3 is broken in to two parts: A radial component R (given by the associated Laguerre polynomials) and an angular momentum component Y (given by the spherical harmonics. The critical point here is that the allowed solutions to the time-independent Schrodinger equation are dependent on the quantum numbers n , l , and m , will be discussed subsequently.

The principal quantum number n represents the shell occupied by the electron and is primarily responsible for determining the energy of the electron. In a rough sense, n can be thought of as representing the spatial extent of the electron's orbital path relative to the nucleus and is quantized to integer values, with a minimum value of $n = 1$. The value of n , in turn determines the possible values of the orbital angular momentum quantum number l , which can range from 0 to $n - 1$. Physically, the l number indicates the particular orbital (*i.e.*, s , p , d , or f) that the electron assumes as it orbits the nucleus and determines the magnitude of the electron's total orbital angular momentum vector $|\vec{L}|$:

$$|\vec{L}| = \hbar\sqrt{l(l+1)}$$

Equation 1.4

From Equation 1.4, s orbitals (with $l = 0$) have zero total orbital angular momentum. The specific forms of the associated Laguerre polynomials for the $l = 0$ state indicate that such an electron has the possibility of orbiting close enough to the nucleus that r can very possibly be zero. If $l > 0$, $r = 0$ orbits are no longer a possibility, given that the system has sufficient angular momentum, such that a centrifugal force can act to push the electron away from the nucleus.

Given l , the possible magnetic quantum numbers m consists of the integers between $-l$ and $+l$. The product of m and \hbar represent the component of the total orbital angular moment $|\vec{L}|$ that is oriented along an applied magnetic field H . A schematic depiction of the relationship between m and H is provided in Figure 1.1 for a p orbital (*i.e.*, a situation where $l = 1$). It is understood that the total orbital angular momentum $|\vec{L}|$ cannot be oriented precisely along the direction of H as a unique ramification of quantum mechanics, but instead precesses about the H -axis. During this

precessional motion, however, the component of $|\vec{L}|$ oriented in the field direction remains a constant.

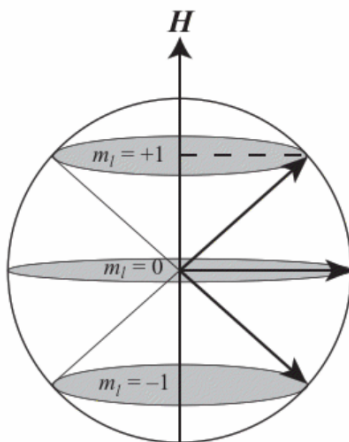


Figure 1.1: The possible m values of an electron in a p orbital relative to an applied magnetic field H . Reproduced from Ref. 1 under the rationale of fair use. © Cambridge University Press.

1.3 Magnetic Dipole Moment from Orbital Momentum

To understand how the quantized orbital angular momentum of an electron can lead to magnetic behavior at the atomic scale, we must first return to the earlier-stated ideas regarding the link between electrical currents and magnetic fields. For a loop of wire with cross-sectional area A carrying electrical current I , the magnetic dipole moment \vec{m} can be calculated using the expression:

$$\vec{m} = IA$$

Equation 1.5

The dipole moment allows for a parameterization of the torque that acts on a magnetic dipole in the presence of a magnetic field. The corresponding torque that the loop would experience in the presence of a magnetic field H is given as:

$$\tau = |\vec{m}|H \sin \theta$$

Equation 1.6

In Equation 1.6, θ is the angle between the surface normal vector of A and the magnetic field H . By integrating Equation 1.6 with respect to θ , an expression for the energy of a magnetic moment relative to an applied field (the so-called Zeeman energy) can be obtained, given as:

$$E_{Zeeman} = -\vec{m} \cdot \vec{H} = -|\vec{m}||\vec{H}| \cos \theta$$

Equation 1.7

Applying these concepts to an electron bound to orbit a nucleus in a circular orbit of radius r with velocity v , Equation 1.5 can be rewritten to read:

$$\vec{m} = IA = -\frac{|e|v}{2\pi r}A = -\frac{|e|vr}{2}$$

Equation 1.8

The velocity of the electron is determined by solving for its orbital angular momentum, given as m_evr . We have previously determined that the component of orbital angular momentum $|\vec{L}|$ oriented in the direction of an applied magnetic field is equal to the product $m\hbar$. Equating these two expressions for the orbital angular momentum yields the electron's velocity as $v = \hbar m/m_e a$. Making this substitution into Equation 1.8 gives a magnetic moment from the orbital motion of the electron, given as:

$$\vec{m} = -\frac{|e|\hbar m}{2\pi m_e} = -\mu_B m$$

Equation 1.9

In Equation 1.9, the parameter $\frac{|e|\hbar}{2\pi m_e}$ has been grouped together to represent a quantity known as the Bohr magneton μ_B and \vec{m} (m) represents the magnetic moment (magnetic quantum number).

The Bohr magneton represents the quanta of orbital angular momentum that an electron can possess. Through this treatment, quantum mechanics defines the possible orbital paths available to a bound electron; in turn, magnetostatics allows for a determination of the associated magnetic behavior.

1.4 Dipole Moment from Spin Angular Momentum

While the orbital angular momentum of a bound electron has an associated magnetic moment, it is not the only electronic property that gives rise to magnetic behavior. The magnetostatic and non-relativistic treatment of quantum mechanics used throughout Chapter 1.2 and Chapter 1.3 does not account for the fact that electrons also possess an intrinsic angular momentum, known as spin angular momentum. The presence of spin angular momentum was first detected in the Stern-Gerlach experiment in 1921, in which a beam of silver atoms was passed through a magnetic field gradient, as shown in Figure 1.2. The trajectory of the silver atoms was found to split in to two well-defined paths. The choice of using silver atoms meant that every atom contained one unpaired electron in the $5s$ state, which has zero orbital angular momentum. Thus, when the silver atoms were passed through the magnetic field gradient, it was expected that there would not be a clear separation of the atoms because no intrinsic magnetic moment should exist. The fact that the atom trajectories did strongly bifurcate indicated that there was an additional source of magnetic moment in atoms, separate from the orbital angular momentum.

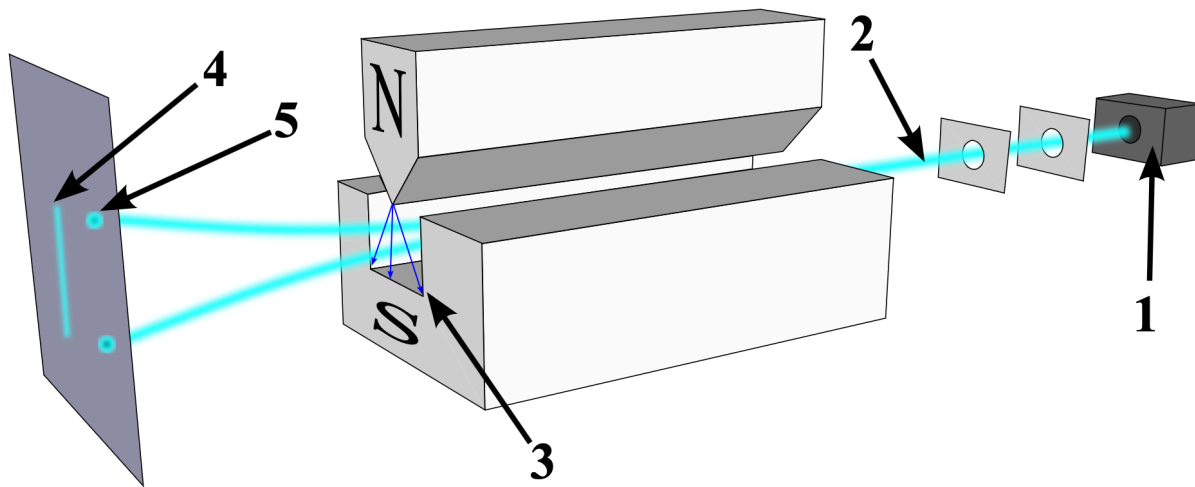


Figure 1.2: A schematic depiction of the Stern-Gerlach experiment, demonstrating how silver atoms are heated and ejected from an oven source (Location 1) to form a beam of atoms (Location 2) that are passed through a magnetic field gradient (Position 3). The beam pattern shown at Location 4 corresponds to the classically predicted trajectory, whereas the pattern at Location 5 corresponds to the experimental result. The figure is reproduced here under the terms of its CC BY-SA 4.0 copyright. © Tatoute

Later, through the relativistic treatment of quantum mechanics proposed by Dirac, this alternative source of magnetic moment was codified as the electron spin. Vectorially, the electron spin can be thought of as the angular momentum vector corresponding to the electron spinning about its own axis, and always has a spin value s of magnitude $\frac{1}{2}$. The spin magnetic quantum number m_{spin} can be either $\pm \frac{1}{2}$, and is independent of the n , l , and m quantum numbers. This means that each orbital within a shell can possess two electrons, each with different spin magnetic quantum numbers. Intuitively, this can be thought of as the electron spinning either clockwise or counter-clockwise about its axis. Much like the total angular momentum $|\vec{L}|$, the total spin angular momentum $|\vec{S}|$ can be expressed as:

$$|\vec{S}| = \hbar\sqrt{s(s+1)} = \sqrt{3}/2 \hbar$$

Equation 1.10

Again, similar to the orbital angular momentum, the component of total spin angular momentum along the direction of an applied magnetic field is given as the product of m_{spin} and \hbar (and is consequentially fixed to values of $\pm\hbar/2$) and precesses about the H axis. This concept is illustrated schematically in Figure 1.3.

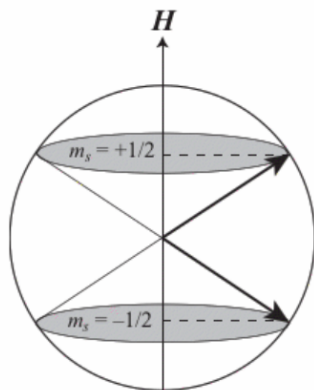


Figure 1.3 The possible orientations of the spin angular momentum with respect to an applied magnetic field H for spin magnetic quantum numbers m_{spin} of $\pm 1/2$. Reproduced from Ref. 1 under the rationale of fair use. © Cambridge University Press.

The magnetic moment associated with the spin angular momentum looks quite similar to that obtained when considering the orbital angular momentum:

$$\vec{m} = -g_e \mu_B m_{\text{spin}}$$

Equation 1.11

Equation 1.11 is differentiated from Equation 1.9 due to the inclusion of the g_e term, known as the electron g -factor. The g -factor is an additional, dimensionless proportionality needed to match quantum mechanics with experimental observations and has been experimentally determined to be

2.0023192 Through Equation 1.11 and Equation 1.9, both the orbital and intrinsic spin angular momentum of an electron can be identified as sources of magnetism in an atom.

1.5 Coupling of the Spin and Orbital Angular Momenta

Thus far, we have treated the magnetic moment arising from the orbital and spin angular momenta as separate, independent quantities. In reality, the magnetic moment due to the orbital motion of the electron has an impact on the spin moment and vice-versa. This behavior is known as spin-orbit coupling (SOC). The ramifications of SOC are encapsulated within Hund's rules for determining the angular momenta in systems more complicated than the hydrogen atom. Hund's first rule states that electrons in a partially filled electronic shell will maximize their total spin angular momentum $|\vec{S}|$ by distributing themselves in each l state available for the given n , such that the electrons all have the same spin magnetic quantum number m_{spin} . By maximizing $|\vec{S}|$ through spatially separating the electrons between the various orbitals within a partially filled electronic shell, the Coulombic repulsion between the electrons will be minimized. In a similar vein of energy minimization, Hund's second rule states that the total orbital angular momentum $|\vec{L}|$ should be maximized as well. Physically, this encapsulates the idea that a more substantial total orbital angular momentum means that there is a favorability for the electrons to orbit in the same direction around the nucleus. If the electrons orbit in the same direction, the frequency with which the electrons are in close proximity is lowered, which also minimizes the Coulombic interaction. Hund's third rule offers instruction for determining the total angular momentum (both spin and orbital) of the atom \vec{J} . For electronic shells that are less than half-filled, $\vec{J} = |\vec{L} - \vec{S}|$. For electronic shells that are more than half-filled, $\vec{J} = \vec{L} + \vec{S}$. Half-filled shells have $\vec{J} = \vec{S}$. Hund's rules

underpinned by the Pauli exclusion principle, which states that no two electrons in an atom can possess the same quantum numbers, which sets limitations on the manner in which electronic states can be filled.

This manner of determining the total angular momentum \vec{J} requires revisions to the previous way that we treated the orbital and spin angular momenta separately when determining the magnetic moment of an atom. It has been shown that systems with more complexity than the hydrogen atom, the projection of the magnetic moment along an applied magnetic field becomes a function of \vec{S} , \vec{L} , and \vec{J} through the definition of the Landé g -factor.³ Much like the g -factor defined in Chapter 1.4, the Landé g -factor is an additional proportionality to the Bohr magneton needed to define the magnetic moment in a system with SOC. The Landé g -factor is given as:

$$g = 1 + \frac{J(J + 1) + S(S + 1) - L(L + 1)}{2J(J + 1)}$$

Equation 1.12

Additionally, a total spin angular momentum quantum number m_j can also be defined, which is limited to the integer values between $-|\vec{J}|$ and $|\vec{J}|$. The total magnetic moment projection along an applied field axis is then given as:

$$\vec{m} = -g\mu_B m_j$$

Equation 1.13

While it was previously stated that the Bohr magneton is the quantum of magnetic moment due to orbital angular momentum, the fact that the Landé g -factor can take on non-integer values indicates that most atoms possess magnetic moments that are fractions of a Bohr magneton – a prediction that matches with experimental observation.

In some cases, however, it may be found that the experimentally measured magnetic moment of a material is much closer to what would be predicted if only the spin angular momenta of the atoms are considered. Particularly, given that Hund's rules are most applicable to the electronic properties of isolated atoms, their applicability to the description of solids (consisting of an ensemble of interacting atoms) can be insufficient to offer a complete understanding. Besides the trivial case of a half-filled electronic shell (*i.e.*, where $|L| = 0$), the orbital angular momentum can be quenched by the crystal fields in a solid.⁴ In a crystalline structure, the electric fields created by the charged particles that constitute each atom set preferences to the electronic orbits that are energetically favorable and break the degeneracy of the different m_l states, particularly when the crystal symmetry dictates a non-central symmetry to the electric fields. In such cases, the angular momentum may no longer be constant with respect to time but averages out to zero – quenching the magnetic moment associated with the orbital momentum. These effects are particularly apparent in systems where the magnetism arises from outer-shell electrons (*e.g.*, d electrons in transition metals) as opposed to electrons that orbit closer to the nucleus (*e.g.*, f electrons in rare-earth materials).

1.6 Magnetic Ordering in Materials

Thus far, our discussion of magnetic properties has primarily relied on simplistic, single atom models. However, in this dissertation, we will be dealing with systems that consist of an enormous number of atoms in solids. When transitioning between single-atom and multiple-atom treatments, we will find that the behavior of atom ensembles can lead to a number of collective behaviors not accessible from single-atom approaches – as alluded to at the end of Chapter 1.5.

Over the subsequent sections, more attention will be given to the phenomenon of ferromagnetism, given that it is the primary focus of the experimental results discussed in this dissertation.

When describing the various magnetic phenomena that materials can exhibit, it is often convenient to categorize based on the magnetic flux that exists in a material in the presence of an applied magnetic field. In order to understand the magnetic flux, we must first develop an understanding of magnetic induction. The magnetic induction of a material B in the presence of an external applied magnetic field H is given as:

$$\vec{B} = \mu_0(\vec{H} + \vec{M})$$

Equation 1.14

In Equation 1.14, μ_0 represents the vacuum permeability (a physical constant that reflects how “easy” it is to generate a magnetic field in a vacuum), and \vec{M} is the magnetization of the material, equal to the vector sum of the magnetic moment of all atoms in the material divided by its volume. In SI units, \vec{M} and \vec{H} are measured in A/m, while the magnetic induction B has the unit of Tesla (T). Once the magnetic induction of a material has been determined, the magnetic flux Φ is calculated by dividing the induction by the cross-sectional area of the material. The experimental techniques used to determine these parameters will be discussed in later chapters.

Having established how the magnetic flux can be calculated, it is now possible to discuss how it is used to classify different magnetic behaviors. For this exercise, we will consider two parameters. The magnetic flux inside the subject material Φ_{inside} and the flux existing outside of the material in free space Φ_{outside} . For systems that exhibit paramagnetic or antiferromagnetic behavior, $\Phi_{\text{inside}} \approx \Phi_{\text{outside}}$ – implying that the magnetic moment of the material has little to no preference for alignment in the direction of the applied magnetic field. The fact that the Zeeman energy expression (Equation 1.07) favors the alignment of magnetic moments in the applied field

direction immediately indicates that additional energetic actors can be in play. Diamagnetic materials, on the other hand, are characterized as having $\Phi_{\text{inside}} < \Phi_{\text{outside}}$ – indicating that the material’s magnetic moment is opposed to the applied field. This anti-parallel relationship between \vec{M} and \vec{H} can be understood in terms of Faraday’s law of electromagnetic induction, which states that a magnetic flux that varies with time generates an electromotive force that acts to produce an electric current that creates a magnetic field that opposes the external flux – a phenomenon known as Lenz’s law. Thus, given that an applied field is needed to generate flux in paramagnetic, antiferromagnetic, and diamagnetic behavior, $\Phi = 0$ whenever $H = 0$. In the case of ferromagnetic and ferrimagnetic materials, $\Phi_{\text{inside}} \gg \Phi_{\text{outside}}$ – indicating that the atomic moments collectively become strongly aligned with the applied field. Furthermore, when the applied field is removed, the flux does not necessarily return to zero, indicating that there are other considerations in play.

In Figure 1.4, schematic depictions of paramagnetism, ferromagnetism, antiferromagnetism, and ferrimagnetism are shown. For paramagnets, it can be seen that in the absence of an applied magnetic field, the magnetic dipole moments of individual atoms are randomly oriented, giving the material a net magnetization of zero. By applying an external magnetic field, the Zeeman energy dictates that individual moments will begin to orient themselves in the direction of the applied field. The Langevin theory and Curie-Weiss law provide specifics as to how this orientation changes with applied field and temperature. Ferromagnetic materials are characterized as having a strong, collective response to an applied magnetic field. Furthermore, this long-range ordering in the direction of the applied field can be preserved once the field is removed. Antiferromagnetic materials exhibit a similar collective behavior, except with neighboring moments being aligned anti-parallel to one another. Thus, in zero magnetic field, antiferromagnets exhibit a net magnetization of zero (much like paramagnets). Ferrimagnets are a

special class of antiferromagnets, in which neighboring moments are anti-parallel to one another, but of unequal magnitude. Thus, in many ways, ferrimagnets exhibit behavior akin to that of ferromagnets.

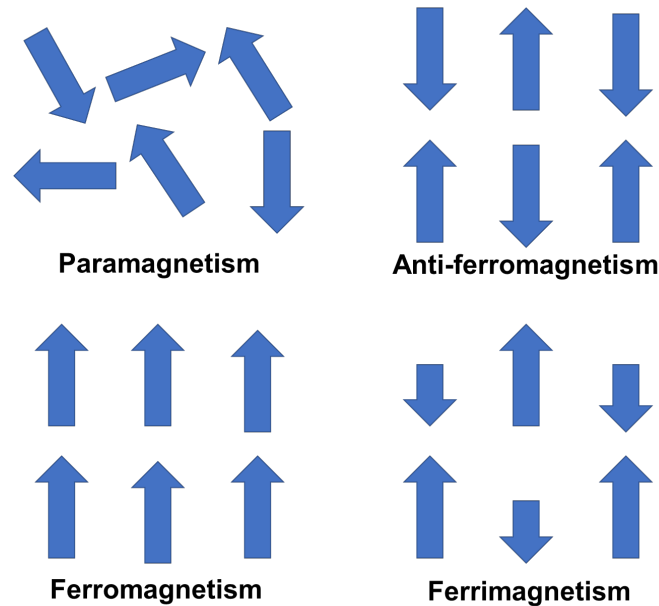


Figure 1.4: The orientation of magnetic dipole moments in paramagnets, antiferromagnets, ferromagnets, and ferrimagnets. This schematic depiction assumes zero applied magnetic field.

1.7 Langevin Treatment of Ferromagnetic Ordering

To understand the origins of ferromagnetic behavior, we must first start with a basic understanding of paramagnetic behavior. Langevin proposed that Boltzmannian statistics can be used to predict the magnetic moment of a paramagnetic material in an applied field. Under this treatment, the probability p that an individual magnetic moment within an ensemble of moments with random orientation will orient itself at a specific angle θ relative to an applied field H is linked to the Zeeman energy. In spherical coordinates, this can be expressed as:

$$p(\theta) = \frac{e^{mH \cos \theta / k_B T} \sin \theta d\theta}{\int_0^\pi e^{mH \cos \theta / k_B T} \sin \theta d\theta}$$

Equation 1.15

Integrating Equation 1.15 from 0 to π accounts for all possible elevation angles relative to the field. If θ is the angle between the applied field H and an atomic magnetic moment m , then the product $m \cos(\theta)$ should represent the component of the total magnetic moment oriented in the field direction. For a system containing N atoms, it is possible to solve for the net magnetization M using Equation 1.15 in the expression:

$$\vec{M} = Nm \int_0^\pi p(\theta) \cos \theta d\theta = Nm \left(\coth \left(\frac{mH}{k_B T} \right) - \frac{k_B T}{mH} \right) = NmL(\alpha)$$

Equation 1.16

In Equation 1.16, the hyperbolic trigonometric function has been grouped into the so-called Langevin function, parameterized in terms of $\alpha = mH/k_B T$. If the Langevin function is then expressed as a first-order Taylor series, Equation 1.16 attains a much simpler form, given as:

$$\vec{M} = \frac{Nm^2 \vec{H}}{3k_B T}$$

Equation 1.17

Going even further, we can remove the magnetic field dependence by framing the Langevin treatment within the susceptibility χ – a dimensionless parameter that expresses the ratio between the magnetization and the applied field as:

$$\chi = \frac{\vec{M}}{\vec{H}} = \frac{Nm^2}{3k_B T} = \frac{C}{T}$$

Equation 1.18

Equation 1.18 is known as the Curie law, and it allows us to decouple the influence of magnetic fields and temperatures on the magnetic properties of a paramagnet. Overall, the Langevin

treatment predicts that the net magnetization of a paramagnet linearly increases with the field if the temperature is held at a fixed value. Conversely, if the magnetic field is held constant, the Langevin treatment predicts that the net magnetization will asymptotically decay with temperature.

As has been a common trend so far, the Langevin function is a simplification of the physics at hand, since it treats the magnetic moment classically. To account for the quantization and restrictions on the total angular momentum J of the ensemble of moments, the Brillouin function $B_J(\alpha)$ must be used. Using Brillouin's treatment, it can be shown that the net magnetization \vec{M} can be expressed as:⁴

$$\vec{M} = NgJ\mu_B \left[\frac{2J+1}{2J} \coth\left(\frac{\alpha(2J+1)}{2J}\right) - \frac{1}{2J} \coth\left(\frac{\alpha}{2J}\right) \right] = NgJ\mu_B B_J(\alpha)$$

Equation 1.19

While the Langevin and Brillouin treatment are a good start towards understanding paramagnetic materials, it cannot explain the spontaneous, collective ordering seen in ferromagnetic materials. In the Langevin treatment, each moment is treated as an independent actor. Weiss built on the work of Curie, by postulating that there exists an internal "molecular" field within ferromagnetic materials, that acts to align individual moments in the same direction. The Weiss molecular field H_W was said to have a set proportionality γ to the material's saturation magnetization, such that $\vec{H}_W = \gamma\vec{M}$. H_W acts in concert with the external magnetic field H , such that the Curie Law can be reformulated as:

$$\chi = \frac{\vec{M}}{\vec{H}} = \frac{\vec{M}}{\vec{H}_W + \vec{H}} = \frac{C}{T}$$

Equation 1.20

Solving for the magnetization, we get the expression:

$$\vec{M} = \frac{C\vec{H}}{T - \gamma C} = \frac{C\vec{H}}{T - T_C}$$

Equation 1.21

In equation 1.21, the term γC has been redefined as the so-called Curie temperature T_C . If Equation 1.21 is used to calculate the susceptibility χ , we now obtain:

$$\chi = \frac{C}{T - T_C}$$

Equation 1.22

From Equation 1.22, when T is cooled to T_C from above, the susceptibility will diverge towards infinity, signifying the collective alignment of all moments in the direction of the applied magnetic field. In essence, while the molecular field is present at all temperatures, it becomes more pronounced at temperatures below the Curie temperature, when the material can retain a net magnetization in the absence of an applied magnetic field.

In order to understand the net magnetization promoted by the Weiss molecular field in a ferromagnet, we can plot both the magnetization predicted by the Langevin function and the Weiss treatment on the same plot as a function of $\alpha = mH/k_B T$, as shown in Figure 1.5. The predicted spontaneous magnetization would be defined where the Weiss treatment curve intersects with the Langevin curve. However, based on the material parameters, the Langevin function does saturate at a particular value, setting an upper limit on the net magnetization attainable – a common point between paramagnetic and ferromagnetic materials.

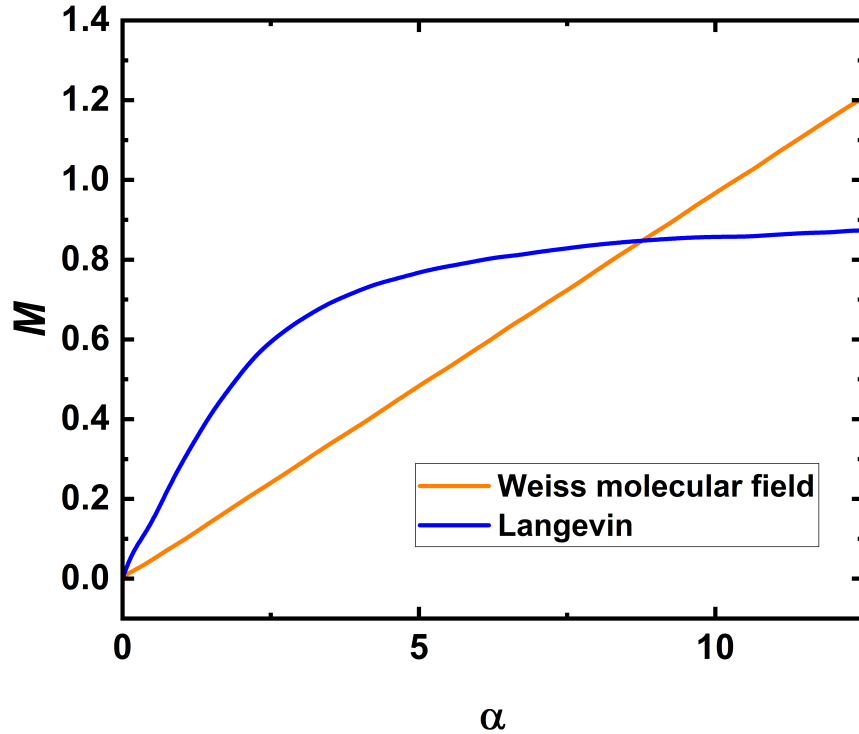


Figure 1.5: Plots of both the Langevin function and the Weiss molecular field as a function of $\alpha = mH/k_B T$.

To appreciate the predictive power of the Langevin function and the Weiss molecular field, it is worthwhile to compare to experimental data. If the Curie temperature of a material is known, the Weiss molecular field constant can be determined using the expression $\gamma = 3k_B T/Nm^2$. This allows for the calculation of the associated net magnetization using the expression $\vec{M} = \alpha \left(\frac{k_B T}{\gamma m} \right)$, which can then be equated to the Langevin function to determine the spontaneous magnetization (provided $T < T_C$). As shown in Figure 1.6, the Langevin function does a decent job predicting the spontaneous/saturation magnetization of the three most common ferromagnetic materials (Fe, Ni, and Co), but the accuracy of the prediction is improved when using the Brillouin function.

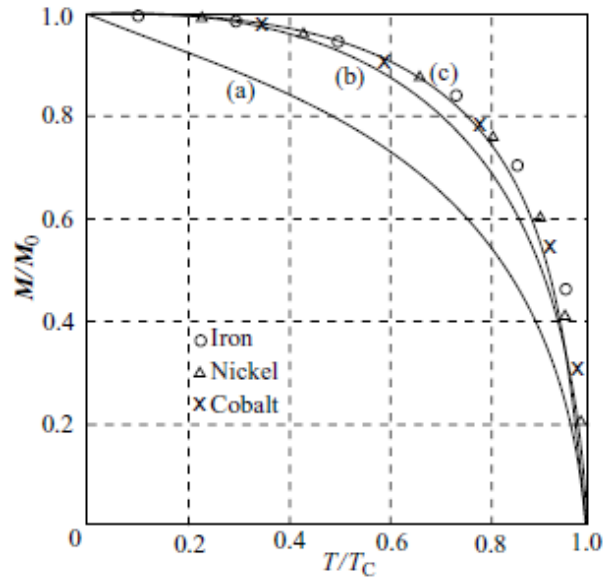


Figure 1.6: Net magnetization (relative to the value at $T = 0$) predicted for Fe, Co, and Ni as a function of temperature (normalized to the Curie temperature). Curve (a) was calculated using the Langevin treatment, while curves (b) and (c) were calculated using the Brillouin treatment with $J = 1$ and 0.5 , respectively. Reproduced from Ref. 5 under the rationale of fair use. © Informa UK Limited.

1.8 Heisenberg Treatment of Ferromagnetic Order

Thus far, the Weiss molecular field has provided a sufficient framework for predicting some of the behaviors of ferromagnetic materials. However, the Weiss molecular field is simply a fictitious actor used to summarize the internal physics that gives rise to the collective behavior of ferromagnetism. Heisenberg was the first to rigorously use the concepts of quantum mechanics to understand the physical origin of the Weiss molecular field. In his treatment, he considered a helium atom, which consists of two electrons. Furthermore, consider that one electron is in the $1s$ orbital, and the other electron is in the $2s$ orbital, such that the spin angular momentum of each

electron is free to be $\pm 1/2$ without violating the Pauli exclusion principle, as shown schematically in Figure 1.7.



Figure 1.7: Possible spin configurations for a He atom where each electron is confined to its own s-orbital.

When writing out the Hamiltonian H for this arrangement, there are three terms in total: Two Hamiltonians (H_1 and H_2) to describe the electron-nucleus interactions for each electron, and one Hamiltonian to describe the interaction between the electrons (H_3). For the electron-nucleus interactions, the Hamiltonian is given as:

$$H_i = \frac{-\hbar}{2m_e} \nabla_i^2 - \frac{Ze^2}{4\pi\epsilon_0 r_i}$$

Equation 1.23

In Equation 1.23, Z defines the atomic number of the element in question ($Z = 2$ for He), ϵ_0 is the vacuum permittivity, and r_i is the distance between the electron and the nucleus. The Hamiltonian for the Coulombic repulsion between the two electrons is given as:

$$H_{ij} = \frac{e^2}{4\pi\epsilon_0 r_{ij}}$$

Equation 1.24

In Equation 1.24, r_{ij} represents the separation between the two electrons. As Equation 1.23 and 1.24 are operators, they only return the energy of the system when they act on the appropriate electronic wavefunctions.

To determine the appropriate wavefunction to use for our He atom system, we must revisit the Pauli exclusion principle. We previously stated that the Pauli exclusion principle simply requires that no two electrons can possess the same quantum numbers n , l , m , and m_{spin} . In terms of the electron wavefunction, the definition becomes somewhat more complicated. For an s orbital with two electrons, if we swap the position of the two electrons, the spin portion of the electronic wavefunction will have to be anti-symmetric, as the m_{spin} value would need to change to obey the Pauli exclusion principle. However, since both electrons remain in the same s orbital, the spatial component of the wavefunction does not change. Conversely, if we consider that situation in which the two electrons are distributed between two different s orbitals but have the same m_{spin} values, the opposite is true; swapping the positions of the two electrons keeps the spin portion of the wavefunction symmetric, while making the spatial component antisymmetric. When considering the swapping of electrons within the same orbital, the total electronic wavefunction is given as:

$$\Psi(\vec{r}_1, \vec{r}_2) = \frac{1}{\sqrt{2}} (\varphi_{1s}(\vec{r}_1)\varphi_{2s}(\vec{r}_2) + \varphi_{2s}(\vec{r}_1)\varphi_{1s}(\vec{r}_2))$$

Equation 1.25

In Equation 1.25, \vec{r}_i symbolizes the radial position of each electron, whereas φ_{j_s} represents the wavefunction of an electron confined to a specific orbital. When swapping the position of electrons of the same m_{spin} between two orbitals, the total electronic wavefunction is given as:

$$\Psi(\vec{r}_1, \vec{r}_2) = \frac{1}{\sqrt{2}} (\varphi_{1s}(\vec{r}_1)\varphi_{2s}(\vec{r}_2) - \varphi_{2s}(\vec{r}_1)\varphi_{1s}(\vec{r}_2))$$

Equation 1.26

In order to determine the energies associated with these two scenarios, we must allow the three components of the total Hamiltonian ($H_{\text{Total}} = H_1 + H_2 + H_3$) to act on each of these wave functions. Within the framework of bra-ket notation, this action can be represented by the term:

$$E = \langle \Psi(\vec{r}_1, \vec{r}_2) | H_{\text{total}} | \Psi(\vec{r}_1, \vec{r}_2) \rangle$$

Equation 1.27

If the two electron-nucleus Hamiltonians and the electron-electron Hamiltonian are distributed correctly, Equation 1.27 can be written in an expanded form as:

$$\begin{aligned} E = & \langle \varphi_{1s}(\vec{r}_1) | H_1 | \varphi_{1s}(\vec{r}_1) \rangle + \langle \varphi_{2s}(\vec{r}_1) | H_1 | \varphi_{2s}(\vec{r}_1) \rangle + \langle \varphi_{1s}(\vec{r}_2) | H_2 | \varphi_{1s}(\vec{r}_2) \rangle \\ & + \langle \varphi_{2s}(\vec{r}_2) | H_2 | \varphi_{2s}(\vec{r}_2) \rangle + \langle \varphi_{1s}(\vec{r}_1)\varphi_{2s}(\vec{r}_2) | H_3 | \varphi_{1s}(\vec{r}_1)\varphi_{2s}(\vec{r}_2) \rangle \\ & + \langle \varphi_{2s}(\vec{r}_1)\varphi_{1s}(\vec{r}_2) | H_3 | \varphi_{2s}(\vec{r}_1)\varphi_{1s}(\vec{r}_2) \rangle \\ & \pm \langle \varphi_{1s}(\vec{r}_1)\varphi_{2s}(\vec{r}_2) | H_3 | \varphi_{2s}(\vec{r}_1)\varphi_{1s}(\vec{r}_2) \rangle \\ & \pm \langle \varphi_{2s}(\vec{r}_1)\varphi_{1s}(\vec{r}_2) | H_3 | \varphi_{1s}(\vec{r}_1)\varphi_{2s}(\vec{r}_2) \rangle \end{aligned}$$

Equation 1.28

In Equation 1.28, the \pm operands correspond to the spatially symmetric and spin symmetric versions of the total electronic wavefunction, respectively. When the Hamiltonians act on each wavefunction component, a total energy expression can be obtained, given as:

$$E = K_1 + K_2 + V \pm J$$

Equation 1.29

In Equation 1.29, K_1 and K_2 represent the sum of kinetic and potential energy (with respect to the nucleus) for electrons in the 1s and 2s orbitals (respectively), V is the Coulomb interaction between these electrons, and J is the so-called exchange interaction. It is clear that depending on the

wavefunction symmetries assumed, the exchange interaction can either increase or lower the total energy of the He atom system. Critically, the lower-energy case corresponds to the spin-symmetric case, where both electrons have the same value for m_{spin} . Thus, the Heisenberg model can predict the development of a net spin angular momentum in a model He atom, corresponding to a spontaneous magnetic moment. Furthermore, a quantum mechanical rationale to Hund's second rule and the Weiss molecular field can be identified.

1.9 Band Theory of Ferromagnetism

While the Heisenberg treatment predicts that a spontaneous magnetic moment and an internal Weiss field can act to promote collective magnetic ordering, these atom-based models do not fully account for the magnetic behavior observed in solid-state ensembles – where the effects of bonding between atoms and the formation of electronic band structures and the delocalization of electrons must be considered. Additionally, the energetic balance between lowering the exchange energy by distributing the electrons between different shells and orbitals (which comes with its own energy penalty) must be weighed. Thus, even though the Heisenberg exchange interaction has been shown to promote ferromagnetism in simple model systems, by no means is ferromagnetism possible in every material.

As mentioned previously, Fe, Co, and Ni are the three archetypal room-temperature ferromagnetic elements. In these elements, there is an energetic overlap between the 4s and 3d electronic bands. Under the rigid band model, we assume that the profile of the density of electronic states is identical between these atoms, and that only the Fermi level changes. Because of the energetic overlap between shells, the 4s and 3d shells are said to be hybridized, in that electrons can be exchanged between them. Because of this hybridization and the statistics of

quantum mechanics, it is possible for the 4s and 3d shells to possess a non-integer number of electrons at any given time.

Although the energies of 3d and 4s bands overlap, there is a difference in the density of electronic states available for each band at the Fermi level. As demonstrated in Figure 1.8(a) and Figure 1.8(b), the 4s band offers a low density of electronic states over a broad range of energy values. On the other hand, the 3d band offers a large density of states, localized near the Fermi level for these three elements, as shown in Figure 1.8(a) and Figure 1.8(c). Consequently, the energy difference that must be overcome for an electron to move between 4s sub-bands is significantly larger than what is needed to move between 3d sub-bands. Thus, the Heisenberg exchange mechanism – which favors spreading electrons across sub-bands such that the electrons have the same spin polarization – can have a stronger impact on how the 3d band is populated, and thus allows for the development of a net spin angular momentum in a solid. It is pertinent to emphasize that the ferromagnetism of Fe, Co, and Ni can primarily be attributed to the fact that these elements have partially filled 3d bands that exhibit a large density of electronic states near their respective Fermi levels. Other 3d transition metals as a rule do not exhibit ferromagnetism in elemental form due to the fact that their 3d bands are occupied by more electrons (as is the case for Cu and Zn) or there is a smaller density of electronic states available at the Fermi level (as is true for Cr and V). In general, the proclivity of a material to exhibit ferromagnetic ordering can be predicted by the Stoner criterion, which states that the product of the density of states at the Fermi level and the change in potential energy due to a flipping of spin angular momentum should be greater than one in ferromagnetic materials.

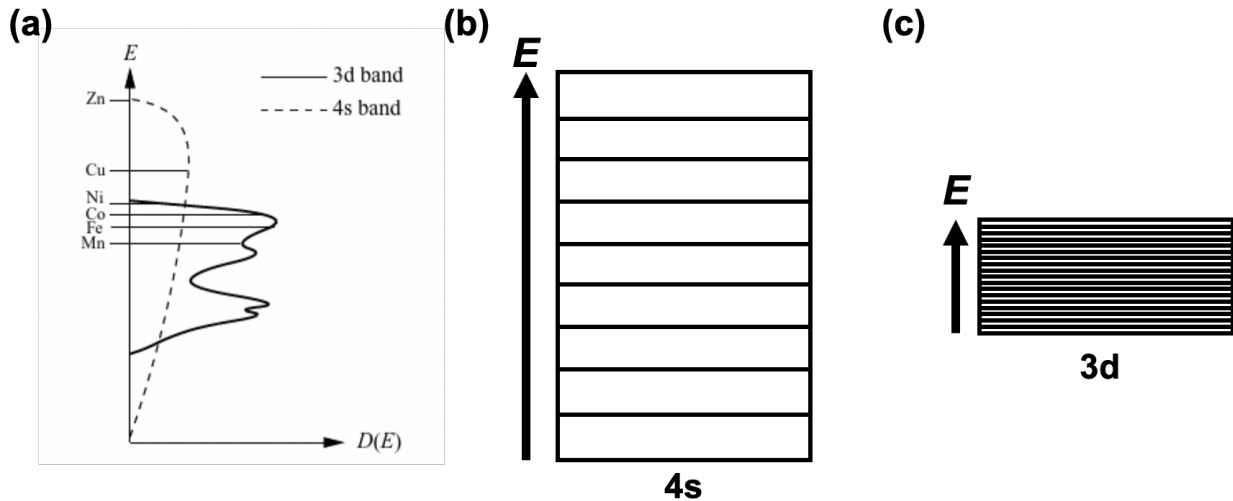


Figure 1.8: (a) Density of electronic states D as a function of energy E under the assumption of the rigid band model for the 4s and 3d electronic bands. The Fermi levels of several 3d transition metals are shown on the E axis. Schematic depictions of the spacing between energy levels and the energy range of the 4s (b) and 3d (c) electronic bands. (a) is reproduced from Ref. 1 under the rationale of fair use. © Cambridge University Press.

1.10 Domains in Ferromagnetic Materials: Demagnetizing Fields and Energy

Having briefly established how ferromagnetic order can originate in individual atoms and large ensembles of atoms, we will now develop an understanding of how ferromagnetic behavior manifests at the macroscopic scale in solids. To begin, we consider an ellipsoidal piece of ferromagnetic material, with its magnetization M oriented along the long axis of the ellipsoid, as shown in Figure 1.9. Within the framework of magnetostatics, it can be imagined that magnetic charges are present at the edges of the sample where the M vector begins and terminates, and these magnetic charges give rise to a magnetic field. Specifically, since the magnetic induction B is well-known to form closed loops, a circuitous field like that shown by the blue lines in Figure 1.9 is formed. Notably, a part of this magnetic field generated by the magnetization passes through the

sample; this magnetic field, which opposes the magnetization of the sample, is known as the demagnetizing field H_d . The demagnetizing field is also sometimes referred to as the stray field.

H_d can be determined using the expression:

$$\vec{H}_d = -N\vec{M}$$

Equation 1.30

In Equation 1.30, N represents the demagnetization factor, which is a geometry-dependent factor that scales the demagnetizing field inside the material based on what direction the sample is magnetized along. It is noted that as a magnetic field, H_d need not form a closed loop like a magnetic induction B . For the ellipsoid shape shown in Figure 1.9, $N \approx 0.18$ when the sample is magnetized along the long axis. For the thin-film geometry (relevant to subsequent chapters of this dissertation), $N = 1$ when the magnetization is oriented perpendicular to the film surface and is equal to zero when the magnetization lies in the plane of the film.

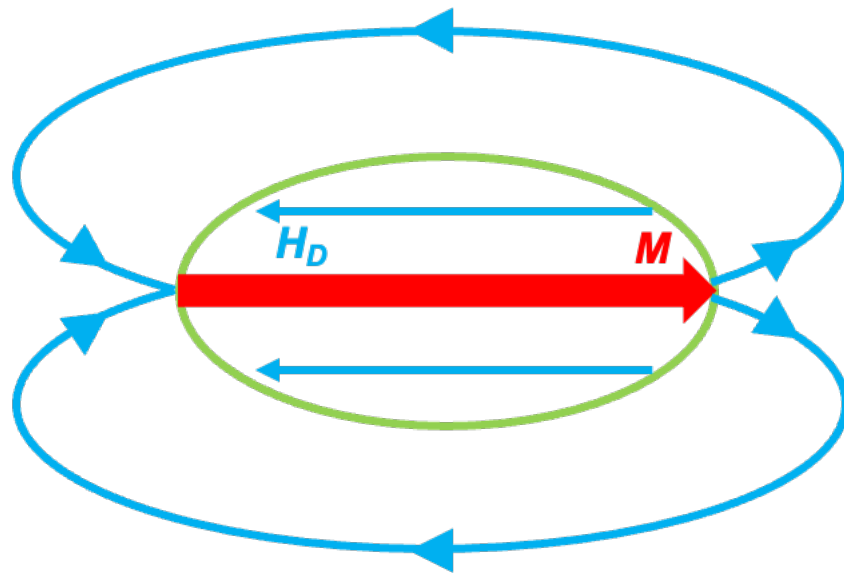


Figure 1.9: Schematic depiction of the demagnetizing field H_d generated when an ellipsoid-shaped sample is magnetized along its long axis.

When a demagnetizing field is present, it acts in opposition to the magnetization of the material. As such, a magnetostatic self-energy is present. This demagnetizing energy E_d can be solved for in the thin film geometry using the expression:

$$E_d = \frac{1}{2} \mu_0 M_s^2 \cos^2 \theta$$

Equation 1.31

Where M_s is the saturation magnetization and θ is the angle of declination relative to the film's surface normal. In agreement with the demagnetization factors listed above, the demagnetizing energy is minimized when the sample magnetization lies in the plane of a thin film. Thus, while the demagnetizing energy would prefer for a thin film to have a spontaneous magnetization in the film plane, we will later show that additional energetic actors can set a preference for perpendicular magnetization.

We now consider a thin film of ferromagnetic material with a preference for spontaneous magnetization perpendicular to the film plane, as shown in Figure 1.10. Based on the magnetostatic arguments presented earlier, we imagine that the magnetization arises from the collective action of many magnetic dipole moments dispersed throughout the material. Each magnetic dipole moment generates its own demagnetizing field, as shown in Figure 1.10. If every dipole moment in the system is oriented in the same direction, the total demagnetizing field will be opposed to the net magnetization of the sample. While this arrangement certainly minimizes the exchange energy of the system, the demagnetizing energy will be quite large. Even before it was technologically easy to observe the mesoscopic ordering of a ferromagnetic system, Weiss, Landau, and Lifshitz realized that in order to minimize the total energy of the system, tradeoffs can be made between

the exchange and demagnetizing energy.^{6,7} Namely, if regions of the sample reverse the perpendicular orientation of their magnetic dipole moment (as also shown in Figure 1.10), the net demagnetizing field (and hence, the demagnetizing energy) can be reduced. At the microscopic scale (where the exchange energy is most impactful) the exchange energy is minimized through the formation of regions or domains where the magnetization is oriented in the same direction, while the reduction in demagnetizing energy is accomplished by alternating the magnetic orientation at the mesoscopic scale.⁸ Thus, while ferromagnetic materials are characterized as possessing spontaneous magnetic ordering, they may not necessarily have a uniform magnetic polarization due to the formation of magnetic domains to minimize the energy of the system.

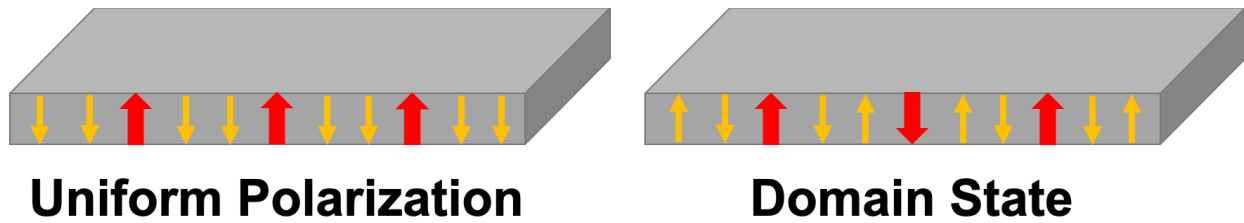


Figure 1.10: Demonstration of the magnetization (red arrows) and demagnetizing fields (yellow arrows) associated with the uniformly polarized and domain states in the thin-film geometry.

1.11 Magnetic Anisotropy

As briefly mentioned in the preceding section, while the exchange energy sets a favorability for the spontaneous alignment of neighboring magnetic spins in a ferromagnet, there are several extrinsic and intrinsic considerations that can set a preference for the magnetization to be oriented along certain directions in a material. Broadly speaking, the tendency for the magnetization in a material to lie in a certain direction is referred to as magnetic anisotropy. For the thin film geometry most relevant to this dissertation, we have already shown that the

demagnetizing energy is minimized when the magnetization lies within the plane of the film. This geometry-dictated preference for in-plane magnetization in thin films is known as shape anisotropy. Based on Equation 1.31, the shape anisotropy K_{shape} can be quantified for a thin film using the expression:

$$K_{shape} = \frac{1}{2} \mu_0 M_s^2$$

Equation 1.32

Which reflects the energy difference between having the magnetization oriented perpendicular to the film plane versus in the film plane. The $\frac{1}{2}$ factor in Equations 1.31 and 1.32 is a consequence of treating the sample's magnetization as a dipole moment whose degree of polarization changes when subjected to an applied field.

Besides geometry, the crystal structure of a magnetic material can set a magnetocrystalline anisotropy to the magnetic properties. To illustrate the origins of this crystalline effect, recall that the spin and orbital angular momenta are coupled quantities. Also, we must realize that the interatomic distance varies between the different crystallographic directions that define a crystal structure. As an example, we show the orientation of the [100], [110], and [111] direction families in a body centered cubic (bcc) crystal in Figure 1.11(a). Fe, one of the archetypal ferromagnetic elements, typically has the bcc-type crystal structure. If we imagine that each atom has an associated dipole moment (both from the electron spin and orbital angular momenta) and consider how the spin moment and orbital moment/trajectory would change in response to an applied magnetic field as shown in Figure 1.11(b), we can schematically understand that depending on the interatomic spacing and the crystal symmetry, certain magnetic polarizations may result in a larger Coulombic repulsion energy than others – meaning that a larger magnetic field would be required to saturate the magnetization in certain directions. Using single-crystal Fe samples, the tendency

of the magnetocrystalline anisotropy to define “easy” and “hard” directions to magnetize a sample has been demonstrated experimentally, as shown in Figure 1.11(c).

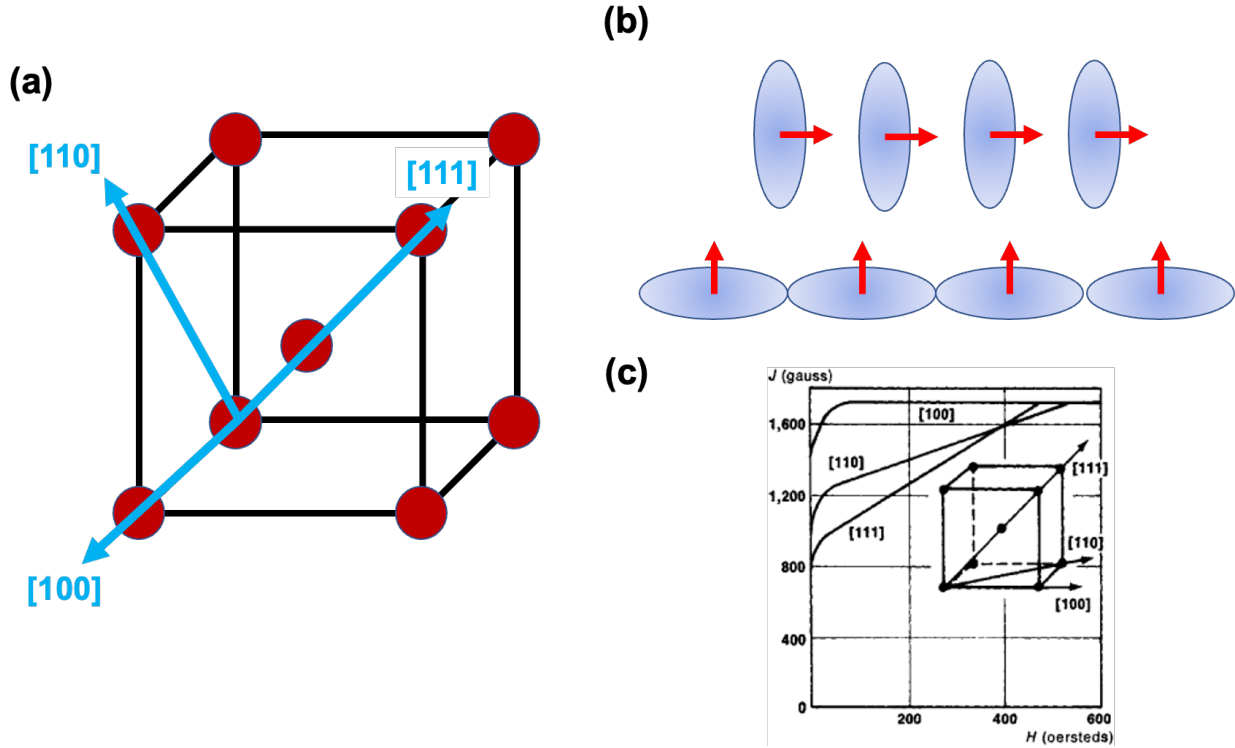


Figure 1.11: (a) Schematic depictions of the [100], [110], and [111] family of crystallographic directions in bcc Fe. (b) Schematic depictions of the degree of electron orbital overlap when a ferromagnetic sample is magnetized along different directions. (c) Experimentally determined magnetization as a function of applied magnetic field along different crystal axes in bcc Fe. (c) is reproduced from Ref. 4 under the rationale of fair use. © John Wiley & Sons, Inc.

Particularly relevant to this dissertation is the concept of perpendicular magnetic anisotropy (PMA) in the thin film geometry. For the materials discussed in this dissertation, the nanometer-scale thickness of the ferromagnetic layers is most responsible for determining the magnetic anisotropy. It can intuitively be understood that as a ferromagnetic layer’s thickness is reduced, the overall degree of atomic coordination will also be lowered. This reduced coordination is particularly apparent at the surface of a thin film, where half of the neighboring atoms are gone

relative to the bulk case. On account of this reduced coordination, energetic considerations dictate a preference for orbital electronic motion in surface plane of a thin film (*i.e.*, orbital motion confined within the ferromagnetic layer). Because there is a coupling between the orbital and spin momenta of an electron, this restriction on the orbital motion of electrons in turn favors that the spin angular momenta of each atom be normal to the surface plane.^{9,10} Because these considerations are not sensitive to the directionality of the orbital motion in the sample plane, this surface anisotropy is said to be uniaxial in nature (*i.e.*, it does not discriminate between the magnetization being “up” or “down” relative to the film plane).

In thin film systems, PMA energy density is often parameterized in the framework of an effective PMA energy density K_{eff} , given as:^{11,12}

$$K_{\text{eff}} = \left(K_v + \frac{2K_s}{t} \right) - \frac{1}{2} \mu_0 M_s^2 = K_i - K_{\text{shape}}$$

Equation 1.33

Where K_v is the volume (or bulk) contribution to the magnetic anisotropy, K_s is the aforementioned surface anisotropy (with a factor of two to account for both interfaces of a thin film), and t is the thickness of the film. The K_v term can be thought of as a catch-all for any magnetocrystalline, magnetoelastic, etc. anisotropy in the system that would favor perpendicular anisotropy. The K_i term represents the sum of K_v and K_s . In essence, K_{eff} quantifies the energetic favorability for perpendicular magnetization relative to the shape anisotropy’s proclivity to pull the magnetization into the film plane. Thus, a positive K_{eff} is indicative of perpendicular magnetic anisotropy, whereas a negative K_{eff} would indicate in-plane magnetic anisotropy.

1.12 Domain Walls

Having established that magnetic domains can form in ferromagnetic thin films, and that under the right conditions, these domains can be perpendicular to the film surface, we will now briefly discuss the manner in which the magnetization reorients in a material when moving between domains of opposite orientation, through what is known as a domain wall (DW). Firstly, we note that a domain is not infinitesimally small; instead, it has a finite width determined by the balance of the exchange and anisotropy energies of the systems. For a system with perpendicular magnetic anisotropy, it can be understood that K_{eff} would favor a narrow DW, minimizing the number magnetic spins that are oriented off the anisotropy axis as the magnetization rotates. However, the exchange energy would favor a larger domain wall, where the transition in magnetic orientation is accomplished with a smaller angular perturbation between neighboring magnetic spins. In the thin-film geometry, the DW width λ is parameterized by the balance between K_{eff} and the exchange interaction stiffness parameter $A_{\text{ex}} = \frac{k_B T_C}{a}$ (where k_B and a are the Boltzmann constant and the interatomic spacing, respectively) by the relationship:

$$\lambda = \sqrt{A_{\text{ex}}/K_{\text{eff}}}$$

Equation 1.34

Secondly, magnetostatic considerations also set a preference for the direction in which the magnetization rotates when moving between domains with opposing magnetic orientations. As shown in Figure 1.12, if the magnetization rotates in the plane of the DW (a so-called Bloch-type DW), the DW entails the formation of surface magnetic charges. Alternatively, if the

magnetization were to rotate perpendicular to the plane of the DW (*i.e.*, a so-called Néel-type DW), volume magnetic charges would be created. For films of reasonable thickness, where the surface area is small relative to the volume of the film, the volume charges associated with a Néel-type DW increase the magnetostatic self-energy of the system more than the surface magnetic charges of a Bloch-type DW. Consequently, Bloch-type DWs are energetically favorable. In subsequent sections, we will discuss ways in which the properties of a thin film can be modified to make Néel-type DWs energetically favorable.

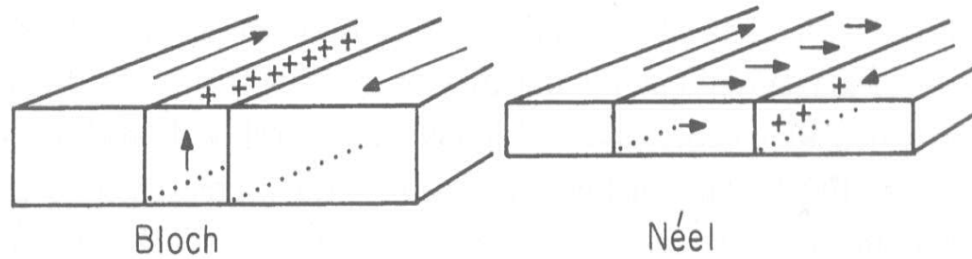


Figure 1.12: Schematic depiction of Bloch and Néel-type DWs in a ferromagnetic thin film. The + signs indicate where the magnetic charges are localized. Reproduced from Ref. 13 under the rationale of fair use. © John Wiley & Sons.

Finally, based on simple magnetostatic arguments, the Bloch-type DWs that typically form in ferromagnetic films with PMA, there is a degeneracy to the handedness with which the magnetization rotates when moving through the DW. This means that when traversing the domain wall separating an “up” domain from a “down” domain, there is not a coherent way of predicting which way the magnetization will rotate solely based on the magnetostatic considerations discussed thus far. This lack of a pattern to the rotational sense is exemplified in Figure 1.13, where spin-polarized low energy electron microscopy (SPLEEM) was used to detect the magnetic orientation within the DWs of a Ni/ [Co/ Ni]₂/ Ir thin film multilayer. In this image, the degeneracy

of the two possible rotational senses of the Bloch wall is apparent – a defining characteristic of so-called achiral magnetic textures.

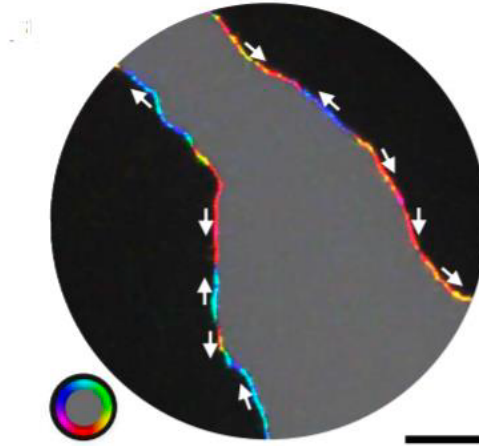


Figure 1.13: SPL-PEEM image of a system exhibiting achiral Bloch-type magnetic domain walls. Reproduced from Ref. 14 under the rationale of fair use. © Nature Publishing Group.

1.13 The Interfacial Dzyaloshinskii-Moriya Interaction

A question we may ask at this point is how can one create a ferromagnetic system whose domain walls contribute to the development of a well-defined chirality with which the magnetization rotates? That is, how can we guarantee that the magnetization rotates in a specific direction as we pass from an “up” domain to a “down” domain and vice-versa? In recent years, an additional energetic contribution known as the Dzyaloshinskii-Moriya interaction (DMI) has attracted significant research attention. First described by Dzyaloshinskii in 1958¹⁵ and Moriya in 1961¹⁶, the DMI was originally suspected to occur in materials that exhibit itinerant ferromagnetism and whose crystal structure is non-centrosymmetric (*e.g.*, MnSi¹⁷, FeGe¹⁸, and MnGe¹⁹). The non-centrosymmetric crystal structure of such a system is demonstrated in Figure 1.14, where the atomic species that exist at position \mathbf{r} differs from that found at position $-\mathbf{r}$,

violating central symmetry. The lack of central symmetry in these systems was postulated to give rise to a relatively weak spin-orbit interaction between the electronic states of the itinerant ferromagnet and the metalloid constituents. Under the influence of off-diagonal terms in the spin-orbit coupling tensor, transitions between the five available d -orbital states of the itinerant ferromagnet can occur, including transitions between orthogonal orbitals (*e.g.*, d_{xz} to $d_{x^2-y^2}$).

Because of the spin-orbit coupling of electron dynamics, a change in the orientation of electron orbital motion due to the DMI could also be expected to impact the orientation of the spin angular momentum. Thus, a perturbation in the orientation of the magnetic moment of one atom relative to its neighbors can occur. This action of the IDMI is best understood by examining its Hamiltonian, given as:²⁰

$$H_{DMI} = -\vec{D} \cdot (\vec{s}_1 \times \vec{s}_2)$$

Equation 1.35

Where \vec{D} represents the strength and handedness of the spin-orbit coupling mediated interaction described above (the so-called DMI energy density). In stark contrast to the Hamiltonian of the Heisenberg exchange mechanism provided in Equation 1.1, the vector product nature of the DMI Hamiltonian implies that the DMI energy is minimized when the spin angular momenta of neighboring spins are orthogonal to one another. While the DMI in its original interpretation offers a pathway for the creation of materials that exhibit ferromagnetism and noncollinear spin alignment, it is restricted in applicability to a relatively narrow class of materials that exhibit weak, itinerant ferromagnetism and a non-centrosymmetric crystal structure. These intrinsic limitations place severe constraints on the temperature and magnetic field space over which the DMI can be strong enough to significantly contribute to the magnetic properties of a system.

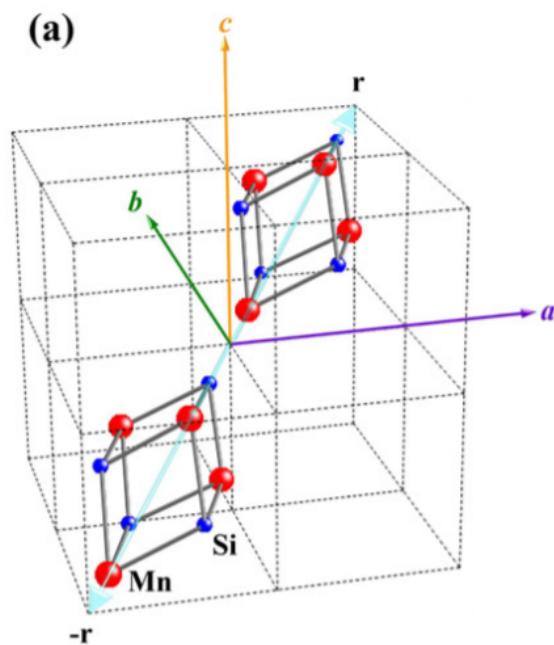


Figure 1.14: The non-centrosymmetric B₂₀-type crystal structure of the weak ferromagnet MnSi. Reproduced from Ref. 21 under the rationale of fair use. © IOP Publishing Ltd.

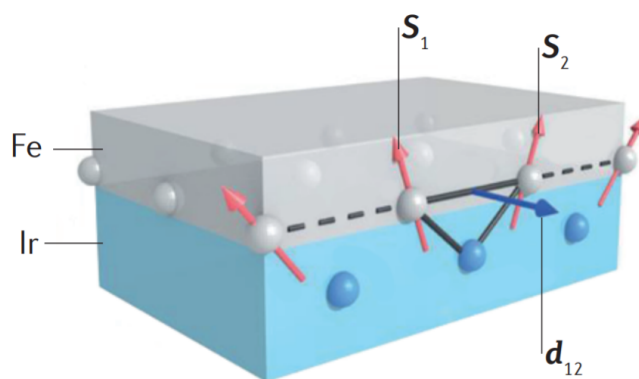


Figure 1.15: The action of the interfacial Dzyaloshinskii-Moriya interaction at an interface between Ir and Fe. Reproduced from Ref. 22 under the rationale of fair use. © Macmillan Publishers Limited.

In 1990, however, it was theoretically demonstrated that an equivalent form of the DMI can be accessed in thin film systems that feature interfaces between ferromagnetic materials and $5d$ heavy metals with a large degree of spin-orbit coupling (SOC), such as Pt, Ta, or Ir.²³ At the interface between these two materials, the spin-orbit coupling of the heavy metal layer can induce a favorability for noncollinear spin alignment in the ferromagnetic layer, provided that there is electronic hybridization between the ferromagnet $3d$ heavy metal $5d$ electronic states. In Figure 1.15, a schematic depiction of this so-called interfacial DMI (iDMI) is provided for an Ir/Fe interface. From the functional form of the DMI provided in Equation 1.35, it is apparent that neighboring spin states become canted relative to one another about an axis perpendicular to the vector that connects the two ferromagnetic atoms. The magnitude and sign of the iDMI energy density D (which expresses both the proclivity and directionality of this canting) can be predicted via the spatial and energetic overlap of the $3d$ orbitals of the ferromagnetic material and the $5d$ orbitals of the heavy metal layer using *ab initio* electronic structure calculations.^{24,25} For example, in Figure 1.3, we demonstrate how when the iDMI sets a preference for transitions between the $3d_{xy}$ and $3d_{yz}$ electronic orbitals in a ferromagnetic material, the preferred magnetic moment orientation (which is antiparallel to the spin angular momentum) follows a specific pattern when through domain walls, between magnetic domains of opposing orientation. For the scenario shown in Figure 1.16, the magnetic moment moves clockwise in the xz plane (*i.e.*, as a Néel-type DW) when moving from an “up” to a “down” domain. Magnetic systems that demonstrate such a fixed handedness to the rotation of the magnetic moment when moving between regions with different magnetic polarization are classified as being chiral. The inherent adjustability of the material properties of thin film systems permits a certain control over the range of temperatures and magnetic fields under which the iDMI can play a strong role in determining the net magnetic

properties of a material system.²⁶ The coherent rotational sense promoted by the iDMI is particularly apparent in the SPLEEM image shown in Figure 1.17, where it can clearly be seen that traversing between an “up” (light grey) and “down” (black) domain, the magnetization of the domain wall is always of one orientation, while the DW magnetization is opposite when moving from a “down” to an “up” domain. The chirality of this rotation is better highlighted in Figure 1.18, where the magnetization orientation across a cross-sectional path spanning an “up”, “down”, back to “up” domain is shown to rotate through one complete revolution in a consistently clockwise manner corresponding to a positive D .

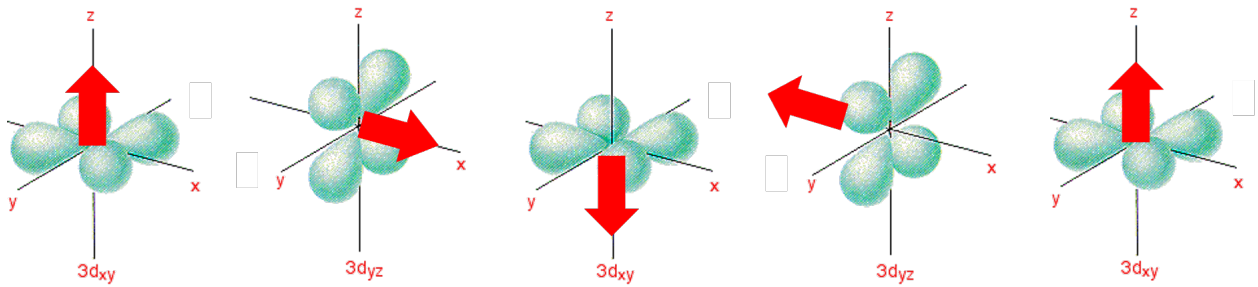


Figure 1.16: Schematic depiction of how the tendency of the iDMI to favor certain transitions between electronic orbitals in turn sets a handedness to how the magnetic moment transitions when moving in space between regions of a ferromagnet with different magnetic polarizations relative to the z-axis. In this specific example, the ferromagnetic system would be said to exhibit clockwise or right-handed Néel chirality.

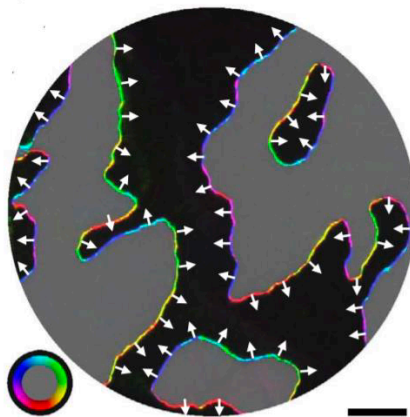


Figure 1.17: SPLEEM image of a system exhibiting chiral Néel-type domain walls. Reproduced from Ref. 14 under the rationale of fair use. © Nature Publishing Group.



Figure 1.18: Cross-sectional profile of the magnetic orientation when traveling from an “up” to “down” to “up” domain in a system with chiral Néel-type domain walls. Reproduced from Ref. 27. © Nature Publishing Group.

Now, attention can be turned to a special kind of magnetic domain that can form as the result of a delicate balance of the exchange, iDMI, anisotropy, and magnetostatic terms discussed thus far – the skyrmion. In 1962, Skyrme proposed that baryons and mesons could be modeled as local, winding like disturbances in the otherwise continuous and ordered vector field that describes their interactions.²⁸ The winding-like nature of these sub-atomic particles was posited to lend them a degree of so-called topological protection – that is to say, they were stable because they could not be continuously deformed to another state.^{29,30} While Skyrme’s ideas failed to gain much traction in the particle physics community, elements of his postulation eventually caught on in the field of solid-state physics.

Mathematically speaking, a magnetic skyrmion can be treated as a special class of cylindrical magnetic domains which have a well-defined integer “winding number” $|S|$, calculated from the x and y components of the magnetic spin orientation of a domain, its domain wall, and its immediate surroundings as:³¹

$$S = \frac{1}{4\pi} \int \vec{m} \cdot (\partial_x \vec{m} \times \partial_y \vec{m}) dx dy = \pm 1$$

Equation 1.36

Graphically, this means that a skyrmion is characterized by the fact that when the two-dimensional vector profile that defines a skyrmion is mapped to the three-dimensional unit sphere,

it will cover the unit sphere exactly one time, as demonstrated in Figure 1.19 for a Néel-type skyrmion that can form under the influence of iDMI. This unique geometric property of a skyrmion lends it a certain degree of “topological protection” against deformation to the uniform magnetic state (as originally formulated by Skyrme for baryons and mesons). In the subsequent sections, the material conditions that generally must be satisfied to stabilize magnetic skyrmions will be discussed, as well as how their unique properties are attractive from an applied perspective.

1.14 Skyrmion Stabilization: Material Considerations

As discussed previously, the iDMI with its preference for non-collinear magnetic ordering, offers a pathway by which magnetic skyrmions can be stabilized in thin film systems. Furthermore, *ab initio* calculations provide a means by which the magnitude and sign of the iDMI generated at different ferromagnet (FM)/ heavy metal (HM) interfaces can be predicted. In Figure 1.20, such calculations of the iDMI energy density created at various HM/FM interfaces is shown. These calculations provide an idea as to the materials systems that could reasonably be expected to exhibit iDMI, and offers some (albeit, limited) periodic trends to its sign and magnitude.

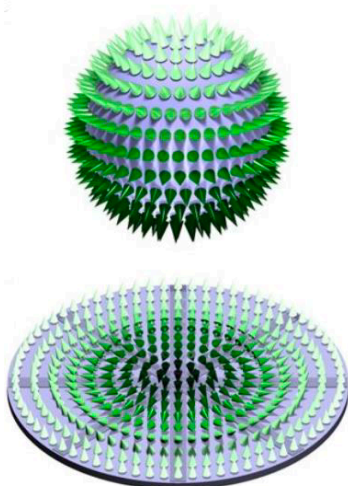


Figure 1.19: Mapping of the two-dimensional profile of a Néel-type skyrmion (bottom) to completely cover the three-dimensional unit sphere exactly one time (top). Reproduced from Ref. 32 under the rationale of fair use. © Nature Publishing Group.

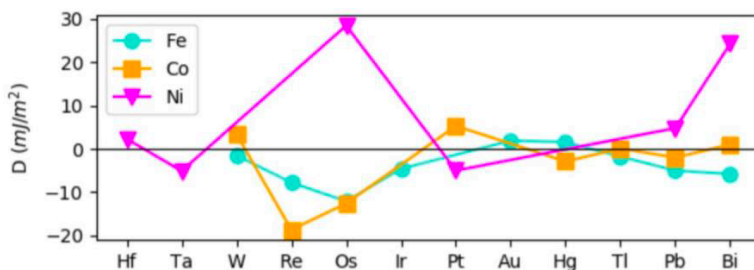


Figure 1.20: The predicted sign and magnitude of iDMI energy density originating at different heavy metal/ferromagnet interfaces. Reproduced from Ref. 25 under the rationale of fair use. © Nature Publishing Group.

While these calculations offer some guidance as to engineering materials with large iDMI, a consequential property of iDMI is obscured. In Fert's initial postulation of the antisymmetric exchange originating at FM/HM interfaces, it was also claimed that given the symmetry of the spin-orbit coupling tensor, structural inversion asymmetry must be present in order for a net iDMI to develop in a FM layer. Practically, this means that a net iDMI will only develop in systems

where there is a difference in the magnitude and/or sign of the iDMI energy density present at the top and bottom interfaces of a FM layer. This difference can originate from the chemical identity of the interface, the interfacial quality (e.g., roughness, intermixing), or some combination thereof.^{23,26,33} A schematic diagram of a material system engineered to have a net iDMI within the FM layers is provided in Figure 1.21.

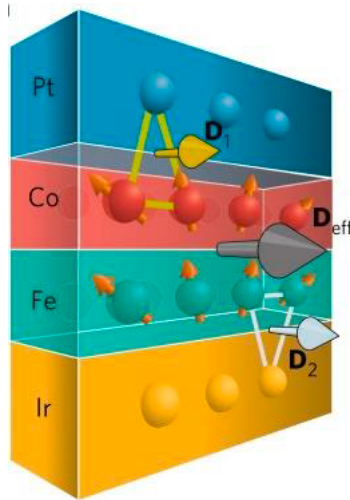


Figure 1.21: An example of how structural inversion asymmetry and material choice can be used to impart a net iDMI to a ferromagnetic layer. Note the parallel alignment of the D vectors indicated at the Ir/Fe and Co/Pt interfaces. Reproduced from Ref. 34 under the rationale of fair use. © Nature Publishing Group.

To better illustrate the concepts of structural inversion asymmetry and iDMI, consider a Pt/Co interface – one of the archetypal iDMI-active interfaces. In the context of the iDMI, structural inversion asymmetry means that a Pt/Co interface and a Co/Pt interface should be expected to have the same magnitude of iDMI but of opposite sign. Thus, a Pt/Co/Pt structure featuring interfaces of identical quality should exhibit zero net iDMI to cancellation of the spin-orbit coupling-induced interorbital transitions in the FM layer. Experimentally, this cancellation of the iDMI has been realized in epitaxially-grown Pt/Co/Pt systems, where the chemical sharpness

and roughness of both the HM/FM and FM/HM interfaces is of a similar quality.³⁵ However, the sensitivity of the iDMI magnitude on the interfacial quality can be inferred from reports of measurable iDMI in other Pt/Co/Pt systems not grown epitaxially, where the emergence of a net iDMI can only be attributed to a variation in quality between the top and bottom Co interfaces.^{36,37,38}

As the name might imply, the antisymmetric action of the iDMI is strongest within the first one to three monolayers of ferromagnetic atoms closest to the FM/HM interface.²⁴ This means that the thickness of the ferromagnetic layer will have an impact as to whether the iDMI will be capable of overpowering the magnetostatic favorability to for achiral Bloch-type DWs to form in a FM film. As the thickness of the FM layer is increased, the surface area to volume ratio of the material decreases – indicating that the material is losing its interfacial character. As the fraction of atoms in the material that are close to the interface decreases, the impact of the iDMI relative to the Heisenberg exchange and magnetostatic energy decreases.³⁹ In the context of Chapter 1.10, an increasing FM thickness will also diminish the effects of the surface anisotropy. This means that in order to leverage the iDMI to stabilize chiral DWs and skyrmions, a limitation is set on the thickness of ferromagnetic materials that can be used.

While the conditions outlined immediately above dictate the conditions necessary to created Néel-walled magnetic domains, the stabilization of Néel-type magnetic skyrmions requires the optimization of several additional material parameters. Broadly speaking, in order to stabilize Néel-type skyrmions, the energetic penalty to forming a domain wall must be low.⁴⁰ The energetic penalty associated with forming a domain wall in a thin film system with iDMI is commonly expressed as:³⁷

$$\sigma = 4 \sqrt{A_{ex}K_{eff} - \pi|D|}$$

Equation 1.37

Where A_{ex} is the previously defined exchange stiffness strength, K_{eff} is the effective PMA constant, and $|D|$ is the iDMI energy density. From Equation 1.37, it can be seen that increasing D and/or lowering A_{ex}/K_{eff} are all valid pathways to reduce the energy penalty associated with forming DWs, and by extension, skyrmions.^{40,41,42}

1.15 Detecting iDMI and Exploitation of Magnetic Chirality

When trying to understand the structure of the domain walls in a magnetic system, quantifying the iDMI energy density D is often one of the first steps. The most direct way to experimentally measure D is using Brillouin light scattering (BLS) spectroscopy. The BLS measurement works based on the principle that if present, the effective magnetic field created by the iDMI will set a non-reciprocity to the propagation of left versus right-handed spin waves or magnons in the film.^{43,44,45} Using laser irradiation at variable incidence angles and a multiple-pass Fabry-Perot interferometer to accurately measure the wavelength of inelastically backscattered light, a Stokes and anti-Stokes signal can be detected. The Stokes (anti-Stokes) signal corresponds to photons that have lost (gained) energy during inelastic scattering with the magnon modes of the system. By measuring the frequency asymmetry between the Stokes and anti-Stokes signal relative to zero frequency $\Delta f(k)$ as the wavevector of the incident light k is varied, the iDMI energy density can be calculated using the expression:

$$\Delta f(k) = \frac{2\gamma}{\pi M_s} Dk$$

Equation 1.38

Where γ is the gyromagnetic ratio, M_s is the saturation magnetization, and k is the wavevector of the incident light.

Typically, BLS measurements of the iDMI in thin film systems with PMA is done in the Damon-Eschbach geometry, where the sample is subjected to a saturating in-plane magnetic field during the measurement that is perpendicular to both the spin-wave propagation direction as well as the incidence plane.⁴⁶ Given that the iDMI is of particular interest in thin film systems that exhibit strong PMA, this can set a limitation on the types of materials that can be studied using BLS, depending on the magnetic field capabilities of the optical setup. Furthermore, as BLS relies on the inelastic scattering of light – a process with an inherently low cross-section – acquiring a suitable BLS spectrum can take the better part of an entire day. Therefore, while BLS offers a very direct measurement of the iDMI, other, faster techniques are often used.

One such technique relies on the use of an energy symmetry-breaking, non-saturating in-plane magnetic field. If one writes out the elastic energy density associated with a domain wall for a system that features iDMI in the presence of an in-plane magnetic field, given as:⁴⁷

$$\sigma(\theta, \varphi) = 4 \sqrt{A_{ex} K_{eff}} - \pi D \cos(\varphi - \theta) - \pi H_x M_s \lambda \cos \varphi + \frac{\ln 2}{\pi} t_f \mu_0 M_s^2 \cos^2(\varphi - \theta)$$

Equation 1.39

Where φ is the angle between the domain wall core magnetization and the in-plane applied field H_x , θ is the azimuthal angle about a circular domain wall, and t_f is the ferromagnetic layer thickness. The first term in Equation 1.39 reflects the resting energy of having a Bloch wall, the second term represents the reduced energy to forming a domain wall initiated by the iDMI (which acts as an effective magnetic field), the third term is the Zeeman energy with respect to H_x at each azimuthal position, and the final term represents the domain wall anisotropy energy which magnetostatically favors the formation of achiral Bloch domain walls over Néel-type walls. From

this expression, it is clear that when considering a roughly circular domain wall in the presence of both iDMI and H_x , the Zeeman interaction between H_x and the local domain wall magnetization profiles leads to an angular dependence of the elastic energy density, and that one side of the domain will have a lower elastic energy than the other side. When an out-of-plane magnetic field is applied in order to expand the domain, this energy asymmetry will manifest as an asymmetry in the growth rate with azimuthal position. This line of thought is schematically depicted in Figure 1.22.³⁷

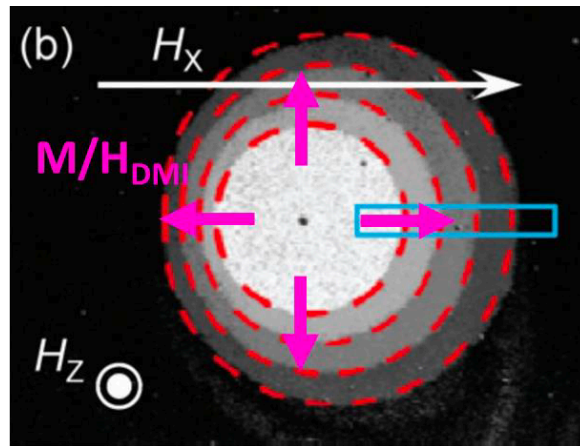


Figure 1.22: Asymmetric domain expansion in a system exhibiting iDMI and PMA exposed to a static in-plane magnetic field (H_x) and a pulsed out of plane magnetic field (H_z). Adapted from Ref. 37 under the rationale of fair use. © American Physical Society.

A major benefit of this energy asymmetry-based probe of iDMI is that it can easily be implemented in a simple polar Kerr effect microscope (as will be discussed in Chapter 2). Furthermore, besides gaining a qualitative sense of the strength of the iDMI based on the asymmetry of domain growth, a quantitative measure of the iDMI energy density D can be obtained as well. Given the structure of a Néel-type domain wall, the greatest disparity in the energy density (and thus, the expansion rate) should be found when comparing between the left

and right side of the domain (*i.e.*, along the axis the in-plane magnetic field is applied). By measuring the velocity of expansion of each side of the domain wall as a function H_x strength, the side with the larger Zeeman energy will exhibit a characteristic minimum in velocity when $H_x = H_{DMI}$. Physically speaking, H_{DMI} is the maximum field at which the iDMI is capable of stabilizing the Néel-type magnetization profile before the DW core magnetization fully rotates in the direction of H_x . From these velocity measurements, D can be calculated using the expression:³⁷

$$D = \mu_0 H_{DMI} M_S \sqrt{\frac{A}{K_{eff}}}$$

Equation 1.40

While this domain growth asymmetry-based technique is certainly more indirect than using BLS to measure iDMI, it can easily be used to study the effects of iDMI in systems that possess large perpendicular magnetic anisotropy and can be performed in a significantly shorter amount of time.

Having discussed two separate ways to measure the iDMI in thin film systems, it is pertinent to discuss the traits that make chiral Néel-type domain walls and skyrmions attractive for use in applications, compared to Bloch-type domain walls. Oftentimes, the stabilization of Néel-type domain walls requires engineering interfaces between ferromagnetic materials and heavy metals with a large degree of spin-orbit coupling to optimize the iDMI energy density. In recent

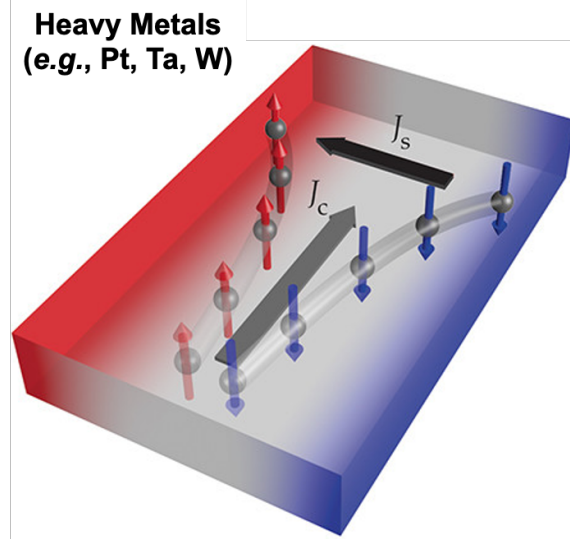


Figure 1.23: Demonstration of how a charge current J_C can lead to the development of a transverse spin current J_S in thin layers of heavy metals with large spin-orbit coupling. Reproduced from Ref. 48 under the rationale of fair use. © AIP Publishing LLC.

years, it has been shown that when an electrical charge current is passed through a heavy metal layer with large spin-orbit coupling, a transverse current of spin angular momentum can develop and migrate to the interfaces of the heavy metal layer via a process known as the spin-Hall effect.⁴⁹⁻⁵⁰ A schematic depiction of the spin-Hall effect is provided in Figure 1.23. When this spin current is transmitted into and absorbed by an adjacent ferromagnetic layer, a so-called spin-orbit torque is exerted on the magnetization textures, which can lead to the motion of domain walls and/or switching of domain polarities.^{51,52,53,54} Particularly, the Slonczewski-like effective field H_{SL} associated with the spin current created by the spin-Hall effect depends on the orientation of the local magnetization relative to the applied charge current, through the proportionality:⁵⁴

$$\vec{H}_{SL} \propto \theta_{SH}(\vec{m} \times (\hat{z} \times \vec{j}_e))$$

Equation 1.41

Where θ_{SH} is the spin-Hall angle (which reflects the efficiency and polarization with which the heavy metal layer converts charge current to a transverse spin current), \hat{z} is the unit vector oriented

out of the plane of a film, and j_e is the applied charge current density. From Equation 1.41, it is clear that the Slonczewski-like field magnitude is maximized when the magnetization and the cross product of \hat{z} and \vec{j}_e are orthogonal to one another. If we imagine a system with perpendicular magnetic anisotropy and an iDMI strong enough to promote the formation of chiral Néel-type domain walls as shown in Figure 1.24, the functional form of Equation 1.41 implies that $|H_{SL}|$ would be maximized within the domain walls, not within the domains themselves. Furthermore, the directionality of H_{SL} is opposite on either side of a perpendicular domain – meaning that the spin-orbit torque in such a system does not promote domain expansion, but instead leads to coherent motion of entire domains.

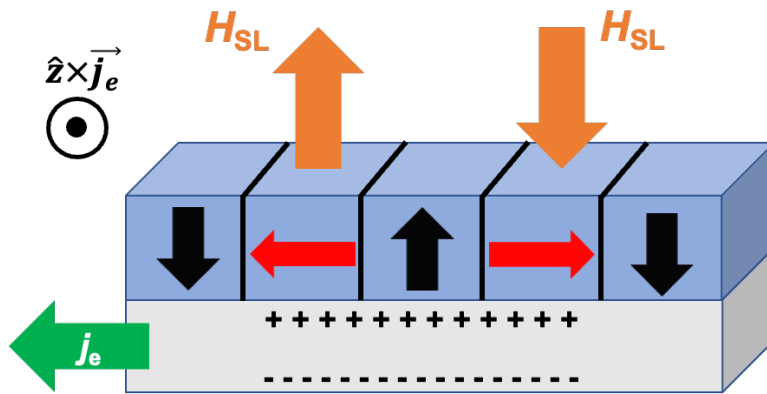


Figure 1.24: Schematic depiction of a ferromagnetic film with perpendicular magnetic anisotropy and right-handed Néel-type domain walls grown on top of a heavy metal layer with large spin-orbit coupling. When the electron flow direction is from right to left and the spin-Hall angle is positive, the functional form Equation 1.41 predicts that $|H_{SL}|$ will be maximized in the domain walls and will be oriented in opposite directions on either side of the domain – resulting in the coherent translation of domains as opposed to domain expansion.

The ability to coherently move perpendicular magnetic domains using spin-orbit torques could form the basis of next generation memory and computing architectures. In 2009, Parkin *et al.* proposed the concept of the DW racetrack memory scheme⁵⁵, demonstrated in Figure 1.25. In

this proposed technology, a stripline is used to encode “bits” as magnetic domains in a wire of magnetic material that exhibits chiral Néel-type domain walls. In the context of the spin-Hall effect, a charge current may then be passed through an underlying heavy metal layer to initiate a spin-orbit torque on the chiral domain walls, leading to the coherent motion of entire magnetic domains. Moving the domains past a magnetoresistive sensor, data stored as magnetic domains can be read out. Such a memory scheme combines the stability of magnetic recording (*i.e.*, hard disk drives) with the speed of solid-state flash memory. Furthermore, unlike hard disk drives, the DW racetrack memory architecture easily facilitates the development of three-dimensional storage arrays. While the racetrack memory scheme was originally envisaged to rely on the use of one-dimensional planar domain walls, skyrmions – with their similar susceptibility to spin-orbit torques and inherent “topological protection” – have become candidate magnetic textures for use in such architectures.

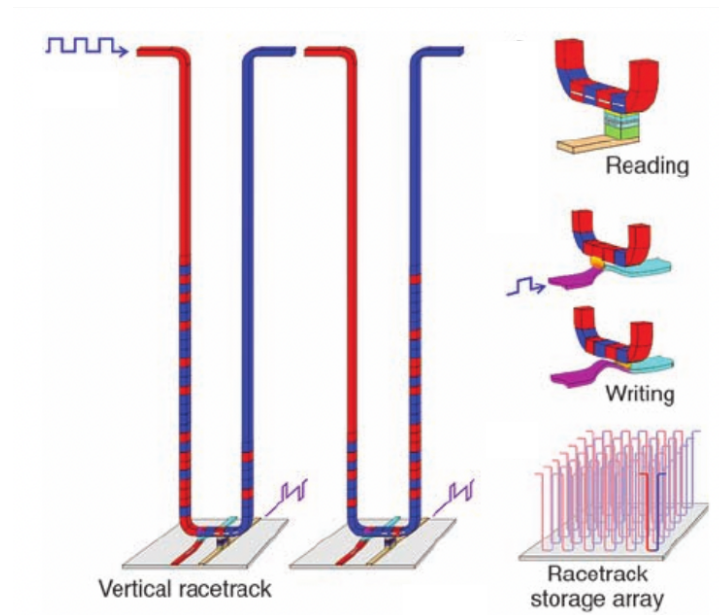


Figure 1.25: Overview of the vertical DW racetrack memory architecture and how data/ domain states can be read using a magnetoresistive sensor and written to the racetrack using the Oersted field created by a stripline. Data is moved through the racetrack through the application of electrical current pulses, which generate spin-orbit torques via the spin-Hall effect. Reproduced from Ref. 55 under the rationale of fair use. © AAAS.

More recently, there has been a concerted research effort in the field of neuromorphic computing, aiming to mimic the manner in which the human brain stores and processes information with unparalleled efficiency using magnetic, electronic, or spintronic systems that are analogous to biological neurons and synapses. A key underlying theme in the field of neuromorphic computing is the fact that dynamical elements (neurons) are connected (by synapses) in a random fashion to give a non-linear output.^{56,57} The “memory” of a neuromorphic system is determined by a training of the coupling strength between neurons, facilitated by the synapses.

While many approaches have been proposed to realize such behavior in solid-state model systems, one such approach has been dubbed skyrmion reservoir computing, as shown in Figure 1.26.⁵⁶ In this neuromorphic computing scheme, a reservoir of magnetic skyrmions is initialized within a magnetic film seeded on a heavy metal layer that exhibits the spin-Hall effect. By distributing voltage input leads at random locations throughout the skyrmion reservoir and inputting data (in the form of voltage pulses), spin-orbit torques will act on the skyrmions – causing them to move. To first order, defects and pinning sites that will inevitably be present in the reservoir material will lead to inhomogeneities in the current density throughout the reservoir device – which will inhibit the uniformity with which the skyrmions in the ensemble move. Because of this and other sources of inhomogeneous response (*e.g.*, inter-skyrmion interactions, edge effects, *etc.*), the configurational state of the skyrmion ensemble (*i.e.*, the position of each skyrmion) becomes a non-linear function of the sequence and magnitude of the voltage pulse inputs. Given that such computing architectures are still in the theoretical or prototypical phase, a robust understanding of the dynamics and stabilization of skyrmions is a key precondition to bringing such ideas into reality.

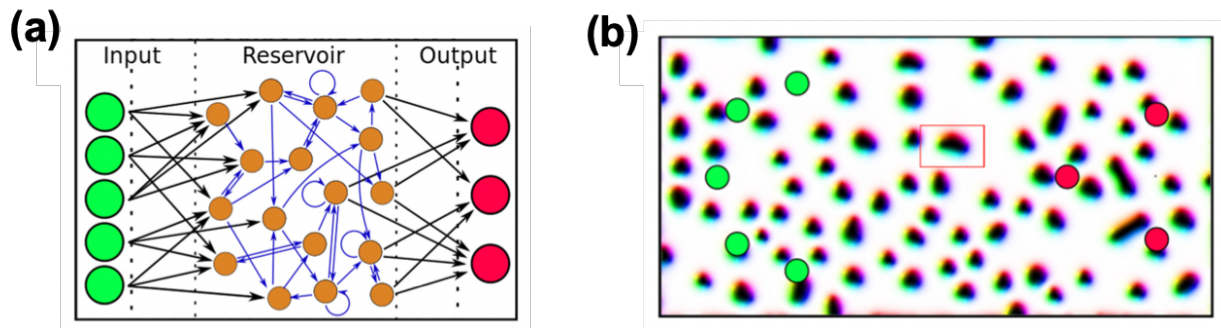


Figure 1.26: (a) Schematic illustration of reservoir computing, whereby the input signals act on a disordered, randomly linked ensemble of dynamical elements to give rise to a non-linear output. (a) illustration of how the memory architecture demonstrated in (a) can be realized in a magnetic system that contains an ensemble of magnetic skyrmions. Reproduced from Ref. 58 under the rationale of fair use. © American Physical Society.

1.16 References

- ¹ N. Spaldin, *Magnetic Materials: Fundamentals and Applications (2nd Edition)*, Cambridge University Press (2010).
- ² NIST Reference on Constants, Units, and Uncertainty. (2019).
- ³ A. Lande, *Zeit. Fur Physik* **5**, 231 (1921).
- ⁴ C. Kittel, *Introduction to Solid State Physics*, John Wiley and Sons (1996).
- ⁵ F. Tyler, *Phil. Mag.* **11**, 596 (1931).
- ⁶ P. Weiss, *Comptes Rendus* **143**, 1136 (1907).
- ⁷ L.D. Landau and E.M. Lifshitz, *Phys. Z. Sowjetunion* **8**, 153 (1935).
- ⁸ A. Hubert and R. Schafer, *Magnetic Domains*, Springer (1998).
- ⁹ L.E.F. Neel, *J. Phys. (Paris)* **15**, 225 (1954).
- ¹⁰ M.A. Howson, *Contemp. Phys.* **35**, 347 (1994).
- ¹¹ M.T. Johnson, P.J.H. Bloemen, F.J.A. den Broder, and J.J. de Vries, *Rep. Prog. Phys.* **59**, 1409 (1996).

-
- ¹² S. Bandiera, R.C. Sousa, B. Rodmacq, and B. Dieny, *IEEE Mag. Lett.* **2**, 3000504 (2011).
- ¹³ R.C. O’Handley, *Modern magnetic materials: Principles and applications*, John Wiley & Sons (2000).
- ¹⁴ G. Chen, A.T. N’Diaye, S.P. Kang, H.Y. Kwon, C. Won, Y. Wu, Z.Q. Qiu, and A.K. Schmid, *Nature Comm.* **6**, 6598 (2015).
- ¹⁵ I. Dzyaloshinskii, *J. Phys. Chem. Solids* **4**, 241 (1958).
- ¹⁶ T. Moriya, *Phys. Rev.* **120**, 91 (1961).
- ¹⁷ X. Z. Yu, N. Kanazawa, Y. Onose, K. Kimoto, W. Z. Zhang, S. Ishiwata, Y. Matsui, and Y. Tokura, *Nat. Mater.* **10**, 106 (2011).
- ¹⁸ A. Neubauer, C. Pfleiderer, B. Binz, A. Rosch, R. Ritz, P. G. Niklowitz, and P. Böni, *Phys. Rev. Lett.* **102**, 186602 (2009).
- ¹⁹ H. Wilhelm, M. Schmidt, R. Cardoso-Gil, U. Burkhardt, M. Hanfland, U. Schwarz, and L. Akselrud, *Sci. Technol. Adv. Mater.* **8**, 416 (2007).
- ²⁰ O. Nakanishi, A. Yanase, A. Hasegawa, and M. Kataoka, *Solid State Commun.* **995** (1980).
- ²¹ T.Y. Ou-Yang, G.J. Shu, J-Y. Lin, C.D. Hu, and F.C. Chou, *J. Phys: Condens. Mat.* **28**, 026004 (2016).
- ²² A. Fert, N. Reyren, and V. Cros, *Nat. Rev. Mat.* **2**, 17031 (2017).
- ²³ A. Fert, *Mat. Sci. Forum* **59-60**, 439 (1990).
- ²⁴ H. Yang, A. Thiaville, S. Rohart, A. Fert, and M. Chshiev, *Phys. Rev. Lett.* **115**, 267210 (2015).
- ²⁵ P. Jadaun, L.F. Register, and S.K. Banerjee, *npj Comp. Mater.* **6**, 88 (2020).
- ²⁶ A. Fert, V. Cros, and J. Sampaio, *Nat. Nanotech.* **8**, 152–156 (2013).
- ²⁷ I. Kezsmarki, S. Bordacs, P. Milde, N. Neuber, L.M. Eng, J.S. White, H.M. Ronnow, C.D. Dewhurst, M. Michizuki, K. Yani, H. Nakamura, D. Ehlers, V. Tsurkan, and A. Loidl, *Nature Mat.* **14**, 1116 (2015).
- ²⁸ T.H.R. Skyrme, *Nuclear Phys.* **31**, 556 (1962).
- ²⁹ E.M. Nyman and D.O. Riska, *Phys. Scripta* **34**, 6 (1986).
- ³⁰ D.C. Ortuno, W. Wang, M. Beg, R.A. Pepper, M.A. Bisotti, R. Carey, M. Vousden, T. Kluyber, O. Hovorka, and F. Fangohr, *Sci. Rep.* **7**, 4060 (2017).
- ³¹ S. Heinze, K. Bergmann, M. Menzel, J. Brede, A. Kubetzka, R. Wiesendanger, G. Bihlmayer, and S. Blugel, *Nature Phys.* **7**, 713 (2011).

-
- ³² M. Hoffmann, B. Zimmermann, G.P. Muller, D. Schurhoff, N.S. Kiselev, C. Melcher, and S. Blugel, *Nature Comm.* **8**, 308 (2013).
- ³³ J. Sampaio, V. Cros, S. Rohart, A. Thiaville, and A. Fert, *Nature Nanotech.* **8**, 839 (2013).
- ³⁴ A. Soumyanarayanan, M. Raju, A.L. Gonzalez Oyarce, A.K.C. Tan, M.Y. Im, A.P. Petrovic, P. Ho, K.H. Khoo, M. Tran, C.K. Gan, F. Ernult, and C. Panagopoulos, *Nature Mat.* **16**, 898 (2013).
- ³⁵ A. Hrabec, N.A. Porter, A. Wells, M.J. Benitez, G. Burnell, S. McVitie, D. McGrouther, T.A. Moore, and C.H. Marrows, *Phys. Rev. B* **90**, 020402(R) (2014).
- ³⁶ A.W.J. Wells, P.M. Shepley, C.H. Marrows, and T.A. Moore, *Phys. Rev. B* **95**, 054428 (2017).
- ³⁷ S.G. Je, D.H. Kim, S.C. You, B.C. Min, K.J. Lee, and S.B. Choe, *Phys. Rev. B* **88**, 214401 (2013).
- ³⁸ M. Quinsat, Y. Ootera, T. Shimada, M. Kado, S. Hashimoto, H. Morise, S. Nakamura, and T. Kondo, *AIP Advances* **7**, 056318 (2017).
- ³⁹ J. Cho, N.H. Kim, S. Lee, J.S. Kim, R. Lavrijsen, A. Solignac, Y. Yin, D.S. Han, N.J.J. van Hoof, H.J.M Swagten, B. Koopmans, and C.Y. You, *Nature Comm.* **6**, 7635 (2015).
- ⁴⁰ F. Buttner, I. Lemesch, and G.S.D. Beach, *Sci. Rep.* **8**, 4464 (2018).
- ⁴¹ S. Rohart and A. Thiaville, *Phys Rev. B* **88**, 184422 (2013).
- ⁴² J.A. Brock and E.E. Fullerton, *Adv. Mater. Inter.*, In Press (2021).
- ⁴³ M. Kostylev, *J. Appl. Phys.* **115**, 233902 (2014).
- ⁴⁴ J.H. Moon, S.M. Seo, K.J. Lee, K.W. Kim, J. Ryu, H.W. Lee, R.D. McMichael, and M.D. Stiles, *Phys. Rev. B* **88**, 284404 (2013).
- ⁴⁵ F. Garcia-Sanchez, P. Borys, A. Vansteenkiste, J.-V. Kim, and R.L. Stamps, *Phys. Rev. B* **89**, 224408 (2014).
- ⁴⁶ M. Belmeguenai, J.-P. Adam, Y. Roussigne, S. Simer, T. Devolder, J.-V. Kim, S.M. Cherif, A. Stashkevich, and A. Thiaville, *Phys. Rev. B* **90**, 020402(R) (2016).
- ⁴⁷ J.P. Pellegren, D. Lau, and V. Sokalski, *Phys. Rev. Lett.* **119**, 027203 (2017).
- ⁴⁸ J. Sinova and T. Jungwirth, *Phys. Tod.* **70**, 38 (2017).
- ⁴⁹ M.I. Dyakonov and V.I. Perel, *Phys. Lett. A* **35**, 459 (1971).
- ⁵⁰ J.E. Hirsch, *Phys. Rev. Lett.* **83**, 1834 (1999).

-
- ⁵¹ L. Liu, O.J. Lee, T.J. Gudmundsen, D.C. Ralph, and R.A. Buhrman, *Phys. Rev. Lett.* **109**, 096602 (2012).
- ⁵² A.V. Khvalkovskiy, V. Cros, D. Apalkov, V. Nikitin, M. Krounbi, K.A. Zezdin, A. Anane, J. Grollier, and A. Fert, *Phys. Rev. B* **87**, 020402 (2013).
- ⁵³ C.F. Pai, L. Liu, Y. Li, H.W. Tseng, D.C. Ralph, and R.A. Buhrman, *Appl. Phys. Lett.* **101**, 122404 (2012).
- ⁵⁴ S. Emori, U. Bauer, S.-M. Ahn, E. Martinez, and G.S.D. Beach, *Nature Mat.* **12**, 611 (2013).
- ⁵⁵ S.S.P. Parkin, M. Hayashi, and L. Thomas, *Science* **320**, 190 (2008).
- ⁵⁶ D. Prychynenko, M. Sitte, K. Litzius, B. Kruger, G. Bourianoff, M. Klaui, J. Sinova, and K. Everschor-Sitte, *Phys. Rev. Appl.* **9**, 014034.
- ⁵⁷ J. Grollier, D. Querlioz, K.Y. Camsari, K. Everschor-Sitte, S. Fukami, and M.D. Stiles, *Nature Electronics* **3**, 360 (2020).
- ⁵⁸ D. Pinna, G. Bourianoff, and K. Everschor-Sitte, *Phys. Rev. Appl.* **14**, 054020 (2020).

Chapter 2: Experimental Techniques

2.1 Sputter Deposition

The materials that form the basis of this dissertation were fabricated using the physical vapor deposition technique known as sputtering. The basic principles of sputter deposition are as follows: On one side of an ultrahigh vacuum (UHV) chamber, bulk pieces (“targets”) of the material one wishes to deposit as a thin film are placed within a shuttered enclosure. The substrate upon which the film will be grown is placed opposite but facing towards the target material. Next, a partial pressure of inert gas (typically Ar) is introduced to the chamber. Then, an electric potential difference is established between the target and the substrate by supplying a negative voltage to the target using a power supply. The electric field created by this voltage causes the free electrons that exist in the UHV environment to be accelerated away from the target. If this acceleration is strong enough, the electrons will have sufficient kinetic energy to ionize the Ar atoms previously introduced to the sputtering chamber – creating a plasma of Ar⁺ ions. These Ar⁺ ions are themselves accelerated towards the target material. When they collide with the target, atoms of the target material are ablated in a cone-shaped profile away from the target, including towards the substrate. It should be noted that the ablated target material is not ionized by the collisions that give rise to their ejection. A schematic depiction of the sputtering process is provided in Figure 2.1.

As mentioned previously, when a negative voltage is applied to the target material, the free electrons in the chamber are accelerated away from the target, towards the substrate. However, these electrons carry significant kinetic energy, and could in turn result in sputtering of material

off the substrate itself. To remedy this issue (and to enhance the density of the plasma formed near the target and increase the sputtering rate), permanent magnets can be placed directly behind the target materials. This magnetic field acts to keep the free electrons confined away from the substrate area and causes the electrons to assume a helical path around the target material – which improves the probability of an ionization event, densifying the plasma. When sputtering is performed using these permanent magnet arrays and a time-invariant voltage, it is referred to as dc magnetron sputtering.

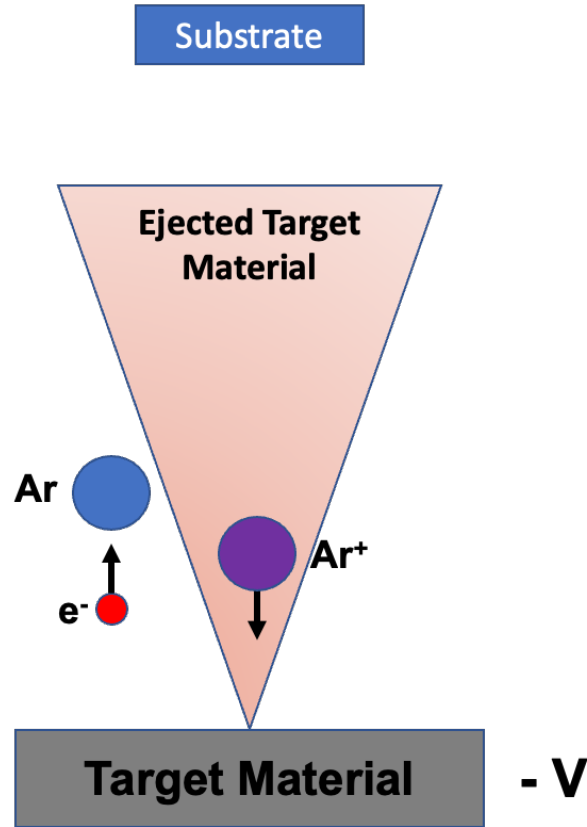


Figure 2.1: Schematic depiction of the sputtering process. When a negative voltage is applied to a target material, free electrons in the chamber are accelerated away from the target. If these accelerated electrons possess enough kinetic energy to ionize the Ar atoms introduced to the chamber, a plasma is formed, and the Ar⁺ ions are accelerated towards the target material. The collision of Ar⁺ ions with the target causes atoms of target material to be ejected in a cone shaped profile away from the target. The atoms of target material become deposited when they collide with the substrate.

To grow the materials discussed in this dissertation, an ATC Orion sputtering tool was employed, manufactured by AJA International. This tool allows for eight target materials to be placed in the UHV chamber at a given time – providing flexibility as to the complexity of multilayer structures that can be grown. A turbomolecular pump is used to ensure a base pressure on the order of 10^{-9} Torr to minimize the effects of contamination. The guns are arranged in a confocal geometry, such that the cone-shaped profile to the ablated materials' trajectory is focused to the same point (the substrate). The uniformity with which the sample is coated with target material is ensured by rotating the substrate about the normal vector of its surface during the deposition process.

2.2 X-ray Reflectivity Measurements

Crucial to the controlled, predictable growth of thin films is understanding the rate at which material is deposited on the substrate by the sputtering process. To quantify the deposition rate, we take advantage of X-ray reflectivity (XRR) measurements. In order to understand the underlying physics of these measurements, we consider a thin film of thickness t , as shown in Figure 2.2. If X-ray radiation is incident on this sample at an angle θ relative to the sample plane, it can be assumed that some light is specularly reflected at the top and bottom interfaces. However, given that the film will generally have a refractive index that differs from that of vacuum, refraction can be expected at the film-vacuum interface. Thus, the X-ray incidence angle at the film-vacuum (θ_1) and substrate-film interface (θ_2) will be different. Snell's law dictates that if vacuum has an index of refraction $n_1 = 1$ and the film has an arbitrary index of refraction $n_2 = 1 - \delta_2$ (where δ_2 is the real component of the film's index of refractive index), the refraction angle θ_2 is given as:

$$\theta_2 = \cos^{-1} \left(\frac{\cos \theta_1}{n_2} \right) \approx \sqrt{\theta_1^2 - 2\delta_2}$$

Equation 2.1

Under the assumption of a small θ_1 . Provided that the wavelength of the X-ray radiation is reasonably lower than the film thickness and the film thickness isn't so large that the X-rays are significantly absorbed, Bragg's law will be satisfied for particular θ values, as given by:

$$n\lambda = 2t \sin \theta$$

Equation 2.2

Where n is an integer greater than zero, λ is the X-ray wavelength, t is the film thickness, and θ is the incidence angle. Physically, Bragg's law allows us to predict the incidence angles at which the path length difference between X-rays diffracted at bottom interface (green lines in Figure 2.2) and top interface is equal to an integer multiple of the X-ray wavelength. To account for the refraction that occurs when the X-ray enters a film, a modified version of Bragg's law for X-ray reflectivity for low incidence angles can be written as:

$$n\lambda = 2t \sin \theta_2 \approx 2t \sqrt{\theta_1^2 - 2\delta_2}$$

Equation 2.3

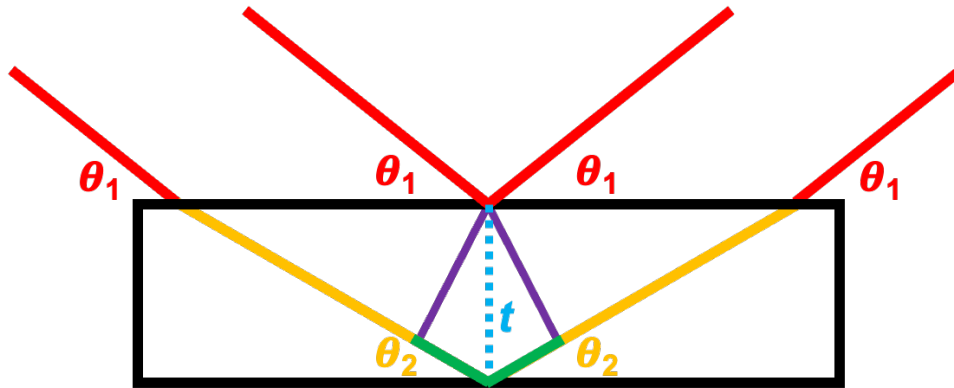


Figure 2.2: Schematic diagram of the geometry and principle of an X-ray reflectivity (XRR) measurement of film thickness. θ values indicate angles of incidence and reflection, whereas t denotes the film thickness. The green line segments indicate the path length difference between X-rays refracted at the top versus the bottom interface of a film of thickness t .

In Figure 2.3, we show an XRR pattern for a CoO thin film, grown on a MgO substrate. It is noted that there is a clear periodicity to the peaks (known as Kiessig fringes) in this low-incidence angle regime. In the case of a uniform film, the angular position of the “troughs” of the Kiessig fringes (*i.e.*, the angles at which destructive interference occurs) are of interest. This is because at the film-vacuum interface - where the X-rays are passing from a material with a low refractive index to a material with a higher index of refraction – the refracted X-rays will experience a 180° phase shift relative to the X-rays specularly reflected at this interface. Thus, when the path length difference between X-rays reflected at the top and bottom interfaces of the film is equal to an integer multiple of the X-ray wavelength, destructive interference is the expected outcome. By assigning each of these troughs an index number m and determining the θ_1 value associated with each m , it is possible to determine the thickness of the film by fitting to a rearrangement of the modified Bragg’s law presented in Equation 2.3:¹

$$\sin^2 \theta_1 = \left(\frac{m\lambda}{2t}\right)^2 + 2\delta_2$$

Equation 2.4

Knowing that the X-ray diffractometer used generates Cu K α radiation ($\lambda = 1.54 \text{ \AA}$), Equation 2.2 was used to determine that the CoO film has a thickness of 36.51 nm.

We note that while XRR was primarily used in this thesis to determine the rate at which sputtered material was deposited on substrates, these measurements can provide a wealth of information regarding thin-films and multilayers.² For example, it is noted that δ_2 can also be expressed as:

$$\delta_2 = \frac{N_A r_e \lambda^2 \rho}{\pi m_{atom}} (Z + f')$$

Equation 2.5

Where N_A is Avogadro's number, r_e is the electron radius, ρ is the atomic density of a material, Z is the atomic number of the film, f' is a correction factor describing the optical dispersion of the atoms in the material, and m_{atom} is the mass of the constituent atoms. Thus, for a film of known elemental composition, careful fitting of XRR spectra can provide information regarding the density of the deposited material. This information is also accessible from the critical angle θ_c measured during an XRR measurement – corresponding to the incidence angle at which total internal reflection is no longer observed – by the relationship $\theta_c = \sqrt{2\delta_2}$.

In this dissertation, calibration growths were performed, whereby the power supplied to a given target material was held constant and the shutter covering the target was opened to allow

target material to reach a substrate. By keeping track of the duration of the deposition, measuring the sample thickness with XRR allows us to calculate a deposition rate for each target material.

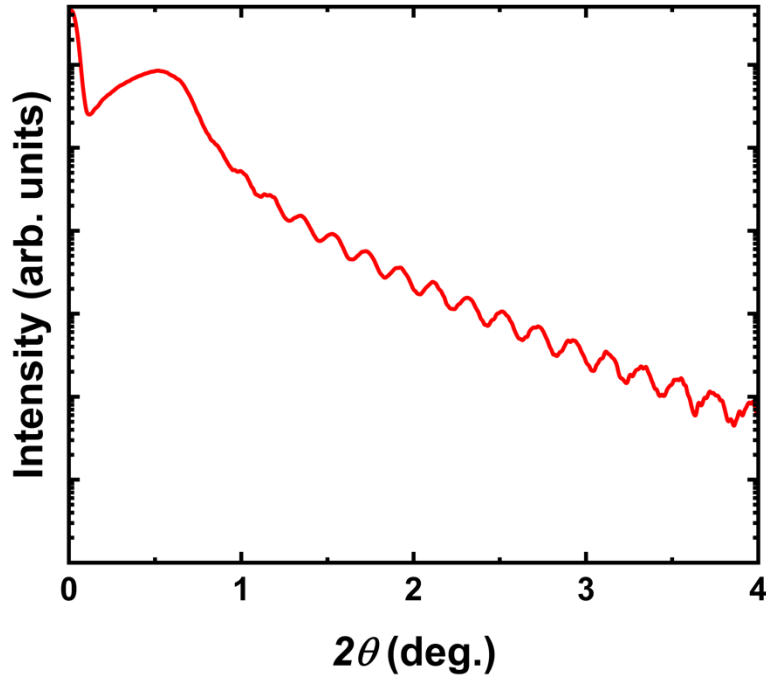


Figure 2.3: X-ray reflectivity (XRR) profile of a CoO thin film, collected using Cu $K\alpha$ radiation.

2.3 UV Photolithography

For some of the studies discussed in this dissertation, there was a need to use patterned magnetic materials as opposed to the isotropic films that are created by the sputtering process. To this end, ultraviolet (UV) photolithography was employed. UV photolithography is an industry-standard patterning technique. The feature resolution of UV photolithography is primarily set by the diffraction limit of the radiation and photoresist used in the process. Photoresists are polymer solutions whose chemical properties (namely, the degree of crosslinking) are affected by exposure to UV light. As the degree of crosslinking impacts the solubility of the resist in a suitable

developing liquid, the selective exposure of a resist-coated surface followed by immersion in a developer solution allows for the definition of patterned structures. Broadly speaking, photoresists can be classified into two categories: Positive resists and negative resists. For a sample coated in positive photoresist, regions exposed to UV light will have the resist washed off during development. For a sample coated in negative resist, regions exposed to UV light will remain covered in resist after developing.

To allow for the selective exposure of resist coated samples, two different exposure techniques were used in the course of dissertation: Photomask lithography and direct-laser write lithography. In photomask lithography, a panel of soda lime glass that contains a duplicate of the pattern you wish to transfer to the substrate (defined using chromium features) is required. After placing the glass panel in direct contact with the substrate using a tool known as a mask aligner, a mercury vapor lamp located above the photomask is energized to provide UV radiation. The chromium features on the photomask block the light from reaching certain parts of the sample – allowing the desired selective exposure of the substrate. Photomask lithography allows for the rapid throughput of samples, at the expense of flexibility in pattern design (*i.e.*, one is limited to the patterns that are present on the photomask). In direct-laser write (or maskless) lithography, the sample is raster-scanned beneath a UV (375 nm) laser diode. The pattern one wishes to impart to the sample is designed using computer-aided design (CAD) software, which controls when the laser diode is energized, and thus, which areas of the sample are exposed to UV light. While maskless lithography is a somewhat slower process than photomask lithography, it provides a great deal of flexibility as to how quickly the pattern can be modified to create different structures.

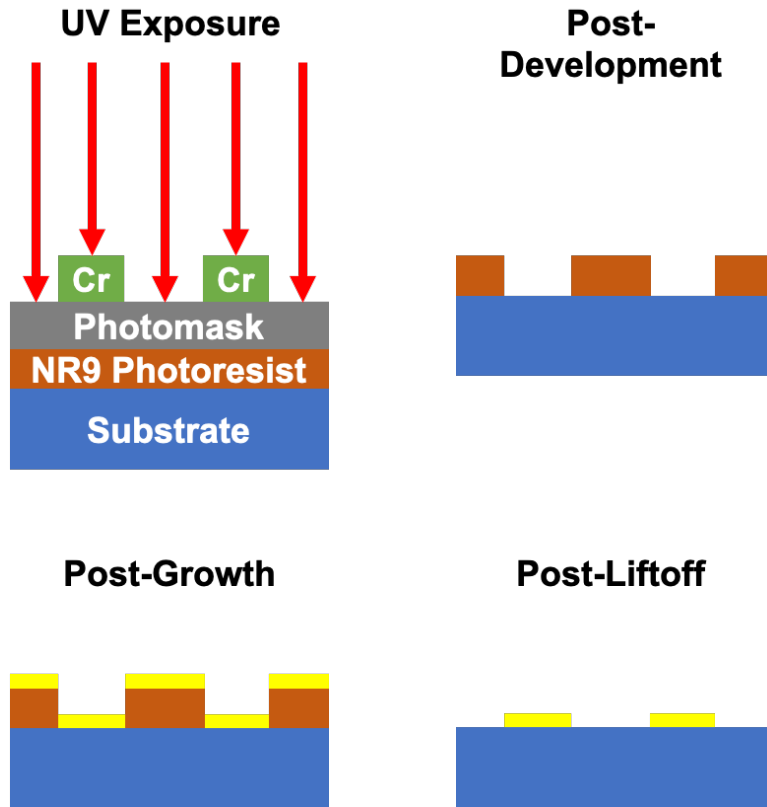


Figure 2.4: Schematic depiction of several important steps of the photomask lithography process when a negative-tone photoresist is used. The yellow layers indicate a generic metal layer deposited using sputter deposition.

For the lithography work performed in this dissertation, the following methodology to the lithography process was followed, in line with the resist manufacturer's specifications:

1. Cleaning of the substrates by sonication in acetone for five minutes, followed by sonication in isopropyl alcohol for five minutes, followed by a rinse spray with deionized (DI) water and drying using a pre-purified nitrogen blowgun.
2. Spin-coating of the substrates with Futurrex NR9-1500-PY, a negative-tone photoresist. The sample was attached to a vacuum chuck placed on the spin axis of a spin coater before ~5 mL of photoresist was placed on the substrate surface using a pipette. The sample was then spun at 4500 rpm for one minute, resulting in a ~1 μm -thick uniform coating.
3. After spin-coating resist onto the substrates, each substrate was heated using a hot plate at 150C for 1 minute to evaporate any remaining solvent from the photoresist mixture.

4. Exposure of the photoresist-covered samples. When using the mask aligner to perform lithography, exposures were performed in “hard contact” mode, and the samples were exposed to the mercury lamp for 13 seconds. When using maskless lithography, the exposure was conducted using a dose of 1300 mJ/cm² of 375 nm UV light, with no over/under focus of the laser beam.
5. Post-exposure baking of the substrates at 100C for one minute to further harden the photoresist layer.
6. Development of the photoresist by gentle agitation in Futurrex RD6 developer solution for 13 seconds.
7. Immediately after removing the sample from the Futurrex RD6 developer, gentle agitation of the sample in DI water for 10 seconds to remove all developer from the sample.
8. Drying of the sample using a pre-purified nitrogen blowgun.
9. Using dc magnetron sputtering, a magnetic film can be grown on top of the patterned substrate. While the film will grow on both the exposed and resist-coated areas of the substrate, rinsing the sample in acetone will remove the portion of the film grown on photoresist from the substrate – leaving the film only at locations that were not exposed to UV light during Step 4. This step is also known as liftoff.

Key steps from the process described above (for photomask lithography) are demonstrated in Figure 2.4.

2.3 Vibrating Sample Magnetometry

To determine the basic static magnetic properties of the samples discussed in this dissertation (such as the saturation magnetization M_s and the hysteresis loop shapes), a measurement technique known as vibrating sample magnetometry (VSM)³ was employed. In the VSM technique, the sample we wish to study is attached to a non-magnetic rod, which in turn is attached to a linear short-throw motor, which causes the sample to vibrate up and down. If the sample is vibrated in and out of a pickup coil and if the sample possesses a component of

magnetization along the axis of the pickup coils, the sample motion leads to the formation of a time-varying magnetic flux Φ_M in the pickup coils. Faraday's law of electromagnetic induction tells us that this magnetic flux will result in an electromotive force V_{EMF} acting on the pickup coils, given by:

$$V_{EMF} = \frac{\partial \Phi_M}{\partial t} = \frac{\partial \Phi_M}{\partial z} \frac{\partial z}{\partial t}$$

Equation 2.6

Where z is the sample position along the axis of the pickup coil. Through electrical detection of the V_{EMF} induced in the pickup coils, it is possible to solve for the sample's net magnetic moment m using the expression:

$$m = \frac{V_{EMF}}{2\pi A \sin(2\pi f t)}$$

Equation 2.7

Where f is the frequency at which the sample is oscillated, and A is the spatial amplitude of the oscillation. Using lock-in amplification (locked to the frequency with which the sample is oscillated), it is possible to obtain very accurate, low-noise measurements of a sample's net m . A schematic depiction of the VSM technique is provided in Figure 2.5.

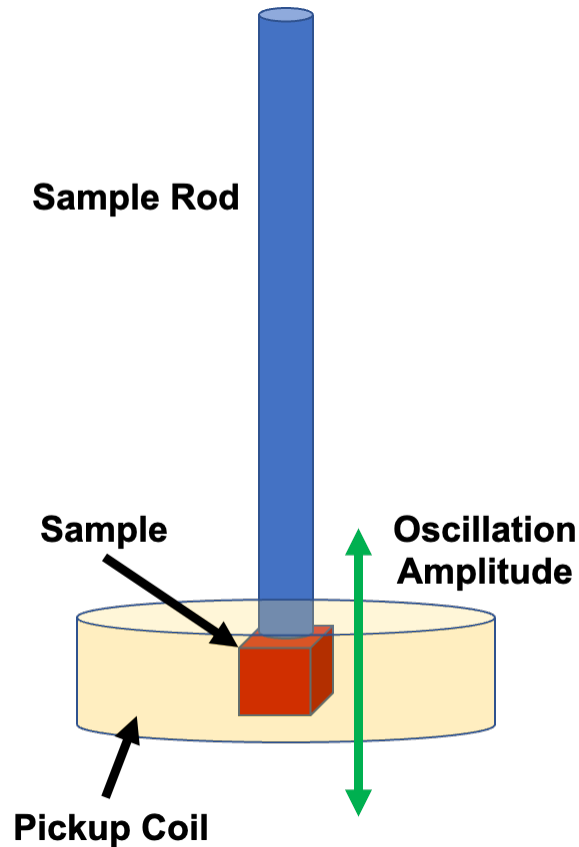


Figure 2.5: Schematic depiction of the vibrating sample magnetometry (VSM) measurement technique, as discussed in Chapter 2.3.

In this work, we have used the VSM option for a VersaLab system, manufactured by Quantum Design, Inc. Besides providing the necessary electronics to perform a VSM measurement, the VersaLab system can change the sample temperature T over the range $50 \text{ K} < T < 400 \text{ K}$ in its default configuration, using a closed-cycle refrigeration unit and a nichrome heater. Besides cooling the sample, the closed-cycle compressor unit is also used to chill a metallic solenoid into a superconducting state, which permits large electrical currents to pass through the solenoid to generate large magnetic fields. The maximum strength magnetic field that the VersaLab can generate is 3 T. It is important to note that a static magnetic field (like that provided by the superconducting solenoid) does not have a direct impact on the VSM-based measurement

of the magnetic moment, as it is not a time-varying field. Thus, any changes in the magnetization measured when changing the magnetic field are a result of the field's effect on the sample's magnetization when using VSM.

2.4 Magneto-optic Kerr Effect Imaging

In several chapters of this dissertation, the domain structure of ferromagnetic thin films was investigated using a magneto-optic Kerr effect (MOKE) microscope. The MOKE is a surface-sensitive, classically understood interaction between linearly polarized light and a sample's magnetization.^{4,5} We imagine the situation shown in Figure 2.6(a), whereby s-polarized light is incident on a sample with a uniform perpendicular magnetization. When one refers to s-polarization, we are implying that the electric field E that describes the light is polarized along an axis that is perpendicular to the incidence plane of the light on the sample. In Figure 2.6(b), we demonstrate the projection of the electric field of s-polarized light onto the sample surface.

The electric field associated with this polarized light will induce slight perturbation of the material's electronic structure back and forth along the axis of the incident \vec{E} . If this oscillation in the electronic structure of the sample is orthogonal to the sample's magnetization, the Lorentz force law (given as $F = q(\vec{E} + (\vec{v} \times \vec{B}))$) would indicate that an additional force will rotate the electronic oscillation axis away from \vec{E} , in a direction given by the cross product between the electronic motion and the magnetization. Consequently, some of the light reflected from the sample will have its polarization axis canted relative to the incident polarization, a so-called Kerr rotation. Using an analyzing polarizer element, we can filter out most of the light whose

polarization axis is unrotated upon reflection and get a signal or image that is primarily sensitive to the sample's magnetization.

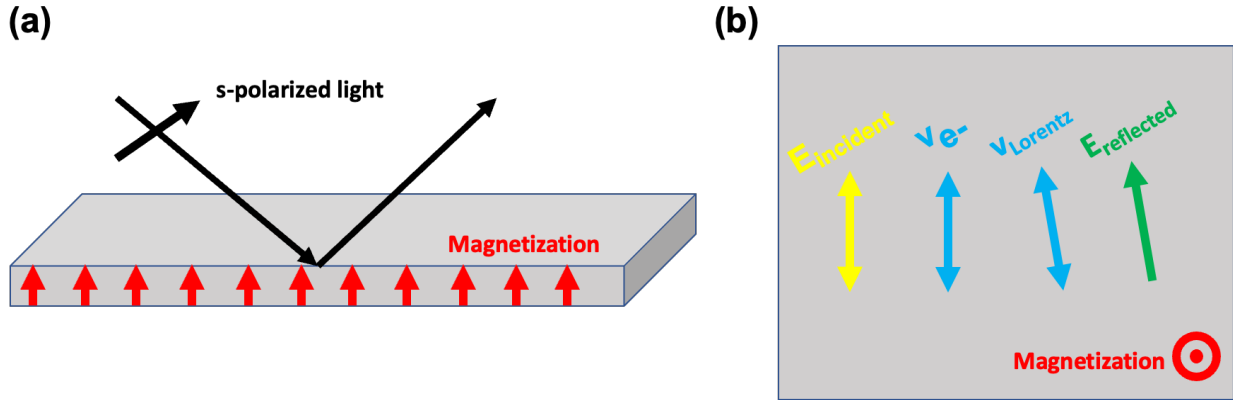


Figure 2.6: (a) Schematic illustration of s-polarized light incident on a sample with a uniform perpendicular magnetization. (b) Schematic illustration of the projection of the s-polarized light's electric field (E_{incident}) on to the sample surface, the electronic perturbation promoted by E_{incident} (v_{e-}), the deflection of the electronic trajectory by the Lorentz force (v_{Lorentz}), and the polarization axis of the reflected light ($E_{\text{reflected}}$).

For the work discussed in this dissertation, we used a MOKE imaging platform manufactured by Evico Magnetics. In this setup, white light created by an LED array is linearly polarized using a film-based transmission polarizer (which uses an array of anisotropically-oriented nanoparticles to define a preferred polarization axis of the light) and passed through a condenser lens onto the sample surface. For polar sensitivity, the off-diagonal components of the permittivity tensor dictate that the optimal incidence angle of the light is normal to the film surface⁶; as such, the incidence angle shown in Figure 2.6(a) is somewhat exaggerated. The reflected light is collected by the condenser lens and passed through an “analyzing” polarizer, which is used to reduce the contribution of light that has not undergone Kerr rotation upon reflection. This light is then directed towards a CCD camera for data recording. By illuminating

the sample in a uniform, Köhler-like fashion and using an objective lens, it is possible to spatially correlate the Kerr rotation (inferred from the intensity of light that passes through the analyzing polarizer) to specific regions on the sample. The magnification of the image is determined by the objective lens used. In this dissertation, objective lenses with 20x and 50x magnification were generally employed. The ultimate resolution attainable is set by the diffraction limit of the illumination used. An example polar MOKE image collected in zero magnetic field using the Evico Magnetics platform is shown in Figure 2.7.

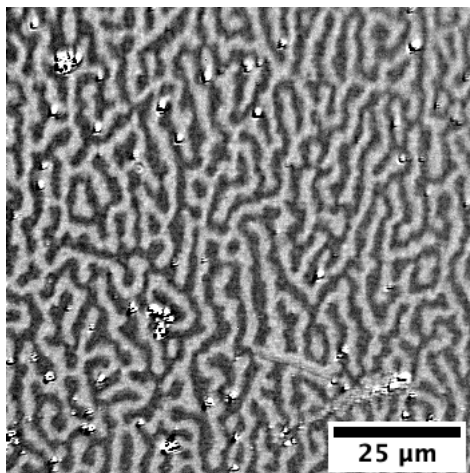


Figure 2.7: Polar MOKE image of a Pt/Co/Ni-based multilayer sample. Dark (light) coloring indicates regions where the perpendicular magnetization component is oriented “up” (“down”) relative to the film plane. This image was obtained using a 50x objective lens.

Using water-cooled electromagnets, static perpendicular magnetic fields up to 0.7 T in strength and in-plane fields up to ~ 0.33 T can be applied while imaging. In several chapters of this dissertation, pulsed perpendicular magnetic fields were applied to the samples in the presence of static in-plane magnetic fields. To accomplish this, small bobbins were fabricated out of plastic using 3D printers and hand-wound with wire to create a solenoid. Knowing the dimensions of the solenoid and the number of wire turns present, a pulsed current source was used to provide pulsed

magnetic fields of known magnitude. In some of our studies, the sample temperature can be controlled in the vicinity of room temperature ($T = 300 \text{ K} \pm 15 \text{ K}$) using a stage that brings a Peltier chip in direct contact with the sample.

2.5 Magnetic Transmission X-ray Microscopy

As mentioned in Chapter 2.4, polar MOKE imaging can be easily implemented in a tabletop format, but the imaging resolution is diffraction-limited by the wavelength of illumination used. For a white light system such as ours, a maximum resolution of $\sim 300 \text{ nm}$ is attainable under the best circumstances. For many magnetic materials (particularly those of technological interest), the domain patterns formed are much smaller than the resolution limit of MOKE microscopy. As such, other imaging techniques are needed to image small magnetic domains.

One way to work around the diffraction limit of visible light is to use illumination with a much smaller wavelength, such as X-rays. Additionally, if the X-rays are circularly polarized, this allows us to access different magnetic contrast mechanisms, namely X-ray magnetic circular dichroism (XMCD). As mentioned in Chapter 1, the occupancy of the 3d shell of a ferromagnetic material becomes asymmetric with respect to electron spin polarization on account of the exchange energy. Independent of the magnetic properties of a material, it is also known that incident radiation can promote electrons from core electronic levels to excited states, provided that the energy of the incident light is equal to the energy difference between the ground and excited electronic states. For the ferromagnetic transition metals, we often consider the 2p to 3d transition, also known as the L-absorption edge. While energy is conserved during such an excitation, angular momentum must be conserved as well. Because of the spin-dependent splitting of the 3d band and

the angular momentum of the incident light, spins of one polarization are more likely to be promoted to the excited state – resulting in a selective absorption of X-rays based on magnetic orientation. Thus, by imaging the intensity of X-ray radiation that is transmitted through a magnetic sample, contrast will be established based on the domain polarity at different regions in the sample.

To facilitate high-resolution imaging of magnetic domain morphologies, we have used the XM-1 microscope,^{7,8} located at Beamline 6.1.1 at the Advanced Light Source, Lawrence Berkeley National Laboratory. The Advanced Light Source (ALS) is a synchrotron facility that can generate linearly and circularly polarized light of energies ranging from the vacuum ultraviolet (VUV) to soft X-ray regime. A synchrotron radiation source is built around a circular accelerator, in which electrons are accelerated to nearly the speed of light by a series of synchronized electromagnets and coils. The concept of Bremsstrahlung or braking radiation dictates that when electrons are accelerated or change trajectory at relativistic speeds, they will emit radiation of an energy commensurate with the degree of acceleration.⁹ Furthermore, based on the fan-shaped profile of radiation emitted by the braking radiation, the light on opposite hemispheres of the circular path of the synchrotron has opposite circular polarizations. The energy of the radiation varies as one moves up or down within one hemisphere of this fan-shaped profile.

Having a source of tunable-energy, circularly polarized X-rays, this beam is directed towards our sample. While glass-based lenses are a mainstay in optical microscopy, such lenses are prohibitively absorptive in the X-ray regime. As such, lensless zone plate optics are used to focus the X-rays on to our sample. Zone plate optics work on the principle of diffraction of the X-rays to a common focal point by passing through a nanoscale circular grating. This focused beam is then directed onto the sample, where the XMCD effect provides magnetic contrast. Through the

use of an electromagnet, perpendicular magnetic fields up to ~ 0.3 T in strength can be applied during imaging. Provided the sample is grown on an X-ray transparent membrane, unabsorbed X-ray radiation can be transmitted through the sample. A second zone plate element known as the micro zone plate is then used to project the transmitted light onto a CCD detector. A schematic depiction of the XM-1 beam path is provided in Figure 2.8.

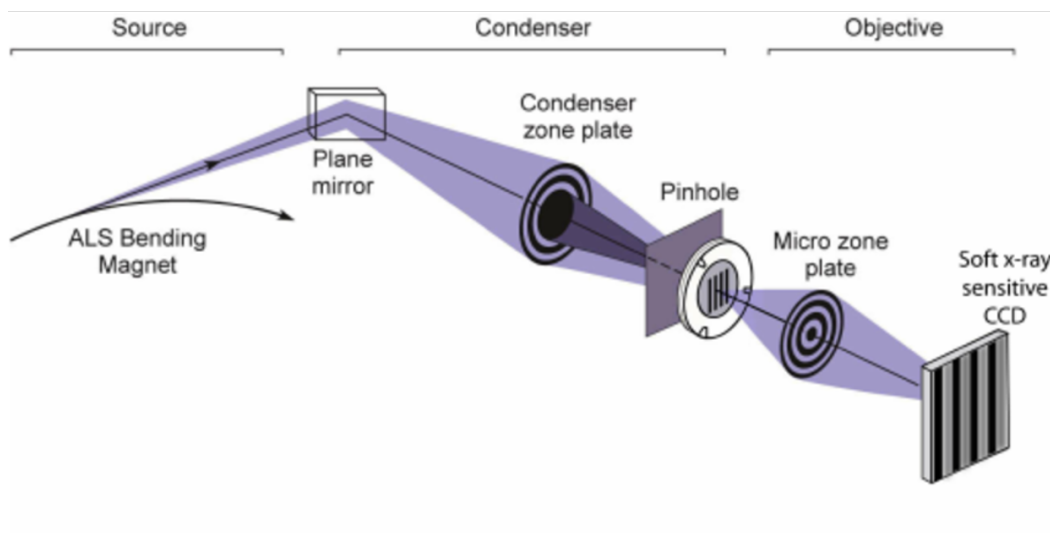


Figure 2.8: Schematic illustration of the beam path of the XM-1 microscope, located at the Advanced Light Source, Lawrence Berkeley National Laboratory. Reproduced from Ref. 10 under the rationale of fair use. © Optical Society of America.

2.6 Micromagnetic and Multiphysics Modeling

For certain studies included in this dissertation, micromagnetic modeling was performed in order to understand the underlying energetic landscapes that give rise to our experimental observations. Micromagnetic modeling provides numerical solutions to the Landau-Lifshitz-Gilbert (LLG) equation that describes magnetization dynamics. The LLG equation is given as:

$$\frac{d\vec{M}}{dt} = -\gamma \left(\vec{M} \times \vec{H}_{eff} - \eta \vec{M} \times \frac{d\vec{M}}{dt} \right)$$

Equation 2.8

Where γ is the gyromagnetic ratio of an electron, M is the sample magnetization, η is a dimensionless damping parameter, and H_{eff} is an effective magnetic field that encapsulates the effects of the exchange interaction, magnetostatic interactions, magnetocrystalline anisotropy, dipolar energy, Zeeman energy with respect to an applied field, and iDMI interaction into one term. The first cross product on the right-hand side of Equation 2.8 is known as the precessional LLG term and describes how the magnetization precesses in space about the effective magnetic field. The second cross product is referred to as the damping term and describes how the precessing magnetization will eventually damp towards the effective magnetic field. The action of these two terms is schematically shown in Figure 2.9.

Micromagnetic simulations are performed in the continuum approximation, where magnetic behavior need not be described on the atomic scale. Instead, the simulation geometry is typically discretized into nm-scale cuboids or tetrahedra (*i.e.*, small enough to describe the walls between neighboring domains). Using the LLG equation to describe the magnetization dynamics in response to stimuli (*e.g.*, applied magnetic fields, spin-orbit torque, *etc.*), micromagnetic simulations work towards finding the minimum energy configuration of all \vec{m} values assigned to each discretization volume. While thermal effects can be incorporated in micromagnetic modeling performed at finite temperatures, this dramatically impacts the time needed to perform simulations. As such, micromagnetic modeling is often performed at zero temperature. In this dissertation, the mumax³ micromagnetic software package¹¹ was used for our simulations. mumax³ can be run on a computer's graphics processing unit (GPU), and significantly reduces the amount of time needed

to perform most simulations, when compared to programs that use the central processing unit (CPU) of a computer.

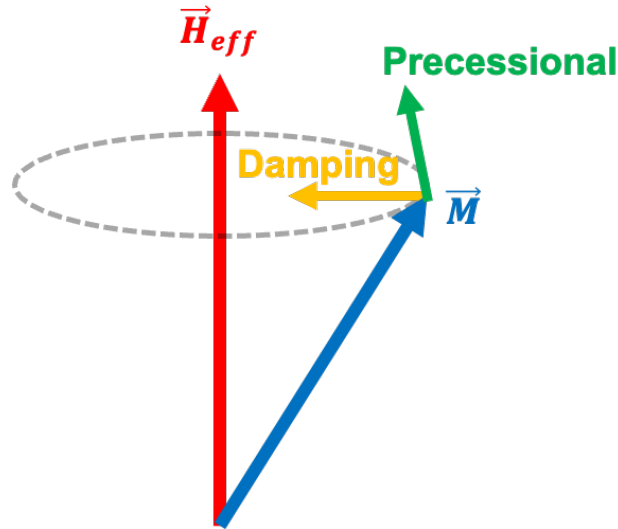


Figure 2.9: Schematic illustration of the damping and precessional terms of the Landau-Lifshitz-Gilbert (LLG) equation that describe the dynamics of the magnetization M about the effective magnetic field H_{eff} .

In several chapters of this dissertation, we have used COMSOL Multiphysics to model the Oersted fields and Joule heating that arise when electrical currents are passed through patterned magnetic features. Similar to micromagnetic modeling, COMSOL Multiphysics operates within the continuum approximation, whereby we subdivide the simulation geometry into nm-scale tetrahedra. The Oersted field created by a model wire is determined by solving Maxwell's equations for a given input current density. By inputting material additional material properties into the model (*e.g.*, electrical conductivity, thermal conductivity, convective cooling), it is also possible to model the temperature increase due to Joule heating of a micron scale wire.

2.7 References

- ¹ P.F. Miceli, D.A. Neumann, and H. Zabel, *Appl. Phys. Lett.* **48**, 24 (1986).
- ² E.E. Fullerton, I.K. Schuller, H. Banderstraeten, and Y. Bruynseraede, *Phys. Rev. B* **45**, 9292 (1992).
- ³ S. Foner, *Rev. Sci. Instrum.* **30**, 548 (1959).
- ⁴ J. Kerr, *Phil. Mag.* **3**, 321 (1877).
- ⁵ Z.Q. Qiu and S.D. Bader, *J. Magn. Magn. Mater.* **200**, 664 (1999).
- ⁶ R. Atkinson and N.F. Kubrakov, *Proc. R. Soc. Lond. A* **449**, 205 (1995).
- ⁷ A.L. Pearson, W. Chao, G. Denbeaux, T. Eimueller, P. Fischer, L.E. Johnson, M. Koehler, C. Larabell, M.A. LeGros, D. Yager, and D.T. Attwood, *Proc. SPIE* **4146**, 54 (2000).
- ⁸ G. Denbeaux, P. Fischer, G. Kusinski, M. Le Gros, A. Pearson, and D. Attwood, *IEEE Trans. Mag.* **37**, 2764 (2001).
- ⁹ A.W. Chao and M. Tigner, *Handbook of Accelerator Physics and Engineering*, World Scientific (1999).
- ¹⁰ W. Chao, J. Kim, S. Rekawa, P. Fischer, and E.H. Anderson, *Optics Exp.* **17**, 17669 (2009).
- ¹¹ A. Vansteenkiste, J. Leliaert, M. Dvornik, M. Helsen, F. Garcia-Sanchez, and B. Van Waeyenberge, *AIP Advances* **4**, 107133 (2014).

Chapter 3: Current-induced Skyrmion Generation in Pt/Co/Os/Pt Thin Films

3.1 Introduction

In recent years, there has been significant interest in exploiting the unique properties of magnetic domain walls and skyrmions in next-generation magnetic data storage, nonvolatile memories, and computation schemes.^{1,2,3,4,5} Skyrmions are particularly attractive, given their efficient motion in response to the spin-transfer and spin-orbit torques that can arise when an electrical current is passed through a sample.^{6,7} Skyrmions may form in ferromagnetic materials that feature competition between the noncollinear Dzyaloshinskii-Moriya interaction (DMI) and conventional ferromagnetic exchange.^{4,8,9} One approach to achieve this competition is by sandwiching thin ferromagnetic (FM) layers between heavy metal layers with large spin-orbit coupling (SOC), where an interfacial DMI can develop when there is an asymmetry between the sign or strength of DMI at the top and bottom interfaces of the magnetic layers.^{3,10,11,12} As the DMI strength is sensitive to the degree of SOC present at each FM interface, the DMI can be tuned by modifying the deposition conditions or chemical identity of the high-SOC layers.^{13,14,15,16}

Besides moving skyrmions, previous works have also shown that electrical currents can lead to the formation of skyrmions, through the action of spin torques on defective sites of lower anisotropy,¹⁷ or from inhomogeneous spin torques (created at constrictions¹⁸ or engineered notches¹⁹) acting on stripe domains. However, more work is needed to understand how skyrmions can predictably be nucleated and moved by electrical means. Previous reports found Pt/Co/Os/Pt thin films to be capable of hosting highly mobile, micron-scale magnetic skyrmions.²⁰ The inclusion of a thin Os layer was found to lower the magnetic moment, Curie temperature, and

perpendicular anisotropy of the Co layer – initiating a spin-reorientation transition (SRT) near room temperature.^{21,22,23,24} However, as discussed in Chapter 5, the interpretation of this transition as an SRT as originally proposed may be complicated by the addition of iDMI. The associated energy landscape of the SRT region facilitates the stabilization of skyrmions. In this paper, we discuss the motion and population dynamics of skyrmions within the same Pt/Co/Os/Pt system as a function of applied magnetic field and dc electrical current. The ability to use real-time magneto-optic Kerr effect microscopy to image these features enables quantitative assessments of skyrmion velocity and population, as well as direct observation of the processes by which skyrmions are generated under the influence of electric currents.

3.2 Experimental Techniques

A thin film of the composition Ta(5)/ Pt(3)/ Co(1.2)/ Os(0.2)/ Pt(3)/ Ta(5) (thicknesses in nm) was grown on Si substrates with a 300 nm-thick thermal oxide layer and photolithographically patterned into 100 μm wide wires using techniques described elsewhere.²⁰ Our choice in layer thicknesses was informed by our previous work, which demonstrated that this composition is the most suited for obtaining a field-induced skyrmion phase at room temperature.²⁰ The properties of the Pt/Co/Os/Pt system are extremely sensitive to the layer thicknesses, so the specific Co and Os thicknesses were the result of significant optimization. The samples were imaged using an Evico Magnetics MOKE microscope in polar detection mode equipped with a custom-built coil capable of applying small magnetic fields perpendicular to the sample plane. The process of collecting data during this study was as follows. Before each measurement, the sample magnetization was saturated in a negative perpendicular field. Next, the field was adjusted over the course of 5 seconds to the target positive field for the measurement. After reaching the targeted positive

magnetic field, 12 seconds elapsed before applying the desired dc electric current for 60 seconds. The ramp time for current application and removal was on the order of 2 seconds. Once the current was removed, another 22 seconds passed before the magnetic field was set to zero. To avoid sample damage and moving the skyrmions out of the field of view faster than the camera capture rate (~ 16 Hz), the maximum current density applied was limited to 0.23 MA/cm^2 . The number of skyrmions present in the videos and their velocities were determined using the APREX TRACK image-processing software.²⁵ The APREX TRACK software is capable of distinguishing between skyrmions and other features present in the field of view (*e.g.*, stripe domains, debris) by defining skyrmions to have surface areas between $2 \text{ }\mu\text{m}^2$ and $22 \text{ }\mu\text{m}^2$ and aspect ratios between 0.7 and 1.6. A visual demonstration of the tracking methodology is provided in Supplemental Video 1 of Ref. 26.

3.3 Skyrmion Velocity and Population Dynamics

Figure 3.1 shows static images taken at the same location of the same sample in an applied perpendicular field $H_z = +1 \text{ Oe}$ before and after applying dc electrical current densities J of 0.03 and 0.17 MA/cm^2 for 10 seconds. Before the current is applied, the film is populated with several field-nucleated skyrmions. After the current has been removed, we observe that the skyrmion population has increased, with a higher population present after higher j . This relationship between j and the skyrmion population demonstrates that the current does not just move skyrmions in the Pt/Co/Os/Pt sample,²⁰ but also leads to the generation of additional skyrmions in a nominally homogeneous wire. We have quantitatively explored the effects of different H_z and j on the current-induced motion and generation of skyrmions. Figure 3.2(a) shows the average skyrmion velocity

as a function of time t for several current densities ($j = 0.03, 0.11, 0.17,$ and 0.23 MA/cm^3) obtained using a H_z of $+1 \text{ Oe}$. Throughout Figure 3.2, $t = 0\text{s}$ corresponds to the time at which the desired magnetic field is reached, as described in Section 3.2. When the dc current is first applied, there is a rapid onset of skyrmion motion in the direction of the conventional current, with the jump in motion being related to the magnitude of j . The average speed achieved by the skyrmions well after the current is applied (*e.g.*, $t = 22\text{s}$) exhibits a strong proportionality to j , as the magnitude of spin torques should scale with current density.

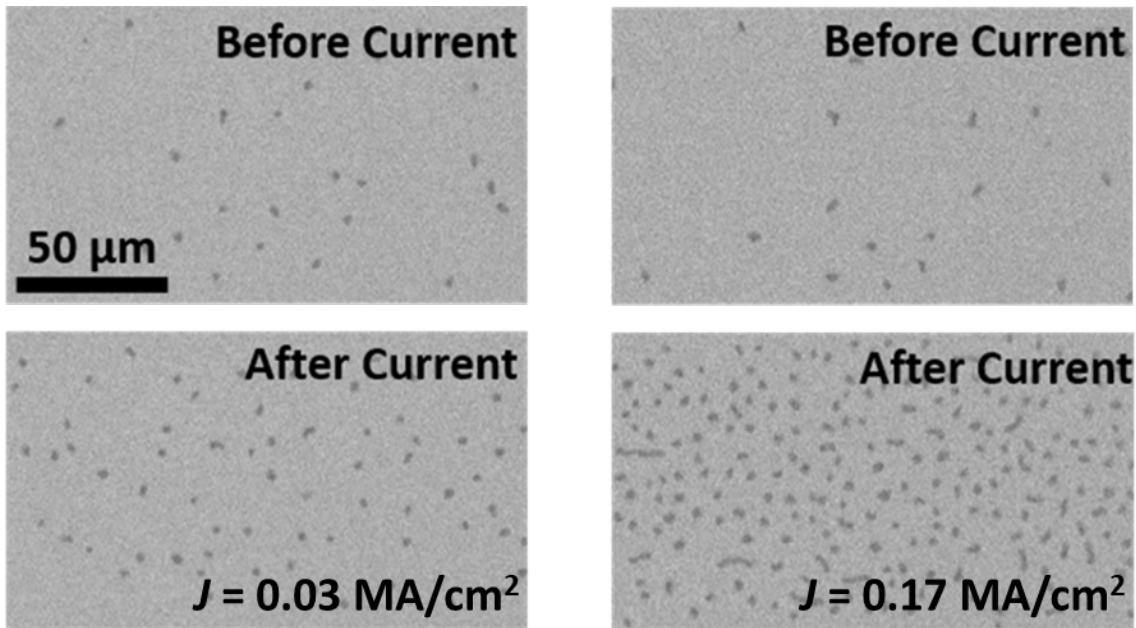


Figure 3.1: MOKE images of the same region of a Pt/Co/Os/Pt sample collected immediately before and 10 seconds after electrical current densities of 0.03 MA/cm^2 and 0.17 MA/cm^2 were applied for 10 seconds in a constant magnetic field of $H_z = +1 \text{ Oe}$. The conventional current flowed from left to right while the current was applied. Darker contrast corresponds to magnetic features oriented into the film plane.

Figure 3.2(b) shows the number of skyrmions present within a $180 \mu\text{m} \times 100 \mu\text{m}$ field of view of the wire as a function of time for the same current densities shown in Figure 3.2(a). In line

with the previous discussion regarding spin torques, it was found that the number of skyrmions present at a given elapsed time t also exhibits a proportionality to j . Furthermore, it was found that at a time after the current was first applied, the number of skyrmions present in the sample saturates – implying that a steady-state population has been reached after ~ 60 seconds. Additionally, Figure 3.2(b) also indicates that over several seconds after the current was removed (*i.e.*, a timeframe in which all spin torques should disappear), a further increase in the skyrmion population occurs. These behaviors are explored in more detail below.

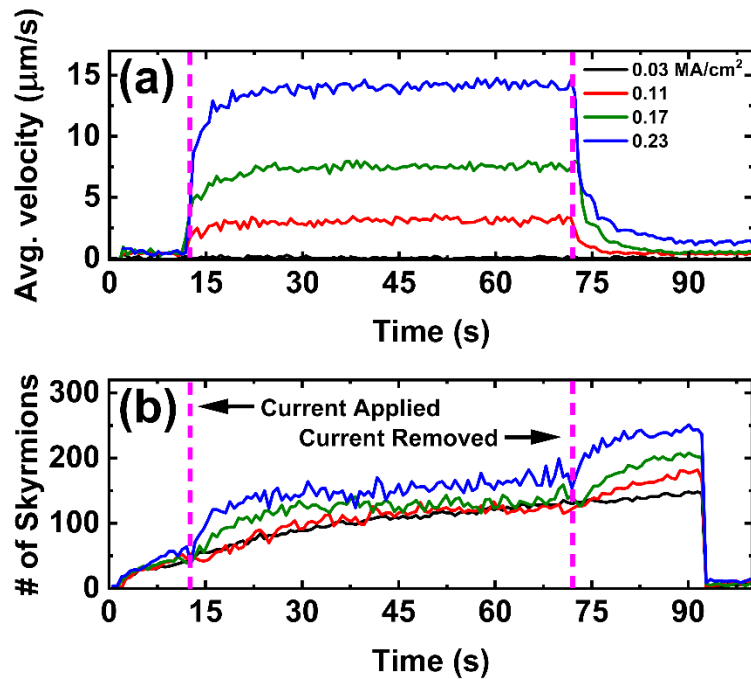


Figure 3.2: (a) Average velocity of skyrmions moving under the influence of several current densities, as a function of time. (b) The number of skyrmions present within the $180 \mu\text{m} \times 100 \mu\text{m}$ field of view as a function of time for a variety of current densities. Both (a) and (b) correspond to data collected in an applied magnetic field of $H_z = +1 \text{ Oe}$. Data are shown for every five frames of video collected, corresponding to a time increment of ~ 0.3 seconds.

Having compared skyrmion behavior under the influence of a single H_z value and several values of j , we now explore the interplay between both parameters and their impact on the

skyrmion population. In Figure 3.3(a), the number of skyrmions present immediately before the current is removed for several applied fields and currents is shown. For the lower current densities (0.03 and 0.11 MA/cm²), the field range over which skyrmions are stabilized is limited to ~1 Oe. At higher current densities (0.17 and 0.23 MA/cm²), not only does the skyrmion population increase, but the field range of stabilization is roughly doubled. Given the sensitivity of the Pt/Co/Os/Pt system to thermal effects,²⁰ the Joule heating associated with larger applied currents may provide sufficient energy to overcome the energetic barrier separating the saturated state from the metastable state, particularly at the defective sites inevitable formed during sample fabrication.²⁷

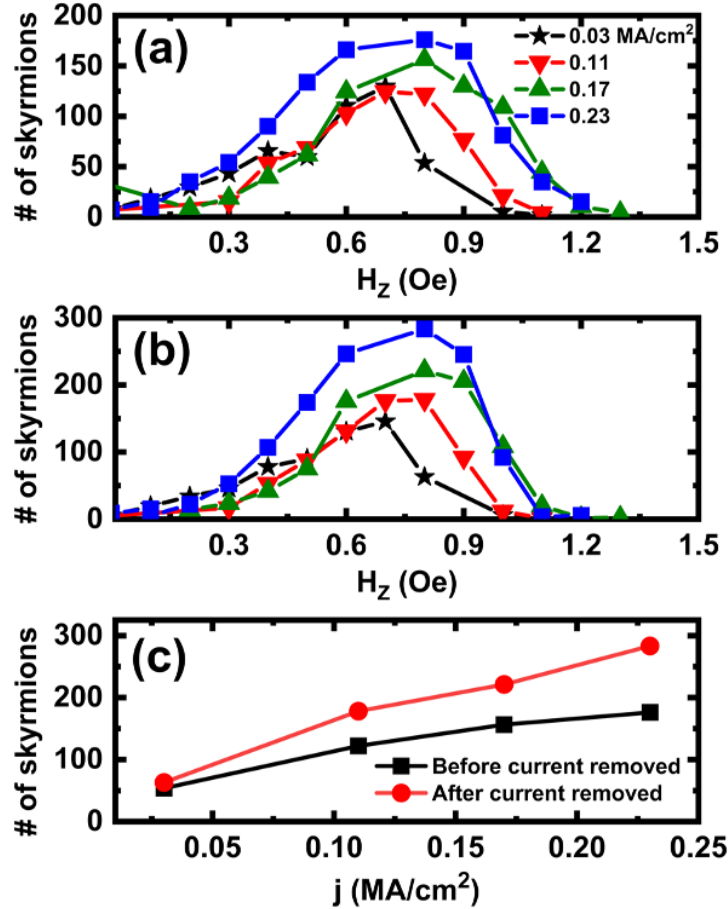


Figure 3.3: (a) Number of skyrmions present in the field of view immediately before the electrical current was removed for several different current densities and applied perpendicular magnetic fields. (b) Number of skyrmions present in the field of view 10 seconds after the electrical current was removed for a variety of current densities and magnetic fields. (c) for an applied field of $H_z = +0.7$ Oe, a comparison of the findings of (a) and (b) for several current densities j .

Using COMSOL Multiphysics, we have estimated the Joule heating and associated temperature increase corresponding to the lowest and highest current densities employed in this study (0.03 MA/cm² and 0.23 MA/cm²). Over the course of 1 minute of current application, the 0.03 MA/cm² was estimated to increase the sample temperature by a maximum of 0.2 K. Over the same period of time, the 0.23 MA/cm² current was estimated to increase the temperature by ~ 3 K; given that it is known that the Pt/Co/Os/Pt sample acquires in-plane anisotropy or a fluctuating domain state if the film is heated by this amount above room temperature,²⁰ the temperature

increase due to the applied current that occurs experimentally must be less, given the continued presence of perpendicular magnetic textures. Nonetheless, these small increases in temperature may be sufficient to lower the energy barrier for skyrmion formation in a sample that experiences a SRT close to room temperature. Additionally, the larger-magnitude spin torques brought about by larger current densities may also assist in the nucleation of skyrmions at defect sites, where the local anisotropy can be lower than in the rest of the film.^{10,28}

While these two effects may help explain the increase in skyrmion population that occurs when the electrical current is being applied, they cannot explain the skyrmion population increase at times after the current is removed, demonstrated in Figure 3.3(b). Interestingly, the increase in the skyrmion population relative to Figure 3.3(a) is proportional to the current density that was previously applied. This proportionality is more apparent in Figure 3.3(c), where the results of Figures 3.3(a) and 3.3(b) are shown for a single H_z of +0.7 Oe and several J values. We have chosen to use data collected when $H_z = +0.7$ Oe since the largest skyrmion populations are observed near this field, both while and after electrical currents were applied (as demonstrated in Figures 3.3(a) and 3.3(b)). It is possible that removing the electrical current may lead to an increase in skyrmion size, making feature previously below our detection size threshold identifiable. However, as discussed in the subsequent section, we do not observe a dramatic change in the width of pre-existing stripe domains and skyrmions once the electrical current is removed. As spin torques cannot be responsible for nucleation after the current has been removed and thermal nucleation of skyrmions is a relatively inefficient mechanism,²⁹ other processes must be responsible for this increase in the skyrmion population. As discussed later, this jump in the skyrmion population can be attributed to the collapse of stripe domains into skyrmions once the current is removed.

3.4 Imaging of Skyrmion Formation Processes

Given that the nucleation and dynamics of skyrmions can be observed optically in real-time in the Pt/Co/Os/Pt system, it is possible to image the various processes by which skyrmions are formed and elucidate the aforementioned trends in skyrmion population. Above, it was shown that electrical current impact the nucleation rate of skyrmions, both while and after the electrical current is applied. In the Pt/Co/Os/Pt system, it was found that when a magnetic field is reduced in strength from the saturation field, skyrmions are repeatedly formed at specific nucleation sites, some of which are indicated in Figure 3.4(k). At low current densities, these sites retain field-nucleated skyrmions as unpinned skyrmions experience slow, sporadic motion biased in the current flow direction (Supplemental Video 2 of Ref. 26). However, when using low currents, the defect sites do not contribute to the creation of new skyrmions. For higher currents, these sites facilitate the nucleation of additional skyrmions through distinct processes. In the simplest case, the stripe or skyrmion pinned at the site depins under the influence of spin torques, forming a moving skyrmion while a new skyrmion forms at the same site.

It is further found that these defect sites play an additional role in the nucleation of skyrmions. Under the effects of spin-orbit torque, a pinned skyrmion can stretch into a stripe

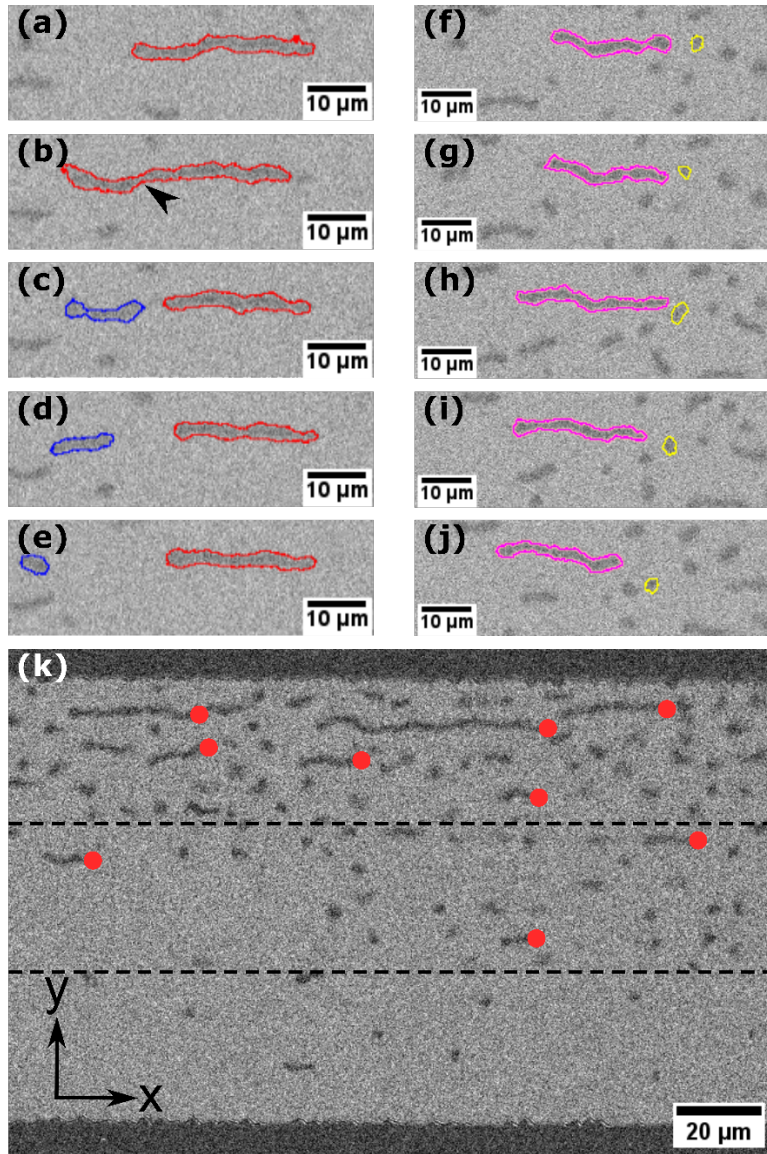


Figure 3.4: (a)-(e) Time-lapse MOKE images of the process by which a stripe domain (red outline) elongates, kinks, and generates a skyrmion (blue outline) over the course of 3 seconds, in time intervals of 0.6 seconds. The arrow in (b) indicates the location at which stripe rupture occurs to form the skyrmion. (f)-(j) Sequential MOKE images of the depinning of a stripe domain (pink outline), mediated by a passing skyrmion (yellow outline) over the course of 2.7 seconds, in time intervals of 0.54 seconds. For (a)-(j), H_z was +1 Oe and a conventional current density $j = 0.11$ MA/cm² was applied from right to left. (k) MOKE image collected in an applied field of +1 Oe, while an electrical current of 0.17 MA/cm² was applied. The image was collected 3 seconds after the current was first applied.

domain with one end pinned at the defect site. As shown in Figure 3.4(c), the pinned stripe domain breaks and skyrmions form from the broken section of the stripe domain. Recent theoretical work has made several predictions as to the various processes and underlying physics that can give rise to the creation of skyrmions from stripe domains. In the most intuitive cases, the use of a geometrically constricted architecture to generate an inhomogeneous spin-orbit torque perpendicular to the long axis of the domain can effectively “chop” skyrmions off of the stripe.^{18,30} In the case of an unconstructed geometry (most analogous to the 100 μm -wide wires discussed in this work), there are several predicted pathways by which skyrmions can be generated from stripe domains. Building off the idea of inhomogeneous spin-orbit torques discussed above, it was argued that the half-skyrmion nature of the tip of a chiral stripe domain can give rise to a transverse torque at the ends of a stripe domain, capable of inducing the separation of a skyrmion.³⁰ In another treatment, the impact of spin-transfer torque on a moving stripe domain subject to a random pinning potential was considered.³¹ As the stripe domain shape deforms under the influence of pinning, it was modeled that for specific applied perpendicular fields and current densities, the breathing-mode dynamics of the stripe domain can lead to the formation of a skyrmion from part of the stripe domain, accompanied by the emission of a spin wave.

In the scenarios discussed above, a strong pinning potential (strong enough to halt the motion of one end of the stripe domain) is not a precondition that must be met to allow for skyrmions to be formed from stripe domains. However, in our experiments, pinning at one end of the stripe is the predominant mechanism by which skyrmions are generated from a stripe domain. This is demonstrated in Figures 3.4(a)-(e) and Supplemental Video 3 of Ref. 26. In line with the previous discussion, the stripe ruptures within a segment of the domain wall that is somewhat transverse to the current flow at a distance removed from the pinning site (denoted by the arrow in

Figure 3.4(b)), leading to the creation of a new skyrmion while leaving the rest of the stripe intact and pinned. While it is not possible to discern the precise mechanism that causes skyrmions to rupture from stripe domains from our MOKE images, commonalities with the theoretical predictions are observed; namely. That domain walls oriented partially transverse to the current flow are prone to rupture and skyrmion formation. These stripe ruptures may explain why applied currents cause the film to become populated with skyrmions more rapidly than from thermal or magnetic field-induced nucleation alone. Another stripe-to-skyrmion transition process is demonstrated in Figures 3.4(f)-(j) and Supplemental Video 4 of Ref. 26, in which a stripe domain detaches from a pinning site and collapses into a skyrmion. In this case, depinning of the stripe appears to be aided by interaction with passing skyrmions, as depicted in Figures 3.4(f)-(j). Repulsive interactions between chiral magnetic textures have been previously predicted and experimentally observed,^{31,32} and it possible that after depinning, a stripe domain may assume the skyrmion state in order to minimize energy.

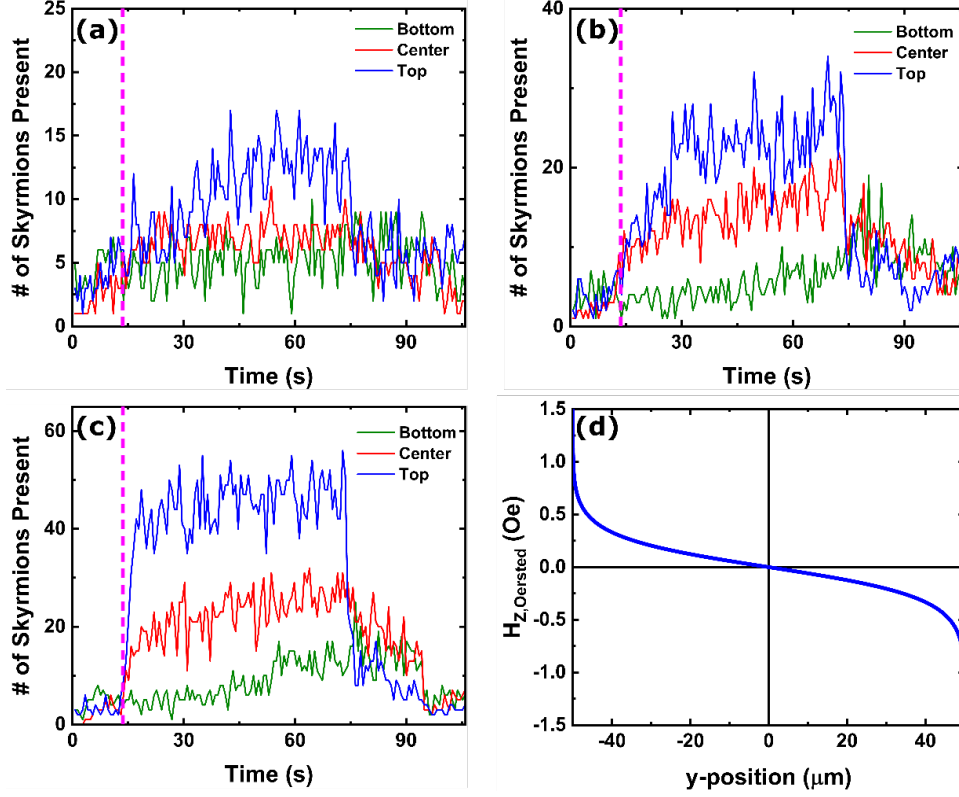


Figure 3.5: (a)-(c) The number of skyrmions present within a $180 \mu\text{m} \times 33 \mu\text{m}$ field of view as a function of time for a variety of regions along the y axis of the wire (indicated in Figure 3.4(k)) in an applied magnetic field $H_z = +1$ Oe when applied current densities of (a) 0.11 MA/cm^2 , (b) 0.17 MA/cm^2 , and (c) 0.23 MA/cm^2 were used. The dashed pink lines indicate the time at which the respective current was first passed through the sample. Data are shown for every five frames of video collected, corresponding to a time increment of ~ 0.3 seconds. (d) the z component of the Oersted field generated by a 0.23 MA/cm^2 electrical current passing through our sample, calculated along the electrical current passing through our sample, calculated along the y -axis of the wire indicated in Figure 3.4(k).

To determine the mechanism responsible for the saturation in the skyrmion population previously noted in Figure 3.2(b), we have tracked the position of individual skyrmions as a function of time. Excluding those skyrmions that travel outside the field of view, it is possible to comment on how skyrmions annihilate and self-limit the total skyrmion population in the wire. It is found that if a skyrmion reaches an edge of the wire, it can lose its energetic stability and consequentially annihilate.¹⁹ As the entire wire becomes more populated with skyrmions and these

skyrmions slightly repel each other and exhibit a deflection transverse to the current flow axis as a result of the skyrmion Hall effect^{18,33,34} known to be present in these samples,²⁰ a fraction of the skyrmions can displace to the edge of the wire and cease to exist, as shown in Supplemental Video 5 of Ref. 26. These effects, coupled with the metastability of the skyrmions formed in this material system, may explain how the annihilation rate can become equal to the nucleation rate over a period of time, leading to a stabilization in the skyrmion population.

It was also possible to image the processes responsible for the increase in skyrmion population after the current has been removed, previously demonstrated in Figure 3.2(b). As seen in Supplemental Video 6 of Ref. 26, pinned stripe domains elongate collinear to the applied electrical current. Absent a current and magnetic field, the stripes would be expected to form a labyrinthine pattern to minimize the sample's dipolar energy. Thus, when the electrical current is removed while the applied field is maintained, there may be two avenues by which elongated stripes can minimize their energy: Collapsing into skyrmions (as shown at the end of Supplemental Video 6 of Ref. 26), or remaining in the stripe domain morphology but losing their pronounced elongation along the applied current direction (apparent in the Figure 3.1 post-current images). In Supplemental Video 6 of Ref. 26, the stripe-to-skyrmion transition is relatively smooth, implying a small energy barrier between the two morphological states. Furthermore, we observe that the width of the magnetic features does not noticeably change as the current is removed. Considering this behavior, the increase and saturation in the skyrmion population several seconds after the current has been removed ($t \approx 90$ seconds) in Figure 3.2(b) would be expected, given that enough time has passed, such that all stripes capable of collapsing into skyrmions have a chance to do so.

Finally, it was found that there is a disparity in the skyrmion population and nucleation efficiency across the width of the wire, as exemplified in Figure 3.4(k). If the 100 μm width of the

wire is subdivided into thirds (dashed lines in Figure 3.4(k)) and the number of skyrmions in each region is tracked as a function of time, differences are observed once the electrical current is applied. For a given time, the skyrmion population markedly decreases when moving from the top of the wire to the bottom, and this effect is enhanced at higher current densities (Figures 3.5(a)-(c)). When the magnetic field orientation is changed while keeping the electrical current flow direction the same, the bottom portion of the wire becomes the more populous side of the wire. While the skyrmion Hall effect in this sample has been shown to give rise to an asymmetric population density over many seconds of dynamics, the fact that the population asymmetry we observe occurs immediately after the current is applied suggests a different origin to the behavior. Furthermore, we observe that the efficiency of specific defect sites to generate skyrmions depends on their positions relative to the field or current direction. This behavior cannot be attributed to the skyrmion Hall effect.

To understand the source of this asymmetry, we have modeled the Oersted field generated when a 0.23 MA/cm^2 current density passed through the wire, using COMSOL Multiphysics. In this model, we account for the current shunting between the various layers of the sample, and solve for the out-of-plane magnetic field $H_{z,\text{Oersted}}$ generated within the Co layer along its $100 \text{ }\mu\text{m}$ width (Figure 3.5(d)). It was found that a gradient in the perpendicular field exists across the width of the wire, and while the fields generated are quite small, they are large enough to have an effect on these low-coercivity, low-anisotropy samples.²⁰ Based on the modeling and experimental data, the more populous portions of the wire correspond to regions where H_z and $H_{z,\text{Oersted}}$ are antiparallel. In the less-populated regions, where H_z and $H_{z,\text{Oersted}}$ are parallel, the net perpendicular field is likely high enough in the positive direction that a domain state is less energetically favorable (as seen in previous studies of this sample's domain morphology as a function of H_z), and the

nucleation sites experience less of an impetus to reverse. Besides limiting the activity of nucleation sites across the width of the sample, this gradient in the field may also lead to a migration of skyrmions from one edge of the wire to the edge where the net perpendicular field is more amenable to their stabilization³⁵ - a process analogous in action to the skyrmion Hall effect, but of a different origin. A similar disparity in the skyrmion population between adjacent wires on account of Oersted fields has been reported recently.³⁶ We note that the asymmetry just described is not present in Figure 3.1, as these images were collected sometime after the electrical current was removed, giving the skyrmions a chance to distribute more evenly across the sample.

3.5 Conclusion

We have performed an experimental study of the electrical current and magnetic field dependence of skyrmion generation in a Pt/Co/Os/Pt thin film using real-time MOKE microscopy. The large size of the skyrmions formed in this system allowed for detailed quantitative assessments of skyrmion motion and population dynamics over a range of applied magnetic fields and electrical current densities. The ability to image in real-time enabled the observation of two specific processes by which skyrmions are formed from pre-existing magnetic defects: (i) stripe domains depinning from defect sites and collapsing into skyrmions, or (ii) skyrmions breaking off from pinned stripes. We further observed an asymmetry in the skyrmion creation across the wire width, which we attributed to the small Oersted field created by passing an electrical current through the sample. Finally, we observe the collapse of stripe domains into skyrmions when the current is removed.

Chapter 3, in part, is a reprint of research published as “Current-induced generation of skyrmions in Pt/Co/Os/Pt thin films” by J.A. Brock, P. Vallobra, R.D. Tolley, S.A. Montoya, S.

Mangin, and E.E. Fullerton in *Physical Review B* 102, 024443 (2020). The dissertation author was the primary investigator and author of the manuscript. This work was supported by the University of California through the Multicampus Research Project Initiative on Electrical Control of Topological Magnetic Order.

3.6 References

- ¹ K. Huang and R. Zhao, *IEEE Trans. VLSI* **24**, 2861 (2016).
- ² X. Zhang, M. Ezawa, and Y. Zhou, *Sci. Rep.* **5**, 9400 (2015).
- ³ A. Fert, V. Cros, and J. Sampaio, *Nat. Nanotechnol.* **8**, 152 (2013).
- ⁴ A. Fert, N. Reyren, and V. Cros, *Nat. Rev. Mater.* **2**, 17031 (2017).
- ⁵ J. Grollier, D. Querlioz, K.Y. Camsari, K. Everschor-Sitte, S. Fukami, and M. D. Stiles, *Nat. Electron.* **3**, 360 (2020).
- ⁶ I.M. Miron, G. Gaudin, S. Auffret, B. Rodmacq, A. Schuhl, S. Pizzini, J. Vogel, and P. Gambardella, *Nat. Mater.* **9**, 230 (2010).
- ⁷ F. Jonietz, S. Muhlbauer, C. Pfleiderer, A. Neubauer, W. Munzer, A. Bauer, T. Adams, R. Georgii, P. Boni, R. A. Duine, K. Everschor, M. Garst, and A. Rosch, *Science* **330**, 1648 (2010).
- ⁸ I. Dzyaloshinskii, *J. Phys. Chem. Solids* **4**, 241 (1958).
- ⁹ T. Moriya, *Phys. Rev.* **120**, 91 (1960).
- ¹⁰ J. Sampaio, V. Cros, S. Rohart, A. Thiaville, and A. Fert, *Nat. Nanotechnol.* **8**, 839 (2013).
- ¹¹ A. Fert, *Mat. Sci. Forum* **59–60**, 439 (1990).
- ¹² M. Bode, M. Heide, K. von Bergmann, P. Ferriani, S. Heinze, G. Bihlmayer, A. Kubetzka, O. Pietzch, S. Blugel, and R. Wisendanger, *Nature* **447**, 190 (2007).
- ¹³ A. Soumyanarayanan, N. Reyren, A. Fert, and C. Panagopoulos, *Nature* **539**, 509 (2016).

-
- ¹⁴ A. Hrabec, N. A. Porter, A. Wells, M. J. Benitez, G. Burnell, S. McVitie, D. McGrouther, T. A. Moore, and C. H. Marrows, *Phys. Rev. B* **90**, 020402(R) (2014).
- ¹⁵ S. Woo, K. Litzius, B. Kruger, M-Y. Im, L. Caretta, K. Richter, M. Mann, A. Krone, R.M. Reeve, M. Weigand, P. Agrawal, I. Lemesh, M.-A. Mawass, P. Fischer, M. Klaui, and G.S.D. Beach, *Nat. Mater.* **15**, 501 (2016).
- ¹⁶ J.-P. Tetienne, T. Hingart, L. J. Martinez, S. Rohart, A. Thiaville, L. Herrera Diez, K. Garcia, J.-P. Adam, J.-V. Kim, J.-F. Roch, I. M. Miron, G. Gaudin, L. Vila, B. Ocker, D. Ravelsona, and V. Jacques, *Nature Comm.* **6**, 6733 (2015).
- ¹⁷ K. Everschor-Sitte, M. Sitte, T. Valet, A. Abanov, and J. Sinova, *New J. Phys* **19**, 092001 (2017).
- ¹⁸ W. Jiang, P. Upadhyaya, W. Zhang, G. Yu, M.B. Jungfleisch, F.Y. Fradin, J.E. Pearson, Y. Tserkovnyak, K.L. Wang, O. Heinonen, S.G.E. te Velthuis, and A. Hoffmann, *Science* **349**, 283 (2015).
- ¹⁹ J. Iwasaki, M. Mochizuki, and N. Nagosa, *Nat. Nanotechnol.* **8**, 742 (2013).
- ²⁰ R. Tolley, S. A. Montoya, and E. E. Fullerton, *Phys. Rev. Mater.* **2**, 044404 (2018).
- ²¹ C. Won, Y.Z. Wu, J. Choi, W. Kim, A. Scholl, A. Doran, T. Owens, J. Wu, X.F. Jin, H.W. Zhao, and Z Q. Qiu, *Phys. Rev. B* **71**, 224429 (2005).
- ²² P. Sharma, H. Kimura, A. Inoue, E. Arenholz, and J.-H. Guo, *Phys. Rev. B* **73**, 052401 (2006).
- ²³ M. Hehn, S. Padovani, K. Ounadjela, and J. P. Bucher, *Phys. Rev. B* **54**, 3428 (1996).
- ²⁴ J. Choi, J. Wu, C. Won, Y.Z. Wu, A. Scholl, A. Doran, T. Owens, and Z.Q. Qiu, *Phys. Rev. Lett.* **98**, 207205 (2007).
- ²⁵ <http://www.aprex-solutions.com/en>
- ²⁶ J.A. Brock, P. Vallobra, R.D. Tolley, S.A. Montoya, S. Mangin, and E.E. Fullerton, *Phys. Rev. B* **102**, 024443 (2020).
- ²⁷ I.-T. Lu and M. Bernardi, *Sci. Rep.* **7**, 3403 (2017).
- ²⁸ F. Buttner, I. Lemesh, M. Schneider, B. Pfau, C. M. Gunther, P. Helsing, J. Geilhufe, L. Caretta, D. Engel, B. Kruger, J. Viehhaus, S. Eisbitt, and G. S. D. Beach, *Nat. Nanotechl.* **12**, 1040 (2017).
- ²⁹ N. Reyren, K. Bouzehouane, J.Y. Chauleau, S. Collin, A.Fert, S. Finizio, K. Garcia, S. Hughes, N. Jaouen, W. Legrand, D. Maccariello, S. McFadzean, S. McVitie, C. Moutafis, H. Popescu, J. Raabe, C.A.F. Vaz, and V. Cros, *Proc. SPIE 10357*, Spintronics X, 1035724 (2017).

-
- ³⁰ S.-Z. Lin, *Phys. Rev. B* **94**, 020402(R) (2016).
- ³¹ W. Koshibae and N. Nagaosa, *Sci. Rep.* **8**, 6328 (2018).
- ³² X. Zhang, G.P. Zhao, H. Fanghor, J. Ping Liu, W.X. Xia, J. Xia, and F.J. Morvan, *Sci. Rep.* **5**, 7643 (2015).
- ³³ C. Reichhardt and C.J.O. Reichhardt, *New J. Phys.* **18**, 095005 (2016).
- ³⁴ K. Litzius, I. Lemesh, B. Krüger, P. Bassirian, L. Caretta, K. Richter, F. Büttner, K. Sato, O. A. Tretiakov, J. Förster, R.M. Reeve, M. Weigand, I. Bykova, H. Stoll, G. Schütz, G.S.D. Beach, and M. Kläui, *Nat. Phys.* **13**, 170 (2017).
- ³⁵ C. Wang, D. Xiao, X. Chen, Y. Zhou, and Y. Liu, *New J. Phys.* **19**, 083008 (2017).
- ³⁶ S. Sugimoto, W. Koshibae, S. Kasai, N. Ogawa, Y. Takahashi, N. Nagaosa, and Y. Tokura, *Sci. Rep.* **10**, 1009 (2020).

Chapter 4: Creating Skyrmion Phases Using Joule Heating

4.1 Introduction

In the previous chapter, we explored the various processes by which skyrmions can be created using spin orbit torque. Lately, however, there has been interest in leveraging the effects of rapid heating to transform magnetic stripe domains into skyrmions.^{1,2,3,4} Micromagnetic and atomistic simulations have shown that a short timescale temperature rise in these systems can transform the sample between a variety of morphological magnetic domain phases, including the skyrmion state.⁵ Crucially, experimental reports have demonstrated that the skyrmions formed via Joule heating exhibit several attractive traits, such as stability against changes in the magnetic field (including at zero field), and even the ability to nucleate skyrmions in zero applied magnetic field in some systems, over certain temperature ranges.¹ However, there are still many open questions as to the physical nature of this thermally driven transformation, including approaches by which the magnetic field and Joule heating necessary to drive the stripe-to-skyrmion transformation can be reduced while still retaining the robust stability of the skyrmion phase.

We have chosen to study a multilayer of the base structure [Co (0.7)/ Ni (0.5)/ Pt (0.7)] (thicknesses in nm). Our choice of materials was motivated by reports suggesting that the Pt/Co and Pt/Ni interfaces can have different strengths of interfacial DMI, such that an additive DMI is obtained when they are incorporated into a structurally asymmetric heterostructure.⁶ Additionally, Co/Ni-based systems have already been the subject of extensive study on account of the inherent

tunability of their basic physical properties, such as the saturation magnetization, spin polarization, strength of perpendicular magnetic anisotropy, and Gilbert damping.^{7,8} Indeed, the ease with which the magnetic properties of Co/Ni-based systems can be adjusted has been capitalized on to experimentally stabilize skyrmions in a variety of structures, including Pt/[Co/Ni]/Ir⁹ and Pt/[Co/Ni/Co]/Au¹⁰, albeit only stabilizing the skyrmion phase in an applied magnetic field.

Using resonant full-field magnetic transmission X-ray microscopy (MTXM) operating at the Co L_3 adsorption edge (778 eV), we imaged the effects of applied magnetic fields and electrical current pulses on the magnetic domain morphology in several 10 μm -wide, 3 mm-long [Co/Ni/Pt]-type patterned devices deposited on SiN membranes. The experimental data, coupled with modeling of the Joule heating effects in our samples, demonstrate that current pulses delivering a Joule heating on the order of ~ 128 K within 50 μs in a 50 mT-strong perpendicular magnetic field are capable of completely transforming all stripes within the field of view of a [Co/Ni/Pt]₂₀ sample into skyrmions, and that these skyrmions remain stable over an extended range of magnetic fields. By reducing the saturation magnetization and effective perpendicular magnetic anisotropy through the insertion of thin rare earth spacer layers within the ferromagnetic layers, the Joule heating needed to accomplish the same transformation was reduced to ~ 15 K while still retaining robust field stability. These results support the idea that Joule heating in a magnetic field allows for the efficient nucleation of skyrmions in a broad class of multilayer systems and identifies pathways toward lowering the Joule heating needed to achieve skyrmions by such means.

4.2 Experimental Methods

Samples of the composition (from the substrate to the top layer) Ta (2 nm)/ Pt (5 nm)/ [Co (0.7 nm)/ Ni (0.5 nm)/ Pt (0.7 nm)]₂₀/ Ta (5 nm) were deposited at ambient temperature by dc

magnetron sputtering. The chamber base pressure was less than 1×10^{-8} Torr, and the argon process gas pressure during deposition was 3 mTorr. For static magnetic characterization and transport measurements, samples were grown on Si substrates with a 300 nm-thick thermal oxide coating. For full-field soft X-ray transmission microscopy experiments, samples were grown on 100 nm-thick Si_3N_4 membrane windows. Samples intended for electrical current studies were patterned into 10 μm -wide, 3 mm-long wires using metal liftoff ultraviolet photolithography. Magnetometry measurements were performed in both the out-of-plane and in-plane geometries using VSM to determine the saturation magnetization (M_s) and effective perpendicular magnetic anisotropy from the saturation field of the hard-axis loop. In calculating volumetric parameters from the VSM data, we considered the nominally deposited thickness of the magnetic layers.

The evolution of the magnetic domain morphology as a function of the out-of-plane field and in response to electrical current pulses was assessed using resonant full-field magnetic transmission X-ray microscopy, available at Beamline 6.1.2 of the Advanced Light Source, Lawrence Berkeley National Laboratory.¹¹ Due to the nonuniformity of the illumination spot projected onto the sample, only representative areas of the entire collected micrographs are shown. All MTXM data was collected using circularly polarized X-rays, resonant to the Co L_3 adsorption edge (778 eV).

During MTXM imaging, electrical current pulses were supplied to the samples using an Agilent Technologies 81150A Arbitrary Pulse Function Generator. For all current densities and pulse durations discussed in this study, the leading/trailing edges of the pulses were set to 6 ns. Before each trial, the magnetization of the sample was saturated in a positive field, followed by saturating in a negative field, followed by stabilization at the target positive field. The shape of the applied current pulses was verified using an oscilloscope connected at the ground end of the circuit.

The electrical resistance of the samples was monitored throughout the experiments to ensure that the current pulses did not appreciably alter the material properties. The pulse energy was calculated from the sample resistance, the pulse duration, and the pulse voltage; calculation of the pulse energy density was performed by dividing this energy by the nominal sample volume.

To understand the relationship between the Joule heating and the temperature change of our samples, we have determined the temperature coefficient of resistance α of a [Co/Ni/Pt]₂₀ patterned device deposited onto a Si₃N₄ membrane by measuring the resistance as a function of temperature, employing a low-current ac lock-in technique [as shown in Figure 4.1(a)]. Subsequent measurements of the resistance of the same sample as a function of current density enabled an estimation of the temperature change as a function of current density [Figure 4.1(b)]. To account for the fact that the Joule heating at a particular current density varies with temperature (due to the associated change in the sample resistance), we have calculated the Joule heating energy densities using both the resistance of the sample at room temperature as well as the resistance at the predicted increased temperature (as shown in Figure 4.1(c)); throughout this chapter, we use the temperature values predicted by the former convention. COMSOL Multiphysics simulations of temperature changes due to Joule heating used a simplified model of the multilayer as a Pt film with the same thickness and average resistivity as the actual multilayer; specifics on the geometry employed are stated in the caption of Figure 4.2.

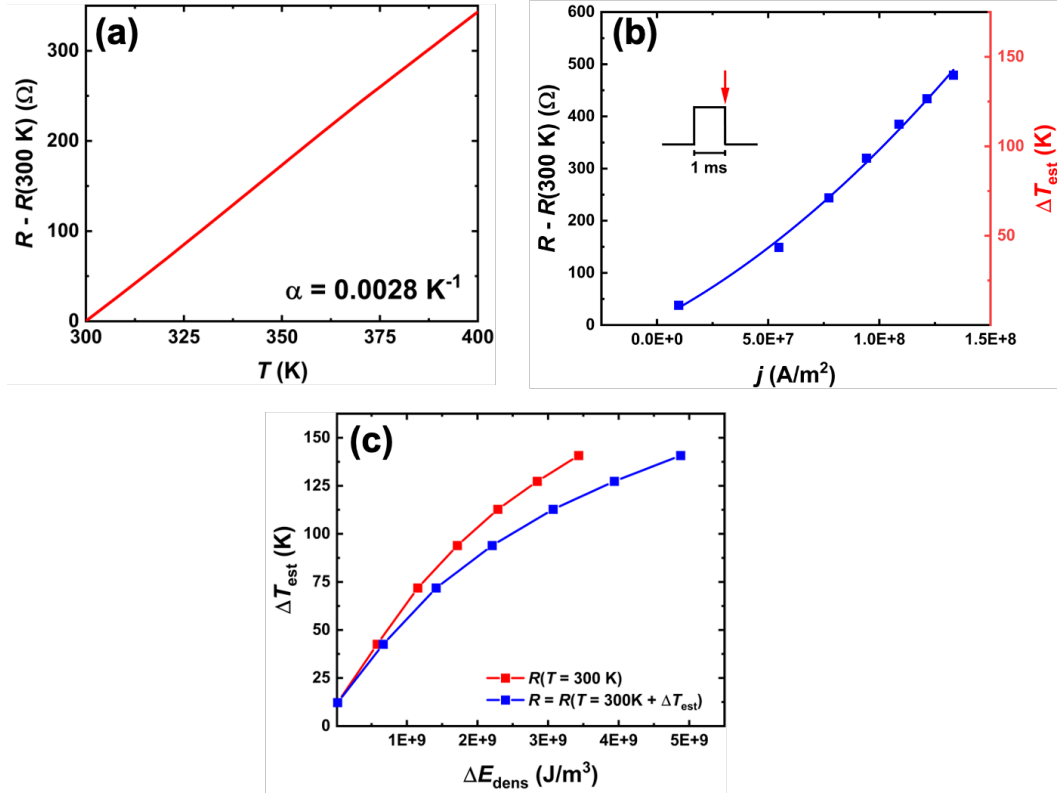


Figure 4.1: (a) Change in resistance (relative to the resistance at 300 K) as a function of temperature for a Ta (2)/Pt (5)/[Co (0.7)/ Ni (0.5)/Pt (0.7)]₂₀/Ta (5) device patterned in to a 3 mm-long, 10 μm -wide wire on a SiN membrane used to calculate the temperature coefficient of resistance α . The data in (a) was collected using an AC lock-in technique, with an excitation current amplitude of 0.1 mA applied at a frequency of 57.98 Hz. (b) Change in resistance (relative to resistance at 300 K) and estimated increase in temperature ΔT_{est} due to Joule heating for several current densities for the sample as in (a). For each current density in (b), the current was applied for 1 ms before a four-point resistance measurement was made (as indicated by the red arrow in the inset) before the current was turned off. (c) ΔT_{est} as a function of Joule heating energy density ΔE_{dens} for the same sample as (a-b). To place an upper and lower limit on the amount of Joule heating for a particular current density, ΔE_{dens} was calculated assuming both the resistance of the sample at room temperature, as well as the resistance at the elevated temperature estimated from (b).

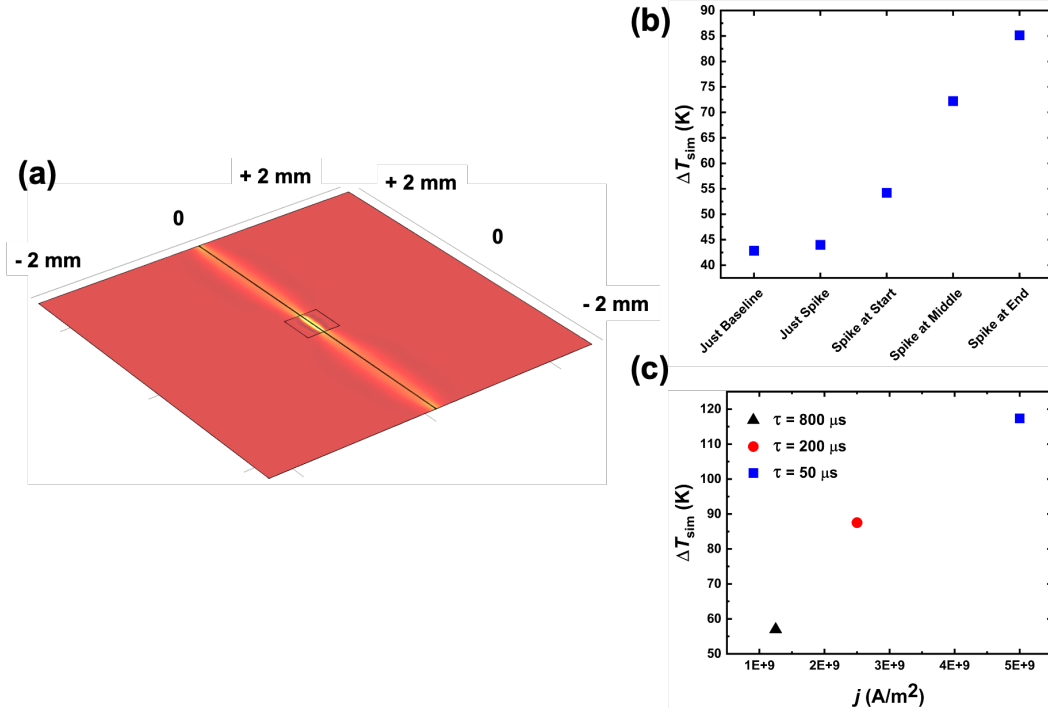


Figure 4.2: (a) Experimental geometry employed in COMSOL Multiphysics simulations of the temperature change due to Joule heating in [Co/Ni/Pt]-based multilayers. The model features a 10 μm x 1 mm x 50 nm Pt wire with a resistivity value that approximates a [Co(0.7 nm)/ Ni (0.5 nm)/ Pt (0.7)]₂₀ multilayer) placed on top of a 0.5 mm x 0.5 mm x 100 nm Si₃N₄ window, surrounded by a 5 mm x 5 mm x 0.5 mm SiO_x frame. Convective cooling to ambient ($K = 5 \text{ Wm}^{-2}\text{K}^{-1}$) was modeled at all structure boundaries. (b) Simulated temperature changes ΔT_{sim} in response to the composite pulse configurations indicated in Fig. 4(a) of the main text, as well as ΔT_{est} from applying only the baseline pulse or spike pulse. (c) ΔT_{sim} in response to the pulses of varying duration τ and current density j but equivalent Joule heating depicted in Figure 4.13(a). The initial temperature of the sample was set to 300 K for all simulations.

4.3 Experimental Results and Discussion

Figures 4.3(a)-(c) show MTXM images of the field-dependent magnetic domain morphology of a [Co (0.7 nm)/ Ni (0.5 nm)/ Pt (0.7 nm)]₂₀ patterned wire (henceforth referred to as the [Pt/Co/Ni]₂₀ sample) as a perpendicular magnetic field $\mu_0 H_z$ was swept from negative saturation to positive saturation at room temperature. The contrast in these images reflects the perpendicular magnetic orientation averaged over the thickness of the film, with opposite

magnetization texture represented as gray ($+M_z$) and black ($-M_z$) contrast. At remanence ($\mu_0 H_z = 0$), the domain morphology consists primarily of disordered stripe domains with a width of $105 \text{ nm} \pm 12 \text{ nm}$ (Figure 4.3(a)). As the perpendicular field strength is increased (to $\mu_0 H_z = +90 \text{ mT}$ and $+250 \text{ mT}$), the disordered stripe domains begin to contract (Figure 4.3(b)) until only a few stripes are observable in the field of view (Figure 4.3(c)). From the detailed field-dependent domain morphology shown in Figure 4.4, however, it can be seen that the $[\text{Co/Ni/Pt}]_{20}$ patterned wire does not exhibit a field-induced skyrmion phase at any point during the field sweep.

Having established that the $[\text{Co/Ni/Pt}]_{20}$ sample does not exhibit a skyrmion phase solely in response to an applied magnetic field at room temperature, we proceeded to investigate the effects of applying electrical current pulses of varying electrical current density j and pulse duration τ on the domain morphology in different applied magnetic fields. At any given field, the domain morphology was recorded before and after injecting a current pulse. After each trial, the domain morphology was reset by cycling the perpendicular field up to positive saturation, then reducing the field to negative saturation, and finally increasing the field to the desired positive value. Figures 4.3(d)-(f) show the domain morphology that was obtained after applying a single $60 \text{ }\mu\text{s}$ -long current pulse of current density $j = 1.7 \times 10^{10} \text{ A/m}^2$ onto the domain states depicted in Figures 4.3(a)-(c). In calculating j , we considered the thickness of the entire sample (including the

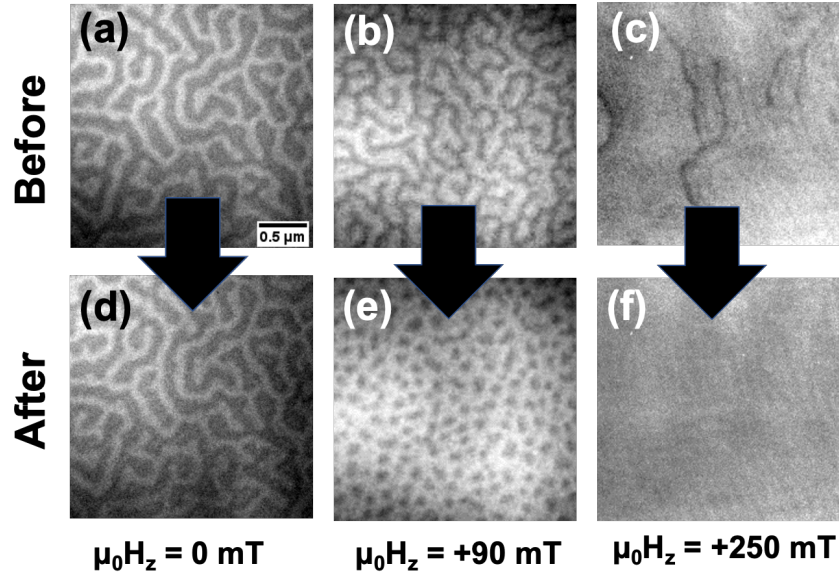


Figure 4.3: MTXM images illustrating the effect of a 60 μs -long current pulse of density 1.7×10^{10} A/m² on the domain morphology of a [Co (0.7 nm)/ Ni (0.5 nm)/ Pt (0.7 nm)]₂₀ wire for $\mu_0 H_z = 0$ (a,d), +50 mT (b,e), and +250 mT (c,f) before and after the current pulse was applied. The indicated perpendicular field $\mu_0 H_z$ was maintained before, during, and after the current pulse was applied. Low-contrast vertical lines observed in the foreground of (c) and (f) are artifacts of the MTXM optics.

seeding and capping layers). At remanence, we find that the electrical current pulse primarily results in the local rearrangement of disordered stripe domains, without the formation of any new types of magnetic features [Figure 4.3(a) versus Figure 4.3(d)]. Under moderate perpendicular magnetic fields ($\mu_0 H_z = +90$ mT), the current excitation transforms a disordered stripe phase into a dense, disordered skyrmion phases [Figure 4.3(b) versus Figure 4.3(e)]; from additional experiments discussed in Section 4.2 and elsewhere in this chapter, we estimate that the temperature increase associated with this current pulse is ~ 128 K. Like most multilayered materials that host field-induced^{12,13} and current-induced¹⁴ skyrmions, we observe that the individual features exhibit a shape that is not perfectly circular, resulting from pinning centers present throughout the film. The skyrmion features exhibit an average diameter of $69 \text{ nm} \pm 11 \text{ nm}$, which

is comparable to the average stripe width of 66 ± 8 nm observed at this magnetic field before the current pulse was applied. Near magnetic saturation ($\mu_0 H_z = +250$ mT), we find that the remaining disordered stripe domains are annihilated after applying the current pulse, with the patterned wire becoming uniformly magnetized in the direction of the applied magnetic field [Figure 4.3(c) versus Figure 4.3(f)].

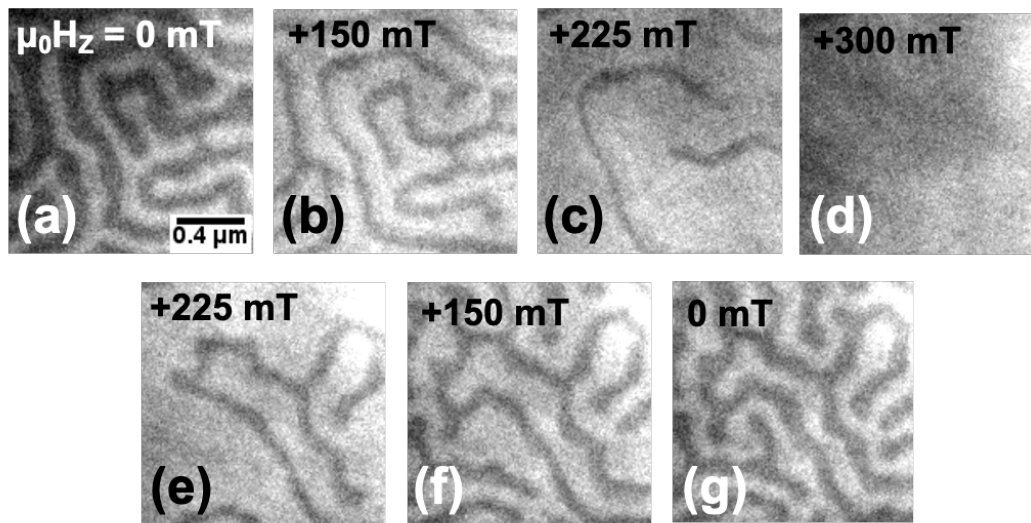


Figure 4.4: MTXM images of the magnetic domain morphology as the out-of-plane magnetic field was swept from zero towards positive saturation then back to zero in a $[\text{Co} (0.7 \text{ nm})/\text{Ni} (0.5 \text{ nm})/\text{Pt} (0.7 \text{ nm})]_{20}$ sample.

Next, the field stability of the skyrmion phase in the $[\text{Co}/\text{Ni}/\text{Pt}]_{20}$ patterned wire was explored as the magnetic field was reduced from the positive field at which the skyrmion phases were nucleated towards negative saturation. Figure 4.5 shows the evolution of the skyrmion phase as the applied magnetic field was varied. As the field was reduced, the individual skyrmion features grew nonuniformly within their local vicinity while retaining their general overall shape. Moreover, the skyrmion features do not elongate or recombine to form a disordered stripe phase,

as is commonly observed in multilayered materials that host field-induced skyrmions. At remanence, the domain morphology consists of a close-packed skyrmion phase [Figure 4.5(b)] that differs from the remanent state obtained using perpendicular fields alone [Figure 4.3(a)]. Reducing the magnetic field further ($\mu_0 H_z = -70$ mT), we observe that the close-packed skyrmion phase continues to persist [Figure 4.5(c)].

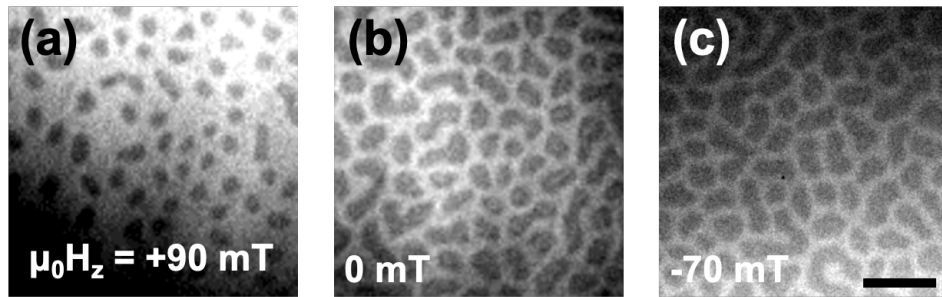


Figure 4.5: MTXM images of the skyrmion phase in the [Co (0.7 nm)/ Ni (0.5 nm)/ Pt (0.7 nm)]₂₀ sample as the out-of-plane field strength was varied. Before imaging, the stripe to skyrmion-transformation was accomplished by applying a 60 μ s current pulse of density 1.7×10^{10} A/m² in a field of $\mu_0 H_z = +190$ mT). The scale bar in (c) indicates 500 nm.

We then explored, in detail, the morphological transformations that occur in the [Co/Ni/Pt]₂₀ patterned wire as a function of perpendicular field strength and current pulse width. Figure 4.6(a) shows the different degrees of stripe-to-skyrmion transformations that can be accessed using different $\tau - \mu_0 H_z$ combinations (including the behaviors noted in Figure 4.3) when applying a single electrical current pulse with fixed density $j = 1.7 \times 10^{10}$ A/m². In Figure 4.6, we also display the estimated temperature increase due to Joule heating ΔT_{est} for each pulse duration, determined experimentally using the techniques described in Section 4.2 of this chapter. The minimum current density necessary to induce the stripe-to-skyrmion transformation was determined as follows: First, the applied field was set to the point at which the hysteretic region of

the magnetization curve for the sample in question first begins to open up when sweeping the field toward positive saturation. Next, the current pulse duration was fixed to 50 μs while applying electrical current pulses of gradually increasing magnitude, until a complete stripe-to-skyrmion transformation was observed. From this point, the pulse duration and applied magnetic fields were systematically varied to explore the morphological response. Like before, the field was cycled after each trial.

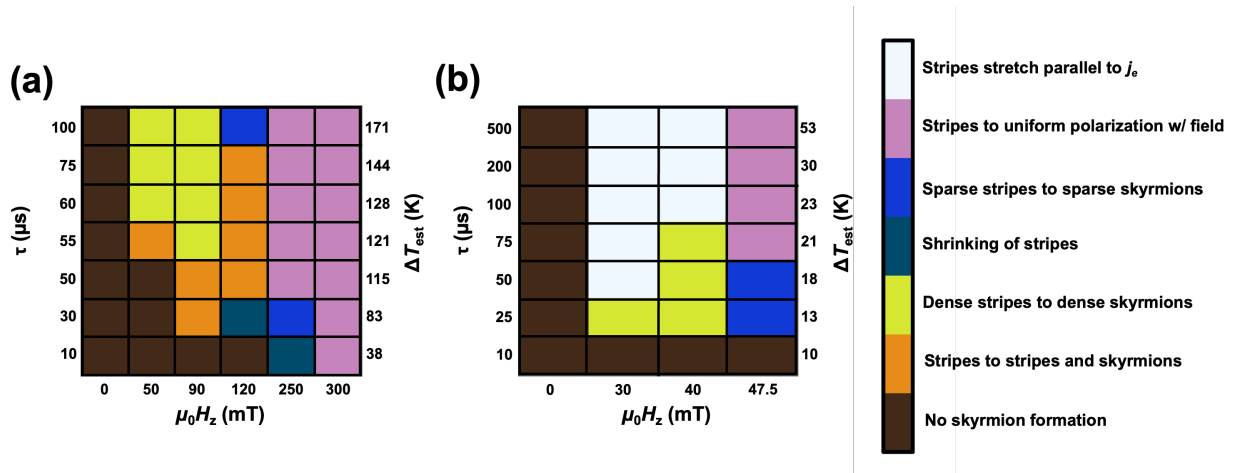


Figure 4.6: $\tau - \mu_0 H_z$ phase maps for the (a) [Co (0.7 nm)/ Ni (0.5 nm)/ Pt (0.7 nm)]₂₀ and (b) [Co (0.7 nm)/ Tb (0.4 nm)/ Ni (0.5 nm)/ Pt (0.7 nm)]₂₀ samples indicating the change in domain morphology observed after pulses of $j = 1.7 \times 10^{10}$ A/m² (a) and 2.4×10^9 A/m² (b) were applied for various durations τ and out of plane magnetic field strengths $\mu_0 H_z$. The experimentally estimated temperature increase ΔT_{est} for each pulse duration is also shown (see Section 4.2 for additional details). Before each measurement, the magnetic field was swept to both positive and negative saturation before setting the target magnetic field strength for the trial. Note that both the τ and $\mu_0 H_z$ axes are not linearly scaled.

At remanence, we find that a single current pulse with durations varying from $\tau = 10 \mu\text{s}$ up to 100 μs is unable to induce a stripe-to-skyrmion transformation within our field of view. A similar observation is noted when applying a $\tau = 10 \mu\text{s}$ current pulse as a function of increasing field ($0 < \mu_0 H_z < +120$ mT). Under moderate fields ($\mu_0 H_z = +50$ mT and +90 mT), we can access

a $\tau - \mu_0 H_z$ phase region where the electrical current pulse first transforms a disorder stripe phase into a coexisting stripe and skyrmion phase; then, as the current pulse width is increased, a high-density skyrmion phase is formed. In general, the density of the skyrmion phase appears to depend on the density of stripe domains present before the current pulse is applied, as shown in Figure 4.6). Under higher applied fields ($\mu_0 H_z = +120$ mT and $+250$ mT), two additional $\tau - \mu_0 H_z$ phase regions can be accessed – the current-induced contraction of stripe domains as well as a sparse stripe-to-sparse skyrmion transformation. Near the saturation field ($\mu_0 H_z = +300$ mT), the application of electrical current pulses annihilates the low-density stripe domains. Overall, the phase diagram illustrates the myriad of morphological phases that can be accessed using electrical current pulses. The physical mechanisms involved in the stripe-to-skyrmion transformations observed will be discussed subsequently.

To explore how material properties can be tuned to facilitate stripe-to-skyrmion transformations using lower current density electrical pulses and perpendicular magnetic fields, we investigated different multilayer structures, all of which possess a moderate degree of interfacial DMI. In general, it has been shown that reducing the saturation magnetization M_s and effective perpendicular magnetic anisotropy K_{eff} can lower the energy barrier that separates the stripe and skyrmion ground states in multilayered materials.^{15,16} One potential pathway towards lowering these two properties is through the incorporation of rare-earth spacer layers between the Co and Ni layers. Rare-earth layers are expected to couple antiferromagnetically with the Co and Ni layers to reduce M_s (through the creation of a net ferrimagnetic structure) while at the same time increasing the thickness of magnetic material in the structure and removing the Co/Ni interfaces, reducing K_{eff} .^{17,18,19,20} Static characterization indicates that the [Co/Ni/Pt]₂₀ sample exhibits M_s and K_{eff} values of 1010 kA/m and 5.1×10^5 J/m³ (respectively), as shown in Figure

4.7. In line with the previous discussion, incorporating a thin spacer layer of rare-earth material in a sample of the structure [Co (0.7 nm)/ Gd (0.4 nm)/ Ni (0.5 nm)/ Pt (0.7 nm)]₂₀ reduces M_s to 488 kA/m, while K_{eff} was roughly halved to $2.5 \times 10^5 \text{ J/m}^3$. The variation was considerably more

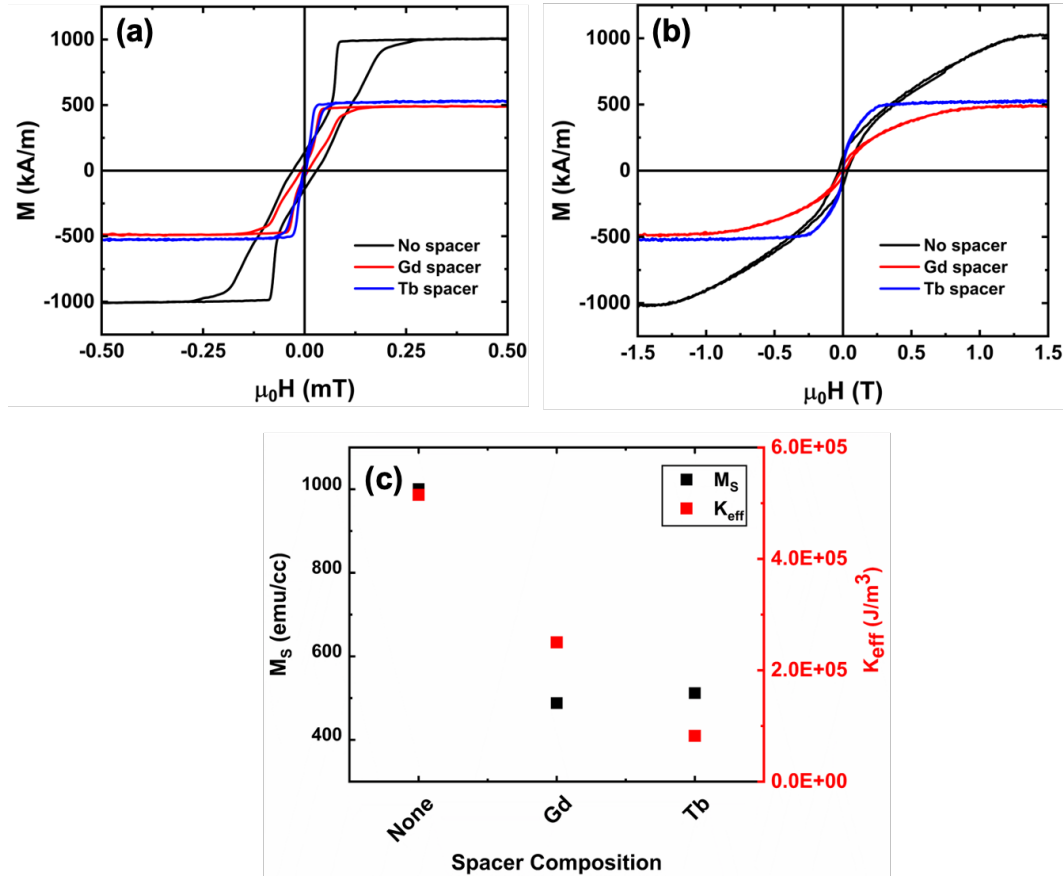


Figure 4.7: (a) Out-of-plane and (b) in-plane vibrating sample magnetometry data for the [Co (0.7)/Spacer (0.4)/Ni (0.5)/Pt (0.7)]₂₀ (thicknesses in nm) samples, collected at room temperature. (c) Saturation magnetization M_s and effective perpendicular anisotropy energy density K_{eff} of the samples determined from (a) and (b).

dramatic when Tb was employed in a structure of the composition [Co (0.7 nm)/ Tb (0.4 nm)/ Ni (0.5 nm)/ Pt (0.7 nm)]₂₀, which exhibited $M_s = 512 \text{ kA/m}$ and $K_{\text{eff}} = 8.2 \times 10^4 \text{ J/m}^3$ – roughly an 80 % reduction in K_{eff} relative to the [Co/Ni/Pt]₂₀ sample. All samples exhibit the “sheared” perpendicular hysteresis loops characteristic of a multidomain state at zero field. Static

characterization of M_s as a function of temperature [Figure 4.8(a)] indicates that the [Co/Tb/Ni/Pt]₂₀ sample does not experience a dramatic change in M_s within the temperature range of 100-400 K, implying that the composition is far from magnetic compensation of the

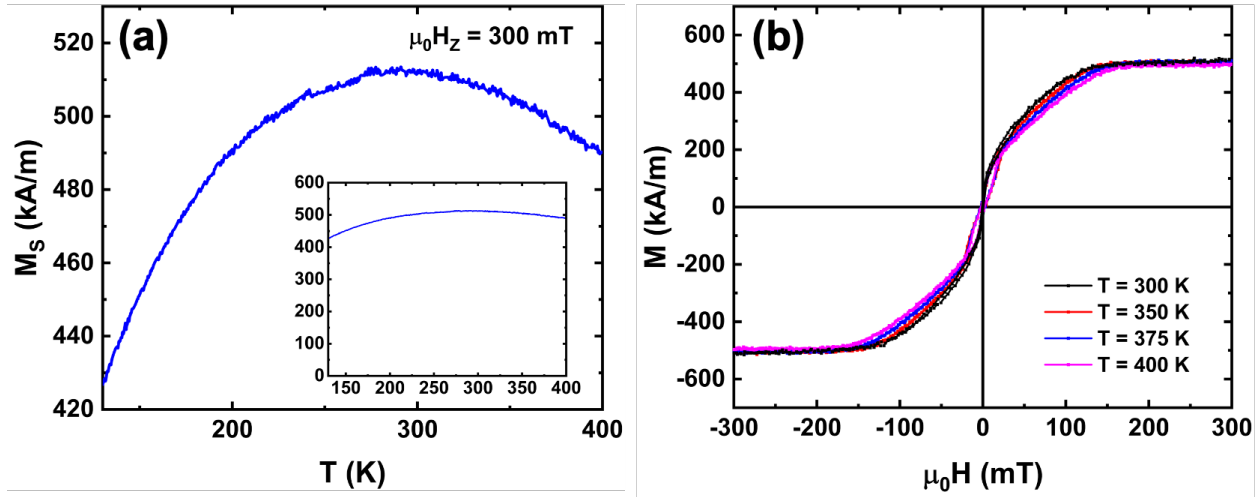


Figure 4.8: (a) the saturation magnetization M_s as a function of temperature and (b) in-plane hysteresis loops at selected temperatures of an unpatterned [Co (0.7)/ Tb (0.4)/ Ni (0.5)/ Pt (0.7)]₂₀ (thicknesses in nm) sample, determined using vibrating sample magnetometry.

ferrimagnetic sublattices. Furthermore, in-plane hysteresis loops of the [Co/Tb/Ni/Pt]₂₀ sample collected at higher temperatures suggest that the anisotropy field does not change remarkably across the relevant temperature scale in the samples with rare-earth spacer layers [Figure 4.8(b)]. The field-dependent domain morphology of the [Co/Tb/Ni/Pt]₂₀ and [Co/Gd/Ni/Pt]₂₀ samples reveals that a purely field-stabilized skyrmion phase is not energetically accessible in these materials, as demonstrated in Figure 4.9. The [Co/Tb/Ni/Pt]₂₀ and [Co/Gd/Ni/Pt]₂₀ samples exhibit disordered stripe domains at remanence, with stripes exhibiting an average width of $142 \text{ nm} \pm 18 \text{ nm}$ and $137 \text{ nm} \pm 13 \text{ nm}$, respectively. Given the reduction in M_s , it might be expected for the stripe domain width to broaden based on magnetostatic considerations.²¹

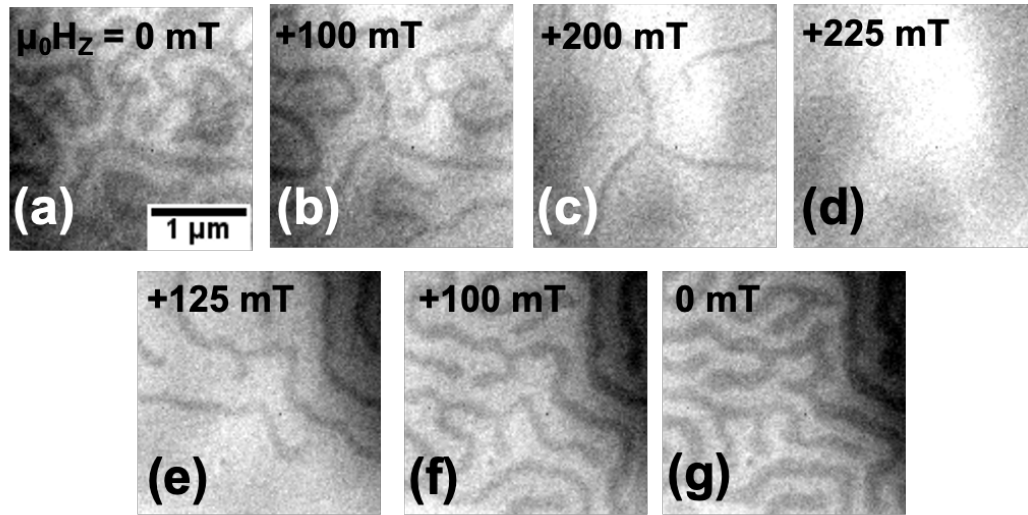


Figure 4.9: MTXM images of the magnetic domain morphology of a $[\text{Co} (0.7)/ \text{Tb} (0.4)/ \text{Ni} (0.5)/ \text{Pt} (0.7)]_{20}$ (thicknesses in nm) sample as an out of plane magnetic field was swept from zero towards positive saturation, then back to zero field.

In Figure 4.6(b), the morphological phases accessible in a $[\text{Co}/\text{Tb}/\text{Ni}/\text{Pt}]_{20}$ patterned wire as a function of perpendicular field and current pulse width are shown. In general, morphological phase transitions comparable to those seen in the $[\text{Co}/\text{Ni}/\text{Pt}]_{20}$ sample are observed, with two main distinctions: The diverse morphological phases can be accessed using a lower-magnitude range of field values and a lower magnitude current density pulse of $2.4 \times 10^9 \text{ A/m}^2$ (*i.e.*, one order of magnitude lower than for the $[\text{Co}/\text{Ni}/\text{Pt}]_{20}$ structure). Furthermore, the $[\text{Co}/\text{Tb}/\text{Ni}/\text{Pt}]_{20}$ sample exhibits a morphological phase that was not seen in $[\text{Co}/\text{Ni}/\text{Pt}]_{20}$ – the elongation of stripe domains collinear to j [Figure 4.10]. Similar behavior has previously been observed in a $[\text{Pt}/\text{CoFeB}/\text{MgO}]_{20}$ sample and was micromagnetically attributed to a balance of ferromagnetic exchange, perpendicular anisotropy, and DMI energy in the high aspect ratio geometry of a narrow wire.¹

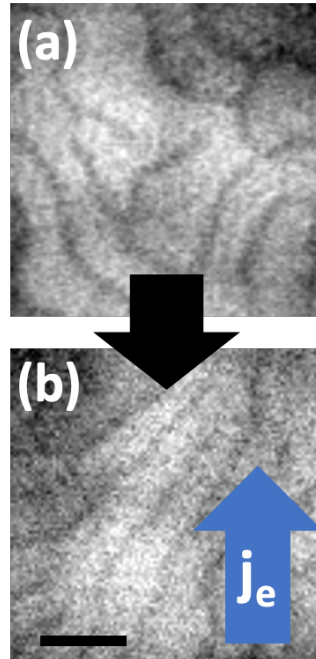


Figure 4.10: MTXM images depicting the domain morphology (a) before and (b) after a 200 μs -long pulse of current density $2.4 \times 10^9 \text{ A/m}^2$ was applied in a perpendicular magnetic field of +40 mT. The blue arrow indicates the electron flow direction j_e , and the scale bar represents 500 nm.

While the phase diagrams shown in Figure 4.6 demonstrate that a diversity of morphological phases can be accessed in [Co/Ni/Pt]-based multilayers, it says nothing as to the physical mechanism responsible for the transformation. Because our multilayer samples are seeded on and capped with materials that are known to exhibit opposite signs of spin-Hall angle,^{22,23} a net spin-orbit torque (SOT) may be acting on the system. Given the relative thickness of the seed and capping layers, we argue that these layers carry more current than any of the individual layers within the interior of the multilayer structure; thus, the capping and seed layers would be the most likely source of SOT. Furthermore, any SOT generated from the interior Pt spacer layers would be mostly negated, in that these layers would generate opposing signs of SOT at the top and bottom interfaces of the ferromagnetic layers. To investigate the possible effects of SOT, we varied the capping layer composition of the [Co/Ni/Pt]₂₀ sample from Ta to Pt to change the sign of the spin-

Hall angle of the capping layer. It is expected that the use of a Pt capping layer should reduce the net SOT acting on the Pt-seeded magnetic layers if a uniform Néel chirality is maintained through the thickness of the film. Alternatively, if the dipolar energy is strong enough to promote the formation of Néel caps,^{24,25} the use of a Pt capping layer would enhance the SOT. In Figure 4.11, we demonstrate that the morphological response to an applied current pulse is equivalent between samples with Ta and Pt capping layers – implying that SOT strength is not central to driving the stripe-to-skyrmion transformation in the [Co/Ni/Pt]-type samples.

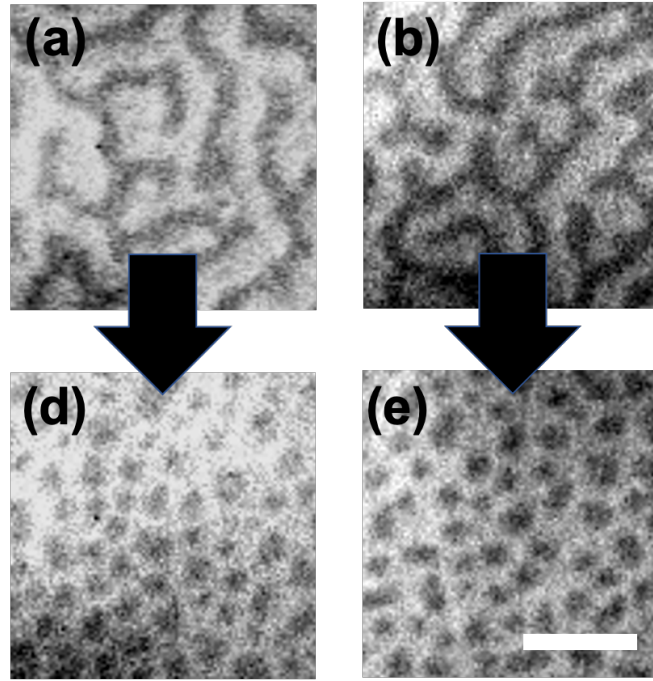


Figure 4.11: MTXM images collected before and after a 50 μs -long current pulse with current density $1.7 \times 10^{10} \text{ A/m}^2$ was applied to a [Co/Ni/Pt]₂₀-type sample capped with Pt (a,c) or Ta (b,d) in an applied magnetic field of +50 mT. The scale bar indicates 400 nm.

We have performed additional experiments to discern the effects of Joule heating on the skyrmion nucleation observed in the [Co/Ni/Pt]-type samples, as originally proposed in Ref. 1. In the first set of tests, a composite pulse (consisting of a baseline and a spike component) was utilized

to deliver the same net electron flow/SOT and Joule heating, while varying the maximum temperature attained by the sample; this was accomplished by modifying the relative delay of the spike pulse to the beginning, middle, and end of the baseline pulse [Figure 4.12(a)]. The baseline pulse, of pulse duration and current density $72 \mu\text{s}$ and $2.5 \times 10^9 \text{ A/m}^2$, did not result in a

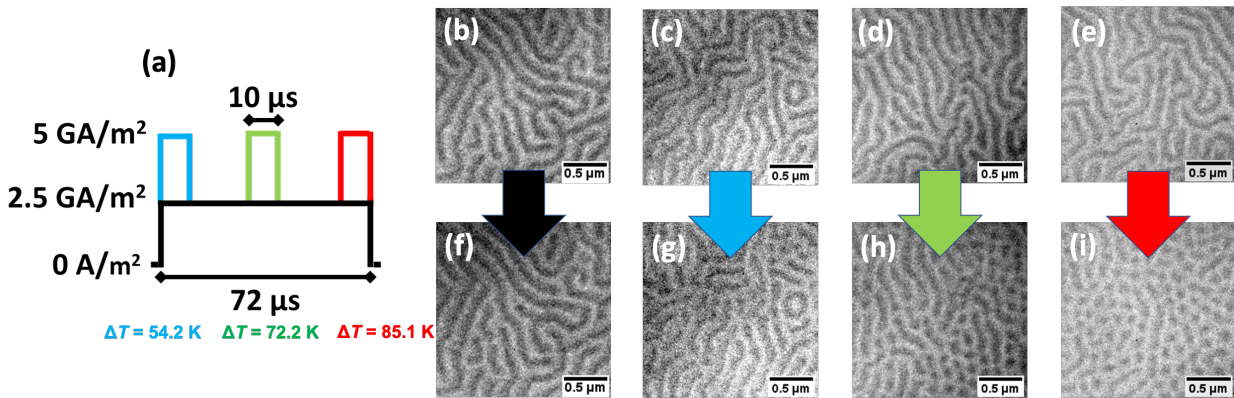


Figure 4.12: (a) depiction of the composite pulse employed to delineate between Joule heating and spin-orbit torques. (b-i) MTXM images of a $[\text{Co} (0.4)/ \text{Tb} (0.4)/ \text{Co} (0.4)/ \text{Ni} (0.5)/ \text{Pt} (0.7)]_{20}$ sample (thicknesses in nm) illustrating the effects of delivering the same Joule heating and net electron flow by changing the relative delay of the spike pulse to the beginning (c,g), middle(d,h), and end (e,i) of the baseline pulse in a perpendicular magnetic field of $+173 \text{ mT}$. (b,f) demonstrate the effect of only applying the baseline pulse.

morphological transformation when applied on its own to a $[\text{Co} (0.4 \text{ nm})/ \text{Tb} (0.4 \text{ nm})/ \text{Co} (0.4 \text{ nm})/ \text{Ni} (0.5 \text{ nm})/ \text{Pt} (0.7 \text{ nm})]_{20}$ patterned wire in an applied field of $+173 \text{ mT}$ [Figures 4.12(b,f)].

Like the other samples discussed thus far, this sample does not exhibit a purely field-stabilized skyrmion phase; the skyrmion phase is accessed by applying electrical current pulses within a $\tau - \mu_0 H_z$ window unique to the sample. The spike pulse had a duration of $10 \mu\text{s}$ and was of current density $5 \times 10^9 \text{ A/m}^2$ [Figure 4.12(a)]. For a spike pulse applied at the beginning of the baseline pulse [blue pulse, Figure 4.12(a)], the field-stabilized stripe phase rearranged slightly, as shown in

Figures 4.12(c,g). As the relative delay of the spike pulse was increased to the middle and end of the baseline pulse [green and red pulses, Figure 4.12(a)], the number of skyrmions present after the pulse increases [Figures 5.12(d,h) and 5.12(e,i), respectively]. These tests suggest that the time-dependent thermal profile from Joule heating plays an important role in the stripe-to-skyrmion transition observed in our [Co/Ni/Pt]-type samples. Specifically, as the delay of the spike pulse

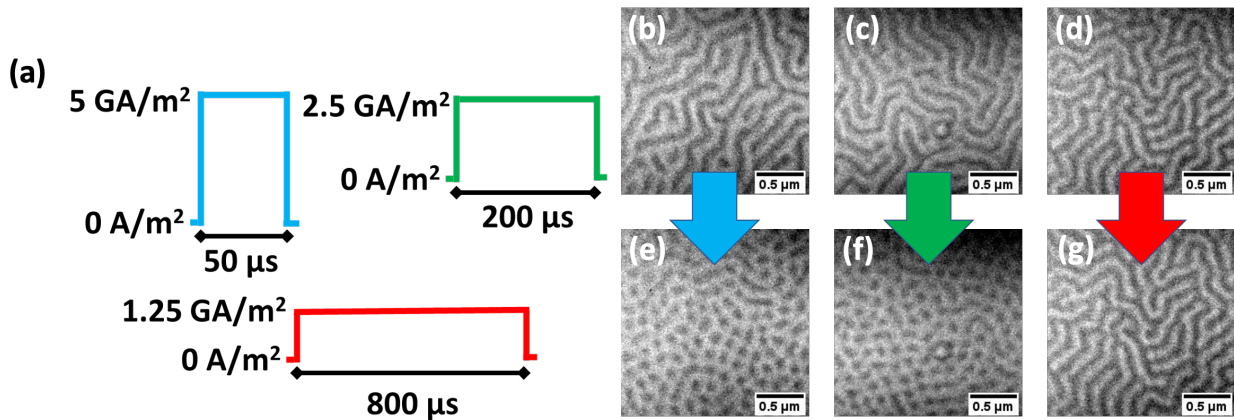


Figure 4.13: (a) Schematic depictions of the variation in pulse duration and current density used to examine the impact of supplying an equivalent amount of Joule heating using 50 μs (blue), 200 μs (green), and 800 μs-long (red) pulses. (b-g) MTXM images of a [Co (0.4)/ Tb (0.4)/ Co (0.4)/ Ni (0.5)/ Pt (0.7)]₂₀ sample (thicknesses in nm) illustrating the effect of delivering the 50 μs (b,e), 200 μs (c,f), and 800 μs (d,g) pulses illustrated in (a) in a perpendicular field of +173 mT.

increases, the maximum temperature change attained by the sample should increase as well – suggesting that temperature plays a strong role in promoting the observed morphological transformations. Using COMSOL Multiphysics, we have simulated the sample temperature change that occurs in response to the three composite pulse configurations discussed above, finding that applying the spike pulse at the end of the baseline leads to a final temperature ~30 K higher than when the spike is applied at the beginning of the baseline (see Section 4.2). However,

since it is known that Joule heating can enhance the effect of SOT acting on a ferromagnetic sample,²⁶ this test does not allow for a complete disentanglement of the effects of Joule heating versus SOT.

In the second set of tests, the current density j and pulse width τ were varied in such a way that the Joule heating previously identified as necessary for a complete stripe-to-skyrmion transformation was supplied at differing timescales. Once again, we have employed COMSOL Multiphysics to simulate the temperature changes resulting from these pulses (see Section 4.2). In Figure 4.13, we schematically demonstrate the different pulses that were injected into the [Co/Tb/Co/Ni/Pt]₂₀ patterned wire in an applied perpendicular field of +173 mT. A complete stripe-to-skyrmion transformation is observed using a 50 μ s-long pulse with current density $j = 5 \times 10^9$ A/m² [Figures 4.13(b,e)], which is estimated to increase the sample temperature by ~ 115 K. As these pulse characteristics correspond to the most rapid heating of the sample, this pulse should lead to the largest increase in sample temperature before the heat dissipates. A similarly complete stripe-to-skyrmion transformation occurs in response to a 200 μ s-long pulse with current density 2.5×10^9 A/m² [Figures 4.13(c,f)], implying that the temperature increase attained under these conditions (~ 85 K) is still enough to promote a complete morphological transformation. However, when the Joule heating is supplied using an 800 μ s-long pulse of current density 1.25×10^9 A/m² [Figures 4.13(d,g)], significant dissipation is expected to occur during the heating process. Consequentially, the temperature change (~ 55 K) is not high enough to promote the nucleation of skyrmions in this sample.

To better understand the impacts of Joule heating on the stability of morphological phases in the [Co/Ni/Pt]₂₀ samples, we have applied the model of Ref. 16 to explore the size and stability

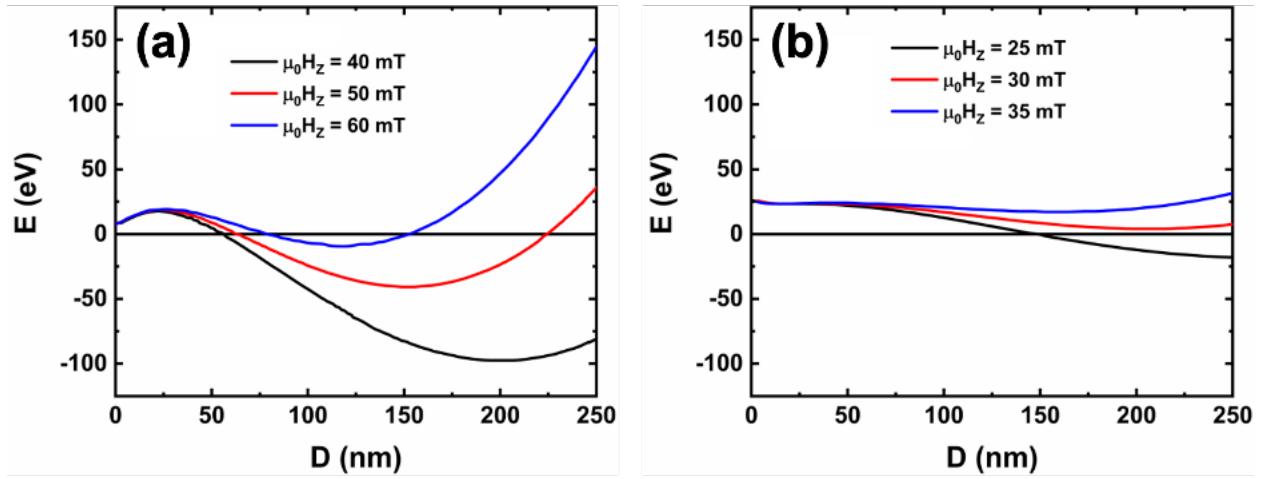


Figure 4.14: The energy profile of isolated bubble domains at several perpendicular field strengths in proximity to the lowest $\mu_0 H_z$ necessary for skyrmion nucleation in the (a) [Co/Ni/Pt]₂₀ and (b) [Co/Tb/Ni/Pt]₂₀ samples. The energy profile was calculated using the analytical treatment proposed in Ref. 16. In calculating (a), we used a M_s value of 1000 kA/m, uniaxial anisotropy constant of 1.1×10^6 J/m³, DMI energy density of 0.6 mJ/m², and an exchange stiffness of 10 pJ/m. In calculating (b), a M_s of 500 kA/m, uniaxial anisotropy of 2.2×10^5 J/m³, DMI energy density of 0.6 mJ/m², and exchange stiffness of 10 pJ/m were used.

of the isolated skyrmion bubble state formed in our samples. These calculations were performed using parameters extracted from the static characterization parameters stated in this section, save for the DMI energy density of $D = 0.622$ mJ/m², which was determined by measuring the in-plane field-induced domain expansion asymmetry²⁷ in thinner samples that reverse via large bubble domains. In Figure 4.14(a), the energy as a function of skyrmion bubble diameter is shown for several $\mu_0 H_z$ values proximal to the minimum $\mu_0 H_z$ needed to elicit the skyrmion phase in the [Co/Ni/Pt]₂₀ sample. In addition to predicting skyrmion diameters close to those observed experimentally, it is apparent that increasing the field even by 10 mT increments can substantially shallow the energy barriers separating different morphological states. Similar calculations for the [Co/Tb/Ni/Pt]₂₀ sample [Figure 4.14(b)] illustrate that the reduced M_s and K_{eff} of this sample lead to shallower energy barriers between morphological states. Nonetheless, for all fields and samples

considered, quasistatic variations in $\mu_0 H_z$ or temperature would likely be insufficient to overcome the potential well necessary to change between ground states.³

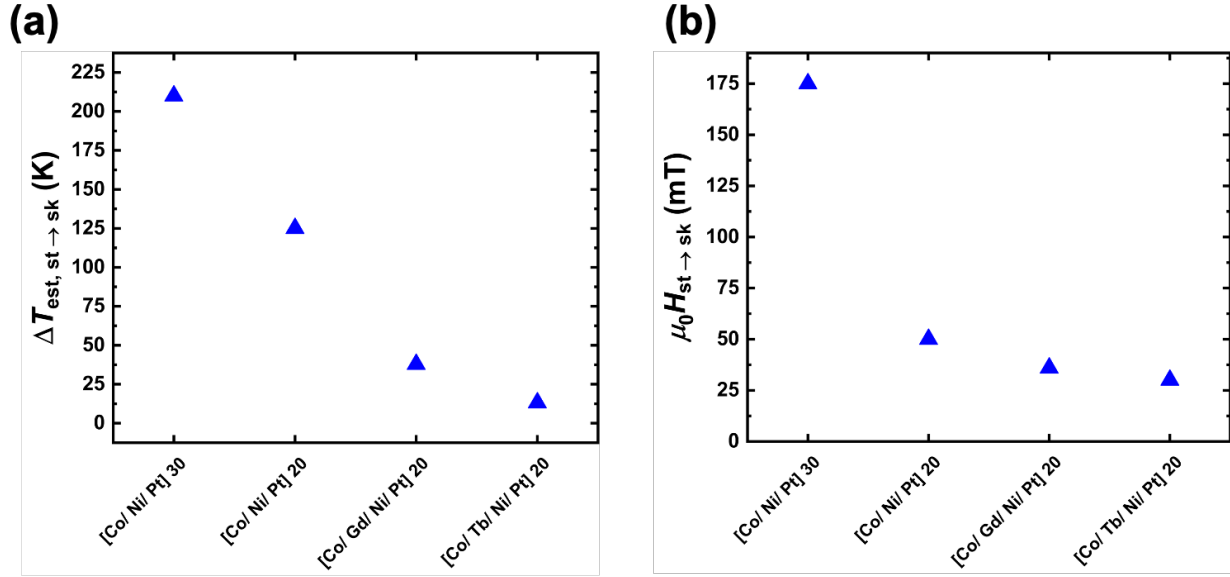


Figure 4.15: (a) The experimentally estimated temperature change due to Joule heating $\Delta T_{\text{est, st} \rightarrow \text{sk}}$ and (b) perpendicular magnetic field ($\mu_0 H_{z, \text{st} \rightarrow \text{sk}}$) necessary to initiate a complete stripe-to-skyrmion transformation in the [Co/Ni/Pt]-based samples discussed in this chapter. Data corresponds to the necessary electrical pulse characteristics at the lowest possible magnetic field.

To glean a picture of how the ease of skyrmion nucleation via Joule heating varies between the samples discussed above, we consider two parameters. The estimated change in sample temperature due to Joule heating that is necessary to induce the stripe-to-skyrmion transformation $\Delta T_{\text{est, st} \rightarrow \text{sk}}$ (determined from the experiments shown in Figure 4.1), and the magnetic field in which the pulse is applied ($\mu_0 H_{z, \text{st} \rightarrow \text{sk}}$). To simplify comparisons, we consider the pulse of minimum τ and j needed to drive a stripe-to-skyrmion transformation in the lowest $\mu_0 H_z$ possible for a given sample at room temperature using the approach discussed earlier. In Figure 4.15(a), a comparison of $\Delta T_{\text{est, st} \rightarrow \text{sk}}$ for our samples is provided. The data for the [Co/Ni/Pt]₃₀ and [Co/Ni/Pt]₂₀ samples indicate that one way to reduce the heating needed to drive a complete stripe-to-skyrmion

transformation is by reducing the total thickness of the sample by one third, which lowers $\Delta T_{\text{est, st} \rightarrow \text{sk}}$ by a similar proportionality. However, reducing M_s and K_{eff} has a more dramatic effect, lowering $\Delta T_{\text{est, st} \rightarrow \text{sk}}$ by upwards of 90 % in $[\text{Co/Tb/Ni/Pt}]_{20}$ relative to $[\text{Co/Ni/Pt}]_{20}$. Compared to other multilayered systems in which skyrmion phases were nucleated using Joule heating, the systems containing rare-earth spacers allow for a complete stripe-to-skyrmion transformation using a favorable amount of heating (*e.g.*, $\Delta T_{\text{est, st} \rightarrow \text{sk}} \approx 70$ K for $[\text{Pt/CoFeB/MgO}]_{20}$ versus ~ 15 K for $[\text{Co/Tb/Ni/Pt}]_{20}$).¹ The plot of $\mu_0 H_{z, \text{st} \rightarrow \text{sk}}$ for different sample compositions [Figure 4.15(b)] shows a similar correlation to the thickness, M_s , and K_{eff} of the samples. Moreover, the $[\text{Co/Gd/Ni/Pt}]_{20}$ and $[\text{Co/Tb/Ni/Pt}]_{20}$ samples exhibit $\mu_0 H_{z, \text{st} \rightarrow \text{sk}}$ values comparable to other materials in which skyrmion phases were formed using Joule heating (*e.g.*, 10 mT for $[\text{Pt/CoFeB/MgO}]_{20}$ ¹ and 17 mT for $[\text{Pt/Co/Ir}]_{10}$ ²).

4.4 Conclusion

We have systematically studied the effect of electrical current pulses on the generation of skyrmion phases in a variety of $[\text{Co/Ni/Pt}]$ -based multilayers, finding that Joule heating is primarily responsible for the observed transformations in domain morphology. Furthermore, we have shown that lowering the saturation magnetization and effective perpendicular magnetic anisotropy significantly reduces the Joule heating and magnetic field necessary to drive a complete stripe-to-skyrmion transformation while still retaining attractive magnetic properties, such as stability in zero applied magnetic fields. In addition to illustrating pathways towards reducing the energetic input needed to create skyrmion phases, these results further support the idea that Joule heating can enable the generation of skyrmions in a broad class of materials, over a wide range of

environmental conditions, and in systems that do not require such a precise balance in energy contributions to be attained during the fabrication process. Our results provide a pathway to tailor material properties to efficiently generate skyrmion phase in multilayers using electrical current pulses.

Chapter 4, in part, is a reprint of research published as “Energy-efficient generation of skyrmion phases in Co/Ni/Pt-based multilayers using Joule heating” by J.A. Brock, S.A. Montoya, M.-Y. Im, and E.E. Fullerton in *Physical Review Materials* 4, 104409 (2020). The dissertation author was the primary investigator author of the manuscript. The imaging work in this chapter was supported by the U.S. Department of Energy (DE-AC02-05CH11231). The sample fabrication, modeling, and electrical measurements were supported by the Quantum Materials for Energy Efficient Neuromorphic Computing, an Energy Frontier Research Center funded by the U.S. Department of Energy, Office of Science (DE-SC0019273).

4.5 References

- ¹ I. Lemesh, K. Litzius, M. Bottcher, P. Bassirian, N. Kerber, D. Heinze, J. Zazvorka, F. Buttner, L. Caretta, M. Mann, M. Weigand, S. Finizio, J. Raabe, M.-Y. Im, H. Stoll, G. Schutz, B. Dupe, M. Klau, and G.S.D. Beach, *Adv. Mater.* **30**, 1805461 (2018).
- ² W. Legrand, D. Maccariello, N. Reyren, K. Garcia, C. Moutafis, C. Moreau-Luchaire, S. Collin, K. Bouzouane, V. Cros, and A. Fert, *Nano Lett.* **17**, 2703 (2017).
- ³ F. Buttner, M.A. Mawass, J. Bauer, E. Rosenberg, L. Caretta, C.O. Avci, J. Grafe, S. Finizio, C.A.F. Vaz, N. Novakovic, M. Weigand, K. Litzius, J. Forster, N. Trager, F. Gross, D. Suzuki, M. Huang, J. Bartell, F. Kronast, J. Raabe, G. Schutz, C.A. Ross, and G.S.D. Beach, *Phys. Rev. Mater.* **4**, 011401(R) (2020).
- ⁴ Z. Wang, M. Guo, H.-A. Zhou, L. Zhao, T. Xu, R. Tomasello, H. Bai, Y. Dong, S. G. Je, W. Chao, H.-S. Han, S. Lee, K.-S. Lee, Y. Yao, W. Han, C. Song, H. Wu, M. Carpentieri, G. Finocchio, M.-Y. Im, S.-Z. Lin, and W. Jiang, *Nat. Elect.* **3**, 672 (2020).

-
- ⁵ W. Koshibae and N. Nagaosa, *Nat. Comm.* **5**, 5148 (2014).
- ⁶ P. Jadaun, L.F. Register, and S.K. Banerjee, *npj Comp. Mater.* **6**, 88 (2020).
- ⁷ S. Andrieu, T. Hauet, M. Gottwald, A. Rajanikanth, L. Calmels, A.M. Bataille, F. Montaigne, S. Mangin, E. Otero, P. Ohresser, P. Le Fevre, F. Bertran, A. Resta, A. Vlad, A. Coati, and Y. Garreau, *Phys. Rev. Mater.* **2**, 064410 (2018).
- ⁸ M. Gottwald, S. Andrieu, F. Gimbert, E. Shipton, L. Calmels, C. Magen, E. Snoeck, M. Liberati, T. Hauet, E. Arenholz, S. Mangin, and E. E. Fullerton, *Phys. Rev. B* **86**, 014425 (2012).
- ⁹ M. Li, D. Lau, M. De Graef, and V. Sokalski, *Phys. Rev. Mater.* **3**, 064409 (2019).
- ¹⁰ A. Hrabec, J. Sampaio, M. Belmeguenai, I. Gross, R. Weil, S. M. Cherif, A. Stashkevich, V. Jacques, A. Thiaville, and S. Rohart, *Nat. Commun.* **8**, 15765 (2017).
- ¹¹ P. Fischer, D.-H. Kim, B. L. Mesler, W. Chao, A. E. Sakdinawat, and E. H. Anderson, *Surf. Sci.* **601**, 4680 (2007).
- ¹² K. Zeissler, M. Mruczkiewicz, S. Finizio, J. Raabe, P. M. Shepley, A. V. Sadovnikov, S. A. Nikitov, K. Fallon, S. McFadzean, S. McVitie, T. A. Moore, G. Burnell, and C. H. Marrows, *Sci. Rep.* **7**, 15125 (2017).
- ¹³ R. Juge, S.G. Je, D. de Souza Chaves, S. Pizzini, L.D. Buda-Prejbeanu, L. Aballe, M. Foerster, A. Locatelli, T. Onur Montes, A. Sala, F. Maccherozzi, S.S. Dhesi, S. Auffret, E. Gautier, G. Gaudin, J. Vogel, and O. Boulle, *J. Magn. Magn. Mater.* **455**, 3 (2018).
- ¹⁴ W. Akhtar, A. Hrabec, S. Chouaieb, A. Haykal, I. Gross, M. Belmeguenai, M. S. Gabor, B. Shields, P. Maletinsky, A. Thiaville, S. Rohart, and V. Jacques, *Phys. Rev. Appl.* **11**, 034066 (2019).
- ¹⁵ M. Herve, B. Dupe, R. Lopes, M. Bottcher, M. D. Martins, T. Balashov, L. Gerhard, J. Sinova, and W. Wulfhekel, *Nat. Comm.* **9**, 1015 (2018).
- ¹⁶ F. Buttner, I. Lemesh, and G.S.D. Beach, *Sci. Rep.* **8**, 4464 (2018).
- ¹⁷ M.A. Basha, C.L. Prajapat, M. Gupta, H. Bhatt, Y. Kumar, S.K. Ghosh, V. Karki, S. Basu, and S. Singh, *Phys. Chem. Chem. Phys.* **20**, 21580 (2018).
- ¹⁸ R.E. Camley and D.R. Tilley, *Phys. Rev. B* **37**, 3413 (1988).
- ¹⁹ M.R. Hossu and A.R. Koymen, *J. Appl. Phys.* **99**, 08C704 (2006).
- ²⁰ Z.S. Shan and D.J. Sellmyer, *Phys. Rev. B* **42**, 10433 (1990).

-
- ²¹ C. Kittel, *Phys. Rev.* **70**, 965 (1946).
- ²² L. Liu, C.-F. Pai, Y. Li, H. W. Tseng, D. C. Ralph, and R. A. Buhrman, *Science* **336**, 555 (2012).
- ²³ M. Althammer, S. Meyer, H. Nakayama, M. Schreier, S. Altmannshofer, M. Weiler, H. Huebl, S. Geprags, M. Opel, R. Gross, D. Meier, C. Klewe, T. Kuschel, J.-M. Schmalhorst, G. Reiss, L. Shen, A. Gupta, Y.-T. Chen, G. E. W. Bauer, E. Saitoh, and S. T. B. Goennenwein, *Phys. Rev. B* **87**, 224401 (2013).
- ²⁴ W. Legrand, J.-Y. Chauleau, D. Maccariello, N. Reyren, S. Collin, K. Bouzehouane, N. Jaouen, V. Cros, and A. Fert, *Sci. Adv.* **4**, 0415 (2018).
- ²⁵ S. A. Montoya, S. Couture, J.J. Chess, J.C.T. Lee, N. Kent, D. Henze, S.K. Sinha, M.-Y. Im, S.D. Kevan, P. Fischer, B.J. McMorrان, V. Lomakin, S. Roy, and E.E. Fullerton, *Phys. Rev. B* **95**, 024415 (2017).
- ²⁶ D. Li, S. Chen, Y. Zuo, J. Yun, B. Cui, K. Wu, X. Guo, D. Yang, J. Wang, and L. Xi, *Sci. Rep.* **8**, 12959 (2018).
- ²⁷ S.-G. Je, D. H. Kim, S. C. Yoo, B. C. Min, K. J. Lee, and S. B. Choe, *Phys. Rev. B* **88**, 214401 (2013).

Chapter 5: Domain Morphology Phase Transitions in the Limit of Low Exchange Stiffness

5.1 Introduction

As discussed in preceding chapters, the interfacial DMI (iDMI) that develops at the interface between thin FM layers and nonmagnetic heavy metals (HMs) with significant spin-orbit coupling¹ can assist with the formation of skyrmion phases. There have been numerous reports on multi-repetition FM/HM heterostructures with perpendicular magnetic anisotropy (PMA), where a large iDMI assists with the formation of skyrmion phases, and the multiple repetitions of the unit structure increases the total volume of magnetic material, leading to enhanced skyrmion stability.^{2,3,4,5,6} Additionally, there have been several reports of skyrmion phases in single magnetic layer HM/FM/HM systems with modest iDMI, where the FM layer thickness was chosen to be large enough that the system is close to experiencing a spin reorientation transition (SRT),^{7,8,9,10} and consequentially has a low effective PMA characterized by $K_{eff} = K_u - \mu_0 M_S^2 / 2$ (where K_u is the intrinsic PMA constant and $\mu_0 M_S^2 / 2$ reflects the shape anisotropy of a thin film).^{11,12,13,14,15} The domain wall energy density σ in thin film systems with iDMI is often approximated as $4\sqrt{A_{ex}K_{eff}} - \pi|D|$, where A_{ex} and $|D|$ are the exchange stiffness and magnitude of the iDMI energy density, respectively.¹⁶ Thus, by lowering K_{eff} while maintaining $|D|$ or increasing $|D|$ while

maintaining substantial K_{eff} , it is possible to lower σ , reducing the energy barrier to forming multidomain states, including the skyrmion phase.^{17,18}

In this chapter, we explore the approach of reducing A_{ex} to lower the energy of forming domain walls to facilitate transition to multidomain and skyrmion phases in ultrathin films while maintaining a reasonable K_{eff} and modest D . Given that the domain wall width is estimated as $\lambda = \sqrt{A_{\text{ex}}/K_{\text{eff}}}$, lowering A_{ex} while maintaining a significant K_{eff} to obtain skyrmion phases has the added benefit of maintaining a lower domain wall width than would be expected from lowering K_{eff} alone. We observe skyrmion phases at room temperature in several FM/HM heterostructures designed to have a low A_{ex} , including Pt/Co/Pt, Pt/Co/NiCu/Pt, Pt/Co/Ni/Pt, and Pt/Co/Ni/Re, with either one or two repeats of the unit structures listed. For the Pt/Co/Pt, Pt/Co/Ni/Pt, and Pt/Co/Ni/Re samples, the exchange stiffness is lowered through the use of ultrathin (< 0.3 nm) Co layers.^{19,20} Similar properties were obtained in a thicker Pt/Co/NiCu/Pt sample by increasing the proportionality of Cu to Ni in the alloy layer.^{21,22} Concomitant to these changes in the static magnetic properties, we find that as the calculated domain wall energy diminishes toward negative values, there is a dramatic transition in the domain morphology. We observe the stabilization of labyrinthine stripe domains at remanence and field-induced skyrmion phases within a narrow window of environmental conditions (*i.e.*, temperature or applied magnetic field). By exploiting spin-orbit torques generated when passing an electrical current through the sample, skyrmion motion is observed. Using micromagnetic and analytic modeling, we demonstrate the strong relationship between the exchange stiffness and the equilibrium domain morphology in thin films with modest iDMI and significant PMA. Additionally, we show how the associated changes in the energy landscape allow for the stabilization of field-induced skyrmion phases within a framework

of understanding like that of previous material approaches,^{11,12,13,14,15} but through control of an unconventional parameter – the exchange stiffness.

5.2 Experimental Techniques

Samples of the structure [Co (t_{Co})/ Pt (1)]_{1,2}, [Co (t_{Co})/ Ni (0.3)/ Re (0.5)/ Pt (0.5)]₂, and [Co (t_{Co})/ Ni (0.3)/ Pt (1)]₂, and [Co (0.4)/ Ni₄₀Cu₆₀ (0.9)]₁ (thicknesses in nm) were used in this study. Through this chapter, these samples are referred to as the [Pt/Co]_{1,2}, [Pt/Co/Ni/Re]₂, [Pt/Co/Ni]₂, and [Pt/Co/NiCu]₁ samples, respectively. A Ta (2 nm)/ Pt (5 nm) seeding layer and Ta (3 nm) capping layer were used for all samples. The samples were grown using dc magnetron sputtering at ambient temperature onto Si substrates with a 300 nm-thick thermal oxide coating. A 3 mTorr partial pressure of Ar and sputtering power of 50 W were used. The samples were rotated at a frequency of ~5 Hz during deposition. It is noted that all thicknesses stated in this chapter were determined by taking the product of the calculated deposition rate (determined from X-ray reflectivity measurements of reference samples) and the deposition time. Through computerized control of the shutter timing, average thicknesses can be controlled with high accuracy. For some samples, the Co layers were grown as wedge-type structures using a slit placed on top of the Co sputtering source – allowing for a 14 % thickness gradient to be achieved during a single deposition over a 4 cm-long substrate. By measuring the film thickness at several locations along a thicker reference sample, the percent change in thickness per unit length along the substrate and was used to quantify the thickness gradient. Some samples were patterned into 100 μm -wide wires using conventional metal liftoff UV photolithography.

Temperature-dependent magnetometry was performed in the out-of-plane and in-plane geometries using vibrating sample magnetometry (VSM). When calculating the volumetric

parameters from magnetometry data, it was assumed that any Pt within 0.2 nm of an interface with a FM layer has become magnetically polarized.²³ Magneto-optic Kerr effect (MOKE) images and hysteresis loops were obtained using an Evico Magnetics microscope, in which perpendicular magnetic fields were applied using an air coil. For some MOKE measurements, the sample temperature was varied using a Peltier chip. The sample temperature during MOKE imaging was determined using IR thermometry. For the MOKE images presented in this chapter, images of the sample when the magnetization was saturated were subtracted as a background. The skyrmion velocity data was calculated using 60 second-long, 50 μm x 175 μm polar MOKE videos using the APREX TRACK software package.²⁴ By defining contrast, size, and shape thresholds to describe the skyrmions, APREX track can track the motion of many individual skyrmions at once. Micromagnetic modeling was performed using the mumax³ solver,²⁵ employing a 5 μm x 5 μm x 1.5 μm geometry discretized into 2 nm x 2 nm x 1.5 nm cells. Periodic boundary conditions were used to account for ten repetitions of the simulation geometry within the film plane.

5.3 Experimental Results

We begin by discussing experimental results for the [Pt/Co]₂ samples. While the Pt/Co/Pt structure is nominally symmetric, previous work has shown that structural asymmetry between the Pt-Co and Co-Pt interfaces can lead to the development of PMA and a modest iDMI.^{26,27} From measurements of the domain expansion velocity as a function of in-plane magnetic field for a [Pt/Co (0.35 nm)]₂ sample, we observe growth asymmetries that are typically associated with the “left-handed” iDMI thought to originate from the lower Pt-Co interface [Figure 5.1(b)].²⁷ As the in-plane magnetic field strength $\mu_0 H_x$ is varied, we find that one side of the domain exhibits a

minimum velocity at a characteristic field referred to as $\mu_0 H_{DMI}$. Knowing $\mu_0 H_{DMI}$, D can be estimated using the expression:¹⁶

$$D = \mu_0 H_{DMI} M_s \sqrt{A_{ex} / K_{eff}}$$

Equation 5.1

The parameters used in Equation 5.1 have been defined in earlier sections of this chapter and are quantified in subsequent sections. From the velocity as a function of in-plane field curves $v(\mu_0 H_x)$ shown in Figure 5.1(c), a D value of -0.14 mJ/cm^2 can be extracted for the $[\text{Pt/Co} (0.35 \text{ nm})]_2$ sample. The left-handedness of the iDMI in this sample (denoted by the negative sign of D) is determined by comparing the responses of “up” to “down” and “down” to “up” domain walls to the direction in which $\mu_0 H_x$ is applied. While there is substantial debate as to the appropriateness of using $\mu_0 H_x$ -induced domain growth asymmetry measurements to determine D , previous reports have demonstrated qualitative agreement between D values rendered by the aforementioned technique and other approaches, such as Brillouin light scattering (BLS) spectroscopy.^{28,29,30} Given that it has been shown that $|D|$ scales with the exchange strength, we take these results as an upper estimate for $|D|$ in samples with $t_{Co} < 0.35 \text{ nm}$, as we will subsequently show that A_{ex} roughly scales with t_{Co} in the ultrathin limit.^{31,32}

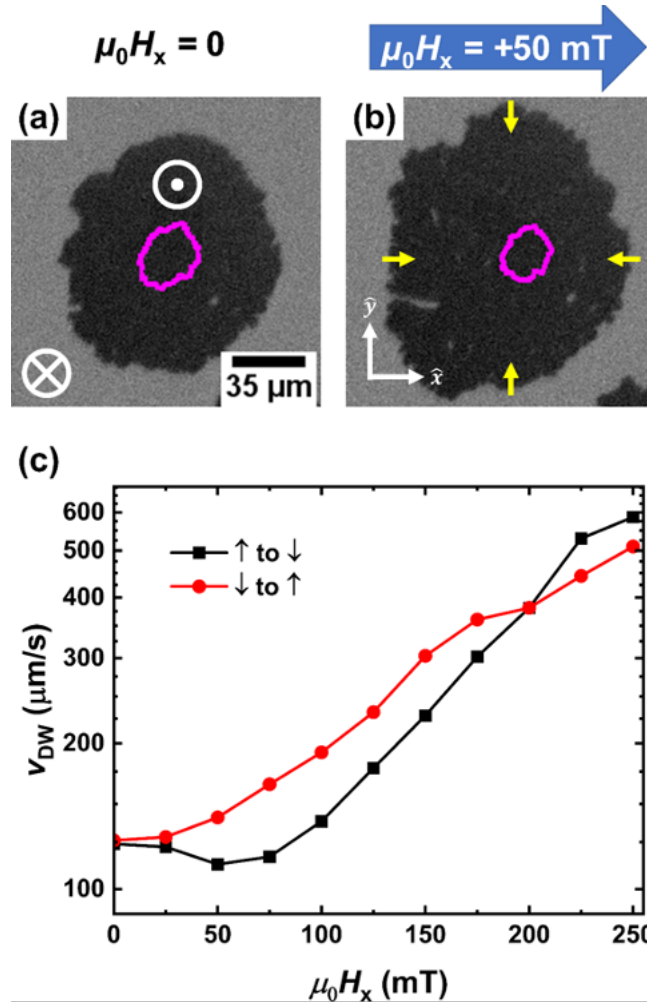


Figure 5.1: Polar MOKE images of domain growth of a $+M_z$ domain in a $[\text{Pt}/\text{Co} (0.35 \text{ nm})]_2$ sample after several out-of-plane magnetic field pulses were applied in in-plane fields $\mu_0 H_x$ of (a) 0 mT and (b) +50 mT. The magenta outlines indicate the initial extent of the nucleated domain. The yellow arrows in (b) schematically depict the left-handed Néel-type domain walls promoted by the Pt-Co interface. (c) the expansion velocity of “up” to “down” and “down” to “up” domains as a function of $\mu_0 H_x$. When collected data to generate (c), the perpendicular field pulse strength was ~ 0.8 mT and the pulse duration was 4 ms.

In agreement with previous studies, the saturation magnetization as a function of temperature $M_s(T)$ plots provided in Figure 5.2(a) show a strong dependence on the Co thickness t_{Co} , and demonstrate that the Curie temperature T_C decreases as t_{Co} is reduced into the ultrathin limit.^{19,20} In particular, Figure 5.2(a) demonstrates that the sample with $t_{\text{Co}} = 0.32$ nm is thermally stable at room temperature, as T_C is well above 300 K. However, decreasing t_{Co} to 0.24 nm

suppresses the room temperature M_s value, and the $M_s(T)$ curve indicates a T_C of ~ 365 K. To first-order, this reduction in T_C is indicative of a reduced A_{ex} , particularly when T is near T_C . However, it should be noted that the proportionality of the relationship between T_C and A_{ex} may be complicated in the ultrathin limit.³³ Further decreasing t_{Co} to 0.2 nm suppresses T_C to near room temperature. While it is anticipated that the uniformity of the Co layers may be compromised in the ultrathin limit (when the magnetic layer thickness approaches a single monolayer), previous reports have shown that well-defined FM behavior is observed even with sub-monolayer FM coverage, provided the FM layer is abutted by materials susceptible to proximity-induced magnetism (*e.g.*, Pt, Pd).^{19,20}

In Figure 5.2(b), we show room temperature ($T = 296$ K) polar MOKE hysteresis loops for $[\text{Pt}/\text{Co}]_2$ samples with different t_{Co} . As expected for FM/HM heterostructures with PMA, we find that films with $t_{\text{Co}} \geq 0.26$ nm have square hysteresis loops with full remanence. However, reducing t_{Co} to 0.25 nm or 0.24 nm, sheared polar MOKE loops are observed – suggesting a multidomain state at remanence in these samples. Further reducing t_{Co} to a nominal thickness of 0.23 nm, the polar MOKE loop has zero remanent magnetization and a hard-axis like character. As Figure 5.2(a) demonstrates that T_C decreases dramatically in this regime of t_{Co} , this may potentially indicate a paramagnetic-like character to this sample or an in-plane magnetization. To understand how these changes in the static magnetic properties impact the room-temperature domain morphology, we have collected polar MOKE images at zero field and $T = 296$ K [Figures 5.2(c-f)]. Before capturing an image, the following field history protocol was employed: First, the sample magnetization was

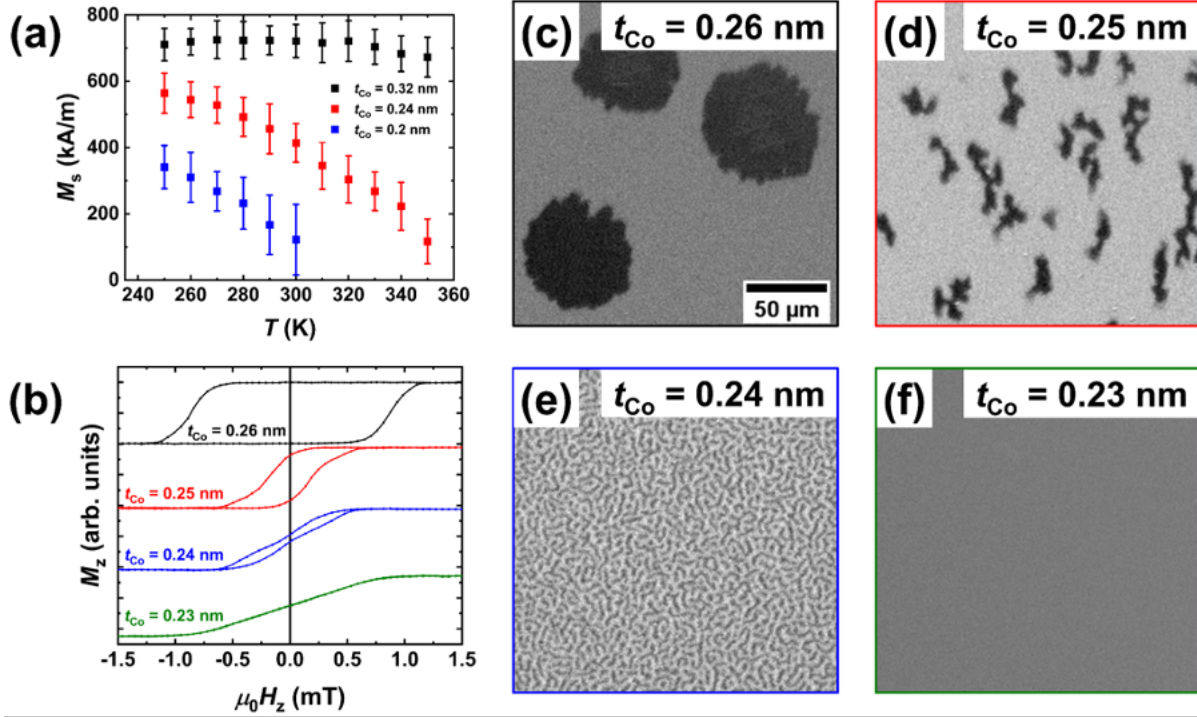


Figure 5.2: (a) Saturation magnetization as a function of temperature for $[\text{Pt}/\text{Co}]_2$ samples with varying Co thicknesses ($t_{\text{Co}} = 0.32$ nm, 0.24 nm, and 0.2 nm), determined using VSM. (b) Polar MOKE hysteresis loops for $[\text{Pt}/\text{Co}]_2$ samples with $0.23 \text{ nm} \leq t_{\text{Co}} \leq 0.26$ nm, collected at $T = 296$ K. The MOKE loops have been offset for clarity. Room temperature ($T = 296$ K) remanent states of the $[\text{Pt}/\text{Co}]_2$ samples with (c) $t_{\text{Co}} = 0.26$ nm, (d) $t_{\text{Co}} = 0.25$ nm, (e) $t_{\text{Co}} = 0.24$ nm, and (f) $t_{\text{Co}} = 0.23$ nm. The remanent states were attained using the field cycling process discussed in Section 5.3.

saturated in the negative perpendicular field direction ($-M_z$). The magnetic field was then gradually increased towards each sample's respective positive coercive field ($+H_C$) before removing the magnetic field. For samples with $t_{\text{Co}} \geq 0.26$ nm, large circular magnetic domains were observed at remanence – as is expected for thin films with PMA. In agreement with the polar MOKE hysteresis loops, a labyrinthine stripe domain pattern with a sporadic density of circular domain textures was observed at remanence when t_{Co} was reduced to 0.24 nm. Further reducing t_{Co} to 0.23 nm, the featureless remanent state may indicate an in-plane magnetic anisotropy, a paramagnetic-like character to the sample, or that the domain morphology is smaller and/or fluctuating faster than

our polar MOKE system can resolve. The nature of these domain fluctuations will be discussed more in Section 5.5. Overall, Figures 5.2(c-f) demonstrate that the domain morphology evolves dramatically with Co thickness in the limit of ultrathin Co.

In Figures 5.3(a,b), we provide more detailed, temperature-dependent magnetometry data for the [Pt/Co (0.24 nm)]₂ sample. From out-of-plane (OOP) hysteresis loops collected in the temperature range of 294 K to 302 K [Figure 5.3(a)], the extreme temperature sensitivity of this sample's magnetic properties can be seen. For $T \leq 292$ K, square hysteresis loops are observed, as is typical for thin films with PMA. As the temperature is increased over the range $294 \text{ K} \leq T \leq 302$ K, the hysteresis loop becomes progressively more sheared – suggesting a multidomain remanent state. For $T \geq 302$ K, the hysteresis loops take on a hard axis-like character (*e.g.*, low remanence and low hysteresis). Thus, the evolution of the OOP hysteresis loops with increasing temperature is similar to the evolution with decreasing Co thickness shown in Figure 5.2(b). The corresponding IP hysteresis loops, collected in the same temperature range over which the OOP loops exhibited such dramatic changes, are shown in Figure 5.3(b). Surprisingly, we find that the IP saturation field is relatively large, giving an anisotropy field (estimated from the saturation field) of $\mu_0 H_K \approx 500$ mT that does not appreciably change with temperature – suggesting that the temperature dependence of K_{eff} is primarily scaled by M_s . The magnetometry data collected at $T = 302$ K shown in Figures 5.3(a,b) demonstrate that both the OOP and IP hysteresis loops exhibit zero remanence and little to no hysteresis. This evolution in magnetic response with temperature, including the formation of stripe domains, is similar in many respects to that observed during the SRT that occurs in the limit of ultrathin FM layers, when the intrinsic PMA equals the shape anisotropy (*i.e.*, when $K_{\text{eff}} = 0$).^{7,8} However, above the SRT temperature, a finite remanence and low saturation field are

expected in the IP loops – behavior that is quite different from our observations. A further comparison of our experimental results to the previously studied SRT is provided in Section 5.4.

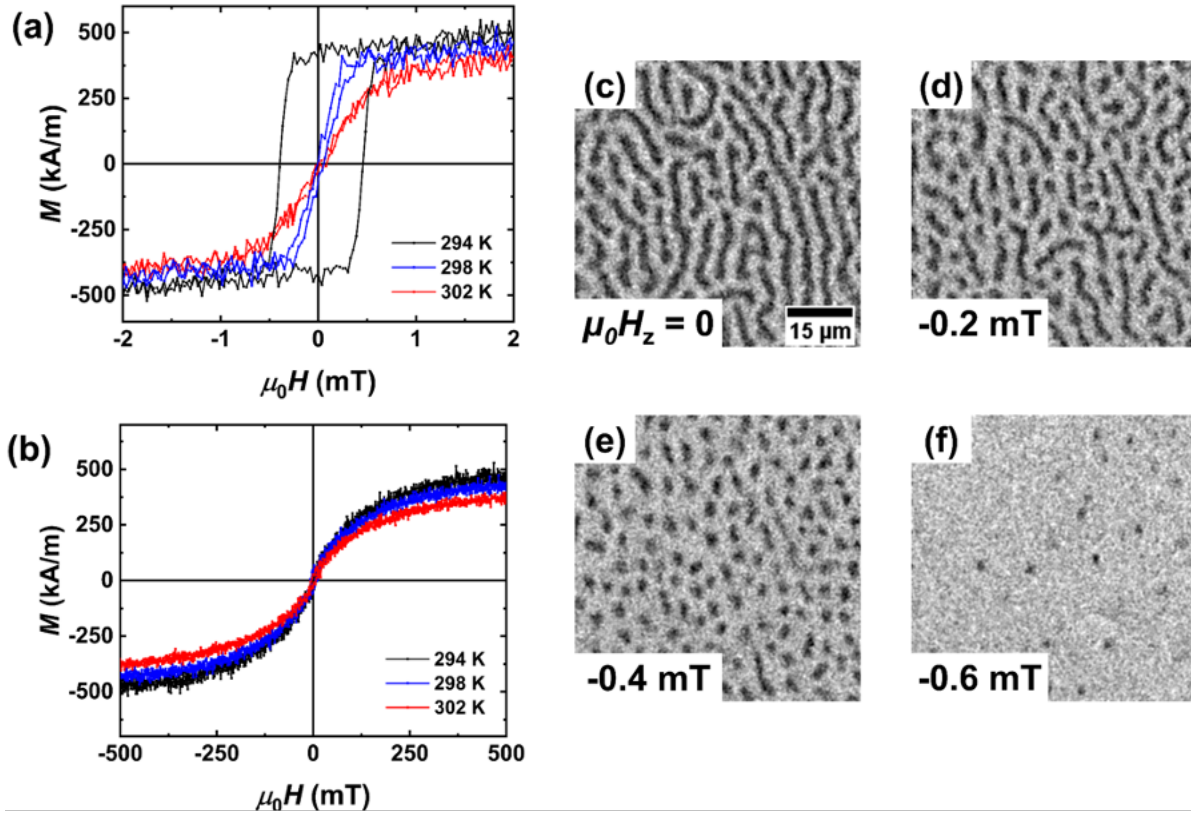


Figure 5.3: For the $[\text{Pt}/\text{Co} (0.24 \text{ nm})]_2$ sample: (a) Out-of-plane and (b) in-plane magnetometry data collected in the temperature range of $294 \text{ K} \leq T \leq 302 \text{ K}$. (c-f) Polar MOKE images collected as the perpendicular magnetic field strength $\mu_0 H_z$ was quasi-statically stepped from $\mu_0 H_z = 0$ toward negative saturation at $T = 296 \text{ K}$.

In Figures 5.3(c-f), we show polar MOKE images of the $[\text{Pt}/\text{Co} (0.24 \text{ nm})]_2$ sample as the perpendicular magnetic field strength $\mu_0 H_z$ was quasi-statically decreased toward negative saturation ($-M_z$) at $T = 296 \text{ K}$. As mentioned previously, a labyrinthine domain pattern with a sporadic population of circular features is present in this sample when $\mu_0 H_z = 0$. As in other systems whose static magnetic properties are extremely sensitive to temperature, we observe that

the remanent domain pattern experiences a significant degree of thermal fluctuation when observed over several seconds,¹¹ particularly for the [Pt/Co]₁ sample (see Supplemental Video 1 of Ref. 34). When a sufficiently strong $\mu_0 H_z$ is applied, some stripe domains collapse into circular features with a characteristic diameter of $\sim 3 \mu\text{m}$. Further increasing $\mu_0 H_z$ causes all the stripe domains to collapse, forming a disordered ensemble of circular textures. A video of this evolution in domain morphology with $\mu_0 H_z$ is provided in Supplemental Video 2 of Ref. 34. While this field-induced stripe-to-skyrmion transition can be observed at room temperature ($T = 296 \text{ K}$) in the [Pt/Co (0.24 nm)]₂ sample, we note that by heating the [Pt/Co (0.26 nm)]₂ sample (*i.e.*, the sample whose room temperature domain morphology is shown in Figure 5.2(c) slightly, similar behavior is observed [Figure 5.4].

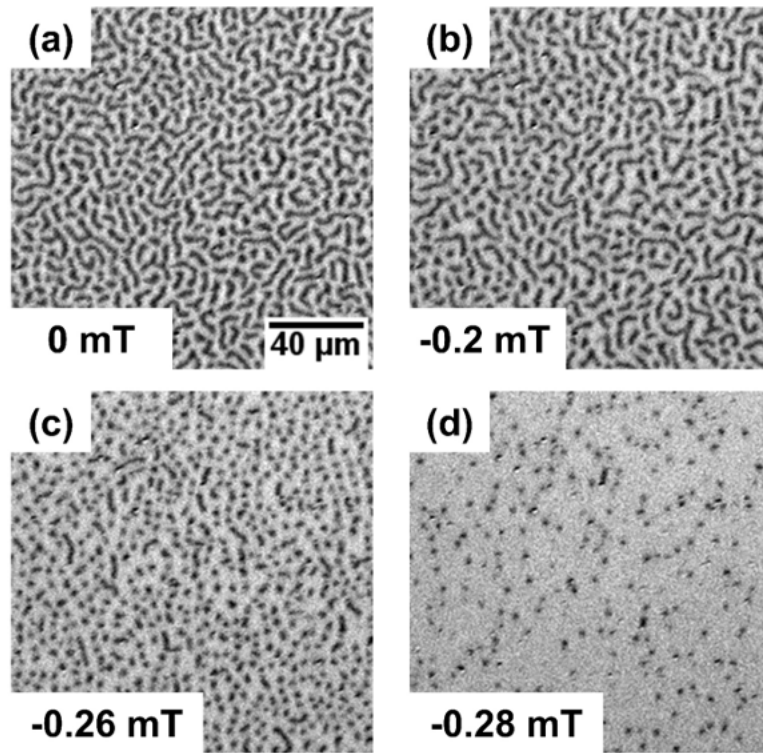


Figure 5.4: Polar MOKE images of the [Pt/Co (0.26 nm)]₂ sample, collected as the perpendicular magnetic field strength $\mu_0 H_z$ was quasi-statically stepped from $\mu_0 H_z = 0$ towards negative saturation. When imaging, the sample temperature was approximately 315 K.

To confirm that these field-induced circular features are magnetic skyrmions with chiral domain walls, the features' response to applied electrical currents was determined. While we have not performed a precise quantification of the spin-Hall angle, Slonczewski-like torque, and field-like torque associated with the spin-Hall effect in our samples, previous reports have shown that Pt/FM/Ta-type structures exhibit a net positive spin-Hall angle,^{35,36,37} which dictates a positive polarization to the spin current injected into the FM layers. As such, if our skyrmions possess a left-handed Néel chirality (as inferred from the data shown in Figure 5.1), they should move in the same direction as the applied electrical current, regardless of the efficiency of the spin-Hall effect. While skyrmions are known to exhibit a deflection transverse to the applied current axis when driven – a phenomenon known as the skyrmion Hall effect – this behavior is muted in the limit of the low driving currents necessitated by the extreme sensitivity of our samples to temperature and magnetic fields.^{38,39,40} Despite these limitations, we find that the circular features stabilized by $\mu_0 H_z$ in the [Pt/Co (0.24 nm)]₂ sample move in the direction of the conventional current density J regardless of the domain polarity, as demonstrated in Figure 5.5 and Supplemental Videos 3 and 4 of Ref. 34. Based on the spin-Hall angles of the Pt seeding and Ta capping layers extensively reported in the literature, this response is consistent with spin-orbit torques acting on the left-handed chirality observed in other Pt/Co-based systems.^{11,41,42,43,44,45} As shown in Figure 5.5(e), we note that no appreciable motion was observed for current densities below $\sim 5 \times 10^9$ A/m² – indicative of the pinning potential that is known to inhibit skyrmion motion in the limit of low driving potential.¹² As shown in Supplemental Video 4 of Ref. 34, we also observed a dramatic increase in the number of skyrmions present in the wire after an electrical current has been applied – a behavior that may be attributed to the previously reported mechanisms by which skyrmions can be generated from stripe domains subject to spin-orbit torques and sporadic pinning.⁴⁶

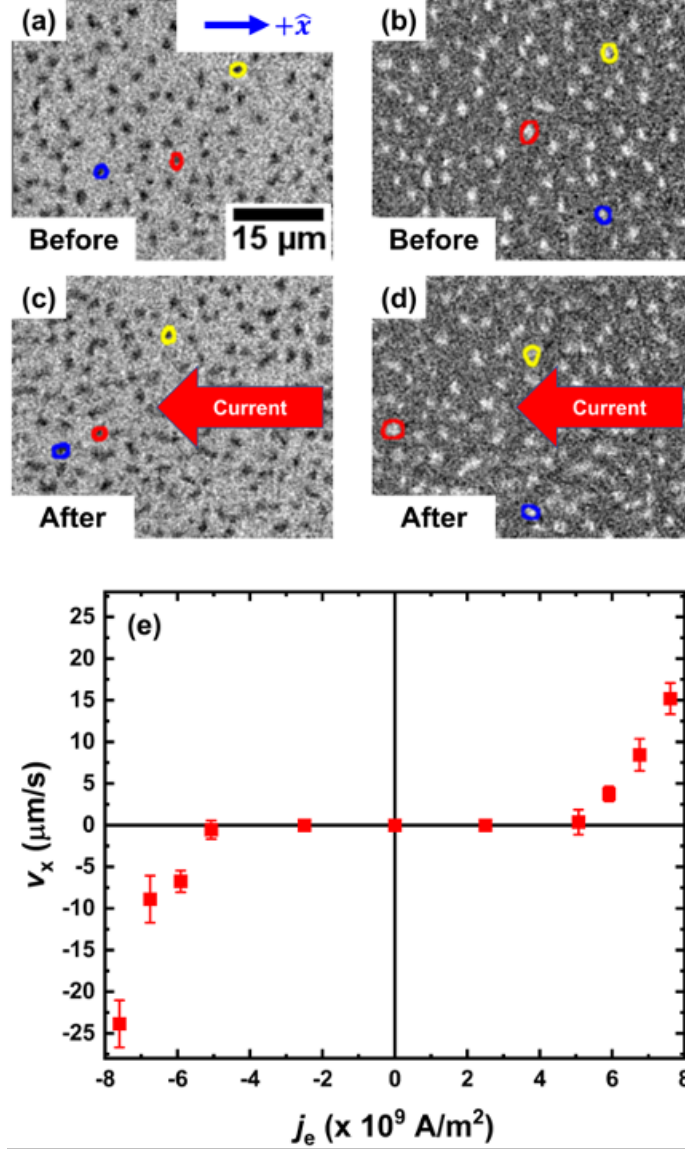


Figure 5.5: (a-d) Polar MOKE images (collected at $T = 296 \text{ K}$) depicting the motion of several skyrmions in the $[\text{Pt}/\text{Co} (0.24 \text{ nm})]_2$ sample before and after a current density of $j_e = 7.6 \times 10^9 \text{ A/m}^2$ was passed through the sample (a) and (b) correspond to $+M_z$ domains (stabilized in $\mu_0 H_z = -0.6 \text{ mT}$), whereas (c) and (d) depict $-M_z$ domains (stabilized in $\mu_0 H_z = +0.6 \text{ mT}$). (e) Velocity of skyrmions along the x -axis (v_x) in the $[\text{Pt}/\text{Co} (0.24 \text{ nm})]_2$ sample as a function of j_e . The velocities shown in (e) were calculated from wide-field polar MOKE videos using techniques discussed in the Section 5.2. The error bars correspond to the standard deviation in velocity of all tracked skyrmions in motion over 60 seconds. The directionality of v_x and j_e are defined relative to the \hat{x} vector shown in (a).

Considering these findings in the $[\text{Pt}/\text{Co}]$ samples in the limit of ultrathin t_{Co} , we now examine how modifying the HM and FM layers to increase the structural inversion asymmetry

(and hence, the total iDMI) impacts the morphological phases accessible in the ultrathin limit. We highlight two other material systems: [Pt/Co (0.24 nm)/Ni/Re]₂ and [Pt/Co (0.24 nm)/Ni]₂ (thicknesses in nm) – all featuring interfaces (Pt-Co, Ni-Re, and Ni-Pt) thought to contribute to an additive iDMI acting on the FM layers due to their compositional asymmetry (*i.e.*, in addition to an asymmetry in interfacial quality, as in the [Pt/Co] samples).^{47,48} While the Co layers of the two structures mentioned above were grown as wedges (using the approach detailed in Section 5.2), we indicate the thickest approximate t_{Co} at which a $\mu_0 H_z$ -induced skyrmion phase was observed at $T = 296$ K. The remanent state of the [Pt/Co/Ni/Re]₂ sample shown in Figure 5.6(a) succinctly demonstrates the compositional sensitivity of the domain morphology in the ultrathin limit, as the stripe domain size dramatically decrease when t_{Co} is varied by as little as 0.06 %. We emphasize that while Figure 5.6(a) is reminiscent of previous studies that showed a strong link between film thickness and domain periodicity on account of proximity to a SRT,^{7,8,9,10} the static characterization does not indicate the presence of the SRT in our FM/HM heterostructure samples near room temperature, given the sizeable in-plane saturation field is indicative of significant PMA.

From the higher-magnification polar MOKE images shown in Figures 5.6(b,d), it can be seen that the [Pt/Co/Ni/Re]₂ and [Pt/Co/Ni]₂ samples exhibit a labyrinthine stripe pattern in zero field at room temperature ($T = 296$ K). In line with the [Pt/Co]₂ samples, temperature-dependent magnetometry of these samples indicate T_C values below 400 K and OOP hysteresis loops extremely sensitive to variations in temperature in the vicinity of 300 K. Much like the [Pt/Co]₂ samples, the stripe domains formed at remanence in the [Pt/Co/Ni/Re]₂ and [Pt/Co/Ni]₂ samples transform into circular textures when a small perpendicular field is applied. By observing these features' response to spin-orbit torques (using the process previously described for the [Pt/Co]₂

samples), it is possible to classify these features as skyrmions with fixed Néel chirality. Figures 5.6(c,e) show polar MOKE images collected at the a $\mu_0 H_z$ value where each sample exhibits its densest skyrmion phase.

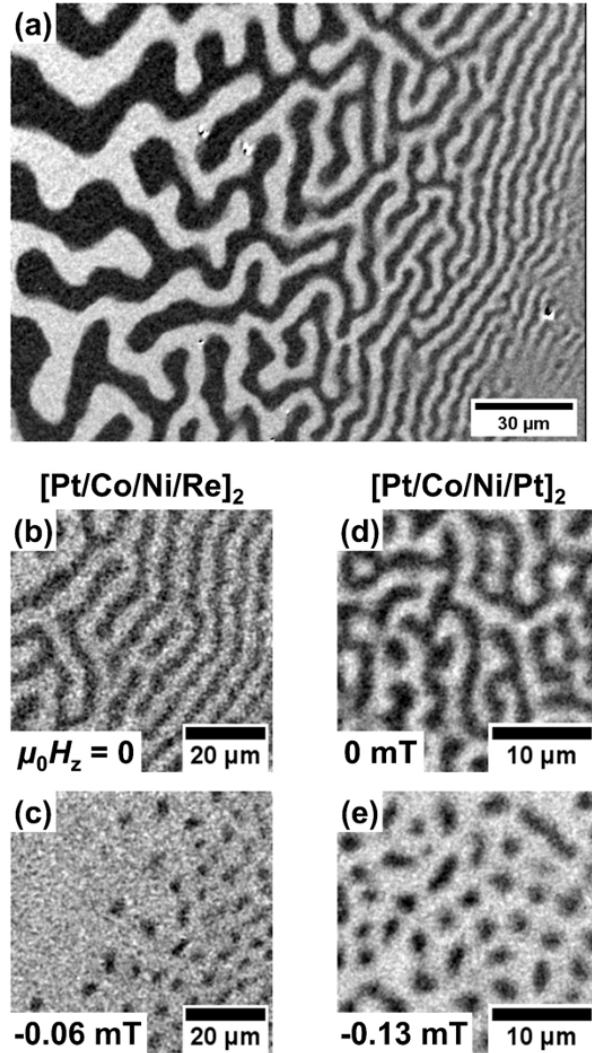


Figure 5.6: (a) Remanent domain morphology of the $[\text{Pt}/\text{Co}/\text{Ni}/\text{Re}]_2$ sample, where the Co layers were grown such that t_{Co} decreases by $\sim 0.06\%$ when moving from left to right across the field of view. The center of the field of view corresponds to an approximate t_{Co} of 0.24 nm. Remanent state and densest $\mu_0 H_z$ -induced skyrmion phases observed in the (b,c) $[\text{Pt}/\text{Co}/\text{Ni}/\text{Re}]_2$ and (d,e) $[\text{Pt}/\text{Co}/\text{Ni}]_2$ samples. All images were collected at $T = 296$ K.

Thus far, the materials systems discussed have shared the commonalities of an ultrathin (< 0.3 nm) Co layer producing a low A_{ex} (inferred from a low T_C). However, if a low A_{ex} is responsible

for the observed domain morphologies, it should be possible to attain similar results in systems with somewhat thicker FM layers. Previous works have shown that alloying Ni with Cu can lower T_C relative to that of elemental Ni, and that this trend is linear with respect to Cu concentration.^{21,49} Based on this, we fabricated a Ta(2)/Pt(5)/Co(0.4)/Ni₄₀Cu₆₀(0.9)/Ta(3) sample (thicknesses in nm) to explore the role of exchange stiffness by optimizing the Cu-Ni ratio. From magnetometry data collected near room temperature [Figure 5.7(a)], it can be seen that the [Pt/Co/NiCu]₁ sample's OOP hysteresis loops are extremely sensitive to temperature; the square loop present at 285 K becomes more sheared as the temperature is increased to 190 K, and becomes hard axis-like when the temperature is increased to 295 K. These findings are similar to those shown for the [Pt/Co(0.24 nm)]₂ sample in Figure 5.3(a).

Much like the [Pt/Co]₂ samples with ultrathin Co layers, the IP hysteresis loops of the [Pt/Co/NiCu]₁ sample do not change significantly in the vicinity of room temperature [Figure 5.7(b)]; given that the sign of K_{eff} does not change over the relevant temperature range, this does not indicate the presence of a SRT. The $M_s(T)$ curve shown in Figure 5.7(c) (generated from hysteresis loops collected over a wide range of temperatures) indicates a T_C of ~ 360 K for the [Pt/Co/NiCu]₁ sample. From polar MOKE images collected at $T = 290$ K, it can be seen that the [Pt/Co/NiCu]₁ sample exhibits a labyrinthine stripe domain pattern at remanence near room temperature, with a characteristic domain width of $\sim 2 \mu\text{m}$ [Figure 5.7(d)]. When a ~ 0.04 mT perpendicular field is applied, the labyrinthine remanent state is transformed into an ensemble of circular textures [Figure 5.7(e)] that display the spin-orbit torque induced dynamics emblematic of skyrmions seen in the previously discussed samples with ultrathin Co layers – indicating that the energetic considerations that give rise to the remanent labyrinthine morphology and field-induced skyrmion phase are not contingent on a reduced dimensionality to the FM layers.

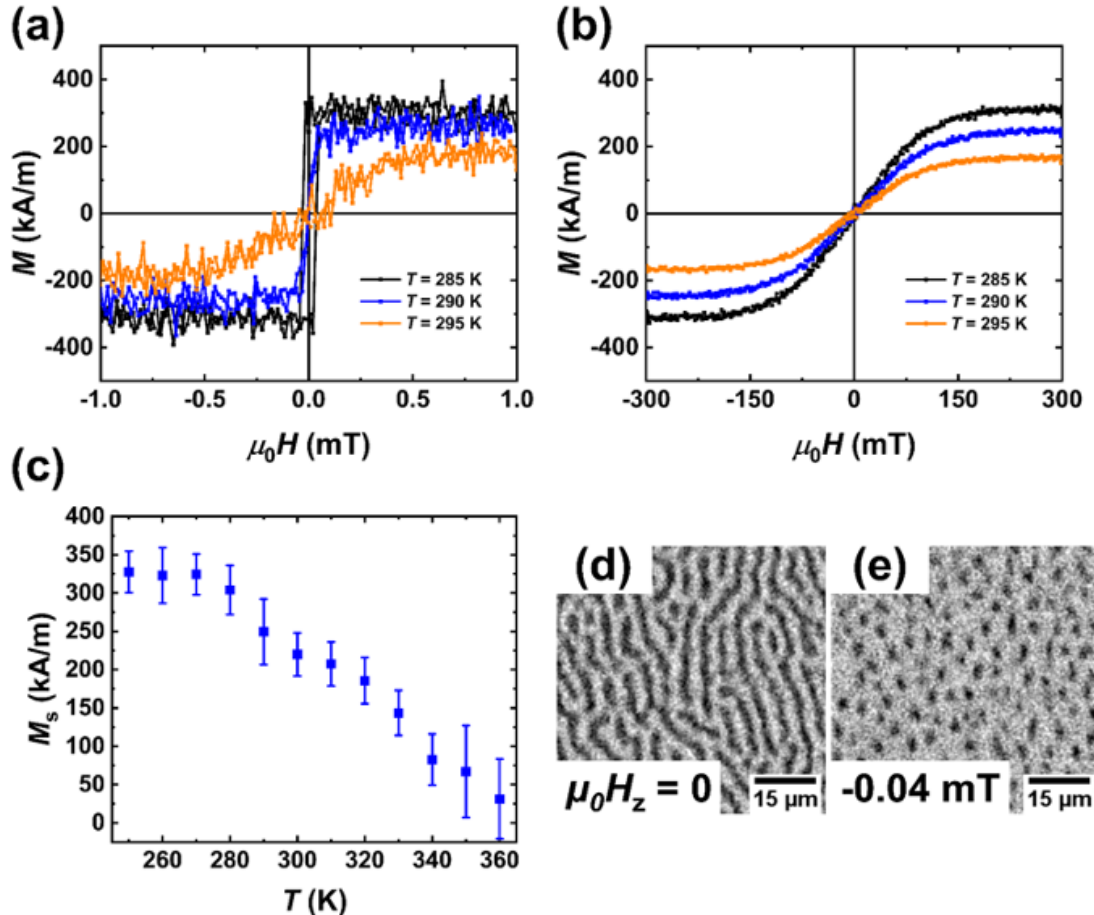


Figure 5.7: For the $[\text{Pt}/\text{Co}/\text{NiCu}]_1$ sample: (a) out-of-plane and (b) in-plane magnetometry data collected in the temperature range of $285 \text{ K} \leq T \leq 295 \text{ K}$. (c) Saturation magnetization M_s over the temperature range $250 \text{ K} \leq T \leq 360 \text{ K}$. Polar MOKE images collected at $T = 290 \text{ K}$ in perpendicular magnetic fields of 0 and -0.04 mT are shown in panels (d) and (e), respectively.

5.4 Discussion and Modeling

Thus far, the temperature dependence of the OOP hysteresis loops, the suppressed T_C values, and the labyrinthian domain morphologies observed at remanence in our samples draw strong parallels to extensive, past studies of the SRT.^{7,8,10} Particularly, the thickness sensitivity exhibited in Figure 5.6(a) is heavily reminiscent of previous studies of a $\text{Cu}/\text{Fe}/\text{Ni}$ structure that was found to exhibit a SRT when the Fe thickness was reduced to ~ 1.25 monolayers.¹⁰ While the

original understanding of the SRT was developed using systems that have little or no iDMI, recent reports have shown that the iDMI can assist in raising the temperature at which the SRT occurs and facilitates a direct transition between the ferromagnetic PMA and paramagnetic states for sufficient D .⁵⁰ However, despite the many similarities between our HM/FM heterostructures and systems that undergo a SRT, our work is differentiated by the fact that K_{eff} does not approach zero when the labyrinthine stripe phase becomes the remanent state in our samples (whether by adjusting the FM layer thickness or the sample temperature) – a key point that rules out a traditional SRT at the thicknesses and temperatures relevant to our samples. Given that the harbinger of a skyrmion phase in our samples has been the observation of a labyrinthine stripe phase at remanence, the treatment of the SRT, while related, may not fully be applicable.

To better understand the factors that give rise to skyrmion phases in thin films with significant PMA, modest iDMI, and low A_{ex} , we have performed micromagnetic and analytic modeling. For our models, a M_s of 250 kA/m, a first-order uniaxial anisotropy constant K_u of 67.5 kJ/m³ (corresponding to $K_{\text{eff}} = K_u - \mu_0 M_s^2 / 2$ in the thin film geometry), and a film thickness t_{film} of 1.5 nm were used to approximate the [Pt/Co/NiCu]₁ sample. While an A_{ex} of 10 pJ/m is often used when modeling Pt/Co and Pt/Co/Ni-based systems, this generally assumes that T_C is closer to the bulk value of Co.^{51,52,53} To reflect the fact that T_C of the [Pt/Co/NiCu]₁ sample is ~75 % lower than that of bulk Co, we use an A_{ex} of 2.5 pJ/m in our calculations. The iDMI energy density D was varied between 0 and 1 mJ/m². All simulations were performed at $T = 0$ K.

In the thin film limit, it is well known that the relative balance between the demagnetization energy and the energy penalty associated with forming a domain wall (which depends on M_s , K , A_{ex} , and D) determines whether the film will break into domains in zero field and the corresponding domain periodicity.^{54,55,56,57} To understand this energetic competition in the [Pt/Co/NiCu]₁ sample

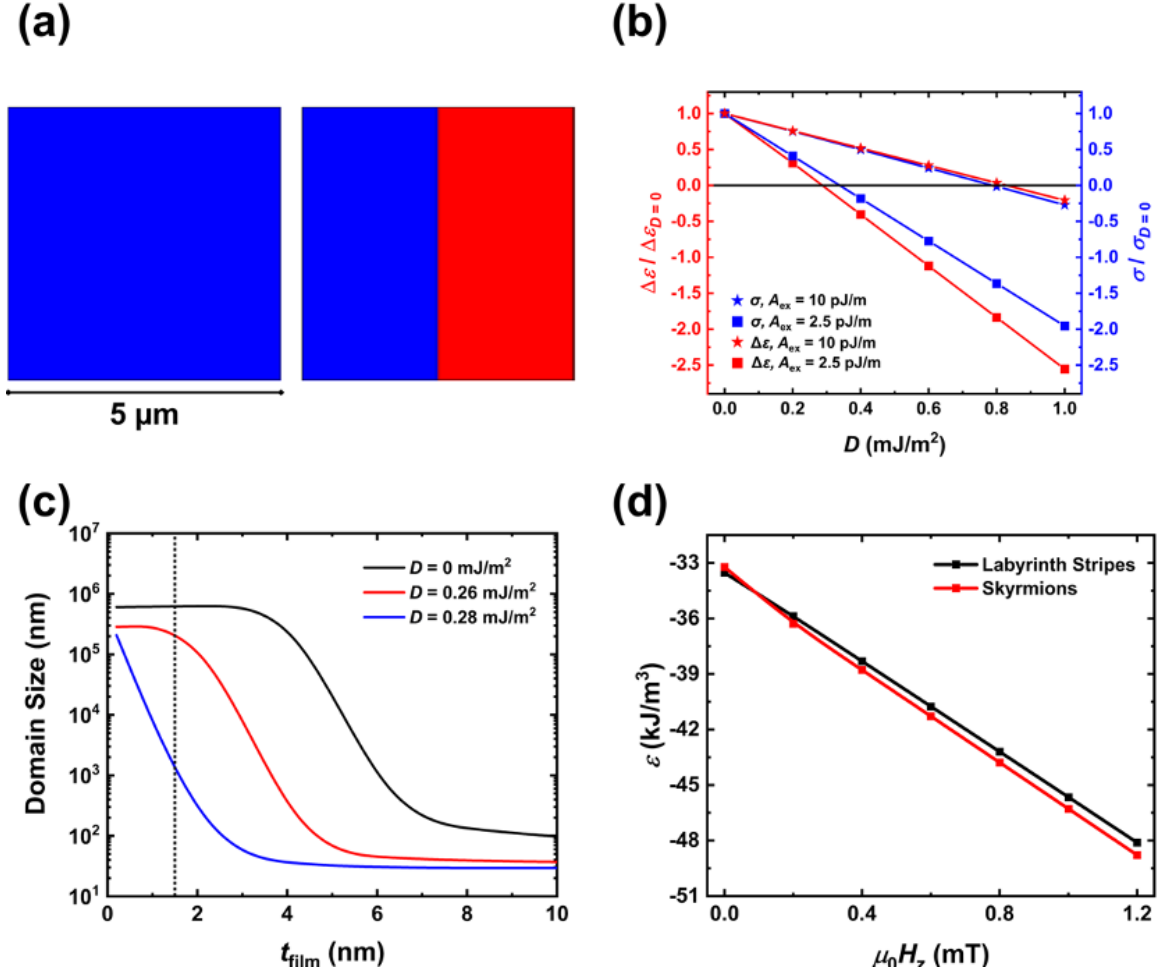


Figure 5.8: Modeling results for the $[\text{Pt}/\text{Co}/\text{NiCu}]_1$ sample: (a) Schematic depiction of the uniform (left) and two-domain (right) states used in the micromagnetic simulations. Blue (red) regions correspond to $+M_z$ ($-M_z$) magnetic orientations. (b) Micromagnetic calculations of the difference in energy density $\Delta\varepsilon$ between the uniform and two-domain states (red) and the analytic domain wall energy density σ (blue) as a function of iDMI energy density D . For each initial state, $\Delta\varepsilon / \sigma$ has been normalized to the value when $D = 0$. Data are shown for $A_{\text{ex}} = 2.5$ pJ/m (squares) and $A_{\text{ex}} = 10$ pJ/m (stars). (c) Analytic modeling of the expected domain size as a function of the magnetic film thickness t_{film} for selected D values. The dashed line indicates the magnetic layer thickness of the $[\text{Pt}/\text{Co}/\text{NiCu}]_1$ sample used in our experiments. (d) ε as a function of $\mu_0 H_z$ for the labyrinthine stripe and skyrmion phases. The material parameters used in the modeling are stated in Section 5.4.

(which can generally be extended to describe the samples with ultrathin Co layers), we first performed a simple micromagnetic calculation of the difference in energy density $\Delta\varepsilon$ between the two-domain state with a single domain wall and the uniform magnetic state (*i.e.*, $\Delta\varepsilon = \varepsilon_{\text{two-domain}} -$

$\varepsilon_{\text{uniform}}$) as a function of D . This calculation of $\Delta\varepsilon$ allows for a micromagnetic estimation that can be compared to the analytical expression for the domain wall energy density $\sigma = 4\sqrt{A_{\text{ex}}K_{\text{eff}}} - \pi|D|$. A schematic depiction of the magnetic states considered is provided in Figure 5.8(a). The ε associated with each state was determined after allowing the domain state to relax from the respective initial state to the minimum energy configuration. From the $\Delta\varepsilon(D)$ plot provided in Figure 5.8(b), it can be seen that the uniform state has a lower ε at lower D – indicating that the energetic penalty associated with breaking into domains/forming a domain wall outweighs the associated reduction in dipolar energy.

As shown in Figure 5.8(b), at a relatively modest value of D (~ 0.28 mJ/m²), $\Delta\varepsilon(D)$ becomes negative, suggesting that the energetic penalty to forming a domain wall has been diminished and the energy landscape is more conducive to the formation of multidomain states. If instead, an A_{ex} of 10 pJ/m is used – as is often the case when describing Pt/Co-based systems – Figure 5.8(b) also shows that the root of $\Delta\varepsilon(D)$ is shifted towards D values which are generally only feasible in material systems optimized to have a large iDMI or a reduced K_{eff} . Calculations of the domain wall energy density σ under the same considerations – also shown in Figure 5.8(b) – show similar trends as the $\Delta\varepsilon(D)$ simulations. We note that accounting for the domain wall anisotropy energy density⁵⁸ in the net σ only slightly modifies the curve for lower A_{ex} , shown in Figure 5.8(b). While these results are most applicable to the [Pt/Co/NiCu]₁ sample, we show how these trends in $\Delta\varepsilon$ and σ with A_{ex} , K , and D in greater detail in Figure 5.9. In keeping with our experimental results, D is not expected to change dramatically when changing the temperature by several K,⁵⁹ we argue that the reduction in $\Delta\varepsilon$ and σ with temperature in our samples is primarily determined by K_{eff} (which itself is scaled by M_s , not μ_0H_K) and the inverse scaling of A_{ex} with temperature.⁶⁰ Indeed, M_s of the [Pt/Co/NiCu]₁ sample changes significantly for small

modifications in temperature within the relevant temperature range [Figure 5.7(c)]. Thus, while the shift in the relative energy of the uniform magnetic state versus a multidomain state is driven by K_{eff} , a low A_{ex} and modest D permit this transition without K_{eff} approaching zero (*i.e.*, away from the SRT).

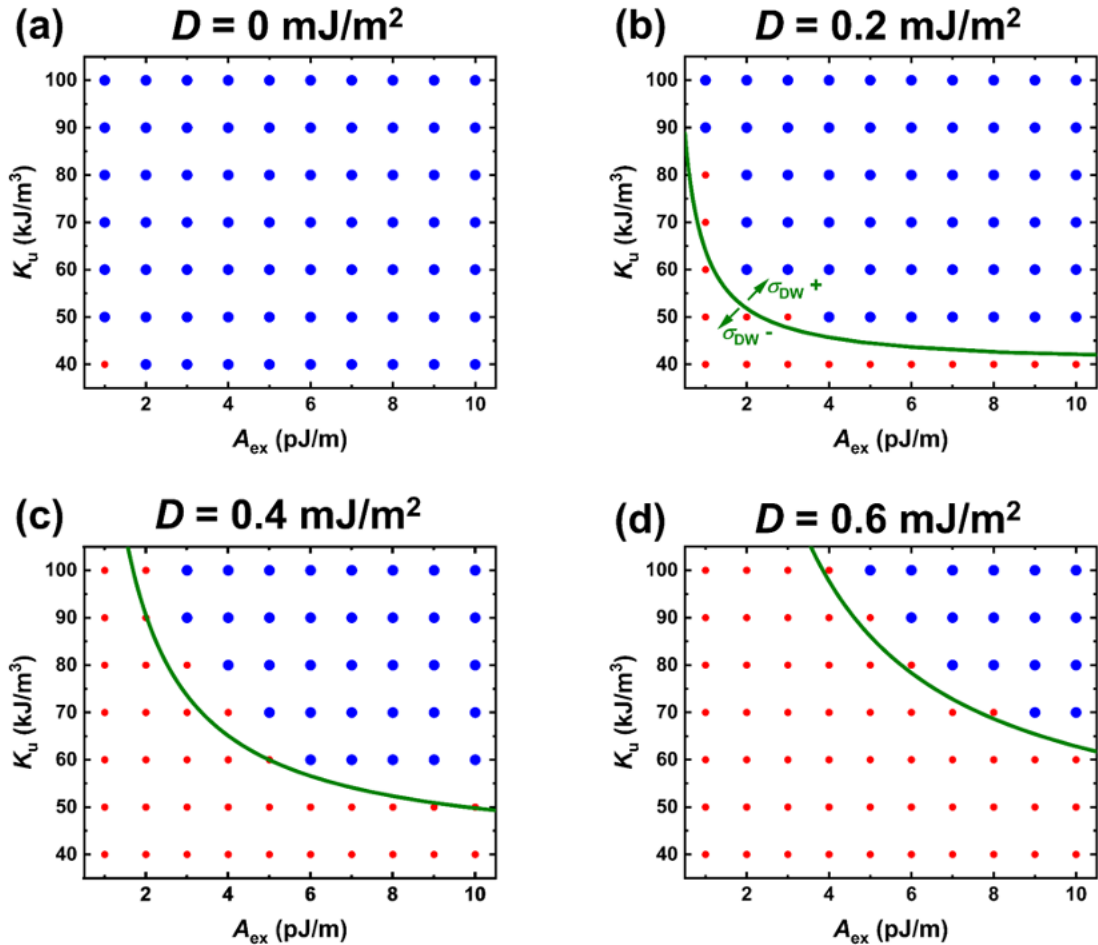


Figure 5.9: $\Delta\varepsilon$ and σ as a function of A_{ex} and K_u for different values of D . $\Delta\varepsilon$ was calculated micromagnetically using the approach stated in the main text, whereas σ was calculated as $4\sqrt{A_{\text{ex}}K_{\text{eff}}} - \pi|D|$. For all calculations, we took M_s as 250 kA/m. The blue (red) circles indicate parameter combinations where the micromagnetic simulations resulted in a positive (negative) $\Delta\varepsilon$. The green line demarcates positive and negative σ values, as indicated in (b). Note that in (a), the absence of iDMI dictates that the sign of σ does not change for any combination of A_{ex} and K_u , hence the lack of a σ .

To understand how these energetic balances impact the equilibrium domain size in the [Pt/Co/NiCu]₁ sample, we have employed the analytic model of Ref. 61. In Figure 5.8(c), we show the equilibrium domain width predicted as a function of magnetic film thickness t_{film} for the [Pt/Co/NiCu]₁ sample (using the same static parameters as those used in the micromagnetic modeling) for several values of D . For the lower D values (0 and 0.26 mJ/m²), a sample with $t_{\text{film}} = 1.5$ nm is predicted to exhibit mm-scale domains, which may be considered as a uniform magnetic state. This calculation agrees with the micromagnetic modeling, which suggested that it was energetically disadvantageous for a sample with $t_{\text{film}} = 1.5$ nm to break into domains at lower D . For $D = 0.28$ mJ/m² (*i.e.*, close to the D value where $\Delta\varepsilon$ and σ become negative), the equilibrium domain size decreases exponentially with the film thickness in the vicinity of the t_{film} values relevant to the [Pt/Co/NiCu]₁ sample. Knowing that $t_{\text{film}} = 1.5$ nm and the experimentally determined domain size is ~ 2 μm , the analytic model indicates that 0.28 mJ/m² is a reasonable estimation for $|D|$ in the [Pt/Co/NiCu]₁ film.

Taken in concert, the micromagnetic and analytic modeling suggest that a modest D can enable the formation of a labyrinthine stripe phase a remanence in samples with low A_{ex} – behavior that is not typical to thin films with low M_s and appreciable PMA. However, the appearance of a labyrinthine stripe phase at zero field does not necessarily guarantee the presence of a field-induced skyrmion phase. To understand the nature of the field-induced morphological transition between stripe domains and skyrmions, we have performed additional micromagnetic simulations, comparing the $\mu_0 H_z$ -dependence of ε between the labyrinthine stripe and skyrmion phases at $T = 0$ K.⁶² For these calculations, the material parameters were the same as those employed when generating Figure 5.8(b), using $D = 0.28$ mJ/m². The initial state of the simulation was set to a random magnetization pattern or a skyrmion lattice (for the labyrinthine stripe and skyrmion

phases, respectively). At each $\mu_0 H_z$ step in the simulation, the system was relaxed to its minimum total energy configuration. In line with the experimental results, comparing the $\varepsilon(\mu_0 H_z)$ profiles of these two morphological phases [Figure 5.8(d)] demonstrates that the skyrmion phase becomes the ground state when $\mu_0 H_z = 0.09$ mT, which is reasonably close to the experimental findings. While an energetic barrier must be overcome to transition between morphological ground states, finite-temperature atomistic simulations have shown that bringing the system closer to T_C can shallow this barrier.⁶² Given that all the samples that exhibit skyrmion phases discussed herein have a T_C less than 400 K, we argue that the energy barrier separating the morphological phases may be easily overcome by the thermal energy present near room temperature.^{62,63}

We have yet to comment in detail on the magnetic state present when the hysteresis loops indicate PMA [Figures 5.2(b), and 5.3(a,b)], but polar MOKE contrast has disappeared and there is little or no hysteresis [Figure 5.2(b,f)]. In the simplest scenario, the domain size in this uniform-appearing phase may have become too small to resolve with polar MOKE. In the context of the SRT, however, such observations have been interpreted as an indicator of a phase transition, and there has been extensive debate in the literature as to whether this consists of a transition from the ferromagnetic state to a paramagnetic “gap” state with PMA,^{10,64} or a fluctuating stripe domain phase.^{65,66,67} While our samples do not have the low K_{eff} emblematic of the SRT, the static magnetic properties are similar in many regards; thus, further investigations with higher spatiotemporal resolution are needed to fully understand the nature of the temperature/thickness-induced domain morphology transformations observed in our samples. Regardless of the end result of the transformation, the modeling discussed above permits an understanding of the energetic balances responsible for skyrmion stabilization in our samples with low exchange stiffness, appreciable PMA, and modest iDMI.

5.5 Spatiotemporal Dynamics of the Domain Fluctuations

As mentioned towards the end of Section 5.5, we have yet to comment in detail on the specific characteristics of the morphological phase transformation that occurs where our MOKE imaging system begins to lose spatial resolution. In other words, how does the domain morphology in our FM/HM systems transition between the labyrinthine remanent state shown in Figure 5.2(e) to the featureless remanent state shown in Figure 5.2(f)? To begin answering this question, we briefly reiterate that our experimental results indicate that in the limit of ultrathin FM layer thickness, an equivalent morphological phase transition can be brought about by minute reduction of the FM layer thickness or by increasing the sample temperature. As such, we begin by exploring how the domain periodicity changes with sample temperature. For a [Pt/ Co (0.24 nm)]₂ sample, polar MOKE images of the remanent morphology at several temperatures in the vicinity of room temperature are shown in Figures 5.10(a-d). From these micrographs, it is readily apparent that in the limit of ultrathin FM layer thickness, minute changes in sample temperature lead to dramatic changes in the domain periodicity. Using the fast-Fourier transform (FFT) of micrographs collected in the temperature range of $294 \text{ K} \leq T \leq 296 \text{ K}$, the relationship between the domain periodicity and sample temperature was quantified, as shown in Figure 5.10(e); from this plot, it can be seen that during the temperature-induced morphological phase transition, the domain size rapidly approaches the resolution limit set by the optics of our MOKE imaging system. While we have previously differentiated the phase transition observed in these samples from the SRT (on account of the high K_{eff} of our FM/HM samples), this strong relationship between domain periodicity and sample temperature draws strong parallels to the SRT.^{10,65}

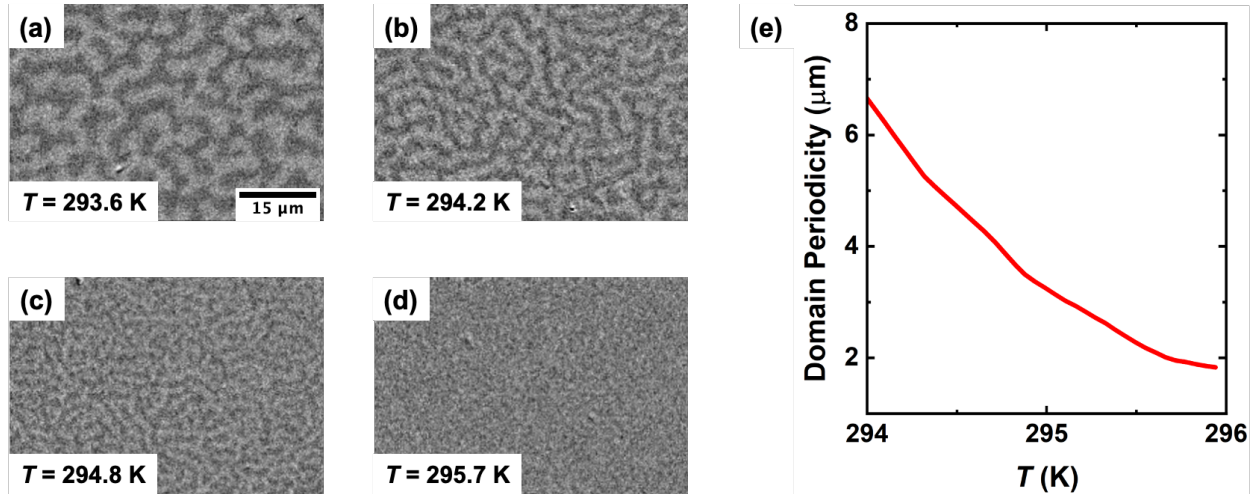


Figure 5.10: Images of the remanent domain morphology in at $[\text{Pt}/\text{Co} (0.24 \text{ nm})]_2$ sample collected at temperatures of (a) 293.6 K, (b) 294.2 K, (c) 294.8 K, and (d) 295.7 K. (e) The measured domain periodicity as a function of temperature for the same $[\text{Pt}/\text{Co} (0.24 \text{ nm})]_2$ sample.

As noted in the discussion of Supplemental Video 1 in Ref. 34, the labyrinthine remanent morphology of our low-exchange FM/HM samples exhibits a significant degree of fluctuation when imaged near room temperature. To better understand the role that fluctuation plays in defining the temperature/thickness-induced morphological phase transition observed in our FM/HM samples, we have quantified the temperature dependence of the degree of fluctuation as follows: First, we collect 60-second-long videos at a capture rate of 16 Hz (*i.e.*, the highest time resolution available with our MOKE imaging system) at several different temperatures. Next, we binarize the greyscale MOKE images that comprise the video, such that the $+M_z/-M_z$ polarized regions correspond to purely black/white contrast. Taking the first collected frame as a reference, we then compare the image pixel states at subsequent times to initial reference frame to obtain the number of pixels that have changed their magnetic orientation relative to the initial state (*i.e.*, the number of pixels that have changed from black to white and *vice versa*) over time. A pixel fraction change is then determined dividing this count by the total number of pixels in the image. By this methodology, a pixel fraction change of 0.5 corresponds to a complete randomization of the pixel

states relative to the initial state, and thus, a randomization of the domain morphology pattern over the 60 s imaging timeframe. In Figure 5.11(a), we show how the pixel fraction change proceeds with time in the [Pt/ Co (0.24 nm)]₂ sample at a variety of different temperatures. Clearly, the amount of time needed for the pixel state to completely randomize relative to the initial state decreases dramatically with increasing sample temperature. As an alternative representation, we quantify the average pixel change fraction per video frame (*i.e.*, the change between any two images separated by the minimum sampling time) and find that it also dramatically increases with temperature [Figure 5.11(b)]. As can be seen in Figure 5.11(b), the fact that the average pixel change fraction per video frame extrapolates to 0.5 at roughly 296.5 K indicates that by this temperature, the domain structure is fluctuating faster than the temporal resolution of our microscope – possibly explaining the lack of magnetic contrast observed at higher temperatures. Given that these changes in the pixel state are representative of changes in the domain configuration, these measurements imply that the domain state both decreases in size and increasingly fluctuates with increasing temperature – both points of commonality with the SRT,^{65,68} but observed here in samples that have significant perpendicular magnetic anisotropy.

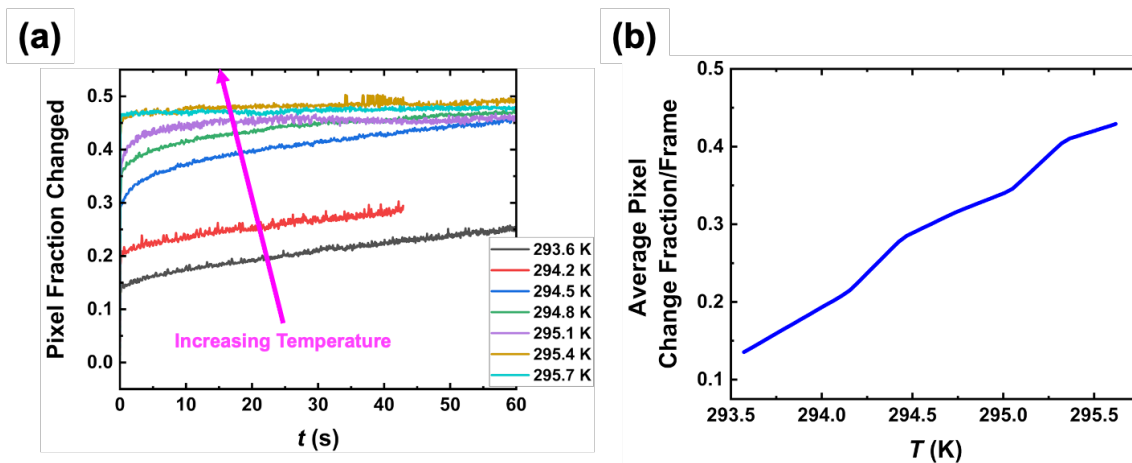


Figure 5.11: For a [Pt/ Co (0.24 nm)]₂ sample, (a) the pixel fraction changed as a function of time at various temperatures, and (b) the average pixel fraction change per frame as a function of temperature.

Having established that the fluctuations in our sample are increasing with temperature using the pixel fraction change metric, it is relevant to develop an understanding of what component of the domain morphology is fluctuating. To this end, we have taken videos of the remanent morphology collected at different temperatures and counted the number of times each specific pixel in the image changes its magnetic orientation over the 60 second duration of the video. By assigning a color scale to the number of switching events observed, “heatmaps” of switching activity were created. For clarity, these heatmaps have been overlaid onto the greyscale polar MOKE image collected at $t = 0$ s. In Figure 5.12(a), we show a heatmap for a video of the domain morphology collected at $T = 293.6$ K overlain to the initial state. It can clearly be seen that at this temperature, the pixels that experience the most switching events (and hence, are fluctuating the most) are strongly localized to the domain walls of the labyrinthine stripe domains. That is, the fluctuations in the system are fluctuations of the domain walls about their equilibrium positions. Increasing the temperature to $T = 294.8$ K, it can be seen that the fluctuating areas take up a larger fraction of the field of view. However, we previously demonstrated in Figure 5.10 that the domain periodicity decreases dramatically with increasing temperature. As this means that more domains are contained within the field of view at higher temperatures, this would also imply that a larger fraction of the imaging area is comprised of domain walls – enhancing the measured fluctuation with temperature. However, our present measurements make differentiating between a larger fraction of the sample fluctuating or an increased rate of fluctuation difficult. Using a measure of the variance in domain wall length normalized to the total length of domain walls in a system, past work has shown that an increased rate of domain wall fluctuation occurs in the vicinity of the SRT known to occur in the limit of low K_{eff} .⁶⁶

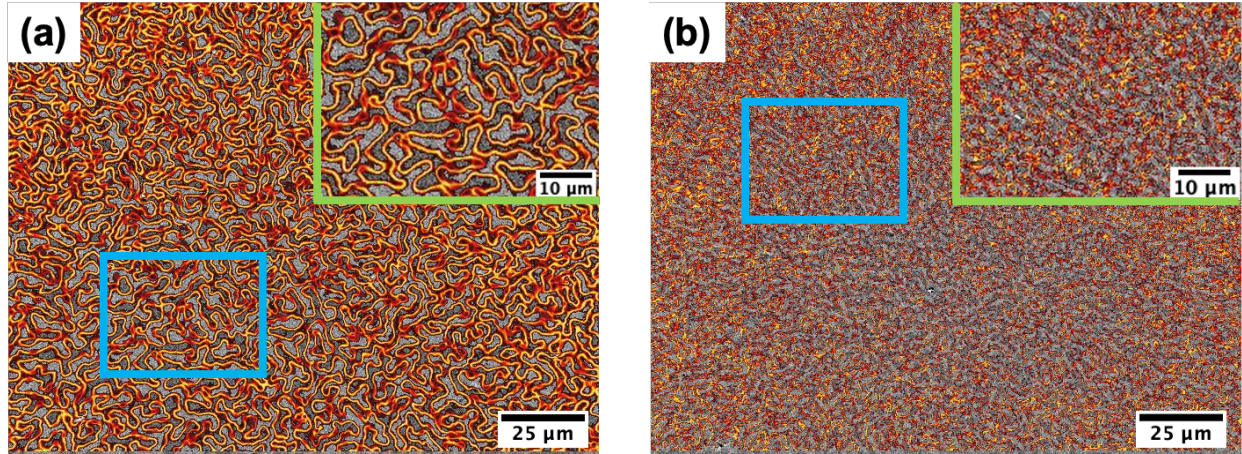


Figure 5.12: “Heatmaps” for a $[\text{Pt}/\text{Co} (0.24 \text{ nm})]_2$ sample, indicating the switching activity of each pixel over the course of 60 s of observation in zero applied magnetic field. Red areas correspond to areas that fluctuate the most, whereas yellow areas were found to fluctuate less. Regions that appear in greyscale did not significantly fluctuate over the course of the measurement. The heatmaps have been overlain on top of a greyscale polar MOKE image collected at the beginning of the measurement. (a) was collected at a temperature of 293.6 K, whereas (b) was collected at 294.8 K. The upper-right insets show the areas bordered in blue in greater detail.

While polar MOKE imaging permits the analyses discussed above, its temporal resolution is limited by the capture rate of the CCD camera (16 Hz), which limits the extent of the morphological phase transition we can study using optical measurements. To better understand the temporal fluctuations of our HM/FM systems, we have performed magnetic susceptibility measurements via the anomalous Hall effect (AHE) resistance of our samples.⁶⁹ The anomalous Hall effect (AHE) is yet another consequence of spin-orbit coupling,⁷⁰ and dictates that after subtracting out the ordinary Hall contribution, the measured Hall resistance of a magnetic sample is proportional its magnetization perpendicular to the film plane. In the simplest set of measurements, we have determined the dc susceptibility of the $[\text{Pt}/\text{Co} (0.24 \text{ nm})]_2$ sample by quasi-statically stepping the perpendicular magnetic field and measuring the Hall resistance, as shown in Figure 5.13(a). As noted in our previous discussion of similar samples’ perpendicular VSM hysteresis loops [Figure 5.3(a)], it can clearly be seen that the remanent magnetization is

dramatically suppressed with increasing temperature in this [Pt/Co (0.24 nm)]₂ sample. The susceptibility χ is calculated using the expression:

$$\chi = \left. \frac{dM}{dH} \right|_{H=0} \equiv \left. \frac{dR_{Hall}}{dH} \right|_{H=0}$$

Equation 5.2

where R_{Hall} is the Hall resistance, normalized such that it may be taken as a proxy for M . In simpler terms, the susceptibility is calculated as the slope of the hysteresis loop at $H = 0$. The temperature dependence of the dc susceptibility has shown great utility in probing magnetic phase transitions; when warming through the Curie temperature T_C (*i.e.*, the transition between ferromagnetic and paramagnetic phases), the Curie-Weiss law dictates that the susceptibility will exhibit a peak, followed by exponential decay.⁷¹ In Figure 5.13(b), we show $\chi(T)$, calculated from the data shown in Figure 5.13(a). It can be seen that $\chi(T)$ demonstrates non-monotonic behavior, reaching a peak susceptibility at $T \approx 290.5$ K. In a dc

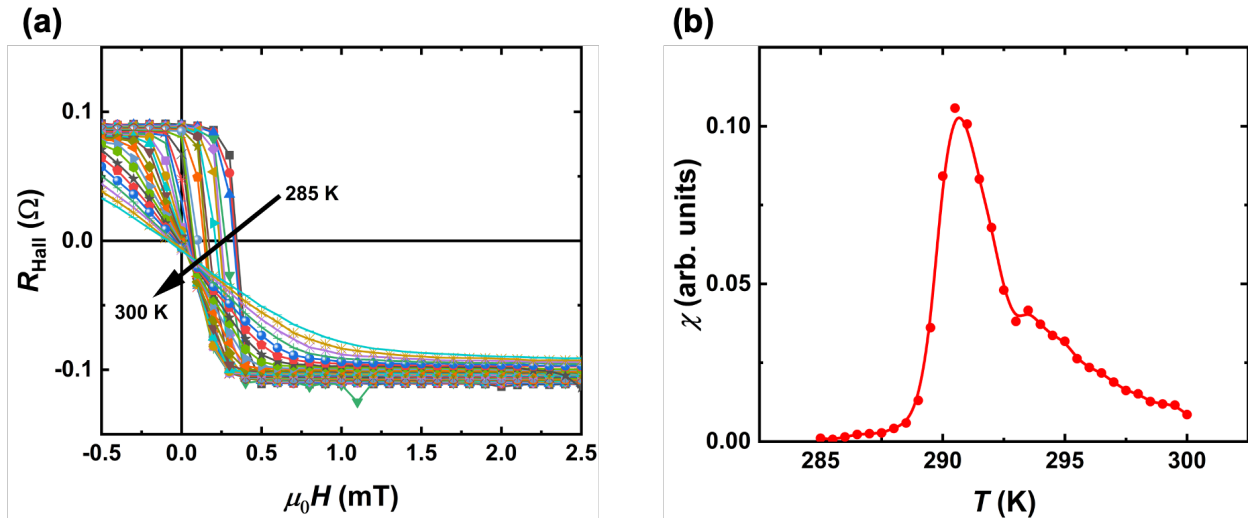


Figure 5.13: (a) Anomalous Hall resistance R_{Hall} as a function of perpendicular magnetic field for a [Pt/Co (0.24 nm)]₂ sample, patterned in to a 50 μm -wide wire using UV metal liftoff photolithography. Measurements were conducted over the temperature range of 285 K to 300 K, in 0.5 K increments. (b) dc susceptibility χ as a function of temperature for the same sample. χ was calculated from the R_{Hall} data shown in (a) using Equation 5.2.

susceptibility measurement, the temporal dynamics we are capable of probing are limited by how quickly the magnetic field can be swept and how long it takes to perform a resistance measurement; with our equipment, our temporal resolution is limited to the mHz range. Nonetheless, the appearance of a peak in the susceptibility data is consistent with the morphological phase transition previously described in this sample.

The true utility of susceptibility measurements often lies in so-called ac susceptibility measurements, whereby a time-varying magnetic field is used to induce a time-varying response in the sample's magnetization. Using a lock-in amplifier, it is possible to make a low-noise measurement of the Hall resistance that is only sensitive to the magnetic response that occurs at the same frequency as the ac drive field. Thus, by varying the frequency of the ac drive field, it is possible to probe the magnetization dynamics at different timescales. In Figure 5.14, we show temperature-dependent ac susceptibility measurements performed at several different frequencies. From Figure 5.14, it can be discerned that the susceptibility peak is shifted to higher temperatures at higher frequencies. This type of frequency dependence has previously been observed at the superparamagnetic phase transition in magnetic particles.⁷² In the limit of nano-scale particle sizes, each particle may become capable of only hosting one magnetic domain. Even if the monodomain particle exhibits uniaxial anisotropy, the energy barrier associated with switching the entire particle's magnetization between orientations along the anisotropy axis will be reduced on account of the particle's small volume. Thus, thermal energy can become sufficient to initiate a spontaneous switching of the magnetic orientation. Because this spontaneous magnetization fluctuation occurs below the Curie temperature (*i.e.*, when the particle would be expected to be ferromagnetic), this behavior has been termed superparamagnetism. The temperature at which the

susceptibility exhibits a peak corresponds to the temperature where the hysteresis in the $M(H)$ loop matches the magnitude of the AC magnetic field.

Mathematically, Néel described the timescales associated with the fluctuating magnetization of superparamagnetic particles in the framework of an Arrhenius law, given as:⁷³

$$\tau_N = \tau_0 e^{E_B/k_B T}$$

Equation 5.3

where τ_N is the mean time required for a superparamagnetic particle's magnetization to switch between orientations along the easy-axis, τ_0 is a material-specific attempt period, E_B is the energy barrier to switching magnetic orientations along the easy axis, and k_B is the Boltzmann constant. From Equation 5.3, it can be seen that the timescale at which superparamagnetic fluctuations occur varies exponentially with temperature. A superparamagnetic particle whose magnetic orientation does not change between measurements conducted at a fixed frequency is said to be “blocked”; a so-called blocking temperature separates the fluctuating superparamagnetic phase from thermally stable, more typical ferromagnetic behavior. In an ac susceptibility measurement, the ac drive field is typically small in magnitude, such that it slightly biases the switching behavior. Thus, by scanning the sample temperature and measuring the ac susceptibility at different fixed frequencies, it is possible to understand how the fluctuation timescales vary with temperature.

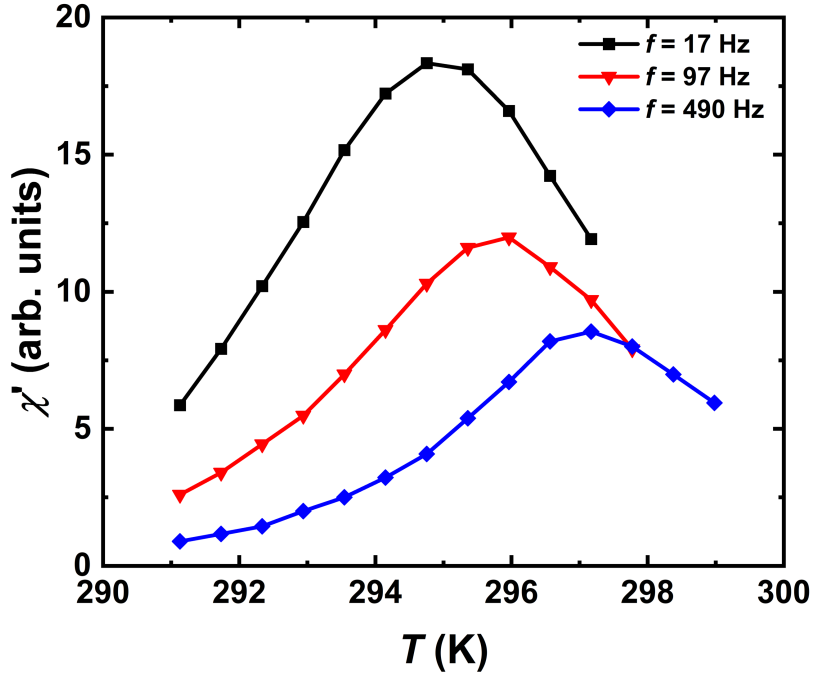


Figure 5.14: ac susceptibility measurements of a [Pt/Co(0.24 nm)]₂ sample, collected at several different frequencies. The amplitude of the sinusoidal ac field used during the measurements was ~0.3 mT. To measure the Hall resistance (and obtain the susceptibility using Equation 5.2), a sensing current of 10 μ A was used.

In the context of the SRT, ac susceptibility measurements of single crystal samples have demonstrated behavior similar to that observed during the superparamagnetic phase transition.⁷⁴ Namely, that the ac susceptibility exhibits a peak in the vicinity of the temperature induced SRT, and that the peak position moves to higher temperatures with increasing measurement frequencies. This is consistent with the characteristic frequency of fluctuation increasing with increasing temperature. Nonetheless, given the dearth of information on the dynamic susceptibility of thin films near the SRT, it is challenging to fully contextualize the ac susceptibility results for the [Pt/Co(0.24 nm)]₂ sample. In previous sections of this chapter, we argued that the energy landscape of our FM/HM samples is scaled by the anisotropy K via its dependence on M_s , as opposed to the anisotropy field. As such, it could reasonably be expected that the quantity KV in Equation 5.3

(which represents the energy barrier to switching magnetic orientation along the easy axis in a superparamagnetic particle) will be reduced as the sample temperature is increased just from a change in K . However, while Equation 5.3 was originally derived to describe nanoparticles with a well-defined volume, assigning a similar characteristic volume to our thin film systems becomes somewhat more complicated. Considering that the domain wall is expected to fluctuate between pinning sites in the sample, the area swept out by the domain wall during this fluctuation multiplied by the sample thickness would give a characteristic volume.^{65,75} If the pinning sites arise due to variations in the anisotropy, K can be replaced by ΔK , which is the difference in anisotropy between the pinning site and the area swept by the domain wall. The product of ΔK and this volume gives an energy scale that sets the probability of thermal fluctuation of the domain wall. Given that we have inferred a reduced exchange stiffness A_{ex} in our FM/HM samples, this would also imply a reduction in the exchange length l_{ex} , which defines the length scale over which ferromagnetic exchange dictates the magnetic properties of a solid.⁷⁶ Given this, it is possible that the characteristic volume over which ferromagnetic exchange acts is scaling with temperature as well, which would also have an impact on the fluctuation dynamics – that is, the energy scale will decrease with increasing temperature. Indeed, past work has shown that the depinning temperature – which sets the characteristic energy barrier between a static and thermally-fluctuating domain wall – decreases dramatically in the limit of ultrathin FM layers.⁷⁷

By applying Equation 5.3 to the data shown in Figure 5.14, a change in temperature alone cannot explain the variation in characteristic fluctuation timescales we are seeing. Namely, if it is assumed that E_B does not change dramatically when the temperature is varied by several K, a < 1 % variation of the thermal energy cannot be responsible for the thirty-fold change in the characteristic fluctuation frequency observed in Figure 5.14. In the context of work presented

earlier in this chapter, the dramatic change in E_B with temperature needed to explain such a variation in fluctuation frequency strongly mimics the trends in DW energy density in the limit of low exchange stiffness. Nonetheless, additional work – including ac susceptibility measurements at higher frequencies and the use of imaging or scattering techniques with higher spatial and temporal resolution – is needed to better understand the dynamics of the morphological phase transition observed in our FM/HM thin films.

5.6 Conclusion

In summary, we have experimentally characterized the domain morphologies present in a number of thin film heterostructures with perpendicular magnetic anisotropy, modest interfacial Dzyaloshinskii-Moriya interaction energy density, and low exchange stiffness. We find that by lowering the exchange stiffness, the remanent domain morphology transitions from a uniform state to a labyrinthine stripe phase – drawing strong, yet nuanced parallels to previous work on the spin reorientation transition that occurs in the limit of vanishing perpendicular magnetic anisotropy. Furthermore, when a small perpendicular magnetic field is applied at this morphological transition, skyrmion phases become stabilized. Spin-orbit torque-induced motion is observed when an electrical current is passed through the samples. Micromagnetic and analytic modeling demonstrates that in the limit of low exchange stiffness, the presence of a moderate interfacial Dzyaloshinskii-Moriya interaction modifies the energetic balance of thin films, allowing for the formation of multidomain remanent states and a shallowing of the energy barrier separating the stripe and skyrmion ground states. A further understanding of the spatiotemporal dynamics of the morphological phase transition is an ongoing effort, but our preliminary results draw strong parallels with previous work on the superparamagnetic phase transition.

Chapter 5, in part, contains a reprint of research published as “Skyrmion stabilization at the domain morphology transition in ferromagnet/heavy metal heterostructures with low exchange stiffness” by J.A. Brock and E.E. Fullerton in *Advanced Materials Interfaces* (2021). The dissertation author was the primary investigator and author of the manuscript. This work was supported by the National Science Foundation, Division of Materials Research (Award #: 2105400).

5.7 References

- ¹ A. Fert, *Mat. Sci. Forum* **59-60**, 439 (1990).
- ² J. Sampaio, V. Cros, S. Rohart, A. Thiaville, A. Fert, *Nature Nanotech.* **8**, 839 (2013).
- ³ A. Soumyanaryanan, N. Reyren, A. Fert, C. Panagopoulos, *Nature* **539**, 509 (2016).
- ⁴ C. Moreau-Luchaire, C. Moutafis, N. Reyren, J. Sampaio, C.A.F. Vaz, N. Van Horne, K. Bouzehouane, K. Garcia, C. Deranlot, P. Warnicke, P. Wohluter, J.-M. George, M. Weigand, J. Raabe, V. Cros, A. Fert, *Nature Nanotech.* **11**, 444 (2016).
- ⁵ S. Woo, K. Litzius, B. Kruger, M. -Y. Im, L. Caretta, K. Richter, M. Mann, A. Krone, R. M. Reeve, M. Weigand, P. Agrawal, I. Lemesh, M.-A. Mawass, P. Fischer, M. Klaui, G.S.D. Beach, *Nature Mater.* **15**, 501 (2016).
- ⁶ K. Everschor-Sitte, J. Masell, R.M. Reeve, M. Klaui, *J. Appl. Phys.* **124**, 240901 (2018).
- ⁷ R. Allenspach, A. Bischof, *Phys. Rev. Lett.* **69**, 3385 (1992).
- ⁸ Z.Q. Qiu, J. Pearson, S. D. Bader, *Phys. Rev. Lett.* **70**, 1006 (1993).
- ⁹ K. Fukumoto, H. Daimon, L. Chelaru, F. Offi, W. Kuch, J. Kirschner, *Surf. Sci.* **514**, 151 (2002).
- ¹⁰ C. Won, Y.Z. Wu, J. Choi, W. Kim, A. Scholl, A. Doran, T. Owens, J. Wu, X.F. Jin, H.W. Zhao, Z.Q. Qiu, *Phys Rev. B* **71**, 224429 (2005).
- ¹¹ R. Tolley, S.A. Montoya, and E.E. Fullerton, *Phys. Rev. Mat.* **2**, 044404 (2018).

-
- ¹² W. Jiang, P. Upadhyaya, W. Zhang, G. Yu, M.B. Jungfleisch, F.Y. Fradin, J.E. Pearson, Y. Tserkovnyak, K.L. Wang, O. Heinonen, S.G.E. te Velthuis, A. Hoffmann, *Science* **349**, 283 (2015).
- ¹³ K. Gaurav Rana, A. Finco, F. Fabre, S. Chouaieb, A. Haykal, L. D. Buda-Prejbeanu, O. Fruchart, S. Le Denmat, P. David, M. Belmeguenai, T. Denneulin, R.E. Dunin-Borkowski, G. Gaudin, V. Jacques, O. Boulle, *Phys. Rev. Appl.* **13**, 044079 (2020).
- ¹⁴ S. Sugimoto, W. Koshibae, S. Kasai, N. Ogawa, Y. Takahashi, N. Nagaosa, Y. Tokura, *Sci. Rep.* **10**, 1009 (2020).
- ¹⁵ M. He, G. Li, Z. Zhu, Y. Zhang, L. Peng, R. Li, J. Li, H. Wei, T. Zhao, X.-G. Zhang, S. Wang, S.-Z. Lin, L. Gu, G. Yu, J.W. Cai, B.-G. Shen, *Phys. Rev. B* **97**, 174419 (2018).
- ¹⁶ S.-G. Je, D.-H. Kim, S.-C. Yoo, B.-C. Min, K.-J. Lee, S.-B. Choe, *Phys. Rev. B* **88**, 214401 (2013).
- ¹⁷ S. Rohart, A. Thiaville, *Phys. Rev. B* **88**, 184422 (2013).
- ¹⁸ F. Buttner, I. Lemesch, G. S. D. Beach, *Sci. Rep.* **8**, 4464 (2018).
- ¹⁹ C. Liu, S.D. Bader, *J. Appl. Phys.* **67**, 5758 (1990).
- ²⁰ D. Li, R. Cuenya, J. Pearson, S.D. Bader, W. Keune, *Phys. Rev. B* **64**, 144410 (2001).
- ²¹ J.B. Sousa, M.R. Chaves, M.F. Pinheiro, R.S. Pinto, *J. Low Temp. Phys.* **18**, 125 (1974).
- ²² M.W. Keller, K. S. Gerace, M. Arora, E.K. Delczeg-Czirjak, J.M. Shaw, T.J. Silva, *Phys. Rev. B* **99**, 214411 (2019).
- ²³ A.G. Kozlov, A.G. Kolesnikov, M.E. Stebliy, A.P. Golikov, A.V. Davydenko, *Phys. Rev. B* **102**, 144411 (2020).
- ²⁴ <http://www.aprex-solutions.com/en/>
- ²⁵ A. Vansteenkiste, J. Leliaert, M. Dvornik, M. Helsen, F. Garcia-Sanchez, B. Van Waeyenberge, *AIP Adv.* **4**, 107133 (2014).
- ²⁶ S. Bandiera, R. C. Sousa, B. Rodmacq, B. Dieny, *IEEE Mag. Lett.* **2**, 3000504 (2011).
- ²⁷ A.W.J. Wells, P.M. Shepley, C.H. Marrows, T.A. Moore, *Phys. Rev. B* **95**, 054428 (2017).
- ²⁸ R. Soucaille, M. Belmeguenai, J. Torrejon, J.-V. Kim, T. Devolder, Y. Roussigne, S.-M. Cherif, A.A. Stashkevich, M. Mayashi, J.-P. Adam, *Phys. Rev. B* **94**, 104431 (2016).

-
- ²⁹ K. Shahbazi, J.-V. Kim, H. T. Nembach, J.M. Shaw, A. Bischof, M.D. Rossell, V. Jeudy, T.A. Moore, C.H. Marrows, *Phys. Rev. B* **99**, 094409 (2019).
- ³⁰ J.A. Brock, M.D. Kitcher, P. Vallobra, R. Medapalli, M.P. Li, M. De Graef, G.A. Riley, H.T. Nembach, S. Mangin, V. Sokalski, E.E. Fullerton, *Adv. Mat.* **33**, 2105124 (2021).
- ³¹ Y. Zhou, R. Mansell, S. Valencia, F. Kronast, S. Van Dijken, *Phys.Rev. B* **101**, 054433 (2020).
- ³² H.T. Nembach, J.M. Shaw, M. Weiler, E. Jue, T.J. Silva, *Nat. Phys.* **11**, 825 (2015).
- ³³ I. A. Yastremsky, O. M. Volkov, M. Kopte, T. Kosub, S. Stienen, K. Lenz, J. Lindner, J. Fassbender, B. A. Ivanov, D. Makarov, *Phys. Rev. Appl.* **12**, 064038 (2019).
- ³⁴ J.A. Brock and E.E. Fullerton, <https://arxiv.org/abs/2108.10973> (2021).
- ³⁵ L. Liu, C.-F. Pai, Y. Li, H. W. Tseng, D. C. Ralph, R. A. Buhrman, *Science* **336**, 555 (2012).
- ³⁶ M. Althammer, S. Meyer, H. Nakayama, M. Schreier, S. Altmannshofer, M. Weiler, H. Huebl, S. Geprags, M. Opel, R. Gross, D. Meier, C. Klewe, T. Kuschel, J.-M. Schmalhorst, G. Reiss, L. Shen, A. Gupta, Y.-T. Chen, G.E.W. Bauer, E. Saitoh, S.T.B. Goennenwein, *Phys. Rev. B* **87**, 224401 (2013).
- ³⁷ S. Woo, M. Mann, A. J. Tan, L. Caretta, G. S. D. Beach, *Appl. Phys. Lett.* **105**, 212404 (2014).
- ³⁸ N. Nagaosa, Y. Tokura, *Nat. Nanotechnol.* **8**, 899 (2013).
- ³⁹ K. Everschor-Sitte, M. Sitte, *J. Appl. Phys.* **115**, 172602 (2014).
- ⁴⁰ W. Jiang, X. Zhang, G. Yu, W. Zhang, X. Wang, M.B. Jungfleisch, J.E. Pearson, X. Cheng, O. Heinonen, K.L. Wang, Y. Zhou, A. Hoffmann, S.G.E. te Velthuis, *Nat. Phys.* **13**, 162 (2017).
- ⁴¹ F. Ajejas, V. Krizakova, D. De Souza Chaves, J. Vogel, P. Perna, R. Guerrero, A. Gudin, J. Camareno, S. Pizzini, *Appl. Phys. Lett.* **111**, 202402 (2017).
- ⁴² S. Pizzini, J. Vogel, S. Rohart, L. Buda-Prejbeanu, E. Jue, O. Boulle, I. Miron, C. Safeer, S. Auffret, G. Gaudin, A. Thiaville, *Phys. Rev. Lett.* **113**, 047203 (2014).
- ⁴³ M. Belmeguenai, J.-P. Adam, Y. Roussigne, S. Eimer, T. Devolder, J.-V. Kim, S. Cherif, A. Stashkevich, A. Thiaville, *Phys. Rev. B* **91**, 180405(R) (2015).
- ⁴⁴ J. Cho, N.-H. Kim, S. Lee, J.-S. Kim, R. Lavrijsen, A. Solignanc, Y. Yin, D.-S. Han, N. J. J. van Hoof, H. J. M. Swagten, B. Koopmans, C.-Y. You, *Nat. Comm.* **6**, 7635 (2015).
- ⁴⁵ N.-H. Kim, J. Jung, J. Cho, D.-S. Han, Y. Yin, J.-S. Kim, H. J. M. Swagten, C.-Y. You, *Appl. Phys. Lett.* **108**, 142406 (2016).

-
- ⁴⁶ J.A. Brock, P. Vallobra, R.D. Tolley, S.A. Montoya, S. Mangin, E.E. Fullerton, *Phys. Rev. B* **102**, 024443 (2020).
- ⁴⁷ P. Jadaun, L. F. Register, S. K. Banerjee, *npj Comput. Mater.* **6**, 88 (2020).
- ⁴⁸ A. Soumyanarayanan, M. Raju, A. L. Gonzalez Oyarce, A. K. C. Tan, M.-Y. Im, A. P. Petrovic, P. Ho, K. H. Khoo, M. Tran, C. K. Gan, F. Ernult, C. Panagopoulos, *Nat. Mater.* **16**, 898 (2017).
- ⁴⁹ L. Fallarino, B. J. Kirby, E. E. Fullerton, *J. Phys. D: Appl. Phys.* **54**, 303002 (2021).
- ⁵⁰ H. Y. Kwon, C. Won, *J. Magn. Magn. Mater.* **351**, 8 (2014).
- ⁵¹ T. Eimuller, T. C. Ulbrich, E. Amaladass, I. L. Guhr, T. Tylizszczak, M. Albrecht, *Phys. Rev. B* **77**, 134415 (2008).
- ⁵² S. Okamoto, N. Kikuchi, M. Furata, O. Kitakami, T. Shimatsu, *Phys. Rev. Lett.* **109**, 237209 (2012).
- ⁵³ Y. Yoshimura, K.-J. Kim, T. Taniguchi, T. Tono, K. Ueda, R. Hiramatsu, T. Moriyama, K. Yamada, Y. Nakatani, T. Ono, *Nat. Phys.* **12**, 157 (2016).
- ⁵⁴ C. Kittel, *Phys. Rev.* **70**, 965 (1946).
- ⁵⁵ C. Kittel, *Rev. Mod. Phys.* **21**, 541 (1949).
- ⁵⁶ P. Agrawal, F. Buttner, I. Lemesh, S. Schlotter, G.S.D. Beach, *Phys. Rev. B* **13**, 319 (2007).
- ⁵⁷ C. Kooy, U. Enz, *Philips Res. Rep.* **15**, 7 (1960).
- ⁵⁸ A. Thiaville, *J. Magn. Magn. Mater.* **140**, 877 (1995).
- ⁵⁹ R. Moreno, R.F.L. Evans, S. Khmelevskyi, M.C. Munoz, R.W. Chantrell, O. Chubykalo-Fesenko, *Phys. Rev. B* **94**, 104433 (2016).
- ⁶⁰ S. Schlotter, P. Agrawal, G.S.D. Beach, *Appl. Phys. Lett.* **113**, 092402 (2018).
- ⁶¹ I. Lemesh, F. Buttner, G.S.D. Beach, *Appl. Phys. Lett.* **113**, 0092402 (2018).
- ⁶² I. Lemesh, K. Kitzius, M. Bottcher, P. Bassirian, N. Kerber, D. Heinze, J. Zazvorka, F. Buttner, L. Caretta, M. Mann, M. Weigand, S. Finizio, J. Raabe, M.-Y. Im, H. Stoll, G. Schutz, B. Dupe, M. Klaui, G.S.D. Beach, *Adv. Mater.* **30**, 1805461 (2018).
- ⁶³ R. Allenspach, *J. Magn. Magn. Mater.* **129**, 160 (1994).

-
- ⁶⁴ M. Carubelli, O.V. Billoni, S.A. Pighin, S.A. Cannas, D.A. Stariolo, F.A. Tamarit, *Phys. Rev. B* **77**, 134417 (2008).
- ⁶⁵ N. Bergeard, J.P. Jamet, A. Mougin, J. Ferre, J. Gierak, E. Bourhis, R. Stamps, *Phys. Rev. B* **86**, 094431 (2012).
- ⁶⁶ M. Kronseder, T.N.G. Meier, M. Zimmerman, M. Buchner, M. Vogel, C.H. Back, *Nature Comm.* **6**, 6832 (2015).
- ⁶⁷ A.B. Kashuba, V.L. Pokrovsky, *Phys. Rev. B* **48**, 10335 (1993).
- ⁶⁸ T.N.G. Meier, M. Kronseder, M. Zimmermann, and C.H. Back, *Phys. Rev. B* **93**, 064424 (2016).
- ⁶⁹ Y. Nishitani, D. Chiba, F. Matsukura, and H. Ohno, *J. Appl. Phys.* **105**, 07C516 (2009)
- ⁷⁰ N. Nagaosa, J. Sinova, S. Onoda, A.H. MacDonald, and N.P. Ong, *Rev. Mod. Phys.* **82**, 1539 (2010).
- ⁷¹ N. Spaldin, *Magnetic Materials: Fundamentals and Applications (2nd Edition)*, Cambridge University Press (2010).
- ⁷² B. Bittova, J. Poltiero, V. Vejpravova, M.P. Morales, A.G. Roca, and A. Mantlikova, *J. Magn. Mater.* **324**, 1182 (2012).
- ⁷³ L. Néel, *Ann. Geophys.* **5**, 99 (1949).
- ⁷⁴ G. Song, J. Jiang, B. Kang, J. Zhang, Z. Cheng, G. Ma, and S. Cao, *Solid State Comm.* **211**, 47 (2015).
- ⁷⁵ E.E. Ferrero, L. Foini, T. Giamarchi, A.B. Kolton, and A. Rosso, *Ann. Rev. Condens. Matter Phys.* **12**, 111 (2021).
- ⁷⁶ J. Dubowik and I. Goscianska, *Acta Phys. Polon. A* **127**, 147 (2015).
- ⁷⁷ V. Jeudy, A. Mougin, S. Bustingorry, W. S. Torres, J. Gorchon, A.B. Kolton, A. Lemaitre, J.-P. Jamet, *Phys. Rev. Lett.* **117**, 057201 (2016).

Chapter 6: Dynamic Symmetry Breaking in Chiral Magnetic Systems

6.1 Introduction

In this chapter, we report on a combined experimental and theoretical study of the magnetic reversal properties of Co/Ni/Pt-based thin-film multilayers with iDMI in response to both in- and out-of-plane magnetic fields. When imaging the reversal behavior, we observe domain growth directionalities that have not previously been reported. Specifically, we find that when the multilayers reverse via dendritic stripe domains, the domain growth is highly anisotropic, and the growth direction changes dramatically depending on the strength of the in-plane field. Furthermore, the growth direction symmetries observed when changing the sign of the in- and out-of-plane fields require a breaking of time-reversal mirror symmetry along both the horizontal and vertical planes that cannot be explained from static energies alone. We posit that the observed domain growth behaviors arise from a dynamic symmetry breaking during domain expansion. Our calculations of the steady-state dynamical reorientation of the DW magnetization profile and the associated changes in the dispersive stiffness permit a quantitative understanding of the experimentally observed behaviors.

6.2 Experimental Techniques

Multilayer stacks of the structure Ta(3)/ Pt(3)/ [Co(0.7)/ Ni(0.5)/ Pt(0.7)]_N/ Ta(3) (thicknesses in nm) were grown on Si substrates with a 300 nm-thick thermal oxide coating by dc

magnetron sputtering, using a power of 50 W in a 3 mTorr Ar pressure. The number of [Co/Ni/Pt] repetitions N was varied between 1 and 5. Our choice of materials was motivated by reports that Pt/Co and Pt/Ni interfaces are predicted to have different signs of iDMI,¹ such that an additive iDMI may be achieved when they are incorporated in a structurally asymmetric Pt/Co/Ni/Pt heterostructure.²

The static magnetic properties were determined using the vibrating sample magnetometry technique at room temperature in both the in-plane and perpendicular geometries. To image the directionality of domain growth, we used a MOKE imaging platform manufactured by Evico Magnetics, configured for polar MOKE sensitivity. Perpendicular magnetic field pulses that were 5 ms-long and 15 mT-strong were used to nucleate and expand the magnetic domains. The static in-plane magnetic fields were varied in magnitude and direction between 0 and 320 mT. As is standard for MOKE imaging, the micrographs presented herein were collected using a background subtraction of the signal when the sample magnetization was fully saturated. Unless otherwise stated, the sample magnetization was saturated opposite to the intended perpendicular field pulse direction between trials. Fresnel-mode Lorentz transmission electron microscopy (LTEM) was performed on an aberration-corrected FEI Titan G2 80-300 operated in Lorentz mode at room temperature. Samples for LTEM measurements were grown on 30 nm-thick SiN windows. Brillouin light scattering (BLS) spectroscopy was performed in the Damon-Eshbach geometry in both field polarities, using a six-pass Fabry-Perot interferometer with the 532 nm-wavelength laser beam incident on the sample at an angle of $\pi/4$. Detailed information on the BLS instrumentation and the methodology of using BLS to determine the iDMI energy density can be found elsewhere.³

6.3 Experimental Results

Hysteresis loops for samples with a varying number of [Co(0.7 nm)/ Ni(0.5 nm)/ Pt(0.7 nm)] repetitions N are shown in Figure 6.1. All samples exhibit strong perpendicular magnetic anisotropy, characterized by a full remanence at zero field in the perpendicular measurement geometry. Loops collected in the in-plane geometry demonstrate that the in-plane saturation field $\mu_0 H_s$ does not change dramatically with N . Given that all samples exhibit a similar $\mu_0 H_s$ (~ 1 T) and saturation magnetization M_s (~ 1000 kA/m), the effective perpendicular magnetic anisotropy energy density K_{eff} of $\sim 5 \times 10^5$ J/m³ is only altered by $< 10\%$ over the range of $1 \leq N \leq 5$.

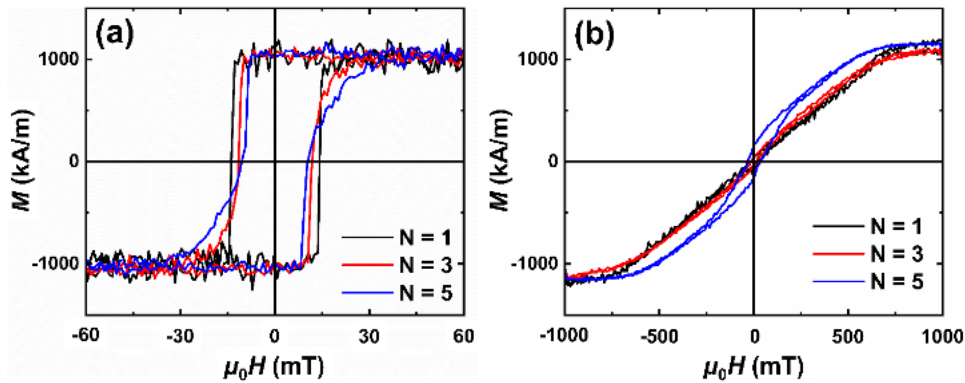


Figure 6.1: Room temperature magnetic hysteresis loops of the [Co(0.7 nm)/ Ni(0.5 nm)/ Pt(0.7 nm)] _{N} samples collected in the (a) out-of-plane and (b) in-plane geometries using vibrating sample magnetometry.

Polar MOKE images of the $N = 2$ sample shown in Figures 5.2(a-d) illustrate that this sample reverses via large, nearly circular domains. Figure 5.2(a) shows that the domains expand isotropically in the absence of a symmetry-breaking in-plane magnetic field. In agreement with previous reports on systems with iDMI,^{4,5,6,7,8,9,10,11} a mild growth asymmetry is present when an in-plane magnetic field is applied, and the favored growth direction is antiparallel to $\mu_0 H_x$ [Figures

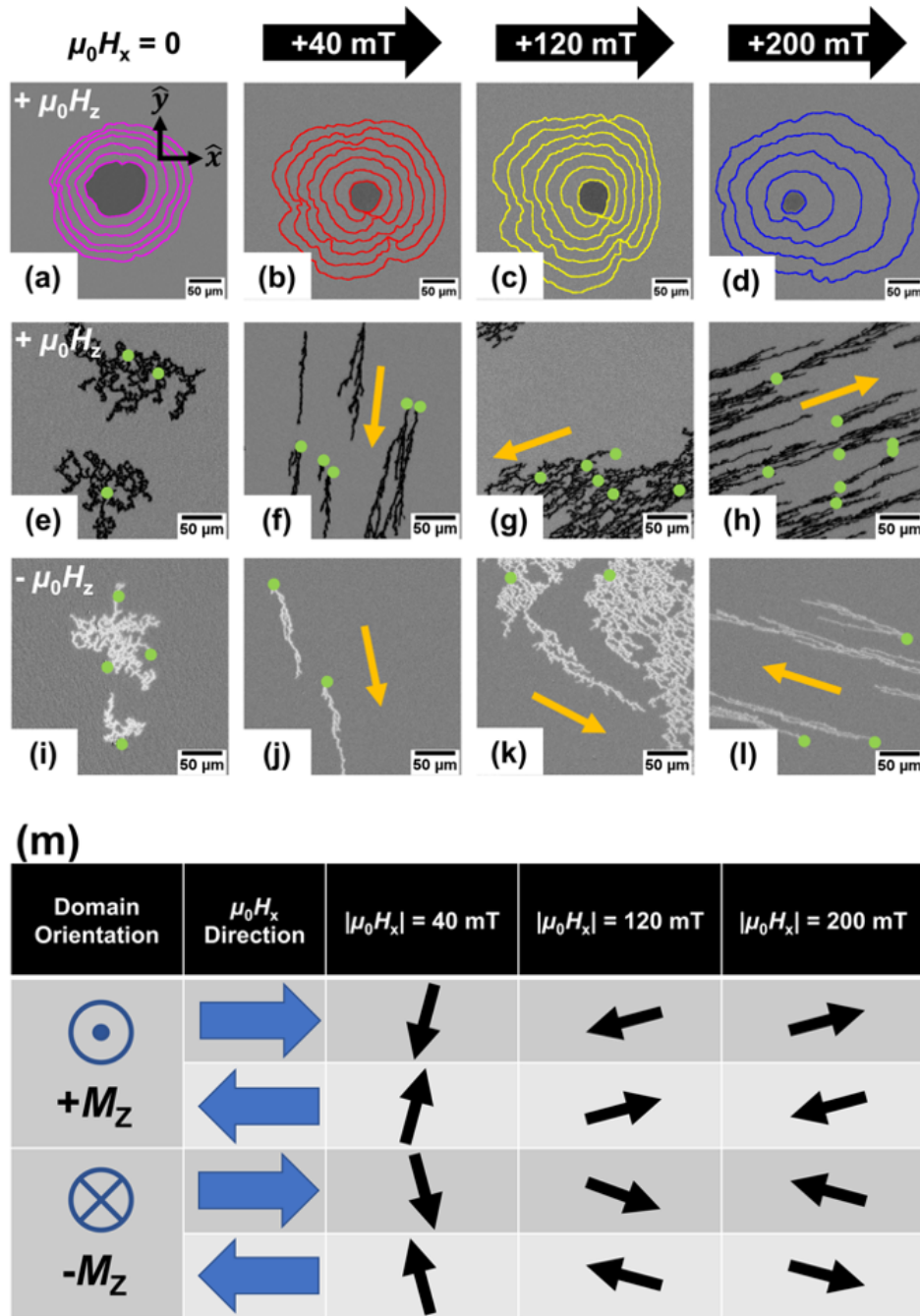


Figure 6.2: Polar MOKE images of magnetic domain growth in the [Co/Ni/Pt]₂ (a-d) and [Co/Ni/Pt]₃ (e-l) samples in response to 5 ms-long, 15 mT-strong out-of-plane (a-h) and into-plane (i-l) magnetic field pulses, collected in static in-plane magnetic fields of $\mu_0 H_x$ of 0 (a,e,i), +40 mT (b,f,j), +120 mT (c,g,k), and +200 mT (d,h,l). (m) The favored growth direction of dendritic stripe domains in the [Co/Ni/Pt]₃ sample for different permutations in domain orientation and in-plane field magnitudes and directions. Each colored ring in (a-d) represents the extend of the domain after three perpendicular field pulses were applied. The images in (e-l) were collected after three magnetic field pulses were applied, while the green markers represent the initial nucleation sites of reverse domains.

5.2(b,c)]. Knowing the perpendicular orientation of the domain, this is consistent with a left-handed Néel chirality, as observed in other Pt/Co/Ni-type systems.^{6,7}

The velocity v of \uparrow to \downarrow and \downarrow to \uparrow DWs as a function of in-plane applied field $\mu_0 H_x$ was determined for the $N = 2$ sample using the process employed by Je *et al.*,⁴ and later used by many others. These velocity curves are shown in Figure 6.3. In Figure 6.3, each type of DW exhibits a respective minimum in velocity depending on the direction in which $\mu_0 H_x$ is applied. By calculating the field at which this minimum in velocity occurs ($\mu_0 H_{DMI}$), the iDMI energy density (D_{DMI}) can be determined using the expression:

$$D_{DMI} = \mu_0 H_{DMI} M_S \sqrt{\frac{A}{K_{eff}}}$$

Equation 6.1

Save for the exchange stiffness A , all other parameters have previously been defined. From the data shown in Figure 6.3, we have extracted a $\mu_0 H_{DMI}$ of 120 mT, which for the material parameters of the $N = 2$ sample corresponds to $D_{DMI} = -0.63$ mJ/m². The left-handed D_{DMI} is inferred from the configuration (*i.e.*, \uparrow to \downarrow versus \downarrow to \uparrow) of the DWs and the $\mu_0 H_x$ direction. Throughout this work, a negative value of D denotes a left-handed chirality.

For higher magnitude in-plane fields, the favored growth direction reverses, as shown in Figure 6.2(d). There have been similar reports of the high-energy side of a bubble domain growing faster than its low-energy counterpart above a threshold in-plane field strength.^{7,8,11} Subsequently, it was analytically and micromagnetically demonstrated that in systems with iDMI, the elastic energy of the DW (which governs motion in the creep regime) differs significantly from the linear DW energy generally employed in DW creep models.⁷ As such, this behavior in the [Co/Ni/Pt]₂ sample can be explained within the context of surface stiffness in the long-wavelength regime. In

Figure 6.4, we plot the 1D elastic energy σ and the long-wavelength stiffness $\tilde{\sigma}$ of a $+M_z$ domain in the $N = 2$ sample as a function of in-plane applied magnetic field strength (σ and

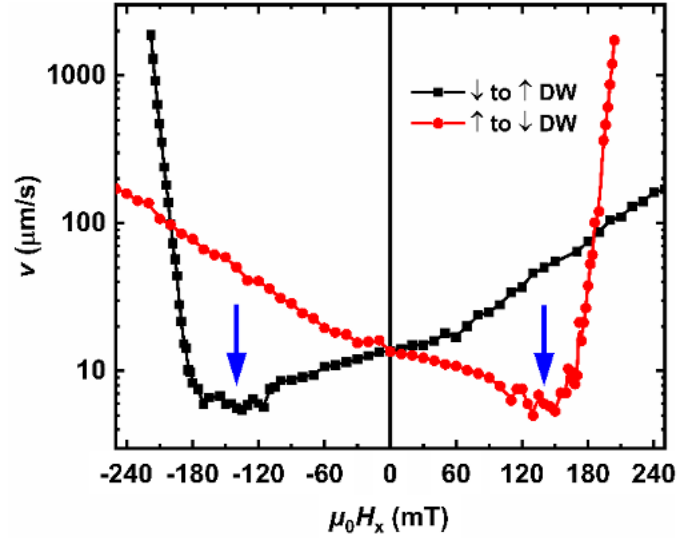


Figure 6.3: Expansion velocity as a function of in-plane magnetic field $\mu_0 H_x$ of \uparrow to \downarrow and \downarrow to \uparrow domain walls in the $[\text{Co/Ni/Pt}]_2$ sample. Data was collected using 5 ms-long perpendicular field pulses of 15 mT. Blue arrows indicate the commonly attributed measure of the effective magnetic field generated by the iDMI $\mu_0 H_{\text{DMI}}$.

$\tilde{\sigma}$ are defined and discussed in greater detail in subsequent sections of this chapter. In Figure 6.4, we consider the situations in which the domain wall normal is parallel and opposite to the applied in-plane field axis. Under the treatment of elastic stiffness in the long-wavelength regime, the onset of “unphysical” stiffness values roughly corresponds to the $\mu_0 H_x$ values at which a reversal in the circular domain growth direction was experimentally found to occur in the $[\text{Co/Ni/Pt}]_2$ sample [Figures 6.2(a-d)].

In agreement with the quasi-static magnetometry data, the samples with $N \geq 3$ reverse via dendritic stripe domains, as shown for the $[\text{Co/Ni/Pt}]_3$ sample in Figures 6.2(e-h). Much like the circular domains in the samples with $N = 1$ or 2, the growth of these ~ 3 μm -wide stripe domains

is nearly isotropic when $\mu_0 H_x = 0$, as shown in Figure 6.2(e). The green dots show the initial nucleation sites of the dendritic domains in Figures 6.2(e-1). This lack of a favored growth direction persists until $\mu_0 H_x = +40$ mT, at which point the domains exhibit a strong directionality to their

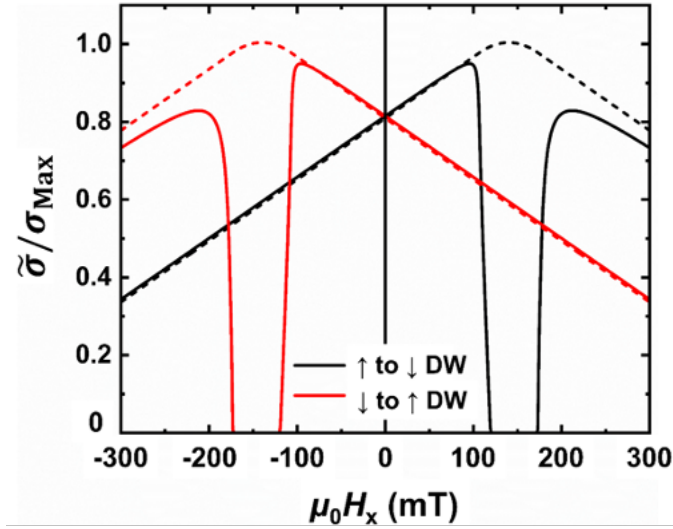


Figure 6.4: The long-wavelength stiffness $\tilde{\sigma}$ (solid lines) and 1D linear DW energy density σ (dashed lines) of a domain wall as a function of in-plane applied magnetic field $\mu_0 H_x$ for \uparrow to \downarrow and \downarrow to \uparrow domain walls in the $[\text{Co/Ni/Pt}]_2$ sample. The $\tilde{\sigma}$ and σ have been normalized to the resting energy of a Bloch domain wall σ_0 .

growth, as opposed to the mild asymmetry seen for the same field in the circular domains; that is, once nucleated, the domains prefer to grow in one specific direction, as indicated by the arrows in Figures 6.2(f-1). Surprisingly, the favored growth direction is nearly perpendicular to the $\mu_0 H_x$ axis for modest in-plane fields – growth behavior that would not be expected from the chiral Néel-type DWs favored by the iDMI. From Lorentz TEM images of $[\text{Co/Ni/Pt}]_5$ multilayers collected in the absence of applied fields [Figure 6.5], a preference for Néel-type DWs was observed in these samples. As shown in Figure 6.2(g), when $\mu_0 H_x$ is increased to +120 mT, the growth direction becomes more collinear to the $\mu_0 H_x$ axis in a manner more consistent with the left-handed chirality

interred in the $[\text{Co}/\text{Ni}/\text{Pt}]_2$ sample. However, when $\mu_0 H_x$ is increased above +140 mT, a rapid, $\sim 180^\circ$ change in the growth direction occurs, as shown in Figure 5.2(h) for $\mu_0 H_x = +200$ mT. The favored growth direction of dendritic stripe domains in the $[\text{Co}/\text{Ni}/\text{Pt}]_3$ sample for various permutations in domain orientation and $\mu_0 H_x$ magnitudes/directions are summarized in Figure

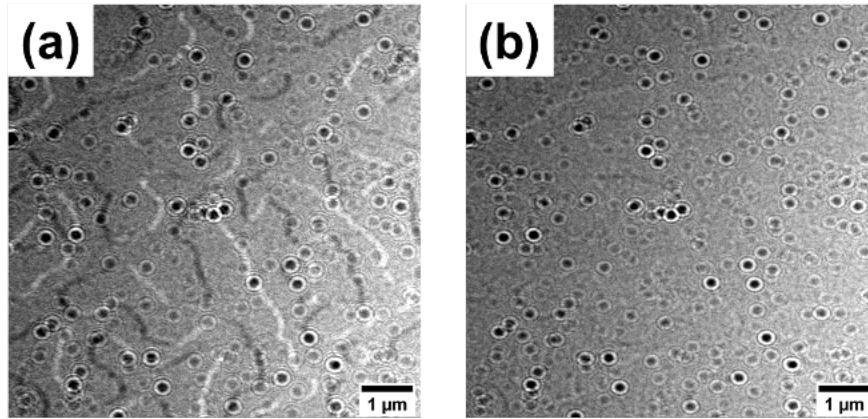


Figure 6.5: Lorentz TEM images of the $[\text{Co}/\text{Ni}/\text{Pt}]_5$ sample, collected in zero applied magnetic fields when the sample was tilted (a) 30° and (b) 0° relative to the imaging beam. A domain state was formed before imaging through the application of a perpendicular magnetic field. The circular black features correspond to voids in the sample and/or debris on the surface.

6.2(m); a version of this figure where MOKE images have replaced the schematic arrows is provided in Figure 6.6. As a measurement of D_{DMI} in the $[\text{Co}/\text{Ni}/\text{Pt}]_{N \geq 3}$ is complicated by the $\mu_0 H_x$ -dependent domain growth directionality, Brillouin light scattering (BLS) spectroscopy was performed on a $N = 5$ sample – indicating a D_{DMI} value similar to that measured in the $N = 2$ sample (-0.622 mJ/m²; see Figure 6.7).

In Figure 6.8(a), we plot the domain growth direction θ_{growth} of “up” ($+M_z$) and “down” ($-M_z$) domains as a function of in-plane magnetic field strength $\mu_0 H_x$ using the θ_{growth} and $\mu_0 H_x$ conventions defined in Figure 6.8(b), where a positive $\mu_0 H_x$ is defined as pointing in the positive

\hat{x} -direction and θ_{growth} is measured counterclockwise relative to this axis. While an analytical model elucidating these trends is presented later in this chapter, we first discuss some of the noteworthy features of domain growth demonstrated in Figures 6.2 and 6.8. First, we note that for a fixed perpendicular orientation of reverse domain and $\mu_0 H_x$ magnitude, changing the $\mu_0 H_x$ direction by 180° also changes θ_{growth} by 180° , as would be expected in a chiral magnetic system.⁴

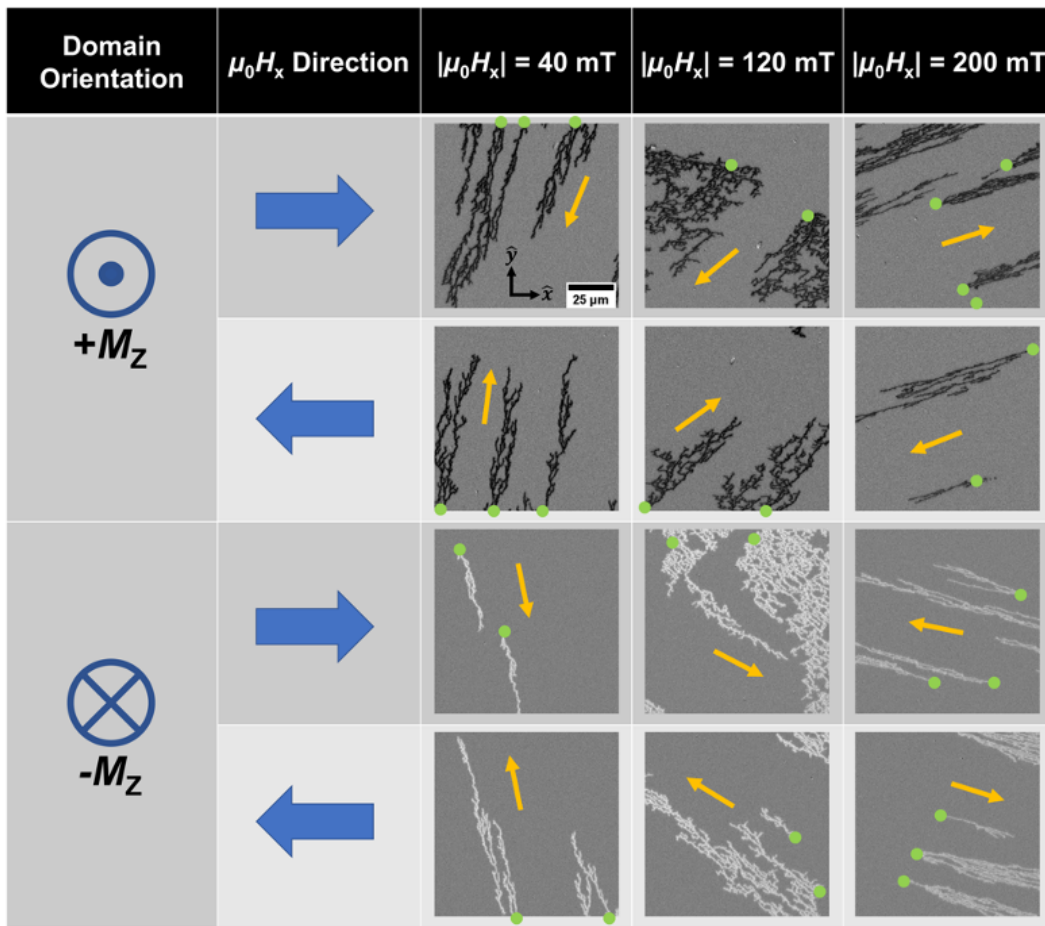


Figure 6.6: MOKE images depicting the growth of dendritic stripe domains in the $[\text{Co/Ni/Pt}]_{0.7}$ sample for different permutations of domain orientation and in-plane field $\mu_0 H_x$ magnitudes and directions. The images were collected as 5 ms-long, 15 mT-strong out-of-plane magnetic field pulses were applied. Orange arrows indicate the favored growth direction. Green dots in the images indicate the initial nucleation sites; dots at the edge of the images indicate a nucleation site out of the field of view.

However, when considering the expansion of domains with opposite perpendicular orientations, we find that the \hat{x} -component of the growth direction changes sign while the \hat{y} -component (vertical direction in the MOKE images) is invariant. This peculiar behavior is particularly apparent in the limit of $|\mu_0 H_x| = 40$ mT, where $+M_z$ and $-M_z$ domains grow in nearly the same direction, primarily vertical to the $\mu_0 H_x$ axis – clearly demonstrated by comparing Figure 6.2(f) with Figure 6.2(j). Moreover, this vertical asymmetry changes orientation upon inversion of the $\mu_0 H_x$ direction. These

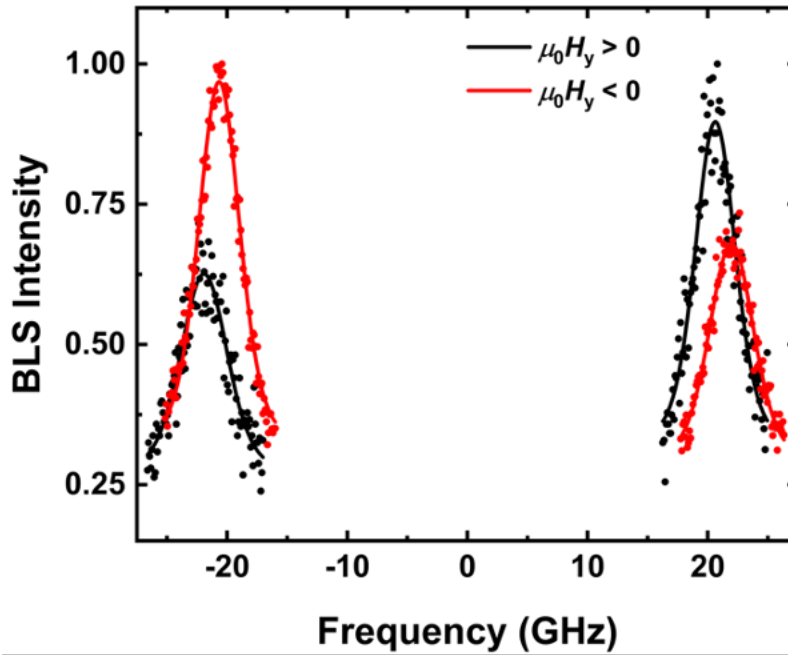


Figure 6.7: Brillouin light scattering (BLS) spectroscopy of the $[\text{Co/Ni/Pt}]_5$ sample, collected in the Damon-Eshbach geometry using a 532 nm-wavelength laser beam at an incidence angle of $\pi/4$. The sample magnetization was saturated in the film plane during the BLS measurement. From the absolute value of the frequency shift measured in this sample ($|\Delta f| = 653 \text{ MHz} \pm 36 \text{ MHz}$), a DMI energy density of 0.622 mJ/m^2 was determined using the static properties listed in the main text and the volume-averaged spectroscopic splitting factors for Ni and Co using a treatment detailed elsewhere.³

surprising observations are not commensurate with Bloch- or Néel-type chiral DWs in which intrinsic energetic factors set the chirality. Besides these trends to the $\theta_{\text{growth}}(\mu_0 H_x)$ profiles, the

directional growth characteristics of the dendritic stripe domains are independent of the in-plane field history, as the in-plane field strength and direction can be changed during the reversal process, and the growth direction varies “on-demand” [Figure 6.9]. This history-independence indicates that the energy landscape governing the observed growth asymmetries is not set during the initial nucleation of a domain. Additionally, we note that similar growth behaviors are seen in samples with $N = 4$ or 5 , and the results are insensitive to modest changes in the Co, No, or Pt thicknesses (and thus, modest changes in the static properties, such as K_{eff} , D , and M_s).

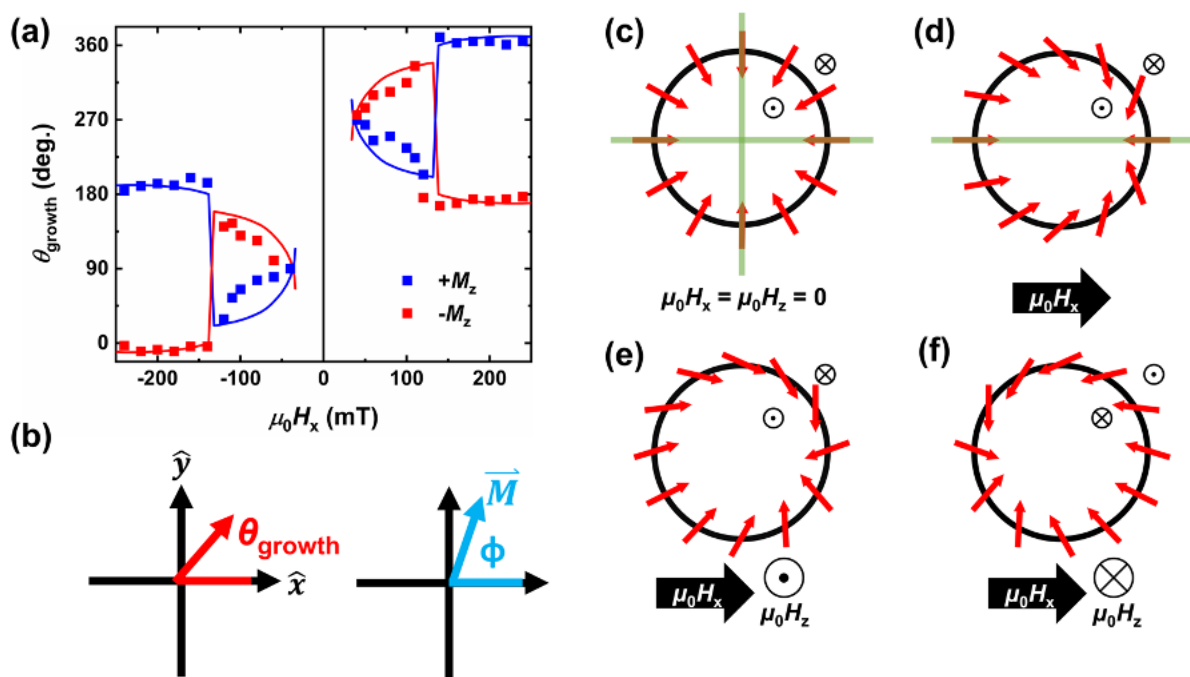


Figure 6.8: (a) The growth direction θ_{growth} of “up” ($+M_z$) and “down” ($-M_z$) dendritic domains as a function of $\mu_0 H_x$, determined both experimentally (symbols) and analytically with steady-state dynamics and dispersive stiffness (lines). When plotting the analytically predicted θ_{growth} profiles, we only display data for in-plane fields where at least a 60 % growth asymmetry between the fastest and slowest azimuthal positions is predicted (i.e., $|\mu_0 H_x| > 40$ mT). (b) The conventions used through this work to define the domain growth direction θ_{growth} relative to the in-plane field $\mu_0 H_x$ direction and the DW core magnetization angle ϕ . Schematic depictions of the DW magnetization profiles in (c) zero applied magnetic field, (d) an in-plane magnetic field, (e) an in-plane and out-of-plane magnetic field, and (f) an in-plane and into-plane magnetic field. Green lines in (c,d) indicate planes of time-reversal mirror symmetry.

Second, there is a strong selectivity to the growth direction of dendritic stripe domains [Figures 6.2(f-h)], compared to the mild growth asymmetries seen in the samples that reverse via large circular domains [Figures 6.2(b-d)]. In films with perpendicular anisotropy, dendritic stripe domains form out of a balance between ferromagnetic exchange and long-range dipolar fields. The energetic impetus for the formation of different types of domain morphologies has been extensively studied in films without iDMI, starting with the work of Kittel in the 1940s.^{12,13,14} In the thin-film limit, the balance between the demagnetizing energy and the energy of forming DWs implies that the equilibrium domain size should decrease exponentially with increasing film

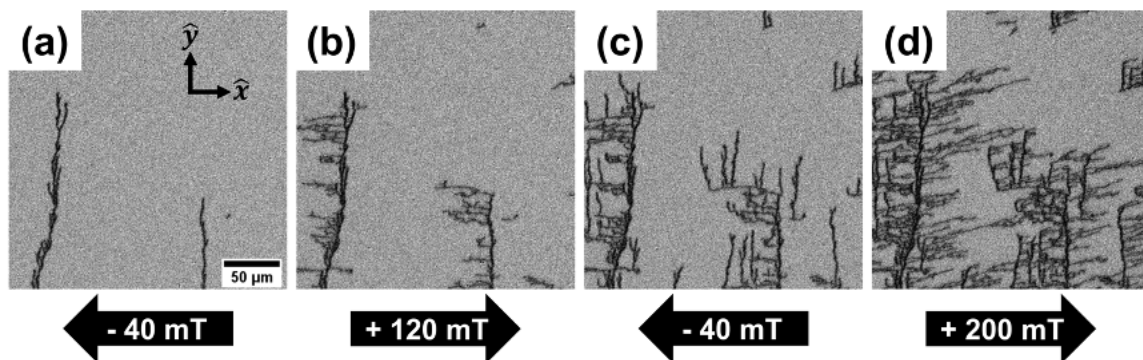


Figure 6.9: Polar MOKE images of the $[\text{Co/Ni/Pt}]_3$ sample as 5 ms-long, +15 mT perpendicular magnetic field pulses were applied in static in-plane fields of (a) -40 mT, (b) +120 mT, (c) -40 mT, and (d) +200 mT. The initial dendrite state was obtained by applying several perpendicular field pulses in a static in-plane field of -40 mT.

thickness. In contrast, for thicker films, an increase in domain size proportional to the square root of the film thickness is expected. This results in a minimum domain size at an intermediate thickness. Throughout the various thickness regimes, the balance of the dipolar and DW energies (which depend on the saturation magnetization, anisotropy, and exchange stiffness) determine the finer details of this trend. While the iDMI is known to lead to smaller equilibrium domain sizes, a

similar relationship between film thickness and equilibrium domain size holds in films with this additional energy term.¹⁵ For the [Co/Ni/Pt] films discussed here, we observe a transition from relatively large domains to stripe domains when increasing the number of repetitions N from 2 to 3 (*i.e.*, within the thin film limit, where the equilibrium domain size decreases exponentially with increasing film thickness). Magnetic reversal via dendritic stripe domains occurs by means of growth from a nucleation site, as the stripe tip curvature (and thus, the stripe width) stays more or less constant while the length of the stripe domains increases to fill the area of the film.¹⁶ This reversal phenomenon is markedly different from thinner films with larger domains, where domains tend to uniformly expand in all directions, filling the area of the film to obtain the reverse domain state. In concert with the localized chirality of the DW magnetization profile (and hence, the localized energy profile at the tips of the domains¹⁷), the dendritic domain morphology allows for a stronger link between the azimuthal energy asymmetry and the expansion asymmetry. As we discuss in the subsequent section, this leads to the larger-aspect ratio domains and stronger directional growth observed in the [Co/Ni/Pt]₃ sample reversing via stripe domains compared to the thinner samples.

6.4 Analytical Modeling

As shown in Figure 6.10, domain growth in the [Co/Ni/Pt]₃ sample falls within the thermally activated creep regime for the magnetic fields employed experimentally throughout this work.^{4,18,19,20} Within the creep regime, the velocity of domain expansion v follows an Arrhenius scaling law, given by:^{21,22}

$$v = v_0 e^{-\chi(\varepsilon/H_z)^{1/4}}$$

Equation 6.2

Where v_0 is the velocity scaling factor, χ is an energy barrier scaling constant, H_z is the perpendicular field strength, and ε is the elastic energy of the DW. A defining hallmark of Equation 6.2 is that v scales inversely with ε . In the case of magnetic domains, ε is generally taken as the 1D linear DW energy density σ , expressed as:⁷

$$\sigma(\theta, \phi) = \sigma_0 + \frac{\ln 2}{\pi} t_f \mu_0 M_s^2 \cos^2(\phi - \theta) - \pi D_{DMI} \cos(\phi - \theta) - \pi \lambda \mu_0 M_s H_x \cos(\theta)$$

Equation 6.3

In Equation 6.3, θ is the azimuthal orientation of a given DW section and ϕ is the DW core magnetization angle – both defined using the conventions shown in Figure 6.8(b). The first term of Equation 6.3 is the resting energy of a Bloch-type DW ($\sigma_0 = 4\sqrt{AK_{eff}}$). The second term

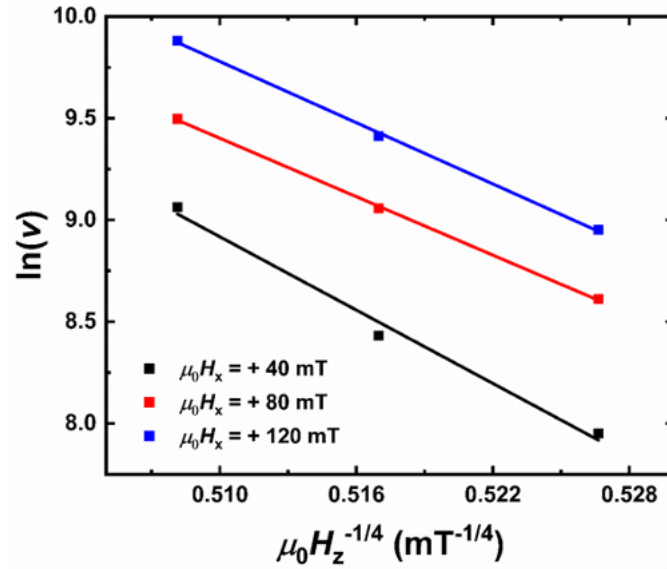


Figure 6.10: Verification of the creep scaling law in the [Co/Ni/Pt]₃ sample, obtained from measurements of the expansion velocity v (in $\mu\text{m/s}$) for different perpendicular fields $\mu_0 H_z$ and in-plane fields $\mu_0 H_x$. The data was collected using a $+M_z$ domain, subjected to 5 ms-long $\mu_0 H_z$ pulses. Given the strong growth asymmetry observed in the sample, the velocity was determined at the azimuthal position that exhibits the fastest expansion for each $\mu_0 H_x$.

represents the DW anisotropy energy, which increases with film thickness (t_f) and degenerately favors Bloch DWs of either chirality. The third term gives the contribution of the effective field due to the iDMI, which stabilizes Néel DWs of the handedness determined by the sign of D . The final term is the Zeeman energy emerging from the application of an in-plane magnetic field along the x -axis. In Equation 6.3, μ_0 is the vacuum permeability and $\lambda = \sqrt{A/K_{eff}}$ (where A is the exchange stiffness) is the DW width. To obtain the resting equilibrium energy and in-plane magnetization of a DW segment with azimuthal orientation θ , the energy functional is minimized with respect to φ . As shown in Figure 6.8(c), Equation 6.3 predicts a DW magnetization profile – and hence, an energetic profile- that has time-reversal mirror symmetry about the horizontal and vertical axes of the domain.

In Figure 6.11, we show the static equilibrium DW magnetization profiles $\varphi(\theta)$ predicted by Equation 6.3 for the [Co/Ni/Pt]₃ sample for various $\mu_0 H_x$ values using the sample properties listed in the figure caption. When $\mu_0 H_x = 0$, the DWs are predicted to exhibit a significant Néel character despite the higher DW anisotropy expected in samples with a higher number of [Co/Ni/Pt] repetition – a prediction confirmed from the Lorentz TEM images shown in Figure 6.5. As the magnitude of $\mu_0 H_x$ is increased, the DW magnetization profile is progressively pulled in the direction of $\mu_0 H_x$. From the static equilibrium treatment of the DW magnetization profile, growth asymmetries collinear to the in-plane field axis are the expected outcomes, as the time-reversal mirror symmetry of the DW profile is only broken about the vertical axis [Figure 6.8(d)].

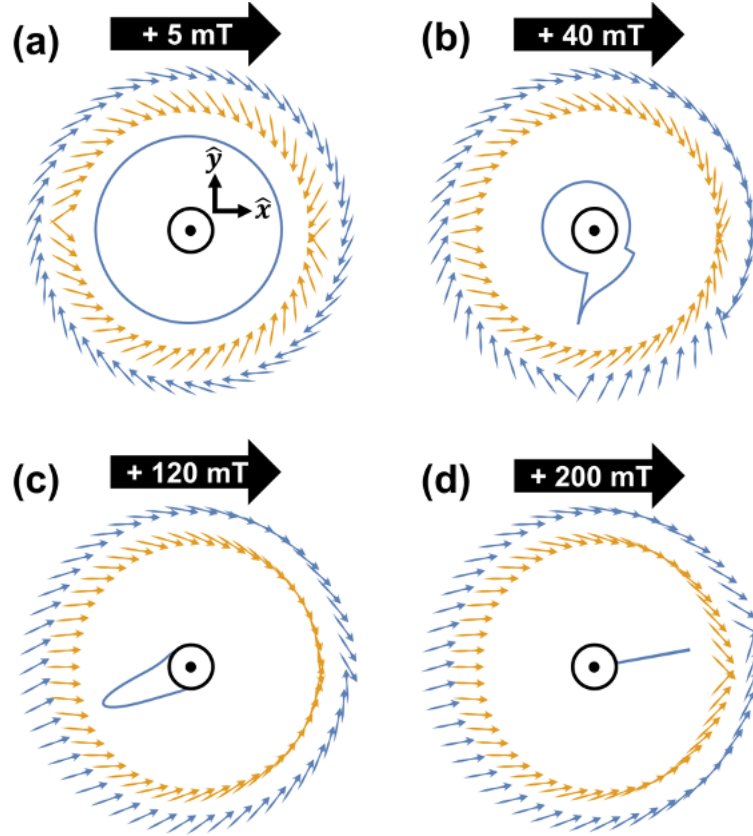


Figure 6.11: Predicted DW magnetization profiles in the $[\text{Co/Ni/Pt}]_3$ sample under the assumption of static equilibrium (gold arrows) and steady-state dynamic reorientation (blue arrows) under applied in-plane fields of (a) $\mu_0 H_x = +5$ mT, (b) $+40$ mT, (c) $+120$ mT, and (d) $+200$ mT. The polar profile shown in the center of each diagram represents the relative velocity of expansion (v/v_{max}) as a function of azimuthal position predicted from Equation 6.6. When using Equations 6.3 and 6.4 to calculate the static equilibrium and steady-state dynamic profiles (respectively), the sample properties were as follows: $M_s = 1000$ kA/m, $K_{\text{eff}} = 5 \times 10^5$ J/m³, $t_f = 3.6$ nm, $D_{\text{DMI}} = -0.45$ mJ/m², $\alpha = 0.208$, and $\mu_0 H_z = +15$ mT.

In addition to the static energies reflected in Equation 6.3, when a perpendicular magnetic field $\mu_0 H_z$ is used to propagate a reverse domain, a torque will act on the internal magnetization of the DW, rotating $\varphi(\theta)$ away from the static equilibrium profile predicted by Equation 6.3. This field torque will be counteracted by the balance of the effective fields, also captured by Equation 6.3. While large perpendicular fields will cause a DW's core magnetization to precess,²³ a DW within the creep regime is expected to experience a steady-state dynamical reorientation of its internal magnetization, described within the Landau-Lifshitz-Gilbert framework by:²⁴

$$\dot{\phi} = \frac{\gamma\mu_0}{1 + \alpha^2} (-\alpha\Omega_A + H_z) = \frac{\gamma\mu_0}{1 + \alpha^2} \left(-\frac{\alpha\sigma_\phi}{2\lambda\mu_0 M_s} + H_z \right)$$

Equation 6.4

In Equation 6.4, γ is the gyromagnetic ratio and α is the Gilbert damping parameter. In Equation 6.4 and henceforth, subscripts to the DW energy density σ denote a partial derivative. The balance of these competing factors can result in a steady-state $\phi(\theta)$ profile that differs from the static equilibrium case, which in turn modifies the relevant energy-related terms. From the schematic depictions of the effect of this torque on chiral Néel-type walls [Figures 6.8(e,f)], it can be surmised that it acts in the same rotational sense for both $+M_z$ and $-M_z$ domains – akin to the promotion of Bloch-type walls of opposite chirality depending on the orientation of the reversal domain/sign of $\mu_0 H_z$, thus breaking the mirror symmetry of the DW magnetization profile along both the horizontal and vertical axes.

Recently, Pellegren *et al.* showed that when DW energies are anisotropic in θ , the elastic energy scale ε is no longer given simply by the 1D static DW energy σ , but by the dispersive stiffness.⁷ As the dispersive stiffness accounts for the pinning length scale and the local curvature of the energy landscape through additional energy terms, a more accurate picture of the elastic behavior of DWs can be obtained. For a DW of arbitrary length L , we employ the generalized dispersive stiffness $\tilde{\sigma}$ to fully capture the steady-state reorientation using the expression:

$$\tilde{\sigma}(\theta, \varphi, L) = \sigma + \sigma_{\theta\theta} - \frac{\sigma_{\phi\theta}}{\sigma_{\phi\phi}} \zeta \left(\frac{L}{2\Lambda} \right)$$

Equation 6.5

where $\zeta(l) = 1 - \frac{3}{l^3} (l - \tanh(l))$ and $\Lambda = \lambda\sqrt{\sigma_0/\sigma_{\phi\phi}}$. In Equation 6.5, all derivatives are evaluated at the steady-state magnetic orientation φ corresponding to each θ . The second and third terms of Equation 6.5 represent the curvature contributions that emerge due to anisotropy in the

DW energy with respect to both θ and φ . The third term expresses the dependence of the stiffness on L and the exchange length scale Λ ; for finite values of L , it is recognized that for vanishing values of $\sigma_{\phi\phi}$, $\lim_{\sigma_{\phi\phi} \rightarrow 0} \frac{\sigma_{\phi\theta}^2}{\sigma_{\phi\phi}} \zeta\left(\frac{L}{2\Lambda}\right) = -\frac{\sigma_{\phi\theta}^2 L^2}{10\sigma_0 \lambda^2}$. Consequently, by calculating the dispersive stiffness in the steady-state configuration as a function of θ , the relative velocity of a wall segment at all azimuthal orientations can be computed, and the most favorable growth directions of a dendritic stripe domain can be determined. For θ positions where $\tilde{\sigma} < 0$, the DW magnetization profile is expected to facet, adopting the orientation and magnetization of the neighboring segments (as predicted by the Wulff construction), driving the $\tilde{\sigma}$ values to zero.⁷

Defining θ_{growth} as the azimuthal position having the lowest $\tilde{\sigma}$ value, we obtain the most suitable match between the experimental and analytically predicted $\theta_{\text{growth}}(\mu_0 H_x)$ profiles when the parameters $D_{\text{DMI}} = -0.45$ mJ/m², $\alpha = 0.208$, and $L = 70$ nm are used in the modeling, along with $A = 10$ pJ/m, uniaxial anisotropy energy density $K_u = 1.13 \times 10^6$ J/m³ (corresponding to a K_{eff} of $\sim 5 \times 10^5$ J/m³), and the experimentally determined M_s value, as shown in Figure 6.8(a). While $L = 70$ nm was used in the present calculations, a similar degree of agreement between the experimental data and the modeling was found over a wide range of L values. Also, when the experimentally determined D_{DMI} value of -0.63 mJ/m² is used, qualitatively similar results are obtained, with a modest offset to the characteristic $\mu_0 H_x$ at which the $\sim 180^\circ$ change in growth direction occurs. In Figures 6.12(a-d), we show the dispersive stiffness $\tilde{\sigma}$ and predicted relative velocity of expansion v/v_{max} as a function of azimuthal angle θ for the [Co/Ni/Pt]₃ sample in several in-plane fields $\mu_0 H_x$; an alternative depiction of the azimuthal dependence of the velocity is provided in Figure 6.11. $\tilde{\sigma}$ was determined using the approach discussed above, whereas v/v_{max} was determined using a

modified expression for the creep velocity that takes the dispersive stiffness into account, given as:⁷

$$v = v_0 \exp\left(-\frac{\kappa(\tilde{\sigma}(H_x))^{1/4}}{H_z(\tilde{\sigma}(H_x = 0))^{1/4}}\right)$$

Equation 6.6

where the velocity scaling and energy barrier scaling parameters (v_0 and κ , respectively) are determined from fitting to the experimental $v(\mu_0 H_x, \mu_0 H_z)$ data, as demonstrated in Figure 6.10.

For low magnitude $\mu_0 H_x$ values [Figure 6.12(a)], $\tilde{\sigma}$ is rather invariant with θ , consequentially, the velocity asymmetry with respect to θ is muted. However, as $\mu_0 H_x$ is increased to +40 mT, the $\tilde{\sigma}(\theta)$ and $v(\theta)$ profiles become substantially more anisotropic [Figure 6.12(b)], favoring domain growth in a direction similar to that observed experimentally. While the degree of growth asymmetry seen experimentally when $\mu_0 H_x = +40$ mT is more heightened than what is predicted in Figure 6.12(b), we believe that differences in the DW width, L , and our field-induced pinning not accounted for in the modeling strengthen the preference for growth in the experimentally observed direction. We also note that under the long-wavelength limit of the stiffness model (*i.e.*, $L \rightarrow \infty$) for $35 \text{ mT} < |\mu_0 H_x| < 70 \text{ mT}$, the calculated stiffness profiles strongly favor growth in both the experimentally observed vertical direction, as well as in a direction collinear to the applied $\mu_0 H_x$ [Figure 6.13]; growth along the latter direction could be suppressed for the same reasons mentioned above. Nevertheless, our analytical modeling explains how both horizontal and, more crucially, vertical asymmetries can develop in the magnetization profile, giving rise to the observed growth behaviors. Additionally, the model correctly predicts the symmetries reflected in Figure 6.2(m) and Figure 6.6 – namely, that the vertical growth direction under a given in-plane field does not change with the domain polarity. Coupled together, these two

traits of our modeling punctuate the critical role that dynamic symmetry breaking plays in describing our experimental results.

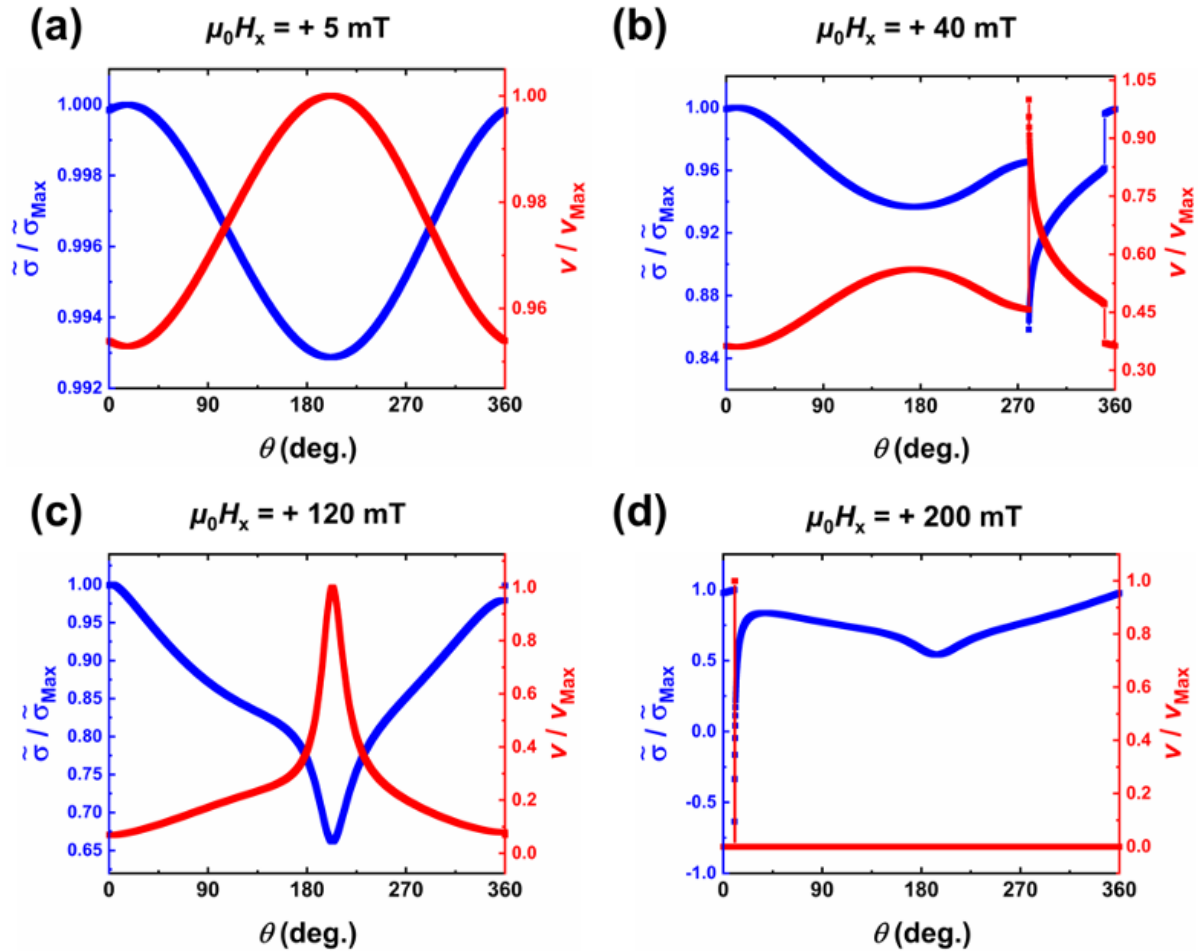


Figure 6.12: Dispersive stiffness $\tilde{\sigma} / \tilde{\sigma}_{\text{max}}$ (blue lines) and predicted relative expansion velocity v / v_{max} (red lines) as a function of azimuthal position θ for $+M_z$ dendritic stripe domains in the $[\text{Co}/\text{Ni}/\text{Pt}]_3$ sample in applied in-plane fields $\mu_0 H_x$ of (a) +5 mT, (b) +40 mT, (c) +120 mT, and (d) +200 mT. Throughout Figure 6.12, θ is defined using the angular convention shown in Figure 6.8(b), and L is 70 nm.

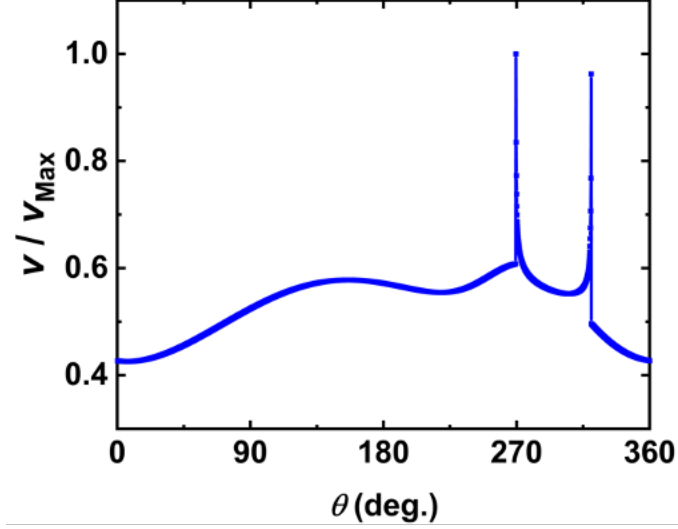


Figure 6.13: Relative velocity v/v_{\max} as a function of azimuthal position θ for $+M_z$ dendritic stripe domains in the $[\text{Co}/\text{Ni}/\text{Pt}]_3$ sample in an applied in-plane field of +37 mT, calculated using the long-wavelength ($L \rightarrow \infty$) dispersive stiffness treatment. θ is defined using the angular convention shown in Figure 6.8(b).

Further increasing $\mu_0 H_x$ to +120 mT [Figure 6.12(c)] and +200 mT [Figure 6.12(d)], a strong correspondence is maintained between the experimental and predicted $\theta_{\text{growth}}(\mu_0 H_x)$ and $v(\theta)$ behavior. As shown in Figure 6.11, the θ positions of minimal $\tilde{\sigma}$ correspond to regions where the $\phi(\theta)$ profile exhibits discontinuities (short of the full 2π rotations seen at Bloch points in DWs), where the local energy and net restoring torque approach an inflection point and a local maximum respectively [Figure 6.14]. As previously reported by Sanchez-Tejerina *et al.*, this abrupt reorientation of the magnetization profile stems from variations in the driving and restoring torques acting on the DW, which arise from the θ -dependent competition between the effects of $\mu_0 H_x$, $\mu_0 H_z$, iDMI, and DW anisotropy.²⁴ The highly localized nature of these minima in $\tilde{\sigma}$ – combined with the heightened configurational sensitivity of dendritic stripe domains- enables the strong directionality to the domain growth observed. We do note that in several reports of in-plane field-induced bubble expansion asymmetries in systems with iDMI, small growth components

transverse to the in-plane field axis have been previously observed.^{25,26,27} While we limit our modeling to the [Pt/Co/Ni]-type samples discussed herein, the analytical treatments employed predict that dynamic symmetry breaking – particularly, the strong vertical growth behavior seen in the [Co/Ni/Pt]-type samples for low $\mu_0 H_x$ – is possible in other materials with the right balance between the iDMI and DW anisotropy energies, provided there is also a proper balance between the Gilbert damping and the driving field.

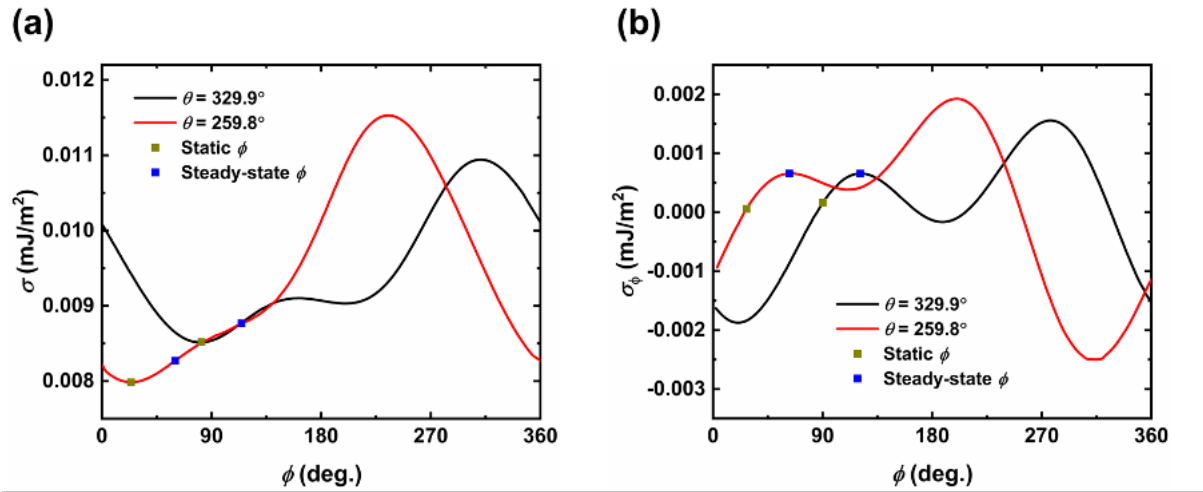


Figure 6.14: Plots showing the ϕ -dependence of the (a) calculated domain wall energy σ and (b) normalized restoring torque σ_ϕ at azimuthal positions of $\theta = 80^\circ$ (black) and $\theta = 150^\circ$ (red) for the [Co(0.7 nm)/Ni(0.5 nm)/Pt(0.7 nm)]₃ sample. These wall positions correspond to the discontinuities present in the $\varphi(\theta)$ profiles for $\mu_0 H_x = +40$ mT. The φ solutions for the static (gold squares) and steady-state (blue squares) treatments are labeled for each θ , using the angular definition provided in Figure 6.8(b). The full $\sigma(\varphi)$ profiles for the static and steady-state cases for this $\mu_0 H_x$ are shown in Figure 6.12.

6.5 Conclusion

We have reported on the in-plane field-induced magnetic domain growth asymmetries present in several Co/Ni/Pt-based thin film heterostructures engineered to possess an interfacial DMI that favors chiral Néel-type DWs. For thinner samples that reverse their magnetization via

large circular domains, growth asymmetries collinear to the symmetry-breaking in-plane magnetic field were observed, as predicted by the current understanding of the interfacial DMI within the typical long-wavelength stiffness model of the elastic energy of a DW. For thicker samples, where reversal occurs via dendritic stripe domains, anomalous growth directionalities with respect to the in-plane field strength and direction emerged – most notably, growth perpendicular to low-magnitude in-plane fields. Through an analytic treatment of steady-state dynamical symmetry breaking and the dispersive stiffness of DWs, the magnetization configurations that would give rise to this unexpected growth behavior and its symmetries with respect to the out-of-plane field direction were modeled. These results shed light on the mechanisms governing the dynamics of Néel-type DWs and provide new opportunities for the control of chiral magnetic systems.

Chapter 6, in part, is a reprint of research published as “Dynamic symmetry breaking in chiral magnetic systems” by J.A. Brock, M.D. Kitcher, P. Vallobra, R. Medapalli, M.P. Li, M. De Graef, G.A. Riley, H.T. Nembach, S. Mangin, V. Sokalski, and E.E. Fullerton in *Advanced Materials* 33, 2101524 (2021). The dissertation author was a co-primary investigator and author of the manuscript. This work was supported by Quantum Materials for Energy Efficient Neuromorphic Computing, an Energy Frontier Research Center of the U.S. Department of Energy, Office of Basic Science (DE-SC0019273).

6.6 References

- ¹ P. Jadaun, L. F. Register, S. K. Banerjee, *npj Comput. Mater.* **6**, 88 (2020).
- ² M. Bode, M. Heide, K. von Bergmann, P. Ferriani, S. Heinze, G. Bihlmayer, A. Kubetzka, O. Pietzsch, S. Blugel, R. Wiesendanger, *Nature* **447**, 190 (2007).
- ³ H.T. Nembach, J.M. Shaw, M. Weiler, E. Jue, T.J. Silva, *Nat. Phys.* **11**, 825 (2015).

-
- ⁴ S.-G. Je, D. H. Kim, S.C. Yoo, B.C. Min, K.J. Lee, and S.B. Choe, *Phys. Rev. B* **88**, 214401 (2013).
- ⁵ E. Jue, C.K. Safeer, M. Drouard, A. Lopez, P. Balint, L. Buda-Prejbeanu, O. Boulle, S. Auffret, A. Schuhl, A. Manchon, I.M. Miron, G. Gaudin, *Nature Mat.* **15**, 272 (2016).
- ⁶ A. Hrabec, J. Sampaio, M. Belmeguenai, I. Gross, R. Weil, S.M. Chérif, A. Stashkevich, V. Jacques, A. Thiaville, S. Rohart, *Nature Comm.* **8**, 15765 (2017).
- ⁷ J.P. Pellegren, D. Lau, and V. Sokalski, *Phys. Rev. Lett.* **119**, 027203 (2017).
- ⁸ D.Y. Kim, D.H. Kim, and S.B. Choe, *Appl. Phys. Express* **9**, 053001 (2016).
- ⁹ D. Lau, V. Sundar, J.-G. Zhu, V. Sokalski, *Phys. Rev. B* **94**, 60401 (2016).
- ¹⁰ D.M.F. Hartmann, R.A. Duine, M.J. Meijer, H.J.M. Swagten, and R. Lavrijsen, *Phys. Rev. B* **100**, 094417 (2019).
- ¹¹ A.W.J. Wells, P.M. Shepley, C.H. Marrows, T.A. Moore, *Phys. Rev. B* **95**, 054428 (2017).
- ¹² C. Kittel, *Phys. Rev.* **70**, 965 (1946).
- ¹³ C. Kittel, *Rev. Mod. Phys.* **21**, 541 (1949).
- ¹⁴ O. Hellwig, A. Berger, J.B. Kortright, E.E. Fullerton, *J. Magn. Magn. Mater.* **319**, 13 (2007).
- ¹⁵ P. Agrawal, F. Buttner, I. Lemesh, S. Schlotter, G. S. D. Beach, *Phys. Rev. B* **100**, 104430 (2019).
- ¹⁶ J. E. Davies, O. Hellwig, E.E. Fullerton, G. Denbeaux, J.B. Kortright, K. Liu, *Phys. Rev. B* **70**, 224434 (2004).
- ¹⁷ S. Zhang, X. Zhang, J. Zhang, A. Ganguly, J. Xia, Y. Wen, Q. Zhang, G. Yu, Z. Hou, W. Wang, Y. Peng, G. Xiao, A. Manchon, J. Kosel, Y. Zhou, X.-X. Zhang, *Sci. Adv.* **8**, 1876 (2020).
- ¹⁸ P. M. Shepley, H. Tunncliffe, K. Shahbazi, G. Burnell, T. A. Moore, *Phys. Rev. B* **97**, 134417 (2018).
- ¹⁹ V. Jeudy, A. Mougín, S. Bustingorry, W. S. Torres, J. Gorchon, A.B. Kolton, A. Lemaitre, J.-P. Jamet, *Phys. Rev. Lett.* **117**, 057201 (2016).
- ²⁰ M. Vanatka, J.-C. Rojas-Sanchez, J. Vogel, M. Bonfim, M. Belmeguenai, Y. Roussigne, A. Stashkevich, A. Thiaville, S. Pizzini, *J. Phys.: Condens. Matter* **27**, 326002 (2015).

-
- ²¹ S. Lemerle, J. Ferre, C. Chappert, V. Mathet, T. Giamarchi, P. L. Doussal, *Phys. Rev. Lett.* **80**, 849 (1998).
- ²² K.-J. Kim, J.-C. Lee, S.-M. Ahn, K.-S. Lee, C.-W. Lee, Y. J. Cho, S. Seo, K.-H. Shin, S.-V. Choe, H.-W. Lee, *Nature* **458**, 740 (2009).
- ²³ N.I. Schryer, L.R. Walker, *J. Appl. Phys.* **45**, 5406 (1974).
- ²⁴ L. Sanchez-Tejerina, O. Alejos, E. Martinez, *J. Magn. Magn. Mater.* **423**, 405 (2017).
- ²⁵ A. Hrabec, N. A. Porter, A. Wells, M. J. Benitez, G. Burnell, S. McVitie, D. McGrouther, T. A. Moore, C. H. Marrows, *Phys. Rev. B* **90**, 020402(R) (2014).
- ²⁶ D. M. F. Hartmann, Bachelor Thesis, Utrecht University (2014).
- ²⁷ J.P. Garcia, A. Fassatoui, M. Bonfim, J. Vogel, A. Thiaville, and S. Pizzini, *Phys. Rev. B* **104**, 014405 (2021).

Chapter 7: Half-skyrmions and Spin-orbit Torque

7.1 Introduction

The use of chiral domain walls (DWs) to control the dynamics of magnetic textures have been the subject of intense research interest as of late. In particular, it has been shown that chiral Néel-type DWs permit the coherent, efficient translation of magnetic domains in response to the spin-orbit torque (SOT) exerted by an injected spin current.^{1,2} This scheme can easily be realized via the spin-Hall effect,^{3,4} whereby a transverse spin current is generated when an electrical current is passed through a heavy metal (HM) layer with large spin-orbit coupling; this spin current can then be transmitted into an adjacent ferromagnet (FM) layer.⁵ Furthermore, the interfacial Dzyaloshinskii-Moriya interaction (iDMI) that develops at the FM/HM interface fosters a preference for chiral Néel-type DWs, with the strength and handedness of this interaction being determined by the chemical identity of the interface.^{6,7}

Besides promoting chiral Néel-type DWs, the iDMI assists in the stabilization of novel spin textures, such as magnetic skyrmions.^{8,9,10,11,12} The quantized winding-like structure of skyrmions has been shown to give rise to several application-relevant properties, including a “topological protection” of the magnetic state and efficient SOT-induced motion.¹³ At a more fundamental level, it has been theoretically and experimentally demonstrated that the non-trivial topological charge of a skyrmion gives rise to a Magnus force-like behavior known as the skyrmion Hall effect (SkHE). Because of the SkHE, a skyrmion will experience a transverse deflection relative to the

driving force exerted by the Slonczewski-like component of the SOT \vec{F}_{SL} .^{14,15,16,17} While the skyrmion Hall effect was first studied using skyrmions (with a topological charge $|Q|=1$), recently there have been several reports of skyrmion Hall effect-like behavior during the SOT-induced growth of magnetic stripe domains.^{18,19,20} By considering the tip of a stripe domain to be a half-skyrmion with $|Q|=1/2$, the deflection angle θ of a stripe domain relative to the force exerted by the SOT has often been understood in the context of the skyrmion Hall effect using the expression:¹⁸

$$\theta \approx \tan^{-1} \left(\frac{2Q\lambda}{\alpha r} \right)$$

Equation 7.1

Where λ is the DW width, α is the Gilbert damping parameter, and r is the half-skyrmion radius. While r and λ can be determined using commonplace experimental techniques, measuring α can require more specialized equipment, particularly in systems with strong perpendicular magnetic anisotropy. As such, α has typically been attributed an *a priori* value or has been used as a fitting parameter when interpreting the SOT-induced growth directionality of stripe domains.^{18,19,20}

As discussed in Chapter 6, it has also been shown that the steady-state dynamic reconfiguration of the DW magnetization profile that occurs during the magnetic field-driven expansion of stripe domains with chiral Néel-type DWs can give rise to novel growth asymmetries that cannot be predicted from static understandings.²¹ A key component to understanding the growth behavior in such systems required accounting for the fact that a perpendicular magnetic field will exert an in-plane torque on the DW magnetization profile – twisting the Néel-type extant at static equilibrium to that of a chiral mixed Bloch-Néel-type DW.²² By the same token, the Slonczewski-like SOT generated when spin currents are injected into a ferromagnet (which acts

as an effective perpendicular magnetic field H_{SL} ^{23,24} have been shown to have a similar twisting-like effect on the magnetization profile of planar chiral Néel-type DWs.^{25,26} Furthermore, given that the magnitude and directionality of H_{SL} is sensitive to the core magnetic orientation at each azimuthal position around a DW²⁷ (whereas field-driven growth asymmetries are primarily sensitive to the relative energy of each position²⁸), understanding SOT-induced growth asymmetries may be a more straightforward proposition.

Here, we report an experimental and analytic study of the SOT-induced growth behavior of stripe domains in several HM/FM thin-film multilayers – designed to possess an iDMI and a net SOT acting on the FM layers. Like in previous reports, we find that the stripe domains exhibit a strong growth component transverse to the applied current axis. By modeling the impacts of the torques associated with the SOT effective fields, we find that the reconfigured DWs have an orientational profile that favors growth with a similar directionality and symmetry with respect to domain polarity and applied current direction as observed experimentally.

7.2 Experimental Techniques

Samples of the structure Ta(2)/ Pt(5)/ [Co(0.7)/ Ni(0.5)/ Pt(0.7)]₃/ Co(0.7)/ Ni(0.5)/ Ta(3) and Ta(2)/ Pt(5)/ [Co(0.5)/ Pt(0.7)]₄/ Co(0.5)/ Ta(3) (thicknesses in nm; henceforth referred to as the Co/Ni/Pt and Co/Pt samples, respectively) were grown using dc magnetron sputtering. The sample structure is quite similar to those discussed in Chapter 6. All samples were grown on Si substrates with a 300 nm-thick thermal oxide coating using a 3 mTorr partial pressure of Ar and a sputtering power of 50 W. As Pt and Ta are known to possess opposite-signed spin-Hall angles, the seeding and capping layers were designed such that a net positive SOT should act on the FM

layers if homochirality is maintained through the film thickness.^{29,30,31} For SOT switching experiments, some samples were fashioned into 50 μm -wide wires using conventional metal liftoff UV photolithography. Ti/Au contacts were placed at the wire ends by similar means, using the techniques discussed in Chapter 2. Domain growth was observed using a polar magneto-optic Kerr effect (MOKE) microscope, manufactured by Evico Magnetics. In the polar MOKE images shown in this chapter, dark (light) contrast corresponds to upward (downward) oriented magnetic domains. Electrical current pulses were passed through the samples using a MOSFET-gated power supply, while an oscilloscope was used to monitor the actual voltage supplied to the sample during each pulse. The room temperature static magnetic properties of the samples were determined using the vibrating sample magnetometry (VSM) technique, in both the out-of-plane (OOP) and in-plane (IP) geometries.

7.3 Experimental Results

The Co/Ni/Pt-type sample discussed herein has previously been shown to exhibit a saturation magnetization M_s and effective perpendicular magnetic anisotropy (PMA) energy density K_{eff} of approximately 1000 kA/m and 500 kJ/m³, respectively.²¹ In the same work, the Co/Ni/Pt-type samples were also shown to possess an iDMI energy density $D \approx -0.6$ mJ/m² (with the negative sign of D denoting a left-handed iDMI), which was found to be large enough to promote the stabilization of Néel-type DWs both analytically and using Lorentz transmission electron microscopy. VSM data for the Co/Pt sample [Figure 7.1] indicates M_s and K_{eff} values of 900 kA/m and 415 kJ/m³, respectively. Through measurements of the in-plane field-induced domain growth asymmetries present in a sample with fewer Co/Pt repetitions (where magnetic reversal occurs via large, circular domains), we estimate a D value of approximately -0.4 mJ/m²

in our Co/Pt structure, as shown in Figure 7.2. While the Pt/Co/Pt motif would not be expected to exhibit an iDMI given the symmetry of the structure, in Chapter 5 we discussed how

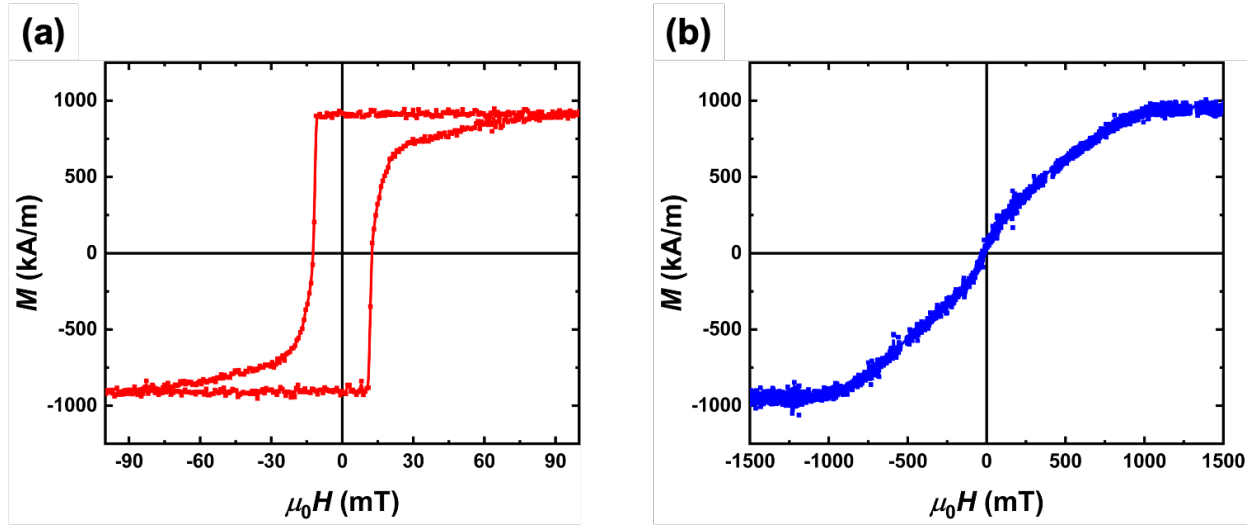


Figure 7.1: Room temperature hysteresis loops for the Pt/Co sample collected in the (a) out-of-plane and (b) in-plane geometry using vibrating sample magnetometry (VSM).

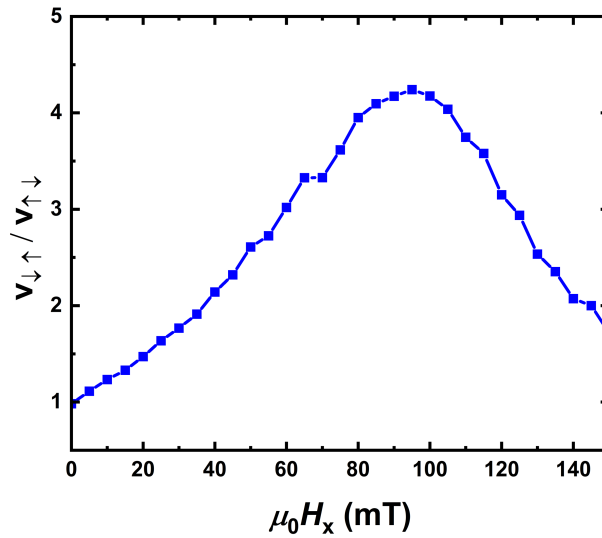


Figure 7.2: Ratio in the velocity of expansion of a $\downarrow\uparrow$ domain wall over that of a $\uparrow\downarrow$ domain wall in a $[\text{Co/Pt}]_2$ sample as a function of in-plane magnetic field $\mu_0 H_x$. The data shown in Figure 7.2 was collected from polar MOKE images, collected after applying 5 ms-long, 15 mT-strong perpendicular magnetic field pulses. Identifying the peak in $v_{\downarrow\uparrow} / v_{\uparrow\downarrow}$ as the iDMI effective field $\mu_0 H_{\text{DMI}}$, an iDMI energy density of approximately -0.4 mJ/m^2 was calculated using techniques described in previous chapters of this dissertation.

differences in the quality of the Pt/Co and Co/Pt interfaces can lead to behavior more associated with structural inversion asymmetry, like PMA and iDMI.

In Figure 7.3(a), we show a polar MOKE image of the Co/Ni/Pt sample after several 10 ms-long current pulses with a current density J of 3.5×10^{11} A/m² were applied along the $+\hat{x}$ direction indicated in the lower-right inset of Figure 7.3(b). Before applying the current pulses, the sample magnetization was saturated into the sample plane ($-M_z$). By comparing the domain growth relative to the points at which $+M_z$ domains are first nucleated in response to the current pulses (indicated by the blue circles), it can be seen that the growth component along the long axis of the wire is parallel to the conventional current density J , as would be expected from domains with left-handed chiral Néel-type DWs subject to a positive net SOT.³¹ Much like in previous studies of the SOT-induced growth of stripe domains, we observe that the domains are strongly pinned to the initial nucleation sites – a behavior that has previously been attributed to the disparity between the driving and pinning forces acting on the domains.^{18,19,20} Furthermore, the domains exhibit a significant inclination transverse to J , and the magnitude of this inclination is relatively similar between domains ($48^\circ \pm 1.6^\circ$). The conventions used to define the growth angle θ relative to the current polarity are shown within the upper-right insets of Figure 7.3. Given that the gyrotropic force that gives rise to the skyrmion Hall effect is given as $\vec{F}_G = -4\pi Q|\nu|(\hat{z} \times \vec{\nu})$ (where ν and \hat{z} are the stripe domain expansion velocity and the unit vector pointing out of the film plane, respectively),¹⁸ it can be seen that the transverse deflection observed in our samples does match the directionality expected from the skyrmion Hall effect.

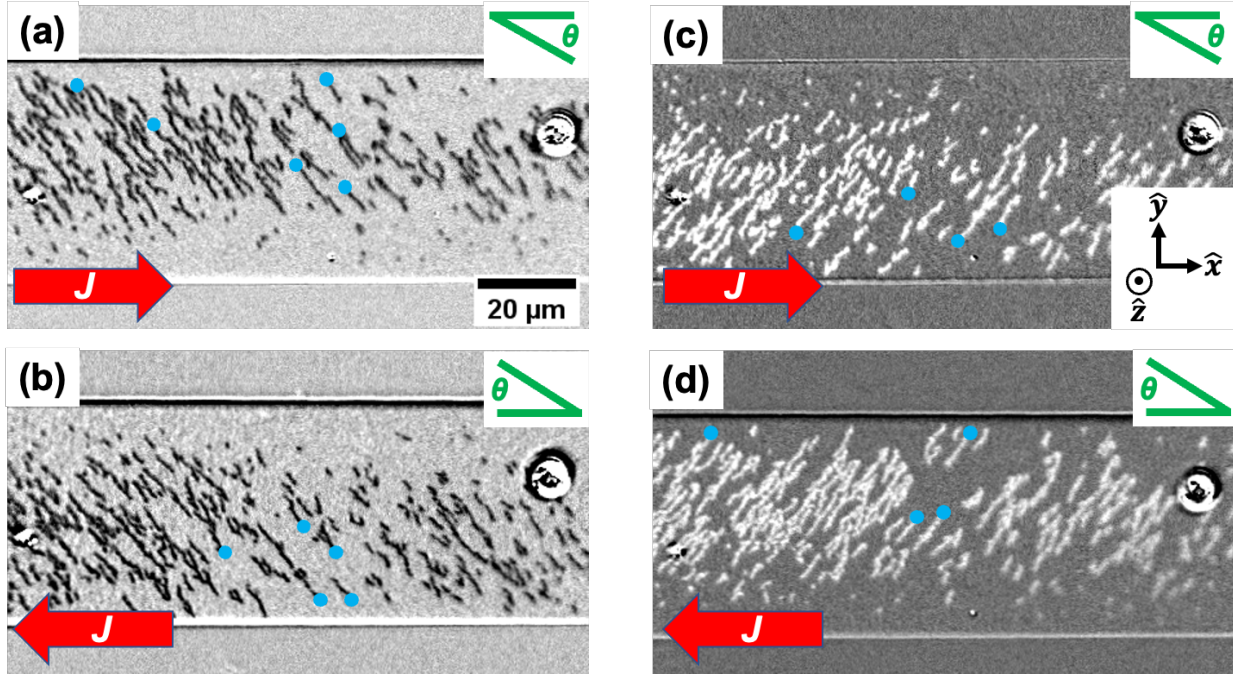


Figure 7.3: Polar MOKE images of the Co/Ni/Pt sample after several 10 ms-long current pulses of current density $3.5 \times 10^{11} \text{ A/m}^2$ were applied in zero magnetic field. The conventional current flow direction is indicated in the lower left corner of each subfigure, whereas the convention used to define θ_{growth} is shown in the upper right corners. The lower-right inset of (c) depicts the directional conventions used throughout this work.

We find that reversing the applied current direction also reverses the growth components collinear and transverse to the applied current axis [Figure 7.3(b)] – as would be expected from chiral Néel-type DWs subject to a spin current of opposite polarization from that present in Figure 7.3(a). If instead the sample is magnetized in the $+M_z$ direction before applying electrical current pulses (so that $-M_z$ domains are nucleated by the current pulses), the growth component collinear to J is the same for $-M_z$ and $+M_z$ domains (which is the expected response for chiral Néel-type DWs), but the transverse growth component is in the opposite direction. Given that the sign of Q is opposite for $+M_z$ and $-M_z$ domains, the sign change of the growth component transverse to J is consistent with the SkHE. Furthermore, the magnitude of inclination relative to J does not vary significantly between these permutations in the sign of J and the domain polarity. Similar growth

trends with respect to domain polarity and the electrical current direction are observed in the Co/Pt-type samples [Figure 7.4].

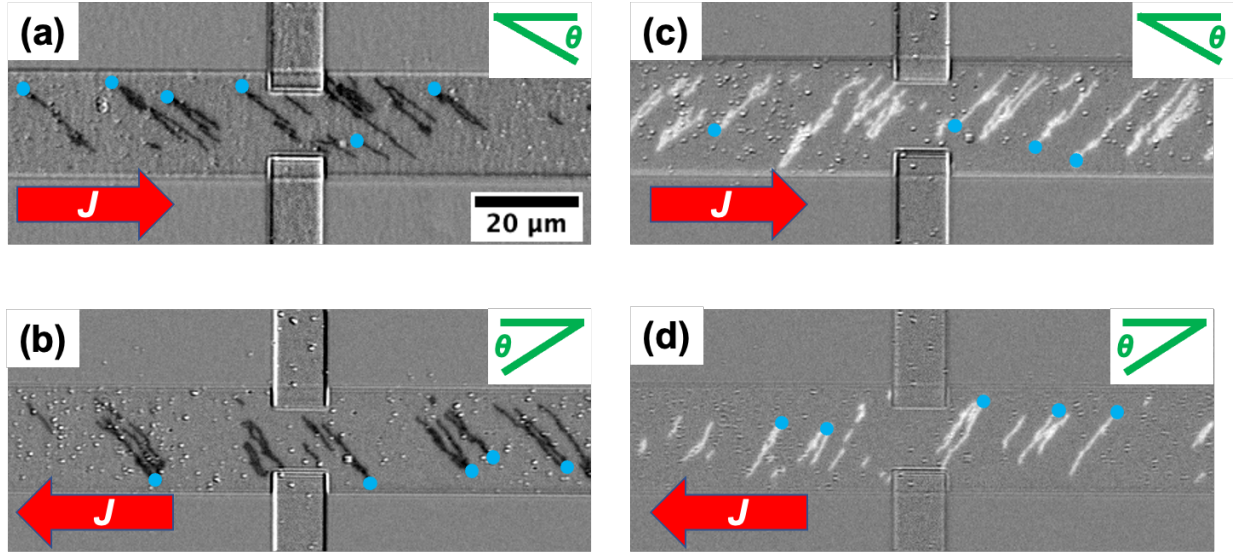


Figure 7.4: Polar MOKE images of the Co/Pt sample after several 10 ms-long current pulses of current density $5.2 \times 10^{11} \text{ A/m}^2$ were applied in zero magnetic field. The conventional current flow direction is indicated in the lower left corner of each subfigure, whereas the convention used to define θ_{growth} is shown in the upper right corners. The lower-right inset of (c) depicts the directional conventions used throughout this work.

In Figure 7.5, we plot the dependence of θ on $J / |v|$ for $+M_z$ domains in the Co/Ni/Pt sample, determined using 10 ms-long current pulses. As has been noted in previous works, we find that θ_{growth} is relatively constant across the J (and hence, $|v|$) values attainable with our experimental setup. While θ_{growth} is expected to saturate in the limit of high $|v|$ - when the impact of pinning relative to the SOT driving force is insignificant (*i.e.*, within the flow dynamical regime)¹⁶ - such behavior at lower speeds, where domain growth is strongly affected by thermally-activated pinning/depinning at defect sites (*i.e.*, the creep dynamical regime^{32,33}) is unexpected. Given that the J values accessible to us are only slightly above the threshold J needed to observe domain

growth, it is reasonable to believe that the domain growth reported here occurs within the creep dynamical regime. As such, the invariance of θ with respect to J is not commensurate with the SkHE in the creep regime.¹⁶

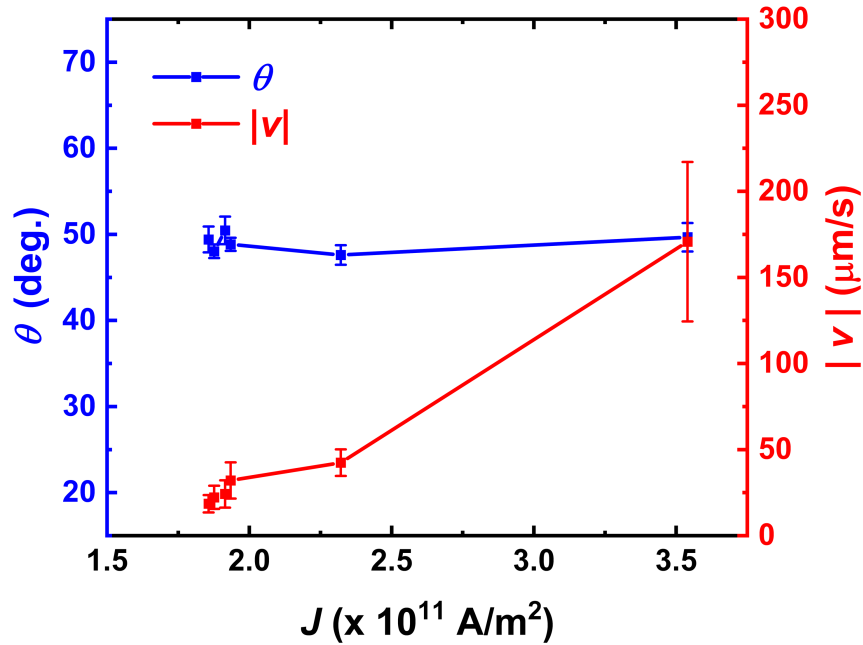


Figure 7.5: For the Co/Ni/Pt sample, the growth direction θ_{growth} and expansion velocity v as a function of applied current density J . The data shown in Figure 7.4 corresponds to the experimental conditions shown in Figure 7.3(a), in which the growth of $+M_z$ domains in response to 10 ms-long current pulses oriented in the $+\hat{x}$ direction was observed.

7.4 Analytical Modeling and Discussion

Based on the earlier discussion of the forces that accompany SOT-based domain expansion, Equation 7.1 can be used to determine the Gilbert damping α that would be required if the transverse domain growth observed in our samples was solely due to the skyrmion Hall effect. When evaluating Equation 7.1, the DW width λ is calculated using the relation $\lambda = \sqrt{A/K_{\text{eff}}}$, assuming that the exchange stiffness $A = 10$ pJ/m, as is typical for FM/HM thin-film multilayers

that have a Curie temperature well above room temperature. Using the static magnetic properties mentioned in Section 7.3, Equation 7.1 dictates that the Co/Ni/Pt sample would need to possess a Gilbert damping of $\alpha \approx 0.01$ if the growth angle of the stripe domains arose entirely from the skyrmion Hall effect. While we have not performed an explicit measurement of α in our samples, past work has shown that an α value of 0.01 is on the lower end of the spectrum of values previously reported for FM/HM structures of similar composition and thickness.^{34,35} It should also be noted that Equation 7.1 was originally derived to describe stripe domain motion in a ferrimagnetic sample near its compensation temperature, where the domain expansion velocity approached 1 km/s,¹⁸ and thus, domain expansion likely occurred within the flow dynamical regime. As such, the applicability of Equation 7.1 to stripe domains moving at the creep-scale velocities reported here is debatable. Based on these points, a further exploration of the possible origins of the significant transverse growth observed in our films in response to SOT is warranted.

When interpreting the growth behavior of stripe domains driven by SOT, the DW magnetization profile is typically assumed to be that which exists at static equilibrium. This static configuration can be determined by minimizing the well-known expression for the DW energy density σ :³⁶

$$\sigma(\theta, \varphi) = 4 \sqrt{AK_{eff}} + \frac{\ln 2}{\pi} t_f \mu_0 M_s^2 \cos^2(\varphi - \beta) - \pi |D| \cos(\beta)$$

Equation 7.2

where t_f is the total ferromagnetic thickness, A is the exchange stiffness parameter, and all other quantities have been defined in previous chapters. We define the DW magnetic orientation (φ) and azimuthal position (β) angles counterclockwise relative to the \hat{x} -direction, as demonstrated in Figure 7.6(a). For the Co/Ni/Pt sample, it is known that the balance between the terms in Equation

7.2 predict the stabilization of left-handed Néel-type DWs in the absence of any external stimulus,²¹ as demonstrated by the half-skyrmion structure shown in Figure 7.6(b).

As detailed in previous works,^{18,20,37,38,39} when SOT acts on a chiral Néel-type DW, four primary forces are thought to govern domain growth: The aforementioned net \vec{F}_{SL} and \vec{F}_G , as well as a viscous drag force \vec{F}_D and the tension due to the pinning potential that opposes domain wall motion \vec{F}_T . When DW motion occurs in the flow regime, the growth directionality in response to SOT is primarily determined by the balance between \vec{F}_G and \vec{F}_{SL} , with \vec{F}_D and \vec{F}_T acting to limit the magnitude of the velocity. In the creep dynamical regime (*i.e.*, the dynamical regime most applicable to our results), however, it is believed that \vec{F}_G should be insignificant relative to \vec{F}_{SL} . \vec{H}_{SL} (which gives rise to \vec{F}_{SL}) can be determined using the expression:

$$\mu_0 \vec{H}_{SL} = \frac{\mu_0 \hbar \theta_{SH}}{2|e|M_s t_f} |J| (\hat{m}_\theta \times \vec{\sigma})$$

Equation 7.3

here \hbar is the reduced Planck constant, θ_{SH} is the spin-Hall angle, e is the charge of the electron, and $\vec{\sigma} = \hat{z} \times \hat{j}_e$ is the spin-polarization axis (where \hat{j}_e is the unit vector in the electron flow

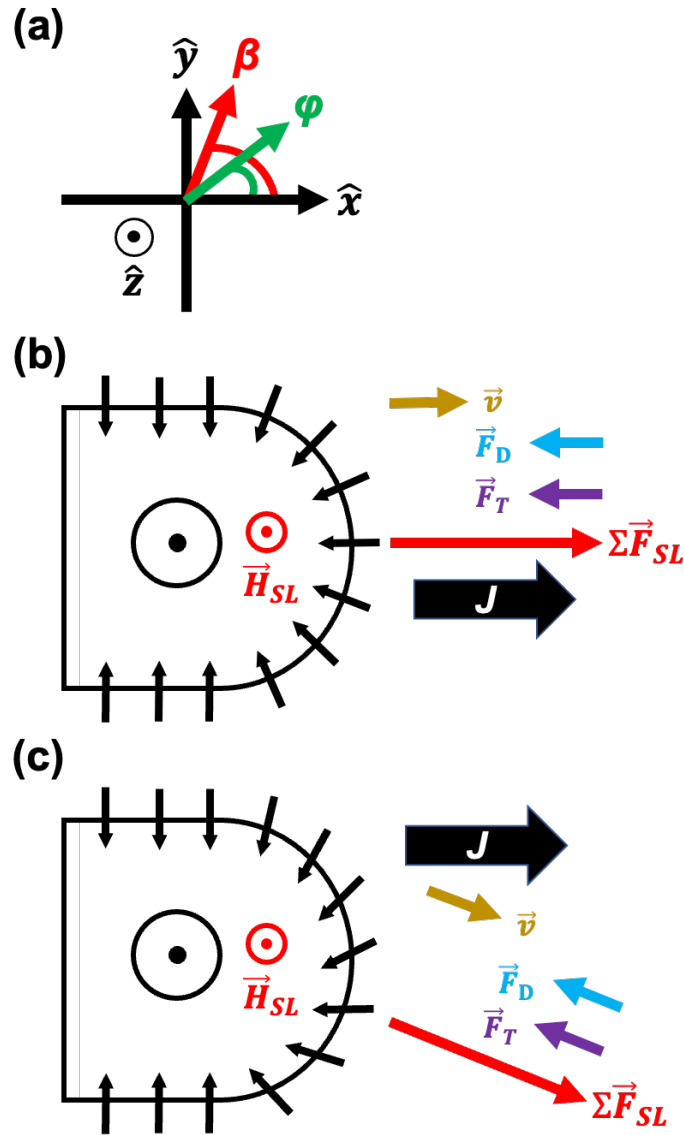


Figure 7.6: (a) The conventions used throughout this chapter to define the azimuthal angle on a half-skyrmion β and the DW core magnetization orientation ϕ . (b,c) Schematic depiction of the DW magnetization profile and SOT force interrelationship in a half-skyrmion assuming the DW magnetization profile is that which exists at static equilibrium (b) and that predicted by the dynamic steady-state reconfiguration.

direction, antiparallel to J). Assuming θ_{SH} is positive (which is reasonable considering the Pt/FM/Ta structure of our samples), a half-skyrmion with chiral Néel-type DWs driven within the creep regime would have the force interrelationship and expansion velocity direction shown

schematically in Figure 7.6(b). Critically, given that the net $\overrightarrow{F_{SL}}$ acting on a half-skyrmion is determined by the azimuthal integration of H_{SL} over the DW and the magnitude and direction of H_{SL} is determined by the orientation of φ relative to J , a half-skyrmion with horizontal mirror symmetry like that shown in Figure 7.6(b) should experience a net $\overrightarrow{F_{SL}}$ that is collinear to J .

As discussed in Chapter 6, it has been shown that the reconfiguration of the DW magnetization profile that occurs when stripe domains with chiral Néel-type DWs are driven by a perpendicular magnetic field within the creep regime dramatically impacts growth directionality of stripe domains when an energy-symmetry breaking in-plane magnetic field is applied.²¹ Since H_{SL} behaves as a perpendicular magnetic field that acts on the DW core magnetization, it should be capable of driving similar reconfigurations of the DW magnetization profile. The steady-state dynamic reconfiguration of the DW magnetization profile (relative to that which exists at static equilibrium) is dictated by the condition:^{21,22}

$$\dot{\varphi} = \frac{|\gamma|}{1 + \alpha^2} \left[-\alpha \left(\frac{\mu_0 \sigma_\varphi}{2\lambda\mu_0 M_s} - \frac{\pi}{2} \mu_0 H_{FL} \right) + \frac{\pi}{2} \mu_0 H_{SL} \right] = 0$$

Equation 7.4

Where $|\gamma|$ is the gyromagnetic ratio and subscripts of σ indicate a partial derivative of Equation 7.3. H_{FL} represents the field-like component of the SOT, which acts as an effective magnetic field collinear to the \hat{y} direction. For a film with PMA, H_{FL} can modify the DW magnetization profile, but is not expected to drive domain expansion. Furthermore, it is believed that the orientation of \vec{H}_{FL} relative to \vec{J} is determined by the composition of the HM layers in which the SOT is generated, not the magnetic configuration of the FM layer.¹ For the Pt seeding and Ta capping layers used in our samples, it has been shown that H_{FL} can be of a similar magnitude as H_{SL} .³¹

A schematic depiction of the steady-state dynamic reconfiguration of the DW magnetization profile predicted by Equation 7.4 for the Co/Ni/Pt sample is shown in Figure 7.6(c).

Comparing Figures 7.6(b) and 7.6(c), the in-plane torque exerted by H_{SL} causes a twisting of the half-skyrmion's DW magnetization profile relative to that at static equilibrium, breaking the horizontal mirror symmetry. For the domain structure shown in Figure 7.6(c), this torque promotes the formation of a DW profile containing a mixture of left-handed Néel and right-handed Bloch components. In line with the previous discussion, the degree of twisting at each azimuthal position is proportional to the scalar product of the magnetic orientation at static equilibrium (*i.e.*, the $\varphi(\beta)$ profile shown in Figure 7.6(b)) and the electron flow direction. Most notably, the azimuthal position at which $|H_{SL}|$ is largest (*i.e.*, where $\varphi = 180^\circ$) is no longer at $\beta = 0^\circ$ but has instead been shifted clockwise around the half-skyrmion. Because of this reconfiguration, the net \vec{F}_{SL} will no longer be purely collinear to \hat{x} , but will contain a component collinear to \hat{y} as well, as has been demonstrated for systems driven by SOT when a magnetic field is applied in the sample plane to realize a reconfiguration of the DW magnetization profile.^{20,40}

In order to compare this theoretical understanding of the impact of in-plane torques on the SOT-driven growth of stripe domains with our experimental results, we have used Equation 7.4 to analytically determine the dynamic steady-state magnetization profile of the Co/Ni/Pt sample induced by H_{FL} . When performing these calculations, we employ the static magnetic properties listed in Section 7.3 along with a Gilbert damping of 0.2, a θ_{SH} value of 0.2,³¹ and assume that $|H_{FL}| = |H_{SL}|$ and is oriented along the $+\hat{y}$ ($-\hat{y}$) direction when J is applied in the $+\hat{x}$ ($-\hat{x}$) direction.¹ Using these parameters, the steady-state DW core magnetic orientation at each azimuthal position around the half-skyrmion $\varphi(\beta)$ was obtained for a variety of J -values, as shown in Figure 7.7(a). Referencing the conventions for φ and β shown in Figure 7.6(a), the SOT effective fields successively twist the magnetization away from the static equilibrium configuration (*i.e.*, that when $J = 0$) in a clockwise manner. Next, we consider how the $H_{SL}(\beta)$ profile is impacted by the SOT-

induced reconfiguration of $\varphi(\beta)$. Using Equation 7.3, we have calculated the H_{SL} experienced at each azimuthal position on the half skyrmion, as shown in Figure 7.6(b). To aid in comparing between curves calculated using different J -values, we have normalized the H_{SL} values to the respective maximum value in each curve. Like the $\varphi(\beta)$ curves, $H_{\text{SL}}(\beta)$ is no longer symmetric about $\beta = 0$ when $J > 0$.

To understand how these changes in the symmetries of the $\varphi(\beta)$ and $H_{\text{SL}}(\beta)$ profiles affect the growth directionality of half-skyrmions, we have employed the Thiele equation-based technique proposed in Ref. 20. Using our calculated $\varphi(\beta)$ profiles to obtain the x and y components of the net F_{SL} via integration, it is possible to assign a directionality to the net F_{SL} acting on a half-skyrmion. As previously discussed, we assume that our experiments occur in the creep dynamical regime; as such, we do not incorporate the skyrmion Hall effect into our determination of a favored growth direction. In Figure 7.7(c), we show the analytically predicted growth direction of half-skyrmions for different permutations in domain polarity, current density magnitude, and current density flow direction, along with experimentally determined data. While the symmetry of the growth directionality is similar between experiment and modeling, there are notable discrepancies between the two – particularly as it relates to the dependence of θ_{growth} on $|J|$. While the analytical modeling suggests that θ_{growth} should show a strong variation with $|J|$, our experimental results show little to no relationship between these two quantities. In previous reports of half-skyrmion growth directionality rooted in the skyrmion Hall effect, a similar, quizzical invariance of θ_{growth} with $|J|$ has been noted.^{19,20} Indeed, in previous studies of the SOT-induced growth directionality of bubble domains in nanoscale-confined architectures that did account for a reconfiguration of

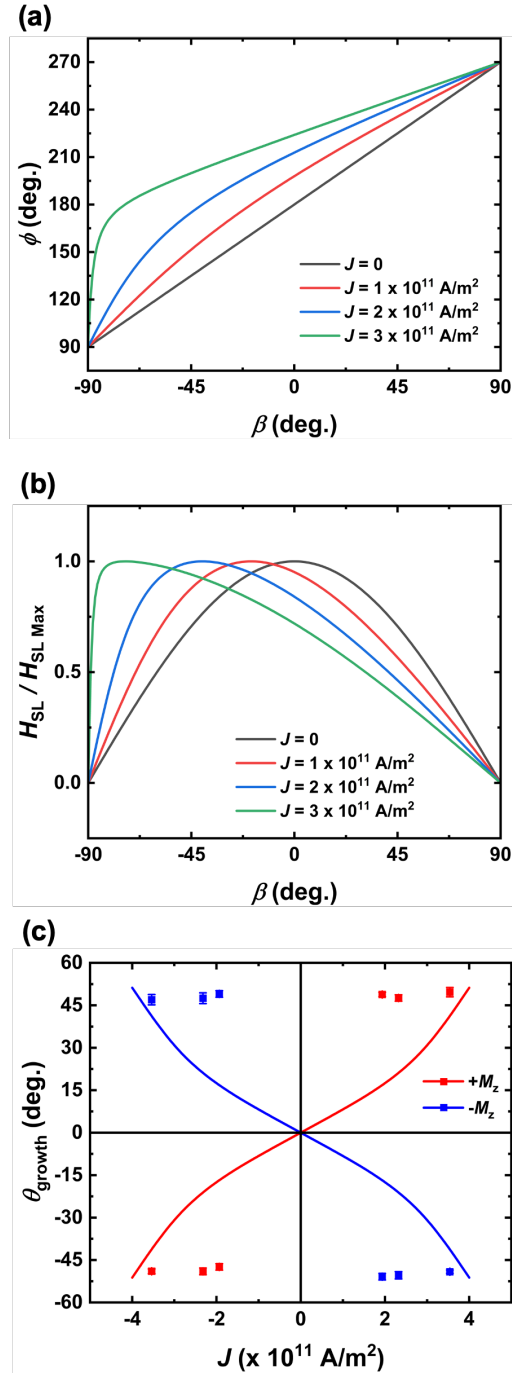


Figure 7.7: (a) DW core magnetization orientation ϕ and (b) normalized Slonczewski effective perpendicular field H_{SL} as a function of azimuthal position β on a $+M_z$ half-skyrmion in the Co/Ni/Pt sample for several current densities. In (a) and (b), the conventional current direction is along the $+x$ -direction indicated in Figure 7.6(a). (c) Experimentally (solid markers) and analytically determined favored growth direction of half-skyrmions in the Co/Ni/Pt sample for different permutations in current density magnitude and directionality and half-skyrmion perpendicular polarization. The domain growth direction θ_{growth} is defined using the conventions shown in the insets of Figure 7.3.

the DW magnetization profile due to in-plane torques, θ_{growth} was found to be static even when the expansion velocity was varied over three orders of magnitude by changing $|J|$.^{41,42} As such, while our analytical approach correctly predicts the symmetries and general directionality of half-skyrmion growth in response to SOT, further work is needed to understand the particular balance of forces that could be responsible for observed independence between $|\theta_{\text{growth}}|$ and $|J|$ in the creep regime of SOT-driven stripe domain growth.

7.5 Conclusion

We have performed an experimental and analytic study of the growth directionality of dendritic stripe domains in response to spin-orbit torque in several ferromagnet/heavy metal multilayer systems. In line with previous reports, it was found that the stripe domains exhibit a significant transverse growth component relative to the applied current axis, and that this growth component exhibits specific symmetries with respect to the domain polarity and conventional current direction. While previous treatments attributed these growth behaviors to the skyrmion Hall effect by considering the tips of stripe domains to be half-skyrmions, we have analytically shown that the in-plane torques originating from the spin-orbit torque effective fields can promote growth directionality with the same symmetries as the skyrmion Hall effect, well within the creep dynamical regime.

Chapter 7 is based on a manuscript being prepared for submission to a journal as “Interplay of the half-skyrmion topology and spin-orbit torque on the growth directionality of magnetic stripe domains” by J.A. Brock and E.E. Fullerton. The dissertation author was the primary investigator and author of the manuscript. This work was supported by the National Science Foundation, Division of Materials Research (Award #: 2105400).

7.6 References

- ¹ S. Emori, U. Bauer, S.-M. Ahn, E. Martinez, and G.S.D. Beach, *Nature Mat.* **12**, 611 (2013).
- ² K.-S. Ryu, L. Thomas, S.-H. Yang, and S.S.P. Parkin, *Nature Nanotech.* **8**, 527 (2013).
- ³ M.I. Dyakonov and V.I. Perel, *Phys. Lett. A* **35**, 459 (1971).
- ⁴ J.E. Hirsch, *Phys. Rev. Lett.* **83**, 1834 (1999).
- ⁵ L. Liu, O.J. Lee, T.J. Gudmundsen, D.C. Ralph, and R.A. Buhrman, *Phys. Rev. Lett.* **109**, 096602 (2012).
- ⁶ A. Fert, *Mat. Sci. For.* **59-60**, 439 (1990).
- ⁷ H. Yang, A. Thiaville, S. Rohart, A. Fert, and M. Chshiev, *Phys. Rev. Lett.* **115**, 267210 (2015).
- ⁸ J. Sampaio, V. Cros, S. Rohart, A. Thiaville, and A. Fert, *Nat. Nanotech.* **8**, 839 (2013).
- ⁹ A. Soumyanarayanan, N. Reyren, A. Fert, and C. Panagopoulos, *Nature* **539**, 509 (2016).
- ¹⁰ C. Moreau-Luchaire, C. Moutafis, N. Reyren, J. Sampaio, C.A.F. Vaz, N. Van Horne, K. Bouzouane, K. Garcia, C. Deranlot, P. Warnicke, P. Woehluter, J.-M. George, M. Weigand, J. Raabe, V. Cros, and A. Fert, *Nature Nanotech.* **11**, 444 (2016).
- ¹¹ S. Woo, K. Litzius, B. Kruger, M.-Y. Im, L. Caretta, K. Richter, M. Mann, A. Krone, R.M. Reeve, M. Weigand, P. Agrawal, I. Lemesh, M.-A. Mawass, P. Fischer, M. Klaui, and G.S.D. Beach, *Nature Mater.* **15**, 501 (2016).
- ¹² K. Everschor-Sitte, J. Masell, R.M. Reeve, and M. Klaui, *J. Appl. Phys.* **124**, 240901 (2018).
- ¹³ S. Rohart, J. Miltat, and A. Thiaville, *Phys. Rev. B* **93**, 214412 (2016).
- ¹⁴ J.D. Zang, M. Mostovoy, J.H. Han, and N. Nagaosa, *Phys. Rev. Lett.* **110**, 207202 (2013).
- ¹⁵ K. Everschor-Sitte and M. Sitte, *J. Appl. Phys.* **115**, 172602 (2014).
- ¹⁶ W. Jiang, X. Zhang, G. Yu, W. Zhang, X. Wang, M.B. Jungfleisch, J.E. Pearson, X. Cheng, O. Heinonen, K.L. Wang, Y. Zhou, A. Hoffmann, and S.G.E. te Velthuis, *Nature Phys.* **13**, 162 (2017).
- ¹⁷ K. Litzius, I. Lemesh, B. Kruger, P. Bassirian, L. Caretta, K. Richter, F. Buttner, K. Sato, O.A. Tretiakov, J. Forster, R.M. Reeve, M. Weigand, I. Bykova, H. Stoll, G. Schutz, G.S.D. Beach, and M. Klaui, *Nature Phys.* **13**, 170 (2017).

-
- ¹⁸ Y. Hirata, D.-H. Kim, S.K. Kim, D.-K. Lee, S.-H. Oh, D.-Y. Kim, T. Nishimura, T. Okuno, Y. Futakawa, H. Yoshikawa, A. Tsukamoto, Y. Tserkovnyak, Y. Shiota, T. Moriyama, S.-B. Choe, K.-J. Lee, and T. Ono, *Nature Nanotech.* **14**, 232 (2019).
- ¹⁹ S. Zhang, X. Zhang, J. Zhang, A. Ganguly, J. Xia, Y. Wen, Q. Zhang, G. Yu, Z. Hou, W. Wang, Y. Peng, G. Xiao, A. Mancon, J. Kosel, Y. Zhou, and X.-X. Zhang, *Sci. Adv.* **6**, 1876 (2020).
- ²⁰ S. Yang, K.-W. Moon, C. Kim, D.-H. Kim, J. Shin, J. Hong, S.K. Kim, and C. Hwang, *Adv. Quantum Technol.* **4**, 2000060 (2021).
- ²¹ J.A. Brock, M.D. Kitcher, P. Vallobra, R. Medapalli, M.P. Li, M. De Graef, G.A. Riley, H.T. Nembach, S. Mangin, V. Sokalski, and E.E. Fullerton, *Adv. Mat.* **33**, 2101524 (2021).
- ²² L. Sanchez-Tejerina, O. Alejos, and E. Martinez, *J. Magn. Magn. Mater.* **423**, 405 (2017).
- ²³ P.P.J. Haazen, *Nature Mater.* **12**, 299 (2013).
- ²⁴ I.M. Miron, *Nature* **476**, 189 (2011).
- ²⁵ S. Emori, E. Martinez, K.-J. Lee, H.-W. Lee, U. Bauer, S.-M. Ahn, P. Agrawal, D.C. Bono, and G.S.D. Beach, *Phys. Rev. B* **90**, 184427 (2014).
- ²⁶ O. Boulle, S. Rohart, L.D. Buda-Prejbeanu, E. Jue, I.M. Miron, S. Pizzini, J. Vogel, G. Gaudin, and A. Thiaville, *Phys. Rev. Lett.* **111**, 217203 (2013).
- ²⁷ A.V. Khvalkovskiy, *Phys. Rev. B* **87**, 020402 (2013).
- ²⁸ S.-G. Je, D.H. Kim, S.C. Yoo, B.C. Min, K.J. Lee, and S.B. Choe, *Phys. Rev. B* **88**, 214401 (2013).
- ²⁹ L. Liu, C.-F. Pai, Y. Li, H.W. Tseng, D.C. Ralph, and R.A. Buhrman, *Science* **336**, 555 (2012).
- ³⁰ M. Althammer, S. Meyer, H. Nakayama, M. Schreier, S. Altmannshofer, M. Weiler, H. Huebl, S. Geprags, M. Opel, R. Gross, D. Meier, C. Klewe, T. Kuschel, J.-M. Schmalhorst, G. Reiss, L. Shen, A. Gupta, Y.-T. Chen, G.E.W. Bauer, E. Saitoh, and S.T.B. Goennenwein, *Phys. Rev. B* **87**, 224401 (2013).
- ³¹ S. Woo, M. Mann, A.J. Tan, L. Caretta, G.S.D. Beach, *Appl. Phys. Lett.* **105**, 212404 (2014).
- ³² C. Reichardt, D. Ray, and C.J.O. Reichardt, *Phys. Rev. Lett.* **114**, 217202 (2015).
- ³³ C. Reichardt and C.J.O. Reichardt, *New J. Phys.* **18**, 095005 (2016).
- ³⁴ S. Mizukami, E.P. Sajitha, D. Watanabe, F. Wu, T. Miyazaki, H. Naganuma, M. Oogane, and Y. Ando, *Appl. Phys. Lett.* **96**, 152502 (2010).

-
- ³⁵ J.-M. Beaujour, D. Ravelosona, I. Tudosa, E.E. Fullerton, and A.D. Kent, *Phys. Rev. B* **80**, 180415(R) (2009).
- ³⁶ J.P. Pellegren, D. Lau, and V. Sokalski, *Phys. Rev. Lett.* **119**, 027203 (2017).
- ³⁷ W. Jiang, P. Upadhyaya, W. Zhang, G. Yu, M.B. Jungfleisch, F.Y. Fradin, J.E. Pearson, Y. Tserkovnyak, K.L. Wang, O. Heinonen, S.G.E. te Velthuis, and A. Hoffmann, *Science* **349**, 283 (2015).
- ³⁸ R. Tomasello, E. Martinez, R. Zivieri, L. Torres, M. Carpentieri, and G. Finocchio, *Sci. Rep.* **4**, 06784 (2014).
- ³⁹ A.A. Thiele, *Phys. Rev. Lett.* **30**, 230 (1972).
- ⁴⁰ X. Zeng, Q. Jia, S. Sun, Y. Guo, B. Wang, Y. Wang, and J. Cao, *J. Phys. D: Appl. Phys.* **54**, 475001 (2021).
- ⁴¹ C.K. Safeer, E. Jue, A. Lopez, L. Buda-Prejbeanu, S. Auffret, S. Pizzini, O. Boulle, I.M. Miron, and G. Gaudin, *Nature Nanotech.* **11**, 143 (2016).
- ⁴² E. Martinez, O. Alejoa, M.A. Hernandez, V. Raposo, L. Sanchez-Tejerina, and S. Moretti, *Appl. Phys. Expr.* **9**, 063008 (2016).

Chapter 8: Conclusion

8.1 Dissertation Summary

In this dissertation, we have presented several studies of the stabilization and dynamics of chiral domain walls in a variety of thin film heterostructures – employing experimental, analytic, and micromagnetic investigations. A key underlying theme between the five separate studies presented herein was the control of magnetic chirality through the interfacial Dzyaloshinskii-Moriya interaction that develops at the interface between thin ferromagnetic layers and heavy metals with large spin-orbit coupling.

In Chapter 3, we presented an experimental study of the impacts of electrical currents and magnetic fields on the processes by which skyrmions can be generated from the dynamics of magnetic textures. Besides demonstrating a correspondence between results in our simple sample geometry to recent theoretical work and experimental studies that employed more complicated sample architectures, we were able to demonstrate the critical role that pinning sites and Oersted fields play in describing our observations.

In Chapter 4, we systematically studied the role that Joule heating can play in driving transitions between domain morphologies, including from the labyrinthine stripe to the skyrmion phase. Through materials engineering, it was possible to demonstrate how modifying the basic physical properties of a material (such as the saturation magnetization and the degree of perpendicular magnetic anisotropy) can dramatically reduce the amount of Joule heating needed to drive morphological phase transitions. These experimental observations were bolstered

extensive simulations of the transient thermal response of our samples due to applied current pulses.

In Chapter 5, we investigated the domain morphology transition that occurs in the limit of low exchange stiffness, and how this transition fosters the stabilization of skyrmions in an applied magnetic field. Using analytic and micromagnetic modeling, we were able to demonstrate how a reduced exchange stiffness drastically reduces the energy penalty associated with forming domain walls, promoting the formation of domain states (including skyrmion phases) in systems with substantial perpendicular magnetic anisotropy. Using experimental techniques with higher spatial and temporal resolution, we have begun to explore the nature of the observed morphological phase transition in greater detail and have identified significant parallels with previous work on superparamagnetic phase transitions.

In Chapter 6, we presented work regarding the field-driven dynamics of dendritic stripe magnetic domains that possess chiral domain walls and characterized a new effect in which domains can unidirectionally expand in response to applied magnetic fields with symmetries that could not be understood from the static energy frameworks typically employed when interpreting such results. Using analytic models, it was found that the in-plane torques generated by perpendicular magnetic fields can stabilize steady-state magnetization profiles that are highly asymmetric in elastic energy, resulting in unconventional growth directionalities that match the experimental observations.

In Chapter 7, we examined the impacts of spin-orbit torque on the growth directionality of dendritic stripe magnetic domains. While our observations are in line with previous reports that attributed this behavior to the Magnus force-like skyrmion Hall effect, we believe that the creep-scale velocity of domain expansion in our experiments precludes this explanation. Building off

some of the work presented in Chapter 6, we demonstrate that the effective perpendicular magnetic fields associated with the spin-orbit torque generate in-plane torques that drive a reconfiguration of the domain wall magnetization profile that matches the experimentally observed growth symmetries with respect to domain and electrical current polarity.

8.2 Future Outlook

The work presented in this thesis has raised additional lines of inquiry that we would be remiss to not acknowledge. As detailed in Section 5.6, we are presently investigating the spatiotemporal dynamics of the morphological phase transition observed in the limit of low exchange stiffness in materials with significant perpendicular magnetic anisotropy. In addition to the ac susceptibility measurements discussed in this dissertation, we are currently laying the groundwork with our collaborators to study the spatiotemporal fluctuations in these samples using specialized techniques, including nitrogen vacancy probes, photoemission electron microscopy, and coherent soft X-ray scattering.

In Chapter 6, we demonstrated how perpendicular driving fields coupled with a Néel-type domain wall chirality and energy symmetry-breaking in-plane magnetic field can induce novel domain growth directionalities in Co/Ni/Pt-based films. However, we have found that this behavior is not ubiquitous to material systems that have a Néel-type domain wall chirality and reverse via dendritic stripe domains. As such, further work is needed to understand the balance in material parameters (*e.g.*, Dzyaloshinskii-Moriya interaction energy density, Gilbert damping, perpendicular magnetic anisotropy, etc.) necessary to elicit the domain growth behaviors seen in the Co/Ni/Pt-type samples.

In Chapter 7, we found that spin-orbit torque effective fields can drive steady-state reconfigurations of the domain wall magnetization profile that match the experimentally observed growth symmetries of dendritic stripe domains – behavior that has previously been attributed to the skyrmion Hall effect. However, as noted in the chapter and in previous works, the invariance in the growth behavior with respect to the current density magnitude is not expected from either explanation. More work is needed to understand the balance of forces that could give rise to this behavior.